Gravitational Instabilities Beneath the Continents

Adam Philip Joseph Beall

OCRID ID: orcid.org/0000-0002-7182-1864

A thesis presented for the degree of

Doctor of Philosophy

Submitted in December 2016

School of Earth Sciences, University of Melbourne

Supported by the Geological Survey of Western Australia

This thesis is being submitted in total fulfilment of the Doctor of Philosophy, and is not being completed under a jointly awarded degree.

Summary

Unlike the oceanic crust and lithosphere, which cover approximately two thirds of the Earth's surface, the continents are generally not considered to participate in any large scale recycling into the Earth's interior. This is a key part of the model of plate tectonics, which is successful in describing the majority of the Earth's large scale evolution, but falls short in describing continental evolution (Turcotte & Schubert 2014). Dense material is expected to form at the base of the continents, such as the formation of almost 7km of dense restite for every 1km of felsic crust (Hawkesworth & Kemp 2006), as well as $60-110$km of negatively buoyant mantle lithosphere (Poudjom Djomani et al. 2001; Cooper et al. 2004). The former must be recycled during the formation of continental crust, as it is generally not present (Rudnick et al. 1995), while the latter is generally present but likely to become unstable at geological time-scales when it is perturbed by tectonic activity (Houseman & Molnar 2001). The purpose of this thesis is to further constrain how this recycling generally occurs and its impact on the continental crust, on the modern Earth, as well as before and during the initiation of tectonics in the Archean.

Sub-continental gravitational instabilities have been observed evolving at the present, predominately using seismic tomography. Arguably the clearest example is the hanging restite beneath the Great Valley and Sierra Nevada, California (Zandt et al. 2004; Jones et al. 2014; Saleeby et al. 2003). Other proposed instabilities occur beneath the Colorado Plateau (Levander et al. 2011), North Island, New Zealand (Stern et al. 2013) and the Carpathians (Houseman & Gemmer 2007). However, some of these could arguably be related to subduction (Carpathians and New Zealand, Wortel & Spakman (2000); Lamb (2011)) or occur within a larger regime of intra-plate activity (Colorado, Roy et al. (2009)). Others have recently finished, such as beneath the Anatolian Plateau (Göğüş & Pysklywec 2008b) and Canadian Cordillera (Bao et al. 2014), so are inferred primarily from remnant dynamic topography. No instabilities have been confidently inferred from the rock record $>$ 1Ga ago, the closest being the debated formation mechanism of intraplate orogenies such as in the Tian Shan (Neil & Houseman 1999) and Central Australia (Pysklywec & Beaumont 2004; Gorczyk et al. 2012).

Instabilities are typically described using the Rayleigh-Taylor Instability (RTI) model, also known

as dripping, which has been rigorously characterised (Chandrasekhar 1961). Dripping evolves by exponential growth of an initially small perturbation at the base of a dense material. Delamination is an alternative mechanism which involves the peeling away of the entire dense material, where the top of the body is displaced at a similar rate to its base (Bird 1979). The term delamination is sometimes applied to the RTI (e.g. Elkins-Tanton (2007)) and its mechanism is poorly understood. How the dynamic topography and volcanism generated by delamination may differ from dripping has received recent attention (Göğüş & Pysklywec 2008a; Wang & Currie 2015), but how the mechanisms may differ in their fundamental growth has been neglected. In **Chapter 3**, the fundamental growth of the two mechanisms is compared. We define delamination morphologically by the ability of the dense material to be displaced while maintaining a constant thickness, as well as the degree to which its internal strain is accommodated by bending. This definition is well suited to distinguishing models of delamination from dripping, as the latter grows through changes to the material's thickness and significant internal shear-strain. We show that whether the RTI mechanism or delamination dominates depends on the viscosity of a lower crustal layer relative to the viscosity of the dense body (η_c') as well as the degree to which the dense body has been thinned (D'), where $D' = 1$ is complete thinning. Delamination requires highly specific conditions to be initiated: a lower crustal layer two orders of magnitude weaker than the dense body ($\eta_c' \leq 10^{-2}$) must be present and one edge of the body must be completely exposed to the asthenosphere ($D' = 1$), through strike-slip displacement or complete thinning. If these conditions are almost met, for example a weak layer is present but not sufficiently weak ($\eta_c' > 10^{-2}$) or an edge displacement occurs, but only penetrates part of the dense body ($D' < 1$), delamination does not occur. We demonstrate that under these circumstances, dripping also does not occur strictly according to the RTI and the mechanism is described as a mixture of dripping and delamination, called triggered dripping.

Using numerical models, we show that displacement by delamination grows exponentially through time, like the RTI, though at an order of magnitude higher growth-rate. We justify the direct comparison by extending the analytical model of Bird (1979) to demonstrate that the delamination growth-rate is linearly proportional to the dense body's buoyancy and inversely proportional to its viscosity, as occurs for dripping. We show that this growth-rate depends on the viscosity (η_c') and thickness (L_c') of the weak lower crustal layer relative to the dense body, varying proportionally to $L_c'^2/\eta_c'^{\frac{2}{3}}$. This order of magnitude higher growth-rate and new scaling only occurs for delamination. Despite a resemblance in initial conditions, triggered dripping grows by thickening, rather than peeling and as a result grows at a time-scale closer to the significantly slower dripping. Triggered dripping can generate a similar magnitude and migration of topography to delamination. Therefore the previously proposed diagnostics for distinguishing between dripping and delamination are not necessarily able to verify the occurrence of the delamination end-member defined here and subsequently its characteristic high growth-rate.

Another difference between dripping and delamination is morphology. Dripping can occur with either a predominately 2D 'planar' morphology or 3D 'drips'. Delamination involves bending around one axis and so by definition requires a planar morphology. As we use 2D models for the delineation of dripping, delamination and triggered dripping, there is the possibility that some models could revert to dripping when modelled in 3D. We analyse this using 3D models with thermal diffusion. The presence of a weak layer encourages the sustenance of a planar perturbation. When $\eta_c' = 10^{-2}$, planar flow survives without reverting to dripping, provided $D' > 0.3$. Therefore any model for which the delamination criteria are met is unlikely to revert to a dripping morphology. Triggered dripping however could begin with a planar morphology and revert to dripping, if $\eta_c' \approx 1$. This may explain why the unstable restite beneath the Sierra Nevada, California, was likely to have initiated with a planar perturbation but now has a drip morphology (Jones et al. 2004; Frassetto et al. 2011). The restite would be required to be strongly coupled to the lower Great Valley crust, which is supported by modern subsidence (Saleeby & Foster 2004).

The contrasting growth-rates of the different instability mechanisms complicates the relationship between lower crustal or lithospheric rheology and growth time-scale. Any prediction of growth-rate from inferred rheology could be erroneous by an order of magnitude if the mechanism is incorrectly determined. The mechanism characterisation supports a general model for the recycling of dense bodies, where material with a relatively high viscosity requires recycling by delamination and therefore must be tectonically activated, whereas weaker bodies are able to drip, all potentially at the typically observed 10Ma time-scale.

If the displacement of a sinking body is predicted from the exponential growth-rate model, which is applicable for both dripping and delamination, its velocity should be extremely high when the perturbation has reached high displacement. If it takes approximately 10Ma for an unstable body to at least double in thickness, as indicated from migration data (Jones et al. 2004; Crow et al. 2011; Stern et al. 2013), the body should only be hanging beneath the continent at a displacement observable in tomography, for $\sim$ 1Ma. The observance of a number of hanging dense bodies on the modern Earth is then either highly coincidental, or their initially rapid exponential growth has at some point slowed down. We propose a stalling mechanism in **Chapter 4**, in which instabilities which begin by delamination and revert to dripping can produce this slowing effect. Stalling occurs as a result of the contrasting growth-rates described for dripping and delamination. A sinking body which exponentially grows by a peeling instability and migrates into a region in which non-linear peeling cannot be sustained will switch to exponential growth by thickening (RTI), with its fundamentally lower growth-rate. The largest stalling occurs when the weak decollement zone is confined to a lateral distance approximately equivalent to the dense body's thickness. In this case, a sinking body which stalls will hang beneath the continent for about five times longer than if it were allowed to continue delaminating. The stalling

can also occur dynamically, if the decollement zone cools down and strengthens more quickly than delamination can occur. This can provide an even greater slowing effect if the cooling also reduces the perturbation D'.

The stalling of instabilities can only occur when delamination switches to dripping. The highest degree of slowing of a dripping instability modelled is $\sim 20\%$, which is negligible. This is because the non-linear feedback which drives the RTI occurs at the base of the dense body, so the growing perturbation would need to be dampened in order to produce significant slowing. The non-linear feedback for delamination occurs in the lower crust and so is extremely sensitive to lateral rheological variation. Observations of stalling on the modern Earth therefore support the occurrence of delamination, which appears to be limited to a rapid episode before stalling occurs and it reverts to dripping.

Generation of stable crust on the modern Earth is often facilitated by tectonic processes. The removal of dense restite for example requires high degrees of offset or thinning for delamination to occur. Another important step in the generation of stable continental crust is the transportation of materials rich in heat-producing elements, such as granite, to the upper crust (Sandiford 2010). This generally occurs by orogenesis. In the Palaeoarchean crust, such as the Pilbara (Western Australia) and Kaapvaal (South Africa), the transport of granite into the upper crust occurred by RTIs in the absence of tectonics (Van Kranendonk et al. 2007; Van Kranendonk 2011). The RTI occurred as a result of the layering of dense greenstone above less dense granite (Mareschal & West 1980), as well as significant weakening of the crust as a result of a high geotherm (Robin & Bailey 2009; Sandiford et al. 2004). The rising granite domes and sinking greenstone keels are preserved as the dome and keel structures. Dome and keel formation is generally considered as occurring in isolation. However, significant amounts of restite are produced during the formation of felsic crust (Bédard 2006), just as in the modern Earth, but also occurring at shallower depths (Smithies & Champion 2000) and therefore close to granite base prior to doming. Modern restite recycling typically produces vertical motions of the crust, which is generally too strong for significant deformation (e.g. Stern et al. (2013)). Instabilities may have caused significant crustal thickening in the past, resulting in intraplate orogenesis (Neil & Houseman 1999), but this is difficult to distinguish from tectonics. As there is no evidence of tectonics and the crust is extremely sensitive to local buoyancy related stresses, the Palaeoarchean crust could be expected to preserve strain resulting from restite recycling below. Unlike the younger Archean such as the Yilgarn (Western Australia), there is little evidence of overprinting deformation during dome formation (Drummond et al. 2000; Van Kranendonk et al. 2007).

In **Chapter 5**, we use analytical models to study the relative growth of the two crustal instabilities; restite recycling and dome and keel formation. In the case that the granite and restite layers have similar viscosities and thicknesses, the two instabilities are likely to have similar growth-rates and grow

predominately at a similar wavelength. In this situation, the growth of the two instabilities can be described by the exponential growth of a single instability, where the restite sinks below where domes are forming. This coupled solution occurs for a reasonable range of relative densities and crustal rheology. The assumption of the similar granite and restite viscosities is supported by the wavelength of the domes, which cannot be reproduced if the base of the granite is fixed by a stronger material below. Additionally, where the upper 5km of the greenstone have not been serpentinised and weakened, the lower greenstone layer is required to be very weak in order to produce the observed dome wavelength. This crustal viscosity structure is independently supported by models incorporating experimental rheology data and a high geotherm (Robin & Bailey 2009).

If the restite layer was able to grow to twice the thickness of the granite, its time-scale and dominant wavelength would have been much faster and larger respectively than dome and keel formation. The weak crust implied by dome and keel formation would allow the sinking restite to impart a large wavelength shear strain on the granite. The restite would also thicken the granite enough to force subsequent dome and keel formation to occur at a larger wavelength than is preserved. If an instability of such a thick restite occurred, it must have been prior to the weakening event required for dome and keel formation.

The viscosity of the lower greenstone layer can act as a switch for dome and keel formation: if its viscosity lowers from equal to the granite to even one order of magnitude weaker, the growth-rate of dome and keel formation accelerates by more than an order of magnitude, supporting the thermal blanketing model of Sandiford et al. (2004). A strong lithosphere beneath the restite can act as a switch for restite recycling. If the lithosphere is two orders of magnitude stronger than the restite, it slows down the restite by an order of magnitude, effectively trapping it. However as soon as the restite grows to twice the thickness of the granitoid, it can drip through at the dome and keel time-scale. The restite is therefore generally recycled at a similar time-scale to dome and keel formation, which is likely to have been at the 10Ma scale. This supports a general model where restite was progressively recycled as a felsic lower crust formed, before dome and keel formation was activated by weakening of the crust. Then any last remnant of restite could have plausibly dripped away simultaneously with the rising domes, generating a stable crust purely through RTIs.

The Palaeoarchean crust is likely to have formed in the absence of tectonics, which is complemented at the lithosphere and mantle convection scale by the stagnant lid convective regime (Solomatov & Moresi 2000). Zones of extreme localised crustal weakness are required to facilitate subduction and in their absence no surface material can be recycled into the mantle (Moresi & Solomatov 1998). When the lithospheric 'lid' is unable to be recycled into the mantle, convection instead occurs rapidly below and the heat is transferred through the lid by conduction or melt transport. The stable thermal

boundary layer in the stagnant lid regime is thick, assuming melt is transported through it, providing a significant amount of gravitational potential energy which is released when plate tectonics initiates (Van Thienen et al. 2004; O'Neill et al. 2007; Moore & Webb 2013). This results in a large scale RTI which generates extremely high stresses (**Chapter 6**). As some lithosphere has survived the transition to tectonics (Griffin et al. 2003; Condie et al. 2009a), the lid breaking process needs to be consistent with the survival of some continental fragments, which are likely to have recorded some major geological event marking the transition.

In **Chapter 6**, we propose that the lid breaking instability shaped the thick cratonic keels which are still preserved beneath Archean crust. The primary motivation is that if the keels began as a harzburgitic layer within the stagnant lid with an extremely high yield strength, the high stress lid breaking event could form the keels and provide keel stability as long as the tectonic Earth has been unable to return the keels to that high stress state. Using numerical mantle convection models of the transition from stagnant lid to mobile lid, following (Moore & Webb 2013), the density and yield strength of a layer of continental material is varied to quantify the conditions for keel formation and stability. For reasonable parameters, a 300km thick keel can form and stabilise during lid breaking. This occurs by significant thrusting within the keel. Due to the thickening of buoyant lithosphere, the crust experiences rapid uplift in the order of 10km when the dense mantle lid breaks off. This predicted regional exhumation could explain why the middle crust of Archean terranes is typically exposed at the surface.

The stress state experienced by the keel through time supports the notion that lid breaking is a high stress event. The keel stress magnitude is about four times higher during lid breaking compared to during the mobile lid regime afterwards. The stress state immediately after the initiation of tectonics is compared to the modern Earth by scaling stress according to a declining Rayleigh number (Ra). For a Rayleigh number decrease of one order of magnitude, corresponding to 200° cooling, convective stresses have not returned to the lid breaking stress state. This return would have occurred about 1Ga for a Rayleigh decrease of two orders of magnitude. Using geochemical models of crustal thickness through time as a proxy for subduction stress, the convective stress increased rapidly from $3 - 1$Ga, before peaking at 75% of the lid breaking stress. Therefore the keel formation by lid breaking model is predicted to have formed keels which would still be stable on the modern Earth. This is consistent with the inference that the most recent craton destruction events have been facilitated by volatile induced weakening (Griffin et al. 1998; Lee et al. 2011).

Abstract

The evolution of dense lower crust or lithosphere sinking from below continental crust is analysed using numerical and analytical models. The dripping and delamination mechanisms are typically used to describe modern instabilities, but their relative growth has not been quantified. Delamination is an exponentially growing instability which scales in the same way as for dripping, but grows more quickly by an order of magnitude. Its growth-rate is highly dependent on the viscosity and thickness of the lower crust which is captured in a scaling law. If specific conditions for its initiation are not completely met, a third mechanism called triggered dripping is activated. It is practically indistinguishable from delamination, but its slower growth is more similar to dripping. The characterisation of these mechanisms leads to a general model in which relatively stronger dense bodies must be recycled by delamination, requiring tectonic activation, whereas weaker bodies are likely to drip. The contrasting growth-rates of dripping and delamination can be used to understand why modern instabilities often appear to grow quickly and then stall. If an instability begins under conditions suitable for delamination, but migrates into a zone of higher lower crustal strength, it will revert to dripping and slow down by at least a factor of five.

The recycling of dense restitic material from beneath Archean crust is explored by predicting how its growth would compare to the intra-crustal instabilities preserved as granite dome and greenstone keel structures. Using the wavelength and lack of overprinting deformation of the preserved granite domes as constraints, a specific crustal viscosity profile can be inferred. Restite recycling and dome and keel formation can plausibly occur simultaneously at the same wavelength, as described by the growth of a single instability. Restite could be trapped by a strong lithosphere and prevented from recycling, but once reaching twice the thickness of the granite, would rapidly sink through. The instability models are consistent with constant, rapid recycling while the felsic lower crust forms, before dome and keel formation is activated by weakening of the greenstone layer and occurs simultaneously with the recycling of any remaining restite.

During the transition from stagnant lid to mobile lid (plate tectonics) convection, a large volume of lithospheric mantle is likely to have been recycled. It is proposed that this generated a uniquely

high magnitude continental stress state which formed the cratonic keels. Through mantle convection scale modelling, it is demonstrated that depleted and therefore strong and buoyant lithosphere forming within the lid can be shaped into thick keels and survive the lid breaking event. The stress during their formation is four times higher than the convective stresses during mobile lid immediately afterwards. It would take a Rayleigh number decrease of almost two orders of magnitude from the initiation of tectonics to the present, to return the keels to this stress state and predict their destruction. The stress at subduction zones through time may have peaked at 75% of the lid breaking stress 1Ga ago. Any keel destruction on the modern Earth is then predicted to require significant keel weakening, which is consistent with observation.

Declaration

The thesis comprises only of original work towards the Doctor of Philosophy, except where indicated in the preface. Due acknowledgement has been made in the text to all other material used. The thesis is fewer than the maximum word limit in length, exclusive of tables, maps, bibliographies, and appendices.

Signed,

Adam Philip Joseph Beall

Preface

The research for this thesis was partly funded by a top-up scholarship from the Geological Survey of Western Australia.

The contents of Chapter 3 have been accepted, as a revised manuscript: Beall A.P., Moresi. L. & Stern T., 2017. *Dripping or Delamination? A Range of Mechanisms for Removing the Lower Crust or Lithosphere, Geophysical Journal International* (Accepted May 5, 2017). 100% of the chapter is my original work, though has benefited from discussions with the manuscript co-authors, Prof Louis Moresi and Prof Tim Stern.

All numerical modelling was undertaken with support from the Pawsey Computing Centre, Perth and the National Computing Infrastructure (NCI), Canberra.

Acknowledgements

Thank you to my supervisor, Louis Moresi, for sharing your passion for geodynamics and teaching me how to flesh out and quantify the fundamental aspects of dynamic Earth processes. I came to you at the end of 2010 hoping to get experience in groundwater modelling and thanks to your comment that "heat-flow is similar to groundwater flow", I somehow ended up in the world of lithospheric instabilities, which I am grateful for. I have appreciated the freedom to explore a variety of ideas, as well as the help in addressing these in a precise way. I am also grateful that you did not hesitate to support me in my failed endeavour to finish an engineering degree or my commitment to unfashionable research topics.

Thank you to Roberto Weinberg for your input at the beginning at the project, which I found extremely useful. Thank you to Tim Stern and Katie Cooper, your feedback and discussions have contributed immensely to the quality and clarity of the dripping and keel formation projects respectively. I am also grateful to Katie for the hospitality during my visit to Pullman.

Many thanks to the Geological Survey of Western Australia, for providing financial support, inspiration and geological advice. The top-up scholarship allowed me to attend the AGU conference in 2015, as well as the providing for the living expenses to give me extra time to pursue additional ideas. Thank you to Klaus Gessner, Hugh Smithies and Ivan Zibra for sharing their insights into the evolution of Archean crust and allowing me to join them in the field. This research owes a lot to the geology you shared with and showed me. I very much appreciated the discussions with Klaus and drew much inspiration from them.

Thank you to my office mates over the last five years. At Monash - Ken, Morena and Ben provided the best environment for starting a PhD. Plenty of tea, coffee, Italian swearing, sing-a-longs, laughs and geodynamic discussions. At Melbourne - Jan, Daniel, Rob and Ben (again) for the fun, discussions, tea, physio exercises, coffee and general camaraderie. Thanks as well to the other geophysics enthusiasts I was not lucky enough to share an office with, but have had great discussions with, namely Dan Sandiford and Dave Willis.

A special thank you to the maestro of inversions, heat-flow and geostatics, Ben Mather. I would certainly have lost my mind (sooner) if I hadn't had the chance to laugh about and debrief every step of this journey with you. From first meeting you and realising someone else had been fooled into studying heat-flow, to starting PhDs and moving to Melbourne together, our friendship has made the last five years what will no doubt be, in the words of Bruce Springsteen, the 'glory days'. I was hoping to quote Dragon or Marky Mark and the Funky Bunch, but never mind. From the radio show to AGU and Ecuador and even just peasant coffee, I don't know how I managed to share every experience with you, but I am incredibly lucky for that.

To Mum, Dad and Kathryn, I am immensely grateful for all of your support since forever. You've patiently listened to my geology stories and been there for me for all of the ups and downs. I hope you know how much I appreciate everything you have done to give me the opportunities that got me here. Life has taken so many turns on this journey and I have been so lucky to be able to depend on you.

Most importantly, thank you to Kara. You have been so incredibly patient and supporting over the past five years and I am so grateful for that. I think I literally would not have been able to finish this, if it weren't for you. You have always been there for me when things weren't going well, while giving me perspective and making me appreciate all the small successes. Having you in my life is the most important thing to me and without you I certainly would not be able to achieve something like this. Thank you with all of my heart.

Contents

List of Figures

Chapter 1

Introduction

Of the terrestrial planets, Earth is unusual in that its surface and the rock beneath it are highly dynamic. Large parts of the surface are not only moving laterally, but also sinking, eventually reaching almost 3000 km depth (Davies 1999). The systematic recycling of the crust results in the large scale circulation of material, responsible for the Earth's current convective heat-loss. This circulation is reasonably well understood: the heat-loss, stresses and lateral velocities agree with predictions from theoretical models (Turcotte & Schubert 2014; Schubert et al. 2001). This success is partly due to the homogeneity of oceanic crust and lithosphere. As the oceans cover approximately two thirds of the Earth's surface, they represent a large part of the Earth convective system. However, the degree to which rock is recycled from beneath the continents and the mechanisms by which this may occur, are unclear. The general purpose of this thesis is to contribute to an understanding of how instabilities form below continents and the role that they play in continental evolution.

In the plate tectonics model, continental material is assumed to be generally buoyant and strong (Turcotte & Schubert 2014). This is to justify their apparent ability to resist sinking and entrainment into the mantle. The regions which are considered to be stable are generally shown to be able to transmit high stresses (Tesauro et al. 2012), are cold (Pollack et al. 1993) and have heat production profiles which minimise weakening by internal heating (Sandiford 2010). Continental strain is generally confined to plate boundaries, though diffuse tectonic strain is distributed for example through Tibet and China (Kreemer et al. 2000). Non-tectonic uplift and volcanism can also occur, for example in the southern Sierra Nevada (Saleeby et al. 2003) or possibly larger scale orogenies in the Tian Shan, China, or Central Australian orogeny (Neil & Houseman 1999; Pysklywec & Beaumont 2004). The continental crust generally has an andesitic composition (Rudnick et al. 1995), which is $< 600\ kg\ m^{-3}$ less dense than the asthenosphere (Turcotte & Schubert 2014). However, dense rocks are able to form within the crust by metamorphic and melting process (Rudnick & Fountain 1995; Lee et al.

2006), while the mantle lithosphere has a higher density than the asthenosphere when it has cooled to a steady-state (Poudjom Djomani et al. 2001). Inferences of dense continental material have been linked to observations of bodies sinking at depth (Levander et al. 2011; Zandt et al. 2004; Stern et al. 2013). Additionally, these observations typically coincide with deformation, volcanism and changes to topography, often away from plate boundaries.

The typical evolution of the continental crust and lithosphere is likely to involve instabilities. The generation of felsic crust from the pyrolitic composition of the mantle requires significant chemical fractionation (Taylor & McLennan 1995; Rudnick et al. 1995; Hawkesworth & Kemp 2006). This generally occurs by the initial extraction of basaltic melt and then either fractional crystallisation or later partial re-melting of the solid basalt. In some cases there may be an additional partial remelting step. The complementary residue which forms during this fractionation process is highly mafic and if it reaches thermodynamic equilibrium in the lower crust or deeper, becomes significantly denser than the mantle (Lee 2014). The degrees of partial melting required to generate felsic crust can vary $< 20\%$ and therefore result in a significantly higher volume of dense residue than buoyant felsic crust (Hawkesworth & Kemp 2006). The felsic composition of the crust therefore requires that the residue is systematically recycled in order to generate continental crust. Though this is a theoretical geochemical argument, the fractionation process is well documented experimentally and some restitic material has been preserved. The fractionation and recycling process has been documented for the Sierra Nevada batholith (Lee et al. 2006; Ducea & Saleeby 1998; Saleeby et al. 2003), where a restitic material which complements the batholith has been found in xenoliths and the recent removal can be inferred from volcanism, uplift and tomography.

The typical time-scales and evolution of sub-continental instabilities are poorly constrained, especially compared to the rich data set which underpins the understanding of subduction and sea-floor spreading (Turcotte & Schubert 2014). The theoretical model of gravitational instabilities growing from a small perturbation predicts that sinking initially occurs at an extremely slow velocity, before accelerating exponentially through time (Chandrasekhar 1961), so that the body is sinking rapidly when it reaches a significant displacement. This very nature is plausibly the reason for poor data, as an instability initially generates little geological activity and the later period of high activity is short lived. Some evolution data may be preserved in the Sierra Nevada (Saleeby et al. 2003), Colorado Plateau (Roy et al. 2009), North Island New Zealand (Stern et al. 2013) and the Carpathians (Houseman & Gemmer 2007), primarily based on the migration of topographic features and volcanism. They appear to generally grow within about 10Ma, which could be a characteristic instability time-scale. However, for each of these examples, aside from the Sierra Nevada, it is difficult to confidently distinguish whether the surface features record tectonic or instability activity. Additionally, as instabilities leave little trace in the rock record, it is unclear whether these modern examples are representative of typical instabilities through

time.

There may be a range of instability mechanisms with contrasting recycling efficiency. Instabilities are typically described as dripping or delamination. Though these terms are sometimes used interchangeably (ie. Elkins-Tanton (2007)), the first generally refers to the Rayleigh-Taylor Instability (RTI), as described by Chandrasekhar (1961), while the second refers to the peeling of the entire dense body, as described by Bird (1979). Any differentiation of these has primarily been used to explain differences in dynamic topography and volcanism (Göğüş & Pysklywec 2008a; Wang & Currie 2015), with little focus on any contrast in recycling dynamics. If one is more efficient in recycling dense restite than the other, it then becomes important to estimate which mechanism is predominant on the Earth. Characterising the difference between such mechanisms is the focus of Chapter 3.

Given the displacement of sinking bodies is predicted to grow exponentially through time, it is surprising that so many dense bodies can be observed hanging beneath continents. For example, if the instabilities below the western USA have taken $\sim$ 10Ma to grow to high displacement, they should be in this state for only $\sim$ 1Ma. This indicates that either sub-continental instabilities are extremely common or there is an issue with the exponential growth model. An alternative growth model could potentially involve an initially rapid, exponential growth, before some kind of stalling event occurs. This hypothesis is developed and tested in Chapter 4, by making use of the mechanisms developed in Chapter 3.

On the modern Earth there is a strong relationship between tectonic processes and instability growth. For example in the Sierra Nevada (Jones et al. 2004), Colorado Plateau (Levander et al. 2011) and North Island, New Zealand (Stern et al. 2013), a high strain or weakening event has preceded rapid instability growth, indicating that the observed instabilities have needed to be triggered tectonically. This agrees with the both models for the Rayleigh-Taylor and delamination instabilities, which require a mixture of large initial perturbations and weakening, such as stress-dependence, in order to grow at the 10Ma time-scale (Houseman & Molnar 2001; Molnar & Jones 2004). Palaeoarchean crust shows little sign of tectonic strain, but shows a propensity for allowing Rayleigh-Taylor Instabilities to grow (Van Kranendonk et al. 2007). Dome and keel structures (Van Kranendonk et al. 2004; Robin & Bailey 2009; Sandiford 2010) indicate that not only could instabilities occur without tectonic triggering, but they could occur in the middle and upper crust, which are the strongest parts of the crust on the modern Earth and somewhere that instabilities are therefore unlikely to occur. The goechemical arguments for restite production by fractionation are also applicable to the Archean Earth and it is likely this occurred within the crust (Smithies & Champion 2000; Bédard 2006). No evidence of restite recycling is preserved, though it clearly occurred, as Archean crust is predominately felsic and thin (Abbott et al. 2013). Given the crust was weak and sensitive to buoyancy related strain in the middle crust, it is perhaps surprising that the large volume recycling of restite below did not alter the dome and

keel wavelength or superimpose strain. This is addressed in Chapter 5, where the conditions at which multiple instabilities can grow and still generate the preserved dome and keel structures, are explored.

In addition to restite, the thermal boundary layer in the early Earth may have been significantly thicker than the modern Earth (Solomatov & Moresi 2000; Moore & Webb 2013), providing an opportunity for a large lithospheric recycling event. If there are no weak zones at the Earth's surface to allow the cold and relatively strong crust and lithopshere to be recycled, Earth's mantle convective system is better described by the stagnant lid model (Moresi & Solomatov 1998). In this model, the thermal lithosphere is significantly thicker than for the modern Earth. When the temperature effects of melt transport through the lithosphere are ignored, the cold lithosphere can develop a high degree of gravitational potential energy, which is released when plate tectonics begins (Van Thienen et al. 2004; O'Neill et al. 2007). If melt transport through the lithosphere is considered, the lithosphere could become anomalously cold compared to a linear geotherm, due to adiabatic transport of melt to the surface Moore & Webb (2013). In the case that melt instead forms intrusions, the lithosphere would be hotter and thinner, reducing the available negative buoyancy (ONeill et al. 2016). The Rayleigh-Taylor Instability of this large volume of material should result in eventual recycling of the entire crust and lithosphere. Crust and lithosphere are preserved from before plate tectonics is thought to have initiated and some crust and lithosphere must have been able to survive this large scale recycling event (Condie et al. 2009a). In Chapter 6, the perquisites for such stable continental material are quantified. Preserved Archean lithosphere is typically anomalously thick, though formed at about a third of their current thickness (Lee 2006; Cooper et al. 2006), therefore requiring a thickening event. Surviving pre-tectonic lithosphere may have thickened into their current form during the lid breaking event, which is explored by quantifying the stresses produced during this large recycling event.

Chapter 2

Review of Gravitational Instability Mechanics

'Instability' refers to a state which, when perturbed, continually evolves away from this initial state rather than returning to it. Momentum is negligible when analysing flow of the solid Earth, so the relevant instabilities are driven by instantaneous forces. The focus of this thesis is on the initial stages of instabilities driven by gravity. These tend to be non-linear, such that not only does the fluid evolve away from its initial state, but it accelerates during its evolution. Gravitational instabilities generally arise in the Earth due to the configuration of material near the Earth's surface which is denser than the mantle below. The sub-surface material may be relatively dense due to a combination of temperature and compositional effects (Lee 2014; Poudjom Djomani et al. 2001). Subducting slabs, where cold and eclogitic ocean crust sinks into the mantle are the primary example of gravitational instabilities beneath the oceans (Turcotte & Schubert 2014). This instability is primarily responsible for driving tectonics, cooling of the Earth and continental deformation. Additionally there are less known gravitational instabilities which remove heat from below the oceanic plates and recycle the lower parts of continents back into the mantle (Houseman & Molnar 1997; Parsons & McKenzie 1978).

The mechanisms of the various sub-surface gravitational instabilities are complex and mechanically contrasting. However, there are fundamental fluid dynamic models which describe gravitational instabilities and provide a cohesive framework from which to analyse more complex systems (Chandrasekhar 1961). The model of the Rayleigh-Taylor Instability is the fundamental characterisation of a homogeneous material sinking into a separate, less dense, material. The term material refers to a volume which has a distinct function of density and a particular constitutive equation which describes how it responds to applied or internal stresses. The constitutive equation in this case is the Newtonian flow law, Eq.

2.1.

$$\sigma_{ij} = \eta(x, y) \left(\frac{\partial u_i}{\partial x_j} + \frac{\partial u_j}{\partial x_i} \right)$$
$$\sigma_{ij} = \tau_{ij} - p \tag{2.1}$$

This relates the stress tensor τ_{ij} to velocity (u) gradients in the fluid. As the stresses and velocity gradients can be horizontal, vertical or shear and either two or three dimensions, the tensor contains either four or nine components. Here the spatial coordinates (x, y, z) and (x_1, x_2, x_3) are interchanged as convenient. The viscosity, η, which is assumed to be independent of orientation, is a parameter which controls the magnitude of velocity gradient and encapsulates the microscopic deformation depending on composition, temperature and mechanism, into the macroscale fluid continuum. This is typically also dependent on stress, resulting in a non-linear relationship, though we generally only consider a linear relationship unless otherwise specified. This choice is based upon observations in instability analyses that a non-linear rheology does not alter the first-order flow characteristics (Conrad & Molnar 1997), though it alters the time-scale by a scale which can be approximately captured by an effective viscosity. This approximation greatly simplifies the analysis and allows us to compare a variety of instabilities.

The stress tensor can be decomposed into two parts: deviatoric stress τ_{ij} and pressure p. Pressure is an invariant measure which does not directly cause deformation. Deviatoric stress is the matrix which subsequently is responsible for deforming a material. Although it does not deform a fluid, pressure is still required for distributing stress in a fluid. For example, a fluid which is at rest does not deform, but has a hydrostatic stress which increases with depth, solely contained in the pressure term. This decomposition greatly simplifies the mathematical solution, as there are conditions under which one of the terms is negligible and pressure can be represented by one component rather than four or nine.

The first of the Stokes Flow equations (Eq. 2.2) uses force balance in each orthogonal direction to link the constitutive relationship at every point in the fluid in a continuum. It relates the local gradients in stress to a driving 'force' term, which in this case is the gravitational acceleration g_i of the local volume of mass, as calculated from the local density ρ. The second part of Eq. 2.2 represents conservation of mass, and adds the final constraint by expressing that any material flowing into a local point must be balanced by material flowing outward. This relationship is a simplified version of the full force balance, the Navier-Stokes equations, formed using two key approximations. Firstly, compressibility is generally ignored as it is small enough for rock that its terms are negligible, except for the force term where it can be significant. The second is that momentum is negligible, as the viscosity of rock is generally at least 10^{16} Pa s. The Stokes equations also require that deformation is infinitesimal, as do the Navier-Stokes equations, such that only the first terms in the Taylor expansion

of stress and strain-rate are non-negligible. This limitation is not an issue if finite flow is calculated from the integration of infinitesimal steps or is only an infinitesimal deviation from an original state. Each of these are simplified by the instantaneous nature of creeping flow, rather than for example the strain dependence encountered in elasticity.

$$\begin{aligned} \frac{\partial \tau_{ij}}{\partial x_j} - \frac{\partial p}{\partial x_i} &= \rho(x, y) g_i \\ \frac{\partial u_i}{\partial x_i} &= 0 \end{aligned} \tag{2.2}$$

The complexity in the Stokes equations as applied to solid Earth flow arises from extreme heterogeneity in the viscosity and density parameters. These parameters capture the behaviour of contrasting rock materials under varying conditions. For example, viscosity can vary by at least ten orders of magnitude depending on the temperature, composition, melt content, and stress limitation of the rock. Near surface rocks can grow to be as much as 10% denser than the asthenosphere, depending on temperature and composition (Turcotte & Schubert 2014). The primary difficulty in quantifying deformation in the solid Earth using fluid dynamics is finding a suitable approximation of these parameters which can characterise fundamental processes.

2.1 Analytic Solutions to the Rayleigh-Taylor Instability

A fundamental understanding of gravitational instability evolution comes from approximate analytic solutions to the Stokes equations. The typical Rayleigh-Taylor Instability setup (Chandrasekhar 1961; Turcotte & Schubert 2014) begins with two separate fluids, one above the other and a discrete interface between the two. If the interface is flat then there is no fluid flow and the stress within the fluids is $p = \rho_1 g y$ for the top fluid and $p = \rho_2 g y + (\rho_1 - \rho_2) g L$. This hydrostatic pressure is taken as a reference and is stable until the flat interface is perturbed by an infinitesimal amount w. Then, the perturbation to the pressure at the interface becomes $\Delta p = \Delta \rho g w$, where $\Delta \rho = \rho_1 - \rho_2$. As the original hydrostatic pressure does not produce a deviatoric stress, it is only this stress anomaly which has the potential to drive flow. In 1D this pressure anomaly is homogeneous in each layer and no flow occurs. In 2D however, lateral variations in the interface perturbation produce an anomalous stress field at the interface which produces deviatoric stress and subsequently deformation. Depending on the shape of the interface and the material viscosities, the anomalous stress diffuses away from the interface. As the anomalous pressure is linearly dependent on the interface perturbation, the anomalous pressure not only produces deformation, but increases with deformation in a non-linear feedback. The resulting

non-linear equations be made linear by approximating the change of perturbation through time, the material derivative of the interface as $\frac{Dw}{Dt} \approx \frac{\partial w}{\partial t}$. This approximation is only valid for small perturbation displacements and is termed the linear stability analysis. Its solution describes the perturbation growth as evolving from an initial displacement w_0 exponentially with time at an exponential rate τ (Eq. 2.3), which depends on the material properties and configuration.

$$w(t) = w_0 e^{\tau t} \tag{2.3}$$

The growth time-scale τ can be predicted by solving the Stokes equations. A simple analytic solution can be found as follows. The stream function ψ is defined as $u = -\frac{\partial \psi}{\partial x}$ and $w = \frac{\partial \psi}{\partial y}$, and can be separated into two space and one time function, $\psi = j(x)r(y)e^{\tau t}$. ψ can be decomposed into orthogonal wave functions, by finding the Fourier transform $\hat{\psi}$ such that $\psi = \int_{-\infty}^{\infty} \hat{\psi}(k) e^{ikx} dk$, where k is the wavenumber of a specific wave, depending on its frequency f as $k = 2\pi f$. Using the stream function in the first of the Stokes equations and taking the Fourier transform results in an expression which links the vertical part of the stream function, to a particular horizontal frequency in the flow field (Eq. 2.4). The vertical part describes how the stress diffuses away from the interface and the wavenumber part provides one Stokes solution which can be reconstituted into the complete solution by integrating over all possible wavenumbers. In practice this is unnecessary as the exponential nature of perturbation growth typically results in only one wavenumber dominating, provided τ varies sufficiently with k.

$$\left(k^2 + \left(\frac{\partial}{\partial y} \right)^2 \right)^2 r(y) = 0 \tag{2.4}$$

As the fluid flow depends on the material properties, a stream function must be found for each material and linked to the adjacent materials by their interface conditions. The solution to Eq. 2.4 is $r(y) = C_1 e^{ky} + C_2 e^{-ky} + C_3 y e^{ky} + C_4 y e^{-ky}$. The coefficients C may be complex and are found by applying four boundary conditions for each material. In the solution of r, the use of boundary conditions which depend on the layer thicknesses, viscosities and densities results in a non-dimensionalisation (Eq. 2.5) which is actually applicable to many varieties of creeping buoyancy-driven flow (Chandrasekhar 1961; Turcotte & Schubert 2014; Davies 1999).

$$\begin{aligned} \tau &= \tau' \frac{\Delta \rho g L}{\eta} \\ k &= k' L \end{aligned} \tag{2.5}$$

Instability growth can then be characterised by solving a set of $4N$ equations for N stacked layers, to find τ or a set of τ if more than density contrast is present. τ' then depends only on relative material properties of the layers and the boundary conditions. Assuming these relative properties do not change, the solution can be applied to a range of materials depending only on their characteristic growth-rate $\Delta\rho g L/\eta$.

The simplest case applicable to the recycling of the lithosphere is that of a homogeneous layer with a no-slip boundary condition at its top, $u = 0$ and $v = 0$, overlying an inviscid, $\eta \to 0$, half-space. The top boundary condition and the half-space in this case represent an undeformable crust and a relatively weak asthenosphere respectively. The solution of τ as depending on k has a $\tau'_{max} = 0.16$ at $k' = 2.12$ (Conrad & Molnar 1997).

Conrad & Molnar (1997) also calculated τ for cases in which the viscosity is dependent upon an invariant stress measure to the power of an exponent n. The quickest growing instability still occurs at the same dominating wavenumber for a Newtonian rheology, but with double the non-dimensional growth-rate. As the growth-rate is non-dimensionalised using the initial effective viscosity, a Non-Newtonian rheology would result in a halving of the instability growth time-scale if the Newtonian and Non-Newtonian rheologies have the same initial effective viscosities. This comparison requires an initial non-zero background stress in the Non-Newtonian case and assumes that the viscosity used for the Newtonian case is an effective value which incorporates such effects. An exponent of three is typical of dislocation creep, and would result in an effective halving of this Newtonian effective viscosity. Temperature dependent viscosity has the effect of lessening the thickness of material which sinks, such that an upper section close to the base of the crust remains undeformed (Conrad & Molnar 1999).

The growth-rate approximately doubles if the surface is free, $u = 0$ and $\tau_{yy} = 0$. If the crust is able to participate, then the extra density contrasts at the Earth's surface and the Moho must be included in solutions of τ'. Bassi & Bonnin (1988) developed a method for such an analytic calculation. Inserting the boundary conditions into the solution of Eq. 2.4 creates the set of equations Eq. 2.6, which has a force term involving the displacement w_j at interface j corresponding to the interface pressure boundary condition.

$$M_{ij} C_j = S_{ij} w_j \tag{2.6}$$

The calculation of the velocity at each interface involves the same coefficients C (Eq. 2.7). Combining the expression for the interface velocities with the set of equations for the Stokes solution gives

a differential equation in terms of interface displacement (Eq. 2.8).

$$\frac{\partial}{\partial y} w_j = T_{ij} C_j \tag{2.7}$$

$$\frac{\partial}{\partial y} w_j = T_{ij} M_{ij}^{-1} S_{ij} w_j \tag{2.8}$$

If there is only one pressure boundary condition, then Eq. 2.8 can be simply solved in terms of just one interface as the original solution Eq. 2.3. For multiple density contrasts and therefore non-zero pressure boundary conditions, Eq. 2.8 becomes a set of partial differential equations which depend on combinations of the different interfaces. This complication is resolved by forming an eigen-decomposition of $TM^{-1}S$, which produces a diagonalise growth-rate matrix Q (Eq. 2.9) such that in a new interface basis, $\hat{w} = Pw$, each differential equation depends on only one interface variable.

$$T_{ij} M_{ij}^{-1} S_{ij} = PQP^{-1} \tag{2.9}$$

In this new basis, each variable is a combination of interfaces, rather than just one. Each combination grows according to a growth-rate component in the diagonal of Q (Eq. 2.10). Moving back into the interface-independent basis, each interface now grows according to the sum of exponential terms (Eq. 2.10).

$$\begin{aligned} &Q_{11} = \tau_1, Q_{22} = \tau_2, \cdots \\ &w_i = P_{ij} \alpha_j e^{\tau_j t} \end{aligned} \tag{2.10}$$

Using this type of approach, Neil & Houseman (1999) showed that a buoyant crust should thicken above a down-welling, though this thickening diminishes once the crust is $\sim 100x$ more viscous than the dense body. Additionally, the topographic response to instability strongly depends on the viscosity and buoyancy of the crust. If the crust can deform and is much more positively buoyant than the dense body is negatively buoyant, $> 2x$, the surface will uplift, otherwise subsidence will occur. Likewise, if a buoyant crust is at least two orders of magnitude more viscous than the dense body, subsidence will occur no matter how buoyant the crust is, as occurs for the simpler no-slip boundary condition case. Otherwise, the surface will uplift as the crust thickens.

2.1.1 Non-Linear Analytic Solutions

Canright & Morris (1993) developed an analytic solution for non-linear perturbation growth, which is valid to high displacements. This was achieved by assuming the interface slope was negligible. Despite this small slope approximation, their model can still describe large interface displacement by assuming that the zones of large displacement are localised and their flow can still be quantified using mass conservation and the model of flow elsewhere in the domain. The small slope approximation results in flow only existing horizontally, which simplifies the change in interface displacement to $\frac{\partial w}{\partial t} + u\frac{\partial w}{\partial x}$ and can be solved simply using a lagrangian reference frame. Their non-linear model reverts to the exponential growth of the linear stability analysis for $w < 0.1L$. After this the perturbation growth can be described by a simple expression Eq. 2.11, which is valid only for high growth.

$$w' = \left(\frac{1}{w_0' + L} - \tau' \, t \right)^{-1} - L \tag{2.11}$$

The non-linear perturbation growth Eq. 2.11 results in a velocity which grows in a hyperbolic manner which is quicker than the linear exponential growth. Its velocity continues to increase until it reaches a singularity at time $t = 1/\left(\tau'(w_0' + L)\right)$, which corresponds physically to a time at which the dripping dense body breaks off or establishes a vertical channel.

2.2 Solutions to the Delamination Instability

When the dense sinking material is much more viscous than the material below and has a free upper surface, the Rayleigh-Taylor Instability occurs at a very large wavelength and the internal stress-state is dominated by horizontal compression in regions which will eventually sink (Canright & Morris 1993). This coincides with the large wavelengths of strong oceanic crust. Oceanic crust however sinks asymmetrically and features a localised weak zone which allows it to sink (Gerya et al. 2008). A similar process may occur beneath the continents, where dense, viscous material forms a weak, free edge and if it is decoupled from overlying material can peel away into the mantle (Bird 1979). A model of this process, delamination, occurs through viscous bending of the dense body. As there is negligible thickening of the dense body if it only deforms by bending at a large wavelength, it is unclear whether delamination is a non-linear process. Bird (1979) modelled delamination as flow of a weak lower crust above the dense material by Poiseuille flow, which generates a pressure gradient which is balanced by viscous bending of the dense material below. The instability in Bird's model was driven by the density contrast between the lower crust and the asthenosphere, produced in-flow of asthenosphere into the

lower crust and continually forced down the peeling dense body. This model therefore differs from the instabilities described previously, which were driven by the anomalous density of the dense body, however could be easily reformulated as a function of anomalous dense body density.

Bird (1979) calculated the initial velocity of a delaminating body, showing that it depends upon not only the thickness and viscosity of the dense body, but also of the lower crust. This theoretical model has not been directly compared to an equivalent Rayleigh-Taylor Instability, though intuitively it is likely that at least initially, delamination would evolve at a quicker time-scale. This is based up on the reasoning that the exponential growth model reaches a relatively high velocity only at high perturbation displacement, while delamination begins with the velocity calculated by Bird. It is also unclear whether the delamination velocity would increase through time at the same rate as the Rayleigh-Taylor or at all. Additionally, the mechanism by which the lower crust flows may not necessarily be Poiseuille flow (Bajolet et al. 2012).

2.3 Numerical Modelling

The analytic Rayleigh-Taylor solution is an approximation which is only valid for small displacements of the interface between the materials of contrasting density. A numerical solution is required for large displacements. Numerical solutions to the Stokes equations have been applied to mantle convection, the Rayleigh-Taylor Instability, subduction of oceanic crust and intracrustal deformation, among others (Schubert et al. 2001; Gerya 2009). Each of these problems generally uses the same formulation of the Stokes equations. Therefore numerical solutions can not only be used for predicting the high displacement exponential growth of gravitational instabilities, but can also be directly compared to other types of instabilities. For example, Göğüş & Pysklywec (2008a) compared the predicted surface expressions of the Rayleigh-Taylor Instability and delamination, using the same numerical approximation, but differing initial conditions.

The most common numerical approximations used for the Stokes equations in geodynamics are the finite element and finite difference method, of which we discuss the former. An introduction to the finite element method requires many mathematical proofs, as summarised by Hughes (2012). Rather than rigorously summarising the mathematical formulation, we briefly summarise the solution's philosophy as it differs from the analytical approach. The finite element method firstly integrates the Stokes equations over arbitrary 'weighting' functions and uses Gauss' theorem (also known as integration by parts) to connect the conditions at the domain edge Γ to the domain interior Ω and reduce the order of the differential equations. Eq. 2.12 is the transformed formulation of the Stokes equations, termed the

'weak' form, with the weighting functions w and q. The weighting functions can be any differentiable function, but in this thesis it is always a linear polynomial. The weighting function is also always chosen such that $w_i = 0$ when $x_i = 0$, which simplifies the element integral. The weak formulation includes the value of any stress boundary conditions h_i explicitly. The mass conservation part in this case also includes a term for compression, which includes a measure of incompressibility λ. This compression formulation is often used for calculation purposes and approximates incompressibility for large λ.

$$\begin{aligned} \int_\Omega \frac{\partial w_i}{\partial x_j}\sigma_{ij}\,d\Omega &= \int_\Omega \rho w_i g_i\,d\Omega + \sum_{i=1}^{n_{el}} \int_{\Gamma_{h_i}} w_i h_i\,d\Gamma \\ \int_\Omega q\left(\frac{\partial u_i}{\partial x_i} + \frac{p}{\lambda}\right) d\Omega &= 0 \end{aligned} \tag{2.12}$$

The finite element formulation typically approximates the velocity and pressure solutions, u and p, as well as their respective weighting functions w and q, by a series with independent contributions from arbitrary basis functions N_A and $\tilde{N}_A$ respectively (Eq. 2.13). These basis functions are able to reproduce an exact solution at discrete points A and an approximation in-between these.

$$\begin{aligned} w^h &= \sum_{A=1}^{n} c_A N_A \\ q^h &= \sum_{A=1}^{n} q_A \tilde{N}_A \\ u_i^h &= \sum_{A=1}^{n} d_{Ai} N_A + v_i N_{n+1} \\ p^h &= \sum_{A=1}^{n} p_A \tilde{N}_A \end{aligned} \tag{2.13}$$

$$\begin{bmatrix} K & G \\ G^T & M \end{bmatrix} \begin{bmatrix} d \\ p \end{bmatrix} = \begin{bmatrix} f \\ 0 \end{bmatrix} \tag{2.14}$$

$$\left(G^T K^{-1} G - M\right) p = G^T K^{-1} f \tag{2.15}$$

The velocity boundary conditions (v_i) are also included in the formulation, albeit more implicitly compared to stress conditions, by dedicating an additional basis function N_{n+1} to them. A matrix

formulation (Eq. 2.14) arises from combining the discrete approximations (Eq. 2.13) with the weak form of the Stokes equations (Eq. 2.12), where K,M, G and G^T are sub-matrices. The weak formulation solution must exist for all c_A and q_A independently, which is why the set of linear equations in Eq. 2.14 is only dependent on d_A and p_A. The solution of these occurs in at least two steps: first p_A is solved using Eq. 2.15, after which this pressure solution is used to solve for d_A, finding the velocity functions. The calculation of p is time-consuming as it is difficult to solve for the effective inverse of K, as its elements can vary by huge orders of magnitude as a result of the large viscosity contrasts which arise in geodynamic problems. This formulation (Eg. 2.15) allows for the use of the penalty method, where λ is taken to be large and results in a small M which approximates incompressibility. The Underworld code is used for all numerical solutions in this thesis (Moresi & Solomatov 1995; Moresi et al. 2001) and uses a combination of pre-conditioners and multigrid to efficiently solve Eq. 2.15 in parallel.

The particle-in-cell method is used in this thesis, as implemented in Underworld (Moresi et al. 2001). This involves tracking materials with an unstructured set of points (particles), which hold material property data such as ρ and η. At a given time, an element contains many particles, often with different properties. These properties are integrated over the volume surrounding each particle and contribute to the integrals in Eq. 2.12. The particles are advected by the velocity field, where their displacement for over each time-step is found using the second-order Runge-Kutta method.

2.3.1 Energy Solution and Temperature-Dependence

Generally, the density (ρ) and viscosity (η) of Earth materials are strongly temperature-dependent. When instabilities develop much more quickly than thermal diffusion and material properties only depend on temperature, ρ and η do not vary with time. They can then be chosen as the material properties evaluated for the initial model temperatures. This assumes that temperature is advected, but does not require its calculation, as the advection of the material particles is already calculated.

In the case that thermal diffusion is significant, the energy equation is solved (Eq. 2.16), where T is temperature, κ thermal diffusivity and H is energy generation in dimensions of $[T][t]^{-1}$.

$$\frac{\partial T}{\partial t} = -\nabla \cdot \kappa \nabla T + u \cdot \nabla T + H \tag{2.16}$$

Using the same process described earlier and in Hughes (2012), the weak form for Eq. 2.16 is:

$$\int_\Omega w_i \frac{\partial T}{\partial t} d\Omega + \int_\Omega \kappa \frac{\partial w_i}{\partial x_i} \frac{\partial T}{\partial x_i} = \int_\Omega w_i H d\Omega + \int_\Gamma w_i h d\Gamma \tag{2.17}$$

w, T and $\frac{\partial T}{\partial t} \equiv \dot{T}$ are discretised for each element A, by $w^h = \sum_{A=1}^{n} c_A N_A$, $T^h = \sum_{A=1}^{n} d_A N_A$ and $\dot{T}^h = \sum_{A=1}^{n} p_A N_A$. The relevant matrix system is then:

$$Mp + Kd = F \tag{2.18}$$

where M,K and F are matrices with elements dictated by the element-wise integrals in Eq. 2.17.

T and therefore p are given as an initial condition and vary only as an integration of $\dot{T}$ for each time-step. $\dot{T}$ and therefore p is the only unknown and is solved for. There are many options for integrating $\dot{T}$ over a time-step to give ΔT at each node. The streamline upwind scheme is implemented in Underworld and used in this thesis. For a particular node, a node is chosen in each direction which is 'upwind' of the velocity field and a temperature gradient is calculated in each direction using these nodes. These gradients are then multiplied by the velocity components in their respective directions, summed and multiplied by the time-step size.

2.3.2 Applications

As well as their previously discussed use for validating analytic solutions, numerical models are used to analyse instabilities for which an analytic solution cannot be used, potentially for a variety of reasons. For example, the small displacement approximation is not useful for comparing models to instabilities which can be observed to currently be sinking at high displacement, such as for the Carpathians (Houseman & Gemmer 2007; Lorinczi & Houseman 2009), the Sierra Nevada (Le Pourhiet et al. 2006), North Island New Zealand (Stern et al. 2013) or the Colorado Plateau (Van Wijk et al. 2010).

The initial geometry may have important complexities, which are important to the instability dynamics and cannot be simplified. For example, Houseman & Gemmer (2007) has proposed that lateral variations in crustal thickness and density, resulting from orogenesis, can generate lateral orogenic collapse and subsequently generate secondary Rayleigh-Taylor Instabilities at its edges. Stern et al. (2013) proposed that if strike-slip movement can generate a high displacement step perturbation, this initial geometry is critical in accelerating flow and generates a mixture of large wavelength lateral flow and small wavelength dripping.

As the Rayleigh-Taylor growth-rate varies inverse proportionally to the lithosphere or crust's viscosity, the typically high viscosities of these materials generally precludes instability flow at the 10 Ma scale (Molnar & Jones 2004), unless some weakening mechanism is invoked. This has been achieved by finding numerical solutions to instabilities with complex rheologies, such as by including stress-dependence

(Lorinczi & Houseman 2009), plasticity (Le Pourhiet et al. 2006; Morency & Doin 2004), history-dependent damage (Paczkowski et al. 2012) and melting (Gorczyk et al. 2012).

Sub-continental instabilities on Earth are likely to be require tectonic and mantle convective processes to be triggered, which may require modelling with a coupled process. Far-field stresses are often represented by constant velocity boundary conditions (Le Pourhiet et al. 2006; Göğüş & Pysklywec 2008a). Coupled processes are also explicitly modelled, such as for subduction (Göğüş 2015) and mantle convection (Bercovici 2003; Morency & Doin 2004; Van Wijk et al. 2010).

Finally, the negative buoyancy which drives the gravitational instability may be complex and dynamic. For example, the transition from basalt to eclogite results in a significant increase in density and can subsequently trigger or accelerate instabilities when it occurs (Van Thienen et al. 2004; Jull & Kelemen 2001; Johnson et al. 2014). If the timing of when these processes initiate is not important, instability growth can be modelled more simply by using an effective buoyancy or viscosity, which reproduces the characteristic growth-rate of the instability when it has been triggered and becomes important for geological processes. This is the general approach in the following chapters.

Chapter 3

Dripping or Delamination? A Range of Mechanisms for Removing the Lower Crust or Lithosphere

Summary

Under some conditions, dense parts of the lower crust or mantle lithosphere can become unstable, deform internally and sink into the less dense, underlying asthenosphere. Two end-member mechanisms for this process are delamination and dripping. Numerical calculations are used to compare the time taken for each instability to grow from initiation to the point of rapid descent through the asthenosphere. This growth period is an order of magnitude shorter for delamination than dripping. For delamination, the growth-rate varies proportionally to the buoyancy and viscosity of the sinking material, as with dripping. It also depends on the thickness (L_c) and viscosity (η_c) of the weak layer which decouples the sinking material from the upper crust, relative to that of the dense lower crust and / or lithosphere, denoted L'_c and η'_c respectively. The delamination growth-rate varies proportionally to $L'^2_c/\eta'^{\frac{2}{3}}_c$. As instabilities commonly resemble a mix of dripping and delamination, the analysis of initial instability growth includes a range of mechanisms in-between. Dripping which begins with a large perturbation and low η'_c reproduces many of the characteristic features of delamination, yet its growth time-scale is still an order of magnitude slower. Previous diagnostic features of delamination may therefore be ambiguous and if rheology is to be inferred from observed time-scales, it is important that delamination and this 'triggered dripping' are distinguished. Transitions from one mechanism or morphology to another, during the initial growth stage, are also examined. 3D models demonstrate that when η'_c is small, a

dripping, planar sheet will only transition into 3D drips if the initial triggering perturbation is less than a third of the dense material's thickness. This transition occurs more easily at large η_c', so rheological heterogeneity may be responsible for morphological transitions through time. We also calculate the rates at which delamination grows too slowly to outpace cooling of the upwelling asthenosphere, resulting in stalling and switching to dripping. Common lithospheric viscosities and observed time-scales indicate that both instability transitions are feasible.

3.1 Introduction

If dense lower crust or lithosphere beneath a continent is perturbed and sinks into the mantle (Fig. 3.1), its evolution is typically thought to evolve by dripping (Houseman & Molnar 1997) or delamination (Bird 1979). Which mechanism dominates depends firstly on whether prerequisite conditions are met and then on which one can develop more quickly. Delamination requires a weak lower crust and has to be triggered by an external tectonic process (Morency & Doin 2004). Dripping doesn't have any such requirements. The length of time it takes each mechanism, once initiated, to recycle dense material into the asthenosphere is less clear. Both instabilities progress rapidly when they have sunk by a distance on the order of the dense material's initial thickness, but the time taken to reach this descent (Fig. 3.2) can vary by orders of magnitude in both cases (Chandrasekhar 1961; Bajolet et al. 2012). For dripping, the length of this growth time depends primarily on the density and rheology of the dense material. For delamination, Bajolet et al. (2012) and Bird & Baumgardner (1981) have shown that the delamination growth time is influenced by the rheology and thicknesses of the lower crust. However, this dependence has been analysed for only a few cases and the influence of the sinking material's rheology is unclear. There is an alternative view that this growth period is instead insignificant and lithospheric rheology does not influence the delamination time-scale (Le Pourhiet et al. 2006). Because the delamination growth-rate immediately after initiation has not been generalised as it has for dripping, it is difficult to compare how quickly the two end-member mechanisms are likely to grow. Our primary objective is to characterise it using numerical models, so that the comparison can be made.

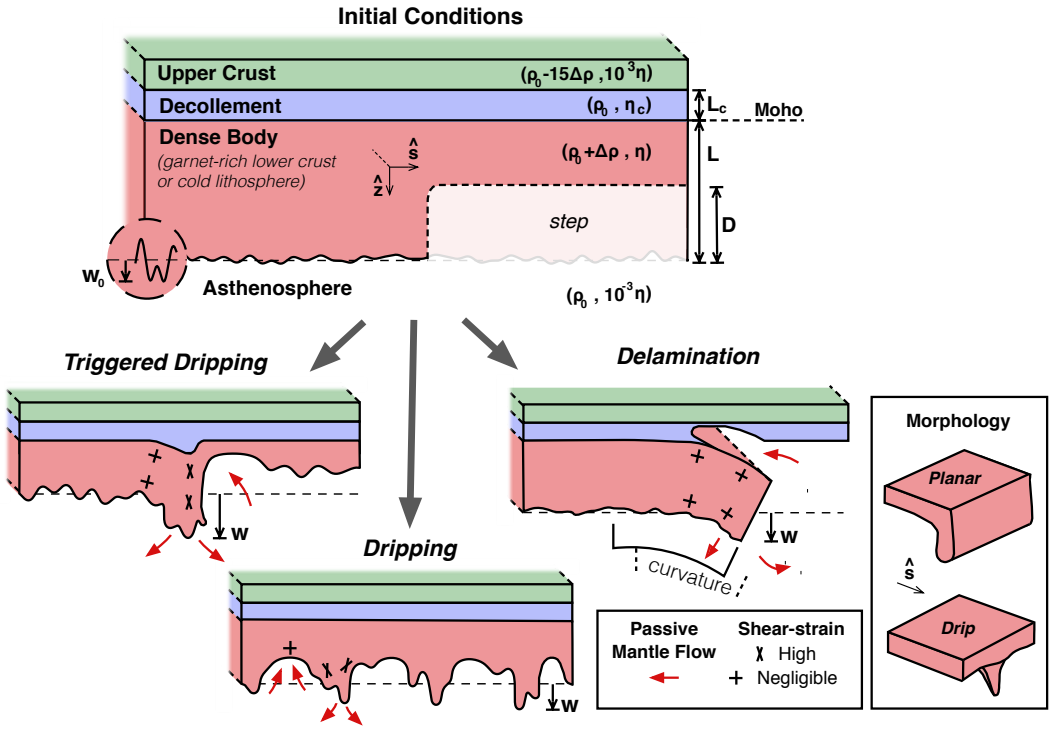

Figure 3.1: Schematic diagram of the initial conditions and the three mechanisms which can develop depending on these conditions. The primary parameters which are varied are the initial step-size D and the decollement viscosity η_c, while the other parameters are described in Table 3.1. Density and viscosity are shown in brackets for each material and the parameters are set up so they can be applied to any dense body thickness, density and viscosity. For an initial $D = 0$, the subsequent flow follows the Rayleigh-Taylor Instability (RTI) model and is referred to as the dripping mechanism. Its flow is characterised by high internal shearing and even though the Moho may be displaced, the top of the dense body remains connected to the decollement layer. Delamination can be triggered when $D = L$, so that the asthenosphere is adjacent to the decollement, which also needs to be weak enough that it can subsequently flow and allow the dense body to peel away. Delamination occurs with negligible shear-strain. If $D > 0$, as may be the case if tectonic strain produces a large perturbation as suggested by Stern et al. (2013), the instability still grows primarily by thickening, but it can no longer be modelled solely by the analytic RTI model. We refer to this hybrid mechanism as 'triggered dripping' and it may have characteristics resembling both dripping and delamination.

Dripping and delamination should be distinguishable based on the consequent topography and volcanism observed (Göğüş & Pysklywec 2008a; Wang & Currie 2015). However, instabilities in nature can rarely be characterised exclusively as dripping or delamination. For example, the migration of topographic and volcanic fronts over time is characteristic of delamination. Some instabilities though have clearly migrated, despite their otherwise characterisation as dripping (Saleeby & Foster 2004; Stern et al. 2013). Dripping and delamination can therefore be considered as end-members, with instabilities behaving as some mixture of the two.

Stern et al. (2013) modelled such a mixed case, by introducing a weak lower crustal layer and large initial perturbation to an otherwise conventional model of dripping lithosphere. The initial conditions were close to, but insufficient to trigger delamination (Morency & Doin 2004). Their models however reproduce the migration of topography and volcanism, as typical for delamination. The entire lithosphere eventually peeled away, also indicative of delamination, but the lithosphere became highly strained in the process, as occurs for dripping. The time taken for the instability to develop is quicker than for the dripping end-member, but it is unclear how it compares to delamination. If the similarity between the hybrid instabilities and delamination is not shared dynamically, the characterisation of instabilities would become much more difficult than simply comparing the end-members. It is therefore important to be able to predict the growth of instabilities which are very close to delaminating, but do not completely reproduce the end-member's behaviour. The degree to which an instability is described by the dripping and delamination end-members is quantified in our numerical models, so that the growth-rates of these mixed cases can be compared.

Finally, sinking lower crust or lithosphere may begin deforming by one mechanism, only to switch to another during its initial growth. For example, lithosphere beneath the western Colorado Plateau appears to have peeled away from the crust by delamination, but now has a drip morphology (Fig. 3.1) at depth (Levander et al. 2011). Also, the dense lower crust beneath the Sierra Nevada batholith may originally have had an elongated, planar geometry but now also clearly has a drip morphology at depth (Frassetto et al. 2011; Gilbert et al. 2012; Jones et al. 2014). For dripping material, the drip morphology grows the most quickly, so an initially planar perturbation may transition into a drip morphology as it sinks (Ribe 1998; Kaus & Podladchikov 2001). This transition is unlikely to occur during the initial instability growth if the initial planar perturbation is significant, but the required perturbation when thermal diffusion and a weak lower crust are significant, is unclear. Alternatively, the conditions for delamination are highly specific and if they only occur for a limited time or region, delamination may stall and revert to dripping. Bird & Baumgardner (1981) showed that it is difficult to stall delamination when > 100 *km* length of material has already peeled away, but stalling during the initial growth phase has not been studied. While analysing the initial growth periods of the various mechanisms, we quantify the thresholds at which these two types of transition occur.

3.1.1 Rayleigh-Taylor Instability Theory

The velocity of dripping material through time has long been described by the Rayleigh-Taylor Instability (RTI) model (Chandrasekhar 1961). It consists of two layers of fluid, in this case the dense lower crust or lithosphere and the asthenosphere of lower density below, separated by a horizontal interface which is slightly perturbed (Fig. 3.1). This configuration is unconditionally unstable and the perturbation

Table 3.1: Commonly Used Symbols

Symbol	Meaning	Non-dimensionalisation
w	Displacement of the dense body-asthenosphere interface perturbation	$w' = w/L$
w_m	Displacement of the dense body-crust interface (the Moho)	$w'_m = w_m/w$
$\dot{w}$	Interface perturbation velocity (vertical component)	$\dot{w}' = \dot{w}\ \eta/(\Delta\rho g L^2)$
t	Time elapsed since triggering	$t' = t\ \Delta\rho g L/\eta$
w_0,$\dot{w}_0$	Values of w and $\dot{w}$ at $t = 0$	
D	Initial step perturbation size	$D' = D/L$
η_c	Decollement viscosity	$\eta'_c = \eta_c/\eta$
η	Dense body viscosity	-
L	Dense body thickness	-
L_c	Decollement thickness	$L'_c = L_c/L$
$\Delta\rho$	Density contrast between the dense body and asthenosphere	-
ΔP	Pressure anomaly at the decollement edge (not an independent variable)	-
ρ_0	Asthenospheric density	-
g	Gravitational acceleration	-
τ	Initial exponential growth-rate	$\tau' = \tau\ \eta/(\Delta\rho g L)$
τ_2	Secondary non-linear growth-rate	$\tau'_2 = \tau_2\ \eta/(\Delta\rho g L)$
σ_s	Isostatic compensation stress	$\sigma'_s = \sigma_s/(\Delta\rho g L)$
$\hat{z}$, $\hat{s}$	Vectors pointing down and perpendicular to step	-
λ, λ_{max}	Perturbation wavelength: individual or specifically the fastest growing	-
	Temperature-Dependent Model Parameters	
Ra_δ, Ra	Boundary layer and mantle convection Rayleigh Numbers	-
T, ΔT	Temperature field and the mantle potential temperature	$T' = T/\Delta T$
κ	Thermal diffusivity	-
α	Coefficient of thermal expansion	-
β	Arbitrary viscosity scaling coefficient	-

w initially grows exponentially with a growth-rate τ (eq. 3.1, symbols in Table 3.1). The growth-rate controls the amount of time between the beginning of instability and high displacement growth, depending on the buoyancy ($\Delta\rho g L$) and viscosity (η) of the dense lower crust of lithosphere, as well as the perturbation wavelength (λ).

$$\begin{aligned} w &= w_0 e^{\tau(\lambda)t} \\ \tau &= \frac{\Delta\rho g L}{\eta}\tau'(\lambda) \end{aligned} \tag{3.1}$$

Due to the exponential growth and linearity of the Stokes equations, the RTI is dominated by the growth of one particular perturbation wavelength. The non-dimensional growth-rate (τ') depends on the model setup and has been calculated analytically for a range of density and viscosity profiles, non-linear rheologies and multiple layers (Conrad & Molnar 1999; Houseman & Molnar 1997; Neil & Houseman 1999), all demonstrating good agreement with the early growth in numerical calculations. This RTI model is only valid for small w. At large w, non-linear effects become prominent. In our analysis, instabilities beginning with small and large w are separated. If the latter do not trigger delamination, they are instead referred to as 'triggered dripping'.

In the case that the sinking body is much more viscous than the asthenosphere and is unrestricted at its top surface, there is a non-linear analytic model (eq. 3.2) which describes the instability growth for large w (Canright & Morris 1993) and agrees with numerical calculations (Neil & Houseman 1999). This model describes a period after the initial exponential growth, in which the sinking velocity grows super-exponentially at the rate τ_2' (Fig. 3.2). This model is applicable for instabilities which are growing non-linearly by internal thickening, but it cannot describe those which grow with significant viscous bending, which includes delamination.

$$w = \left(\frac{1}{w_0 + L} - \tau_2'\ t\right)^{-1} - L \tag{3.2}$$

The small and large perturbation models together form a generalised two-part model for the RTI, which can represent the complete growth of the RTI analytically (Fig. 3.2), up to the point at which the drip breaks off or reaches the base of the upper mantle. This two-part model is taken as a reference, which delamination is compared against.

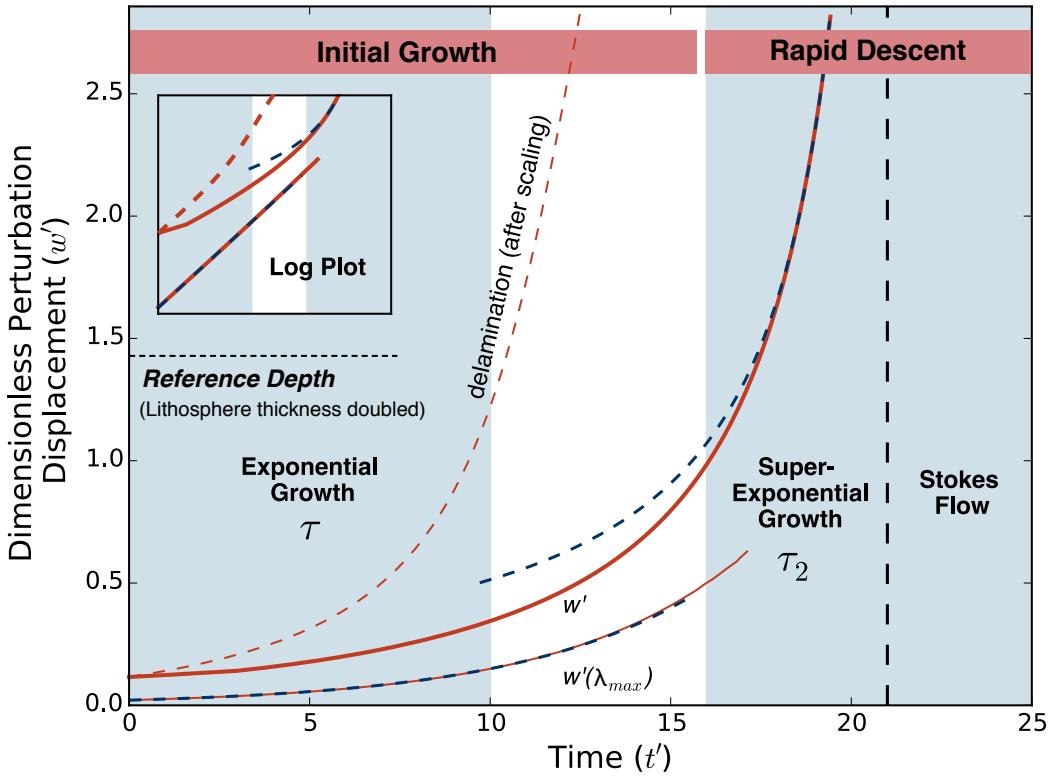

Figure 3.2: Typical non-dimensionalised perturbation displacement (w') over dimensionless time (t') for the RTI (thick, red solid line), $D' = 0$ and $\eta_c' = 1$. The analysis includes both the total displacement w' and the individual contribution from the fastest growing wavelength $w'(\lambda_{max})$. The latter is only important when $D' = 0$. Blue dashed lines denote the fitted analytic models of τ and τ_2 from eqs. (3.1) and (3.2). The delamination model, $D' = 1$ and $\eta_c' = 10^{-3}$, is shown for comparison. Here it is scaled by its initial growth-rate, which requires slowing it down 55x and demonstrates that in addition to its higher growth-rate, the onset of the secondary growth is relatively earlier than the RTI. We only analyse the initial growth, though flow will eventually reach a constant velocity, probably characterised by steady Stokes sinker flow.

3.1.2 Delamination Theory

The fundamental mechanism which allows material to delaminate has not been studied to the same detail as the RTI. Bird (1979) developed an analytic model for predicting the initial sinking velocity ($\dot{w}$) of delaminating lithosphere at small displacement (eq. 3.3). It assumes that the asthenosphere has intruded up into the lithosphere and into a weak middle to lower crustal layer, referred to as the decollement (Fig. 3.1). In their model, the relatively buoyant asthenosphere produces a pressure anomaly at the decollement edge (ΔP), which generates horizontal decollement flow and triggers delamination. The deforming decollement was modelled as Poiseuille flow, for which the pressure anomaly linearly decreases in the decollement away from the dense body edge. This pressure gradient

in the decollement is coupled to the resisting viscous bending stress of the dense body below, as it peels away. By combining the Poiseuille flow and viscous bending models, Bird calculated the initial vertical velocity for delamination (eq. 3.3). This analytic theory depends on additional parameters to the RTI: the thickness (L_c) and viscosity (η_c) of the decollement. ΔP is also not necessarily the same magnitude as the pressure anomaly driving the RTI, depending on the model formulation.

$$\dot{w} = \frac{\Delta P L_c}{6^{\frac{1}{3}} L \eta^{\frac{1}{3}} \eta_c^{\frac{2}{3}}} \tag{3.3}$$

The delamination velocity in analogue models increases with time (Bajolet et al. 2012). Bird & Baumgardner (1981) modelled delamination at high displacement using a combination of analytical and numerical techniques. Their calculated delamination velocity is proportional to the stress load at the edge of the body and therefore the amount of material already delaminated. They reasoned then that its growth should be exponential through time, though this hasn't been tested. Analogue materials engineering models (McEwan & Taylor 1966) have produced a similar relationship between peeling velocity and applied stress.

The delamination model (eq. 3.3) assumes that the initial gravitational energy is dissipated only through decollement flow and dense body bending. As was previously a point of contention in the subduction literature (Capitanio et al. 2007), there remains the possibility that passive mantle flow could play a significant role in dissipating energy. Le Pourhiet et al. (2006) argue that delamination is limited primarily by asthenospheric flow. While this may be true for a delaminating body when it has completely peeled away, it has been unclear if the lithospheric viscosity η limits the initial growth up to this point, as it does for the initial velocity in eq. (3.3).

3.2 Methodology

The initial conditions (Fig. 3.1) assume the triggering of a particular mechanism a priori, so that the focus of the analysis is the initial growing period which immediately follows. Whether dripping, triggered dripping or delamination occurs is controlled by two parameters, D and η_c. D is the size of a large, step perturbation, which is superimposed upon the smaller, random perturbations. It represents a change in the material's thickness which may have been generated by previous deformation, such as strike-slip faulting (Stern et al. 2013) or thinning due to plastic failure (Morency & Doin 2004). η_c has been introduced and controls the strength of the middle to lower crust, where a low value reproduces the jelly-sandwich rheological profile (Burov et al. 2006). Delamination is generally provoked when $D = L$

and η_c is smaller than η by a couple of orders of magnitude. We define triggered dripping as occurring when $D > 0$, provided delamination does not occur. D' and η_c' are generally the only two parameters which are varied, so that the gravitational potential energy and the viscosity of the sinking body are constant.

Anomalously high density rocks could form in the lower crust or lithosphere in a number of ways. In the lower crust, dense garnet-rich rocks can form as a restitic by-product of crustal melting (Lee et al. 2006). In the mantle lithosphere, peridotite cools to become denser than the asthenosphere within ~ 10 *Ma* of emplacement (Poudjom Djomani et al. 2001). The anomalous density of cold mantle lithosphere is typically about a third the magnitude of that for garnet-rich lower crust, though occurs over a larger thickness. Despite this difference, instability models can typically be non-dimensionalised so that one solution can be applied to sinking, dense material of any thickness, density and viscosity. Our models follow this approach and can equally describe the instability of a density anomaly in the lower crust or lithosphere, regardless of origin, which is hereon in referred to as the dense body (Fig. 3.1).

Parameter non-dimensionalisation is described in Table 3.1. Time is always scaled using the buoyancy to viscous stress ratio which arises in the analytic model. Application of this scaling to delamination assumes that flow is generated by the negative buoyancy of the dense body compared to the asthenosphere and the dominant resisting viscosity also belongs to the dense body. The latter would not be the case if energy is primarily dissipated in the asthenosphere, which is ruled out below. Scaling of the decollement parameters are relative to the dense body, as delamination depends on the interplay between dense body and decollement flow.

The models are 2D unless otherwise mentioned. A Newtonian rheology is used, as the primary focus is the comparison of the simplest delamination instability and RTI cases. For the RTI, a stress-dependent viscosity with an exponent of three approximately doubles the maximum growth-rate, but does not affect the corresponding wavelength (Conrad & Molnar 1997). Stress-dependence would therefore effectively halve η in eq. (3.1). In the models, delamination is driven by the same buoyancy stress as dripping, so stress-dependence will likely play an equal or greater role, depending on the magnitude of bending stresses. Our delamination growth time-scales are therefore conservative.

The model domain edges all use the free-slip boundary condition (BC). This is equivalent to assuming that all stresses at the domain top are balanced by topography, that the model base corresponds to a substantial viscosity increase at the 660 km mantle discontinuity and that flow is symmetrical at the walls. Though the ceiling BC is set as free-slip, the decollement and dense body essentially have a no-slip ceiling, as the upper crustal material has a viscosity of three and six orders of magnitude higher than the dense body and asthenosphere respectively. The upper crustal layer represents a strong

intra-plate crust and is set to a constant thickness of $0.21L$. Its density is set to $-15\Delta\rho$, which, for $\rho_0 = 3300\ kg\ m^{-3}$ and $\Delta\rho \geq 30\ kg\ m^{-3}$, results in a crust which is $< 2850\ kg\ m^{-3}$ and strongly resists sinking. The decollement density is set to a neutral buoyancy, ρ_0. This simplification is conservative as the decollement may be mafic or garnet-rich, which would contribute to the dense body's negative buoyancy and increase decollement flow. The asthenosphere viscosity is set as $10^{-3}\eta$, such that it is approximately inviscid. L_c' is set to 0.21 in order to focus on the effect of varying η_c', though it was also varied to test scaling laws. The starting perturbation (w_0) is set as a cosine series of five random wavelengths, chosen from the range of wavelengths with the quickest growth-rates in the analytic models.

The finite-element Lagrangian particle-in-cell code Underworld (Moresi et al. 2007) is used to solve the 2D and 3D Stokes equations. The 2D and 3D models used for the transition analyses are coupled to the thermal advection-diffusion equation. The code has been benchmarked for thermal convection (Moresi & Solomatov 1995) and the RTI (Moresi et al. 2001). The 2D models have length:height ratios of 3:1 and resolutions of 1296 x 432, as required to accurately measure $w'(\lambda_{max})$, which is halved when this measurement is not required. The model domain depth represents the upper mantle and is six times the thickness of the whole lithosphere.

3.2.1 2D and 3D Temperature-Dependent Models

A secondary objective of this work is to quantify the conditions required for thermal diffusion to influence instability growth. 2D models are designed to explore whether delamination can be prohibited by cooling of the initially thinned lithosphere. 3D models are designed to quantify the amplitude of an initially planar perturbation required to prevent 3D drips from growing (Fig. 3.1, '3D Morphology'), particularly as a function of decollement strength and relative thermal diffusion.

A second set of models is required to address these objectives, as the primary set of models are temperature-independent. These secondary models solve for temperature diffusion and may be 2D or 3D, coupling the thermal advection-diffusion equation to the Stokes equations (Moresi et al. 2007). They are designed identically to the primary set of models, except where noted. The temperature-dependence in Underworld has been extensively benchmarked for thermal convection (Moresi & Solomatov 1995). The temperature-dependent 2D models use a coarser resolution of 384 x 128, due to the higher computation cost of the coupled equations and the calculation of more time-steps in order to study the instabilities at high amplitude and with thermal convection. The 3D models use height:length:width ratios of 1:3:2 and a coarser resolution of 128 x 288 x 192. The 3D mesh is also uniformly spaced and each element is populated with at least 20 particles. These temperature-dependent models begin with an arbitrary

temperature (T) field. The surface temperature is maintained as zero and the entire asthenosphere is set to a homogeneous value, ΔT. ΔT is the 'potential mantle temperature' and is the temperature of the mantle if it is adiabatically transported to the surface. It is assumed that no mantle plumes affect the ambient mantle temperature distribution. Therefore, the base of the model domain is maintained as ΔT, to prevent any upwellings. The model walls are set as insulating. The Moho is set to $0.5\Delta T$, while separate crust and dense body linear geotherms are set to ensure the temperature field is continuous. As all temperatures are relative to ΔT, T is non-dimensionalised as: $T' = T/\Delta T$.

Only the density and viscosity of the dense body and asthenosphere differ from the primary (temperature-independent) models. The density of both the dense body and asthenosphere is set according to: $\rho_0(1 - \alpha(T - \Delta T))$, where ρ_0 is the material density at $T = \Delta T$ and α is the coefficient of thermal expansion. ρ_0 is identical for the dense body and asthenosphere, so that the density varies continuously across the asthenosphere-dense body interface. α is set for the dense body such that its average density is $\rho_0 + \Delta\rho$. In the asthenosphere, α is chosen so as to set the thermal convection Rayleigh number, defined as $Ra = \alpha\Delta T\rho_0 gL^3/(10^{-3}\eta\kappa)$, to 10^8, ensuring vigorous convection. κ is the thermal diffusivity and is homogeneous across the model domain and $10^{-3}\eta$ the asthenospheric viscosity at ΔT. The models are intended to be applicable to a range of dimensionalised growth-rates, rather than for example a particular κ or $\Delta\rho$, so the ratio of instability flow time-scale to thermal diffusion time-scale is varied. This relative time-scale only depends on the boundary layer Rayleigh number, defined in eq. (3.4) and varied from $Ra_\delta = 2.79$ to 10^3.

$$Ra_\delta = \frac{\Delta\rho g L^3}{\eta\kappa} \tag{3.4}$$

Temperature-dependent viscosity varies according to an arbitrary exponential law: $\mu\beta e^{E'/(T'+T'_0)}$. E' is the activation energy, after it has been non-dimensionalised by ΔT and the gas constant. It is a constant set to $E' = 13.82$, which results in a maximum viscosity contrast of 10^8. T'_0 is an arbitrary non-dimensional temperature which offsets the non-dimensional temperature T', used for example in mantle convection modelling (Lenardic & Kaula 1996), to avoid the extreme viscosity variations at low temperatures which arise for $T'_0 = 0$. It is a constant set to $T'_0 = 0.5$. β is an arbitrary scaling coefficient, where $\beta = 10^{-7}$ and $\beta = 6.3 \times 10^{-6}$ for the asthenosphere and dense body respectively. These β values give the dense body an initial average viscosity of μ and the asthenosphere a viscosity of $10^{-3}\mu$ at $T' = 1$, both equivalent to the temperature-independent models. The dense body viscosity initially varies by two orders of magnitude. The asthenospheric viscosity varies from $10^{-1}\mu$ to 10μ for $0.5 < T' < 0.25$, so asthenosphere which has risen to the Moho would increase to a viscosity in this lower range once it cools.

3.2.2 Measurements

The interface between the dense body and asthenosphere is tracked using markers which are advected through time. The marker which reaches the reference depth first is used to track the perturbation growth. This reference depth is chosen as the perturbation displacement at which dripping lithosphere has doubled in thickness, $w' = 1.43$ (Fig. 3.2). The typical procedure of fitting τ' and τ_2' to the displacement-time curve is used (Houseman & Molnar 1997; Neil & Houseman 1999). This involves calculating the proportionality constant between $ln(w')$ and t' for τ' and between $-1/(w'+1)$ and t' for τ_2', using linear regression. As the initial perturbation is the superposition of random wavelengths, this measure of τ' can be an underestimate. We also calculate the growth of the individual invoked waveforms, $w'(\lambda)$, using the discrete cosine transform of the interface markers. When $D' > 0$, we include the wavelengths corresponding to the ten largest terms in the cosine series for a step. Growth-rate measurements of individual waveforms have been benchmarked against the analytic solution of $\tau'(\lambda)$ for $D' = 0$ and $\eta_c' = 1$. We report the largest initial growth-rate measured for each instability, which is typically calculated from $w'(\lambda)$ for $D' = 0$ and w' for $D' > 0$. Initial velocity is taken directly from the velocity solution of an instantaneous calculation without time-stepping. This initial calculation begins with only one wavelength, corresponding to the quickest velocity.

The predicted contrast in shear-strain between dripping and delamination (Fig. 3.1) is tested by integrating shear-strain on many markers within the dense body as it deforms. At each time-step and on each marker, the strain-rate is projected onto the reference frame which was initially horizontal, but may since have rotated. The shear-strain in this reference frame is integrated over each time-step and eventually compared for the reference displacement.

In the 3D models, we distinguish between the drip and planar morphology by comparing the largest amplitude from the cosine transform of the vertical velocity component in directions parallel and perpendicular to $\hat{s}$ (Fig. 3.1). The ratio between these should be one for a drip morphology. We also quantify whether or not instability migration occurs in the step direction, by finding the angle between the horizontal velocity component and $\hat{s}$. If migration is dominated by the initial step perturbation, this should be 0°, and larger if 3D instabilities become prominent. Both of these measures are calculated at the base of the dense body and an average value, also compared at the reference depth.

Molnar et al. (2015) define isostatic and dynamic topography as resulting purely from anomalous density and viscous stress respectively. Following this definition, the deviation from the initial density distribution is integrated for many columns, resulting in a profile of isostatic topography. The total topographic response, the sum of the dynamic and isostatic components, is calculated by assuming it balances the stress at the top of the model domain, σ_s. Topography of the Moho, measured as

the displacement of the initially flat upper surface of the dense body, corresponds to seismic reflectors observed in nature (Levander et al. 2011). Its vertical deflection, w_m, is normalised to the perturbation displacement, $w'_m = w_m/w$ and should be close to one for delamination.

3.2.3 Analytic Solution and Scaling

The analytic method of Neil & Houseman (1999) is used to solve for a RTI which includes the decollement layer. Anomalous pressure BCs are applied at both the asthenosphere-dense body and dense body-decollement interfaces, the latter required to be consistent with the assumption that the decollement material is of reference density. There are typically two growth solutions, one growing and the other decaying, of which we take the former. We also solve for the case where the dense body-decollement interface has no initial perturbation, which then has one growing solution.

In the original delamination model of Bird (1979), delamination is driven by the buoyancy contrast between the asthenosphere and decollement layer, while the delaminating body does not contribute any buoyancy contrast. In order to directly compare the delamination model of Bird (1979) to the RTI, we modify the delamination model (eq. 3.3) such that the pressure anomaly at the decollement-asthenosphere interface (ΔP) arises from the anomalous hydrostatic pressure of the dense body. This requires the assumption that the anomalous pressure can be represented as a point load on the end of the dense body. We then non-dimensionalise the decollement length scale and viscosity using the dense body as a reference (Table 3.1). This results in a velocity which is proportional to the buoyancy time-scale, $\eta/\Delta\rho g L$, encountered in the RTI (eq. 3.1). We use this to non-dimensionalise the time-scale of the delamination velocity. The non-dimensional velocity then depends only on the ratios of decollement to dense body thickness and viscosity, L'_c and η'_c, rather than absolute values (eq. 3.5). If the delamination velocity varies proportionally to the amount of dense body which has delaminated, as proposed by Bird & Baumgardner (1981), the growth will be exponential and self-similar like the RTI. The exponential growth-rate should also then be non-dimensionalised and scaled in the same way as the initial velocity (eq. 3.5). This formulation is a simple prediction of the delamination growth-rate depending on the decollement properties, which we test numerically.

$$\dot{w}'_0 \propto \tau' \propto \frac{L'^2_c}{\eta'^{\frac{2}{3}}_c} \tag{3.5}$$

3.3 Results

Dripping, triggered dripping and delamination must initially be distinguished in the models, so that their growth-rates can later be compared. The delamination characteristics are reproduced only for a small range of D' and η'_c. The Moho displacement diagnostic of delamination, $w'_m = 1$, only occurs for $D' = 1$ and $\eta'_c \leq 3 \times 10^{-2}$ (Fig. 3.3). There is a large decrease in Moho displacement for $D' < 1$, marking a change in mechanism from delamination to triggered dripping. The Moho displacement of dripping and triggered dripping can still be $< 60\%$ of the displacement of delamination, when η'_c is small. With decreasing D', the Moho becomes more cuspate and symmetrical (Fig. 3.8). Its displacement becomes negligible once $\eta'_c = 1$, even for $D' = 1$, though this would not be the case for denser decollement and crust.

The shear-strain in the models with $w'_m = 1$ is < 0.04 (Figs. 3.3 and 3.7), which is relatively small. Therefore the deformation of models with $D' = 1$ and $\eta'_c \leq 3 \times 10^{-2}$ can be confidently characterised as delamination. Though the delamination shear-strain is small, it is non-zero, most likely because the dense body is thick enough that the negligible thickness assumption of the viscous bending model used in eq. (3.3) is an approximation. However, it is still clearly lower than for triggered dripping, which remains relatively constant with decreasing η'_c and for dripping, which is significantly larger.

Dripping shear-strain is relatively large, as expected. It reduces significantly as η'_c decreases, because λ_{max} consequently increases. However, it is still substantially larger than for models with $D' > 0$. Triggered dripping can be distinguished from the end-member models using Moho displacement and shear-strain (Fig. 3.3). They do not plot proportionally between the two end-members. The Moho displacement of triggered dripping is similar to that of dripping, yet it deforms by viscous bending much more so than dripping does.

3.3.1 Initial Velocity

The dripping, triggered dripping and delamination models, characterised by their contrasting deformation, also produce contrasting dynamics. The initial velocity ($\dot{w}'_0$) of dripping ($D' = 0$) varies with η'_c, as calculated analytically (Fig. 3.4). The analytic solutions without any initial decollement perturbation provide a better prediction as they match the initial conditions of the numerical models, which for $\dot{w}'_0$ are instantaneous. For triggered dripping ($D' > 0$), the velocity increases by up to an order of magnitude (Fig. 3.4), though not proportionally to D' as would be predicted for the linear RTI. This increasing $\dot{w}'_0$ is approximately independent of η'_c, so its effect can be empirically fitted and scales approximately as $ln(\dot{w}'_0) \propto D'$.

When $D' = 1$ and $\eta_c' \leq 10^{-2}$, the variation of $\dot{w}_0'$ with decreasing η_c' does change and exceeds the empirical variation for triggered dripping. These models correspond to delamination and the scaling for delamination (eq. 3.5) accurately predicts the variation of $\dot{w}_0'$ instead, with a proportionality constant of 0.23. Additional models (not shown) also held $\eta_c' = 10^{-2}$ constant and varied L_c', to test the proportionality between $\dot{w}_0'$ and $L_c'^2$. It holds for $L_c' < 0.5$. There is likely to be a lower bound to the scaling, as the decollement becomes too thin for delamination to occur, which was not explored. The proportionality constant is approximately half of the analytically calculated value. The reason for discrepancy is unclear, though it may be a result of the assumption that the dense body weight can be represented as a point load at its end.

A)

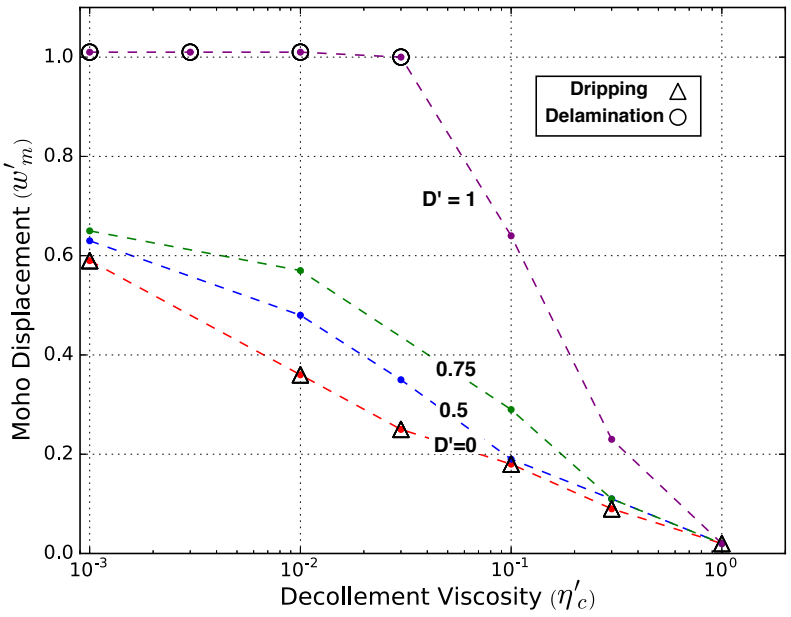

B)

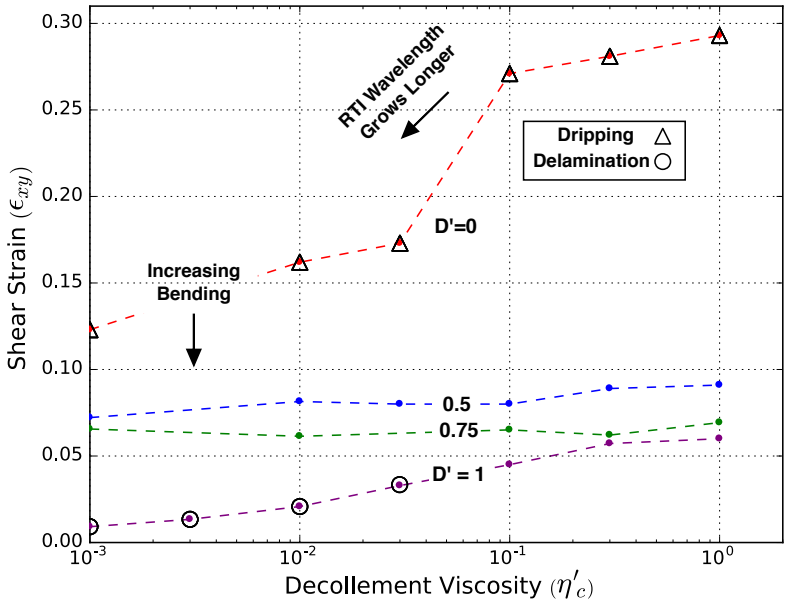

Figure 3.3: Moho displacement (A) and shear-strain (B) for varied η'_c and D'. Models with $D' = 0$ are characterised as dripping, because of their initial conditions and their excellent agreement with analytic RTI models (Figs. 3.4 and 3.6). Models are characterised as delamination if $w'_m = 1$ and shear-strain is relatively low. Triggered dripping models, the points not characterised as dripping or delamination, have Moho displacements and shear-strain bearing greater quantitative similarity to the dripping and delamination end-members respectively, for each η'_c.

A)

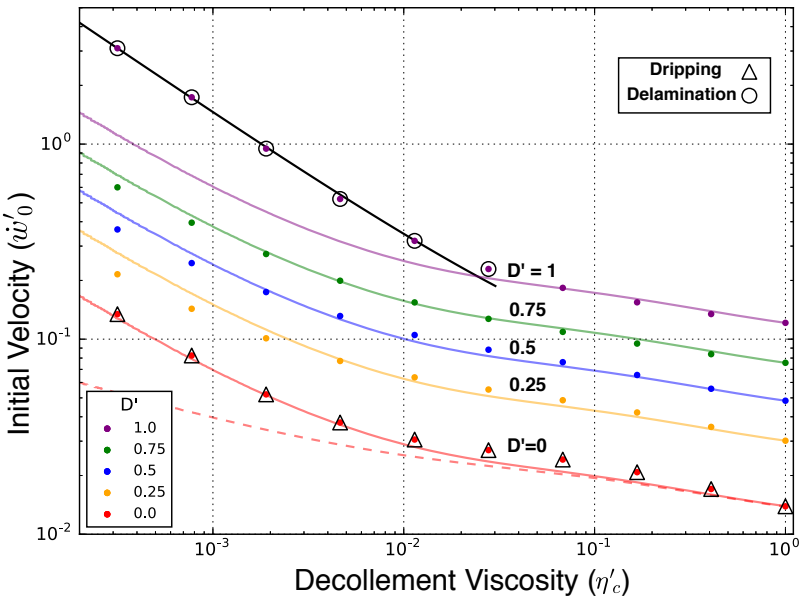

B)

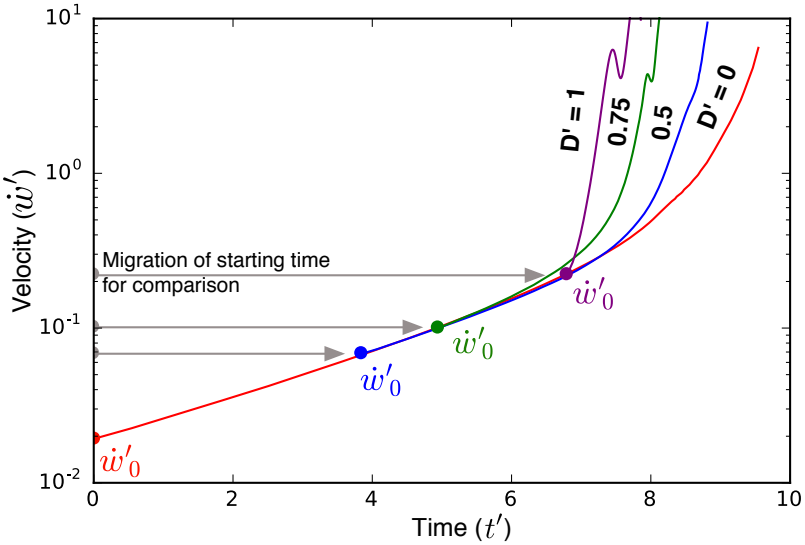

Figure 3.4: **A)** *Initial velocity ($\dot{w}$) for varying D' and η'_c, from instantaneous numerical calculations (points) with $w'_0 = 0.085$. The analytic RTI solutions are shown, with (solid red) and without (dashed red) a growing perturbation of the decollement layer. The latter is also scaled empirically from the $D' = 0$ case (solid curves). The analytic delamination scaling (eq. 3.5, solid black) predicts the correct variation of time-scale with η'_c, for the delamination models.* **B)** *Interface velocity through time for $\eta'_c = 10^{-2}$ and varying D'. Self-similarity of the initial growth period is apparent if the starting times (solid points) of the curves with $D' > 0$ are shifted, to the time at which the dripping model ($D' = 0$) reaches their respective values of $\dot{w}'_0$. Delamination ($D' = 1$) however no longer shares the initial growth-rate. At this low η'_c, the super-exponential growth-rate τ'_2 clearly increases with increasing D'.*

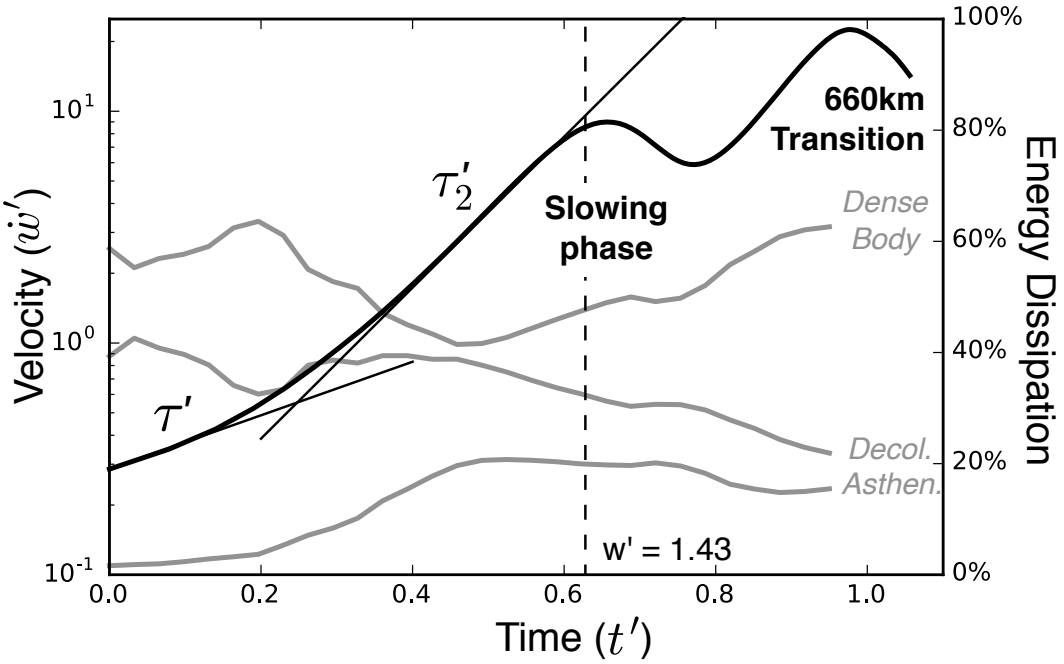

Figure 3.5: Delamination velocity over time, when $\eta_c' = 10^{-2}$. The two growth phases, τ' and τ_2' are shown (note the logarithmic scale) as well as the time at which the reference depth $w' = 1.43$ is reached. The dimensionless time and velocity could be scaled for the example of $\Delta\rho = 30$ kg m^{-3}, $L = 50$ km and $\eta = 10^{21}$ Pa s as $t = 2.15$ t' Ma and $\dot{w} = 2.33$ $\dot{w}'$ cm yr^{-1}. The energy dissipated in each material as a percentage of the total dissipation at a given time (grey) demonstrates the dominating dissipation in the dense body and decollement system, especially during the initial growth.

3.3.2 Growth-Rate Comparison

The analytic dripping solution predicts a 3x increase in the dripping ($D' = 0$) growth-rate, as η_c' decreases from 1 to 10^{-3} (Fig. 3.6). This is matched numerically. The analytic solution which allows the decollement to be perturbed, provides the best fit, indicating that thickening of the decollement layer significantly slows down dripping growth-rates at low η_c'. Triggered dripping models ($1 > D' > 0$) generally share the initial growth-rate of the dripping model at a particular η_c'. This self-similarity means that the initial growth of the triggered dripping models begins as if it is starting from a later point in the $D' = 0$ velocity curve (Fig. 3.4). Therefore, an initial step does not increase the exponential growth-rate of triggered dripping, compared to dripping, but does result in a higher velocity and the second growth phase is reached more quickly. The self-similarity generally does not hold for τ_2', which increases with increasing D'. The spread of τ_2' becomes larger with decreasing η_c'.

The velocity of a delaminating body increases exponentially, immediately after triggering (Fig. 3.5), which confirms the hypothesis of Bird & Baumgardner (1981). Unlike triggered dripping, delamination

does not share the same initial τ' as the dripping model with an equivalent η_c'. Instead, it begins with a τ' which is much larger than for dripping. The variation of τ' with changing η_c' is accurately predicted by eq. (3.5). The accuracy of this scaling in describing the variation of $\dot{w}_0'$ and τ supports the hypothesis that the initial delamination growth occurs as an interplay between viscous bending of the dense body and Poiseuille flow in the decollement.

The exponential growth-rate of delamination is at least an order of magnitude quicker than for dripping (Fig. 3.6). Delamination quickly progresses into the second growth phase (Figs. 3.4 and 3.5), so comparisons between dripping and delamination growth-rates based purely on τ' are an underestimate. It can be used for comparing delamination models however, as τ' and τ_2' vary in the same way with changing η_c'. The integrated mass-flux through the reference depth also increases exponentially at a rate proportional to τ', for all mechanisms. Delamination therefore recycles material at a significantly higher rate, compared to dripping, the latter overestimated in these models with an isoviscous dense body. Delamination has an intermittent slowing phase which does not occur in dripping. This slowing phase also appears in triggered dripping for $D' = 0.75$ (Fig. 3.4). It is brief though and occurs when the instability has already attained a significant velocity. The slowing phase therefore does not influence the time taken to reach the rapid descent phase.

As τ' is generally the same for dripping and triggered dripping, for a given η_c', it is primarily the increase in w_0' which decreases the time taken for instability growth. For delamination, it is instead the increased τ' which plays the biggest role in decreasing its growth time. The growth times of the different mechanisms can all be compared by plotting the time taken for each model to reach the reference depth (Fig. 3.6). Increasing D' for triggered dripping decreases the time taken for growth, independently of η_c'. The higher τ' of delamination results in a growth time which is approximately an order of magnitude lower than dripping or triggered dripping. Both τ' and τ_2' vary in the same way with changing η_c', so although delamination has passed through its second growth phase by $w' = 1.43$ (Fig. 3.5), the growth time also scales to eq. (3.5) (Fig. 3.6).

To summarise, dense material can sink at an order of magnitude quicker rate if it is able to delaminate, compared to if it drips. Though delamination begins with a relatively higher velocity than for dripping or triggered dripping, it is the significantly higher exponential growth-rate which is primarily responsible for this contrast. For example, a dense body with $\Delta\rho = 30\ kg\ m^{-3}$, $\eta = 10^{22}\ Pa\ s$ and $L = 50\ km$ would begin sinking at the geologically insignificant rate of $\sim 2 \times 10^{-2}\ cm\ yr^{-1}$. However, due to the high delamination growth-rate, the sinking body would take $\sim 15\ Ma$ to delaminate from the crust and begin rapidly descending through the upper mantle, for $\eta_c' = 10^{-2}$. This compares to $\sim 350\ Ma$ and $\sim 275\ Ma$ for dripping and triggered dripping ($D' = 0.5$) respectively. Assuming that dense material begins in a state of slow dripping, the conditions for delamination are of greater dynamic

consequence than that of triggered dripping. In the models, a small change from $D' = 0.75$ to $D' = 1$ alters the instability time-scale by almost an order of magnitude.

A)

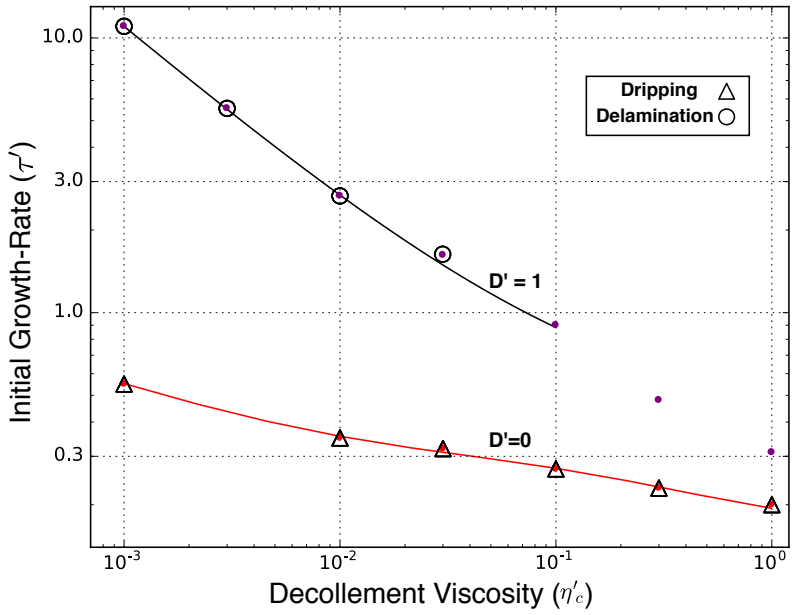

B)

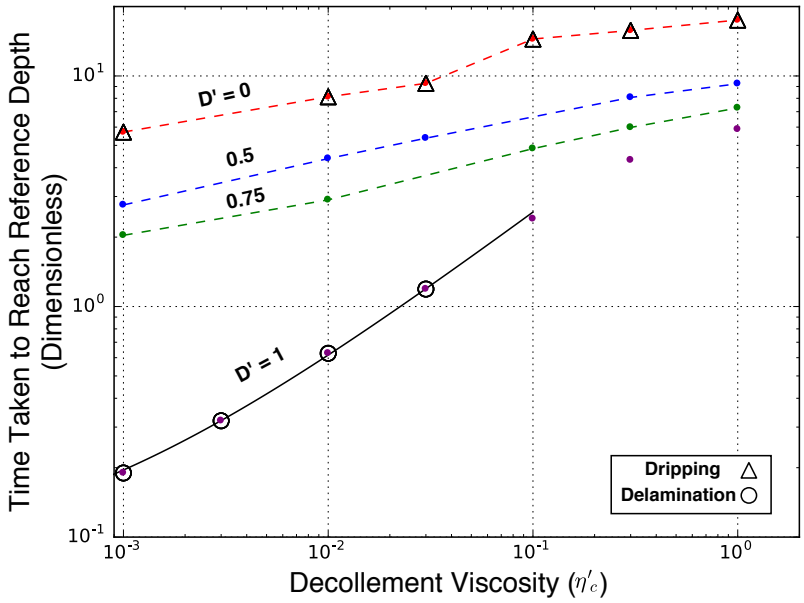

Figure 3.6: **A)** *Small displacement exponential growth-rate for varying D' and η'_c. The analytic RTI solution with a decollemont perturbation is plotted (red). Triggered dripping ($1 > D' > 0$) models are not shown, as they share the same τ as for dripping. The points for $D' = 1$ and $\eta'_c > 10^{-1}$ are exceptions and show the transition from triggered dripping to delamination models. The delamination models show good agreement with the delamination scaling (black), eq. (3.5).* **B)** *Time taken to reach the reference depth for models with varying D' and η'_c. The delamination scaling from eq. (3.5) (solid black) accurately predicts the variation in this time with η'_c. Dashed coloured lines are used purely to mark the model sets for each D'. Time can be dimensionalised, for example by $t/t' = 10$ Ma, assuming $\Delta\rho = 30$ kg m^{-3}, $L = 50$ km and $\eta = 5 \times 10^{21}$.*

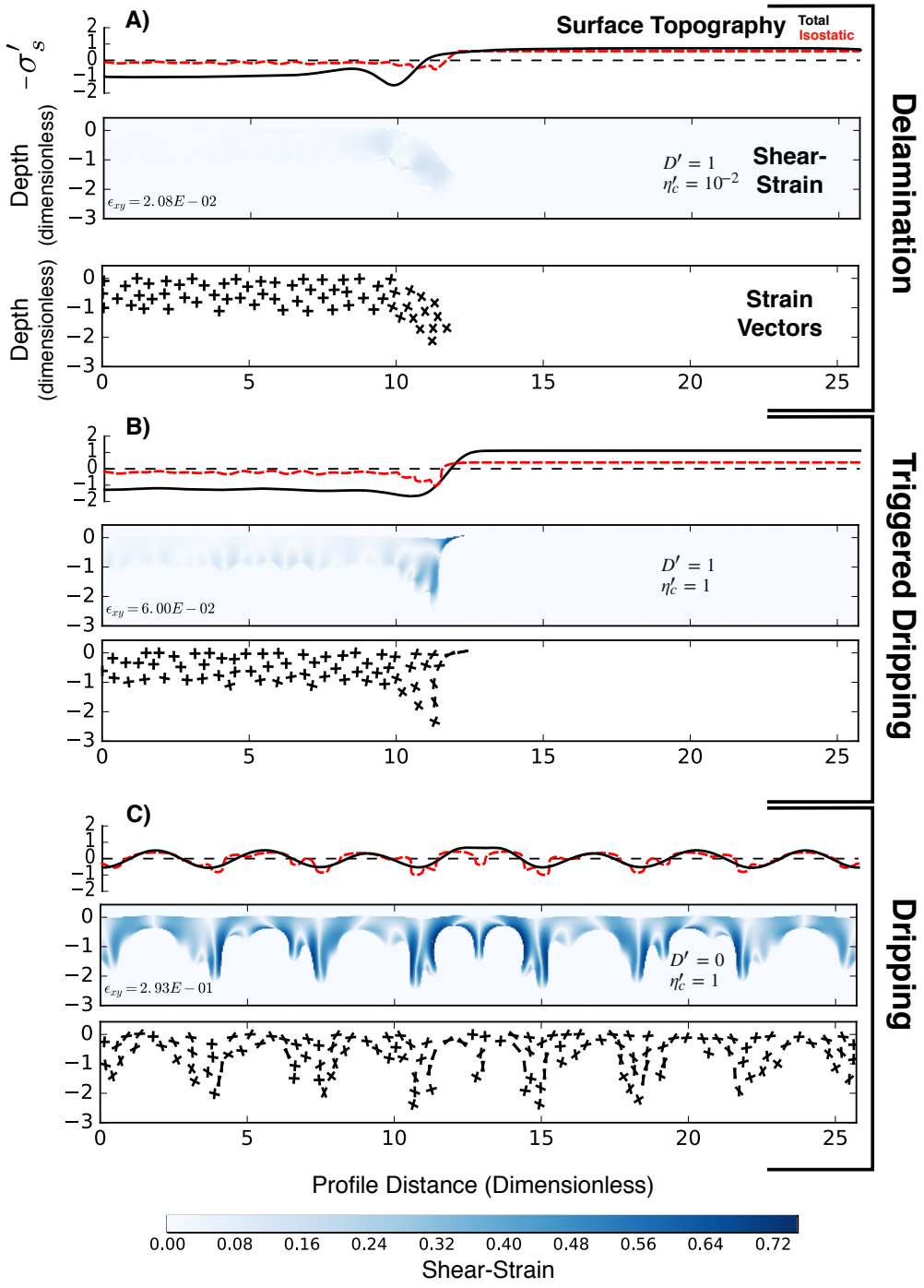

Figure 3.7: Shear-strain for examples of delamination (top), triggered dripping (middle) and dripping (bottom), with parameters inset. Sub-sampled vectors corresponding to the shear-strain measurement are shown, as well as the average shear-strain (ϵ_{xy}) and total topographic profile for each. The non-dimensional stress σ'_s can be scaled to a dimensional elevation using a reference stress, $\sigma'_s \Delta\rho L / (\rho_c L')$, where ρ_c is the upper crustal density. Taking $\Delta\rho = 30$ kg m^{-3}, $\rho_c = 2500$ kg m^{-3} and $L = 50$ km gives an elevation of 0.86 σ'_s km. With these dimensions, topography varies by < 1 km from the reference elevation.

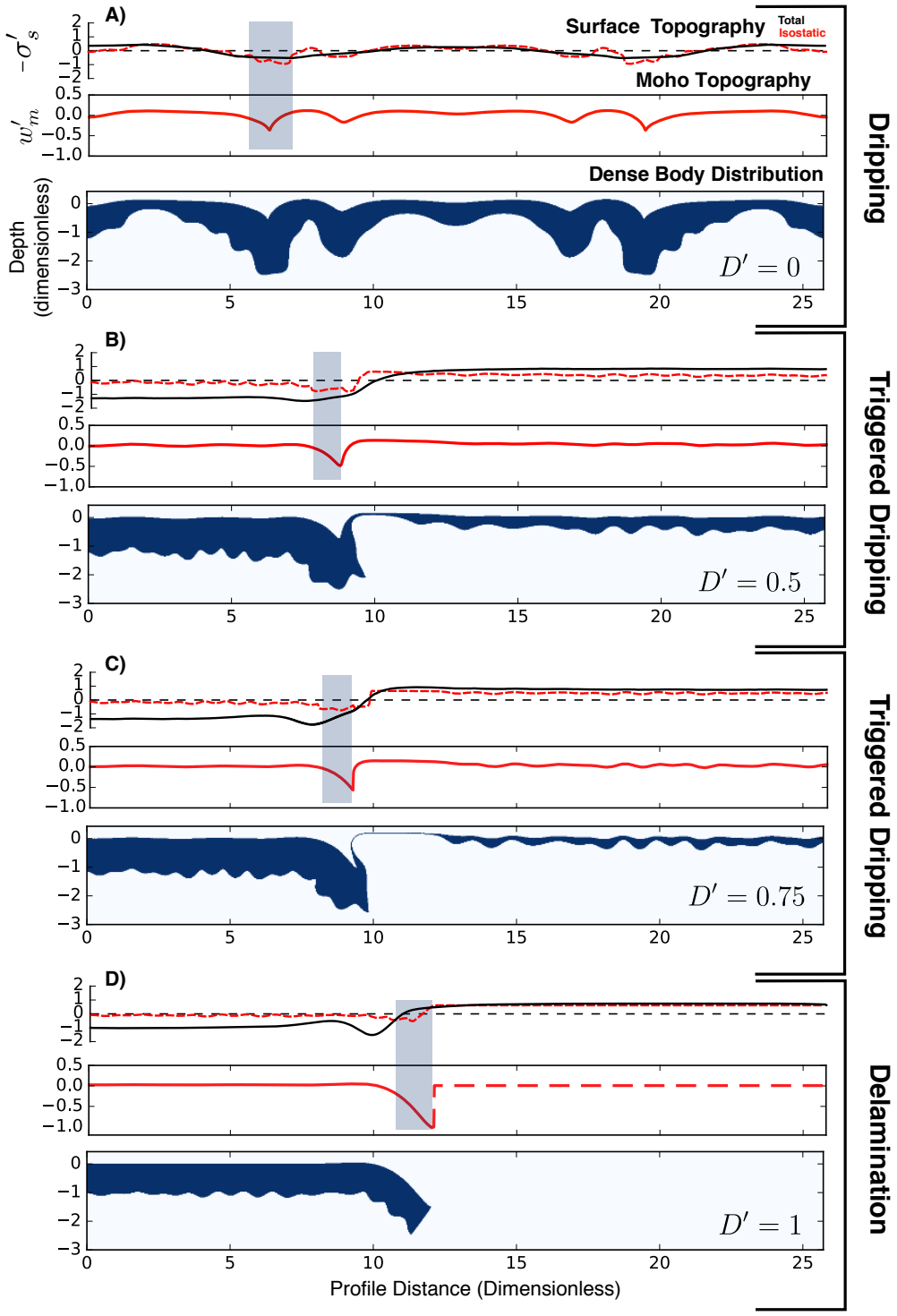

Figure 3.8: Profiles of surface elevation and the depth to the Moho for models with $\eta_c' = 10^{-2}$, shown with the distribution of dense body directly below, all at the same displacement $w' = 1.43$. The location of subsidence in relation to the dipping Moho and the edge of the dense body subtly contrasts between triggered dripping and delamination, as emphasised by the shaded regions.

3.3.3 Energy Dissipation

In scaling delamination by the viscosity of the dense body, rather than that of the asthenosphere, we have followed the assumptions of Bird (1979) that the delamination velocity is primarily limited by flow of the decollement and dense body. The converse is that the asthenosphere provides the only non-negligible resistance, so that delamination would then be modelled by Stokes sinker flow. The dependence of delamination time-scales on η_c' favours the former model, but we need to test whether the latter is also occurring. A simple way to quantify which system, the lithosphere or asthenosphere, the delamination velocity is most sensitive to, is to compare the energy dissipated by viscous flow for each material.

During the first exponential growth phase, the dense body and decollement account for more than 95% of the total energy dissipation (Fig. 3.5). Dissipation by the asthenosphere increases to $\sim 20\%$ during the quicker second phase, but this is still only a minor role. The dissipation in the first half of the instability's growth is consistent with the model that the increasing velocity occurs due to quicker bending of the dense body and Poiseuille flow in the decollement. In the second half, dissipation in the dense body dominates over that of the decollement, until it is 60% of the total dissipation as it nears the 660 *km* transition. This also corresponds to the brief slowing phase, which may mean that the growth switches to a mode in which the sunken dense body is deforming, potentially transitioning to dripping, more than it is decoupling. This could be because the bending velocity is unable to maintain its acceleration, or because deformation of the delaminated portion becomes more efficient than further peeling. Delamination is therefore controlled by lithospheric dynamics, rather than the asthenosphere, even at high displacement. Scaling by η and η_c' holds and the initial delamination growth, before it reaches the lower mantle transition, should not be modelled as Stokes sinker flow.

3.3.4 Surface and Moho Topography

Dripping and triggered dripping produce topography of contrasting morphology and magnitude (Figs. 3.7 and 3.8). Triggered dripping ($D' > 0$) produces subsidence which is more than twice as deep as for dripping. This subsidence is part of an asymmetric system of localised subsidence and adjacent uplift, either side of the step, which contrasts the symmetrical topography of dripping. The localised subsidence and uplift produced by triggered dripping is superimposed onto large wavelength zones of subsidence and uplift, corresponding to the growth of the initial large wavelength step perturbation. The increased subsidence of triggered dripping is due to an increase in the dynamic topography, as the isostatic response is near identical to that of dripping. Overall, topographic morphology and magnitude are diagnostic of dripping or triggered dripping.

Morphology and magnitude, however, are almost identical for triggered dripping and delamination, despite their contrasting dynamics. Their similarity is surprising, given their contrasting mechanisms. For example, the lack of dense body thickening in delamination results in a negligible change to isostatic topography during evolution. Its higher sinking velocity compensates this and produces dynamic topography of similar magnitude to triggered dripping.

Migration of the localised zones of adjacent subsidence and uplift also occurs in both triggered dripping with $\eta_c' < 1$ and delamination. The position of localised subsidence is the result of a different mechanism for triggered dripping and delamination. It occurs in triggered dripping at the dense body edge, the region of highest thickening and acceleration. The zone of highest thickening migrates over time due to the asymmetry of the initial step perturbation. Localised subsidence is generated in delamination in the region where the dense body transitions from strong coupling with the decollement to no coupling and is the result of dynamic, rather than isostatic, stress. This section of the dense body is supporting the weight of the sinking, decoupled part. The weight is supported by a bending stress in the dense body, but also the resistance of the decollement which transfers the stress to the surface. The wavelength of the localised zone of subsidence is much shorter than the wavelength of viscous bending. Comparing the topographic calculation to the distribution of energy being dissipated by viscous bending, the position of localised subsidence corresponds to the largest bending stress, which rapidly decays towards the remainder of the coupled dense body. As this transitional zone with high bending stress is generally at the transition from coupled to decoupled dense body, it migrates as the dense body decouples.

The distance that localised topography has migrated by $w' = 1.43$ generally increases with decreasing η_c'. This distance is actually slightly further for triggered dripping with $0.5 \leq D' \leq 0.75$ and $\eta_c' = 10^{-2}$, than delamination (Fig. 3.8). The edge of the dense body has also migrated further in these triggered dripping models than delamination. This occurs due to the contrasting mechanisms producing topography and demonstrates that the migration of topography is not diagnostic of delamination over triggered dripping.

Triggered dripping and delamination also contrast in their locations of localised subsidence in relation to the dense body edge. The region of localised subsidence is positioned directly above the sunken portion of dense body for triggered dripping and directly above the edge of the 'attached' dense body for delamination (shaded areas, Fig. 3.8). This contrast may be diagnostic of dripping or delamination in nature, if the top of the dense body and the extent of sunken material can be observed as a reflector and in tomography respectively. The contrast occurs because material which has sunk by dripping and is still attached will be thickened and generally produce subsidence directly above by isostatic compensation. Delaminated material has instead decoupled and asthenosphere flowing in above it and

the thinned lithosphere above produces uplift dynamically and isostatically respectively. This may not always be the case however, as dripping may produce uplift above if it sufficiently thickens buoyant crust in the process of sinking (Neil & Houseman 1999).

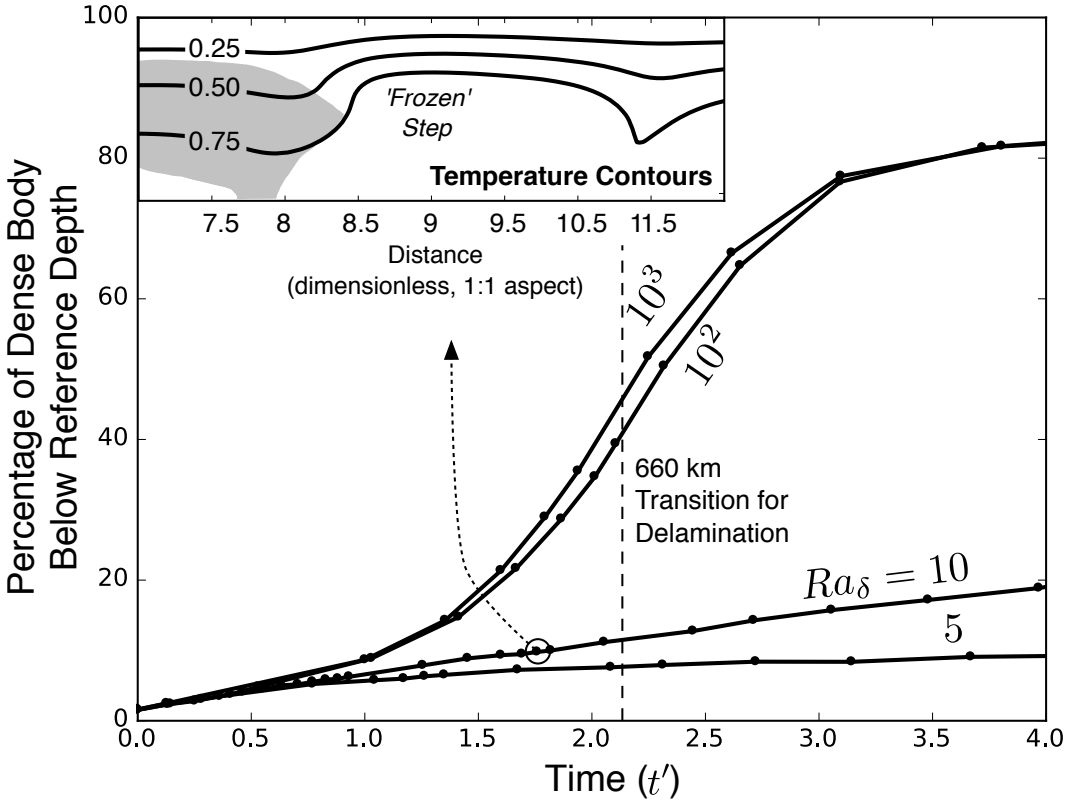

Figure 3.9: Percentage of material which has sunk past the depth corresponding to the initial base of the dense body, for varying boundary layer Rayleigh numbers. Models were 2D and used $\eta'_c = 10^{-2}$, $D' = 1$ and temperature-dependent density and viscosity. Delamination reverts to dripping for $Ra_\delta \leq 10$, as shown inset for a particular time-step from $Ra_\delta = 10$. In this example, the wedge zone above the displaced dense body (the latter shaded) has cooled and further peeling is prevented. Temperature contours are labelled as fractions of the potential mantle temperature.

A)

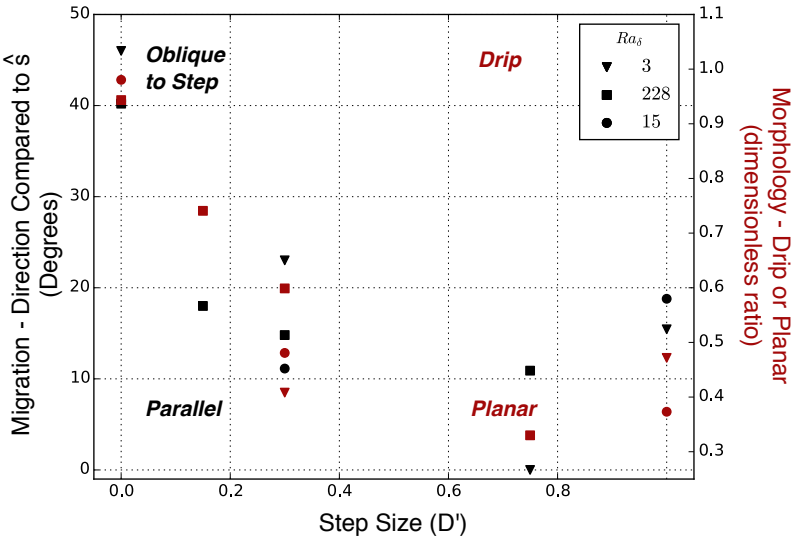

B)

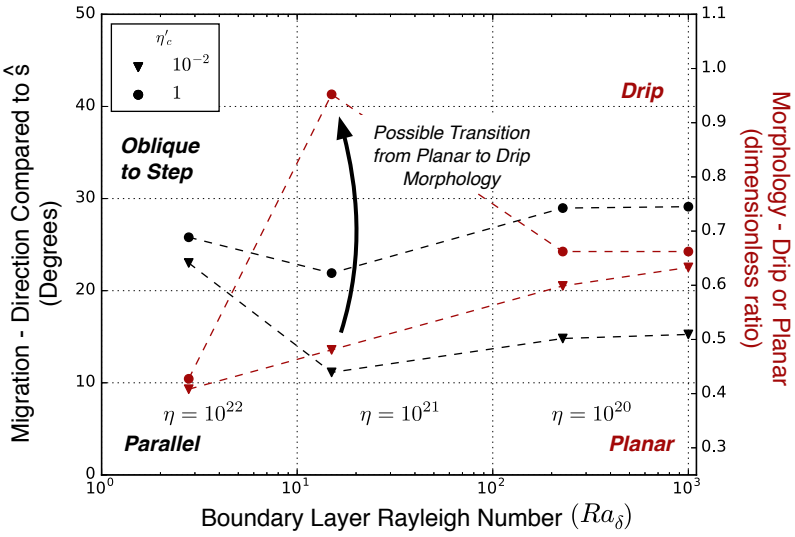

Figure 3.10: Measures of how '3D' the instability morphology and migration are, for varying D′, η'_c and Ra_δ. The models with varying Ra_δ and η'_c (B) have a constant $D' = 0.3$, which is the lowest D′ preventing significant morphology transition (A). A significant switch to the drip morphology occurs near $Ra_\delta = 10$ (B), if $\eta'_c = 1$. This switch is clearly dependent on η'_c, so a change in rheology, marked with an arrow, may potentially produce the transition from a planar to drip morphology. This transition was not explicitly modelled and is based on comparing models with homogeneous decollement rheologies.

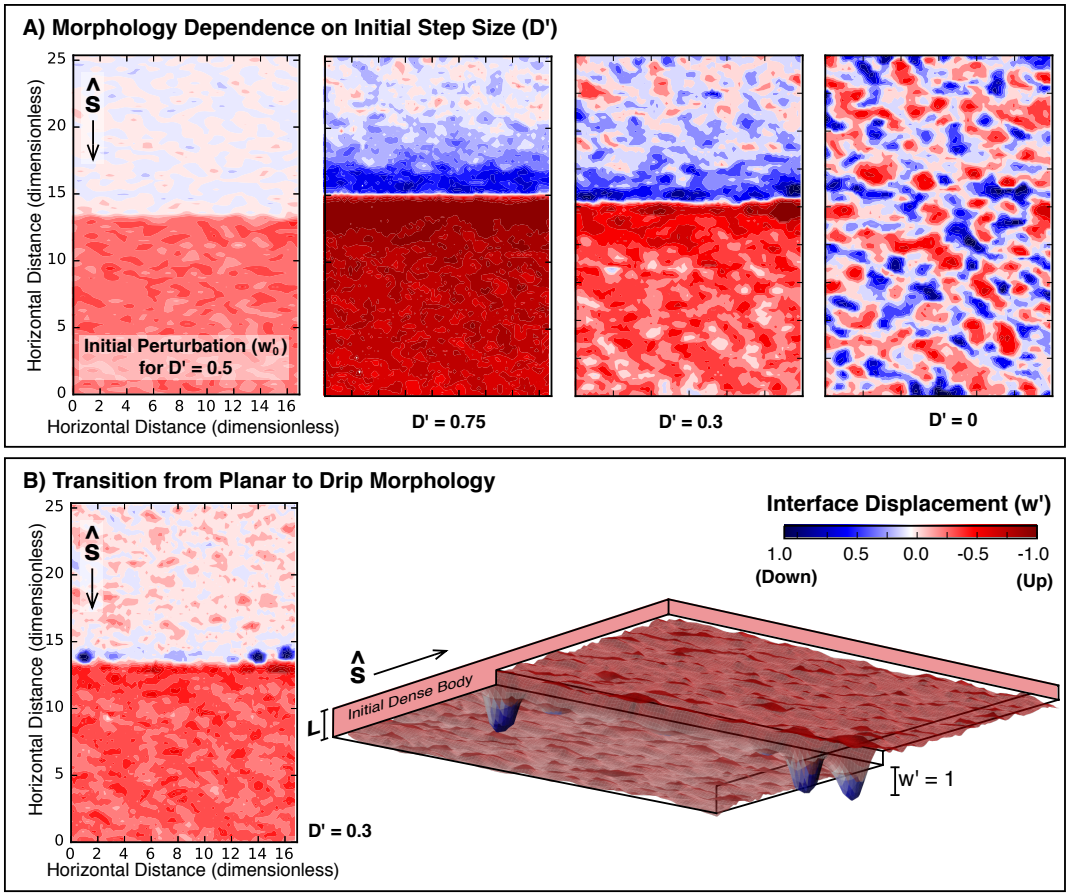

Figure 3.11: Perturbation displacement (w') of representative 3D models, for varying η'_c, D' and Ra_δ (eq. 3.4). Comparisons are made when $w' = 1$ is first reached. For these temperature-dependent 3D models, w' is measured as displacement of the ΔT isotherm from the reference depth L, which is the initial base of the unperturbed dense body. **A)** *Morphology dependence on D', all with $\eta'_c = 10^{-2}$ and $Ra_\delta = 228$. An example of the initial geometry is shown (left) for $D' = 0.5$. For these η'_c and Ra_δ, an initial step size of $D' = 0.3$ is sufficient for the instability to sustain a planar morphology until $w' = 1$ (as in Fig. 3.10a).* **B)** *For the case $Ra_\delta = 15$ and $\eta'_c = 10^{-2}$, the dense body switches from an initially planar morphology (right, shaded pink polygon), to a drip morphology during the time it takes to reach $w' = 1$. In comparison to the $D' = 0.3$ case above (A), the combination of a stronger decollement and lower Ra_δ is responsible for the contrast in morphology at $w' = 1$ (as in Fig. 3.10b). The interface displacement is also plotted as an equivalent 3D surface (right). The 3D surface colours have been shaded to emphasise the drip morphology and so differ slightly to the 2D representations and corresponding colour bar. The $\hat{s}$ vector shows the model orientation, as defined in Fig. 3.1.*

3.3.5 Transitions Due to Thermal Diffusion

Thermal diffusion can potentially halt delamination and force it to revert to dripping or it can cause a morphology switch from planar to drip. In the models, the former occurs if asthenosphere flowing into the wedge above the peeling dense body cools quickly enough to raise the viscosity of the decollement zone. If this happens, the dense body has peeled away by a small amount and stalled, the wedge above it has a cooling geotherm and the base of the dense body transitions to dripping (Fig. 3.9). As this dripping only recycles part of the dense body, the persistence of delamination is measured by the volume of material sinking through time. From this measurement, only the models with $Ra_\delta \geq 10^2$ developed by persisting delamination. The cooling asthenosphere is able to cool to the range of $10^{-1}\eta$ to η at the Moho, so the decollement region will no longer satisfy the $10^{-2}\eta$ viscosity requirement for delamination. The stalling of delamination in this way then depends on whether or not delamination is sufficiently quicker than thermal diffusion, which is quantified by the Ra_δ threshold. When the delaminating body has reached the base of the model, which takes about twice as long as for the isoviscous models, the high rate of recycling slows down for $\Delta t' \sim 1$. By this time, delamination has recycled at least four times more material than the models which have transitioned to dripping.

The second effect of thermal diffusion analysed, the transition from planar to drip morphology, is quantified using 3D models. The focus is on the persistence of the planar morphology of a triggered dripping instability. Only $D' \leq 0.75$ was studied in 3D, which does not include delamination. However, if a planar morphology can persist for the initial growth of triggered dripping at a particular D', this will also be the case for higher D' and therefore delamination. The initial step perturbation of size D' has a planar morphology, so the transition to a drip morphology during the initial growth becomes less likely with increasing D' (Fig. 3.10 and 3.11a). This persistence of the planar morphology, compared for varying D' and $\eta'_c = 10^{-2}$, is observed as both migration in the step direction ($\hat{s}$) and vertical flow with a dominantly planar morphology. The D' threshold for persisting planar morphology is approximately $D' = 0.3$. Therefore if a dense body is decoupled from the upper crust (low η'_c), it requires a planar perturbation which is at least a third of its thickness, in order to grow with a planar morphology. The dependence of these measurements on Ra_δ is secondary to D' for this decoupled case.

When the dense body is decoupled ($\eta'_c = 10^{-2}$), a decrease in Ra_δ and therefore an increase in the influence of thermal diffusion, actually results in increased persistence of planar structures (Fig. 3.10). This is due to the thermal erasure of small wavelength perturbations compared to the invoked large wavelength 3D perturbation. Thermal diffusion however also acts to slow the growth of the 2D step, when $Ra_\delta \leq 3$, resulting in the superposition of drips over the large wavelength planar step. This Ra_δ results in significant formation of a dense thermal boundary layer beneath the dense body, though the sinking velocity at the dense body edge has generally overtaken the rate of diffusion by the time of

measurement at $w' = 1.43$.

Coupling of the dense body to the crust, $\eta'_c = 1$, reduces the persistence of planar structures (Fig. 3.10). This effect is significant for $Ra_\delta = 15$ (Fig. 3.11b), which appears to be a specific point at which the coupled instability is slowed enough for dripping to dominate, but not enough for the dripping wavelengths to be erased. The transition from planar to drip morphology in this case occurs immediately, so that migration is negligible.

3.4 Discussion

The sinking velocity of dense lower crust and/or mantle lithosphere which is delaminating, grows exponentially at a rate which is typically an order of magnitude quicker than for dripping or triggered dripping. This means that material which would typically take 100 *Ma* to reach a significant velocity by dripping, could delaminate on the 10 *Ma* scale. Therefore strong materials, such as pyroxene-dominated restites (Bystricky & Mackwell 2001) or the cold upper part of the mantle lithosphere following an Arrhenius rheology, can be recycled without requiring extreme degrees of weakening, if the appropriate initial conditions are triggered.

Molnar & Jones (2004) showed that the plausibly high strength of the dense lower crust beneath the Sierra Nevada (western USA) is difficult to reconcile with its rapid recycling time-scale, unless the body was thinned by at least 50% prior to instability. Though the equivalent initial condition of $D' = 0.5$ in our models (triggered dripping) also results in a shorter time frame for recycling, this acceleration is much more significant if delamination occurs. The modelled instabilities grow by triggered dripping, rather than delamination, when there is even a thin layer of mantle lithosphere separating the asthenosphere from the thickening decollement layer above the end of the sinking dense body (Fig. 3.8b). The ability to recycle strong material is therefore highly sensitive to whether or not the dense lower crust and / or mantle lithosphere has been completely thinned ($D' = 1$) prior to instability initiation.

Weakening mechanisms within the mantle wedge above delaminating material may be important in sustaining the initial period of growth. Delamination requires the persistence of a step in the lithosphere and a weak decollement. If only the high temperature of the asthenosphere rising into the decollement is responsible for maintaining a weak wedge, a very rapid growth-rate is required to prevent significant thermal diffusion and subsequent stalling. In-flowing asthenosphere is likely to be rich in partial melt and volatiles, which would lower the viscosity and counter the effects of cooling. However, this process needs to be examined. If it is insufficient, then delamination could be constrained to either occurring at the 1 *Ma* scale, or otherwise stalling. It would be difficult to distinguish sustained delamination from

delamination which has stalled and reverted to dripping, so the hypothesis that delamination typically stalls should not be necessarily excluded.

3.4.1 Rheological Inference

If the dense body's viscosity has a negligible influence on the delamination growth-rate, as previously proposed (Le Pourhiet et al. 2006), then crustal and lithospheric rheology could not be inferred from observed time-scales. We have shown, however, that the time it takes for delamination to develop, once the conditions for it are favourable, depends on the viscosity of both the dense body and the decollement. Just as observed time-scales have been used to infer the required rheology for dripping or triggered dripping to occur (Molnar & Jones 2004; Stern et al. 2013), a similar inference can be made for delamination. While this means that observations of delamination can be a powerful indicator of rheology, if the instability mechanism is unclear, there is a greater uncertainty in the estimated viscosity than previously appreciated.

3.4.2 Triggered Dripping vs Delamination

We have identified a mechanism which is a mixture of the dripping and delamination end-members, called triggered dripping. It is similar to dripping in its growth-rate, but resembles delamination in appearance. This has implications for linking observations to instability dynamics. Each of the diagnostics which distinguish delamination from dripping, are also common to triggered dripping. The similarity is due to the similar initial conditions and subsequent deformation. There is a fundamental difference however in the instability mechanism, from thickening by triggered dripping, to the feedback between bending and decollement flow by delamination. A switch in this mechanism results in a major difference in time-scale, but little else of practical diagnostic use.

Viscosity calculated assuming that dripping or triggered dripping is the responsible mechanism, could be overestimated by an order of magnitude if the dominating instability is actually delamination. Given the difficulty in distinguishing triggered dripping from delamination, this introduces a significant uncertainty into rheological inference. The initial conditions required for triggered dripping or delamination can also be indistinguishable, so this uncertainty in instability dynamics may simply be unavoidable.

There are subtle contrasts between triggered dripping and delamination which are worth pursuing, but are difficult to apply in practice. Any observation of subsidence directly above a sinking body cannot be explained by delamination. The restite currently sinking below the Great Valley, California,

for example is likely to require modelling by dripping or triggered dripping, at least for its current evolution and consequent subsidence (Saleeby & Foster 2004). In the western Colorado Plateau, uplift may have recently occurred above dipping reflectors at depth (Pederson et al. 2002; Levander et al. 2011) and without significant crustal thickening, which supports previous assessments of delamination. The uplift history however is contentious and it may be difficult to make such a spatial correlation based on the seismological evidence. Not only are these contrasts difficult to apply to modern instabilities, they are indistinguishable once the instability has completed.

3.4.3 Sierra Nevada, California

The migration of restite from beneath the Sierra Nevada batholith, California, almost 100 *km* westward to its current location beneath the Great Valley (Saleeby et al. 2003), could be modelled by either triggered dripping or delamination. This ambiguity has implications for the recent focus on inferring rheological properties in this region from the observed time-scales (Molnar & Jones 2004; Le Pourhiet et al. 2006). While the mechanism responsible for the initial instability growth is indistinguishable, any estimate of restite or decollement viscosity has at least an order of magnitude uncertainty. There are then two alternative interpretations of time-scale data: either triggered dripping occurred with a high degree of rheological weakening, or delamination with a lesser degree of weakening.

The current morphology and stress-state of the instability and crust above is not necessarily indicative of how the instability initiated. For example, the 2D thermal models demonstrate how easily an instability can begin by delamination and produce the corresponding observations, before reverting to a dripping mode. For significant migration to occur, an initially planar step perturbation is most likely required. The extent of newly infiltrated asthenosphere below the Sierra Nevada, likely to correspond to the initial extent of the restite, is elongated parallel to the batholith and perpendicular to the direction of migration (Frassetto et al. 2011). This observation supports the hypothesis of an initially planar morphology, in which case the morphology has transitioned into a drip morphology.

The 3D calculations demonstrate that a transition from a planar to drip morphology is not a natural progression of instabilities which are capable of migrating. Therefore if such a transition occurred beneath the Sierra Nevada, an additional process is required to trigger this switch. This may be a change in decollement conditions or interference with a competing dynamic process. For the former, the models predict that if the instability migrated into a region with a higher decollement viscosity, a step perturbation could transition into smaller wavelength instabilities with drip morphologies. Whether this transition occurs is dependent on the relative instability time-scale compared to thermal diffusion. Models with a heterogeneous decollement are required for more detailed predictions. Alternatively, the

finite length of the restite may have allowed 3D curvature effects to interfere, a process which we have not modelled. Regardless of whether the instability began by triggered dripping or delamination, it is plausible that the instability has undergone some transition, which could provide further rheological inference if modelled in detail.

3.5 Conclusion

The mechanism by which dense lower continental crust or mantle lithosphere is recycled into the asthenosphere has a strong influence on the initial growth dynamics. Dripping, even if it is 'triggered', grows at an order of magnitude slower time-scale than delamination. This is significant for lithosphere dynamics, considering that mass and energy flux, as well as the migration of surface expressions, follow this initial time-scale. The triggering of delamination requires highly specific conditions: a weak decollement, intrusion of the asthenosphere into the lower crust and a time-scale which can outpace thermal diffusion. Additionally, the time-scale of delamination is highly dependent on its coupling with the upper crust and this dependence can be accurately scaled by $L_c'^2/\eta_c'^{\frac{2}{3}}$. Local tectonic processes and rheology control which mechanism occurs and therefore have a large impact on the dynamics of dense body recycling. This contrast in instability dynamics introduces uncertainty when inferring the viscosity and density of a sinking body if the instability mechanism is unclear. While dripping can be distinguished from delamination, triggered dripping produces similar characteristics to delamination and these would be difficult to discern in nature.

Using the simplistic model setup, the fundamental style of delamination growth has been characterised. It begins at a relatively high velocity which grows exponentially with time in two phases. The time-scale of its initial growth depends on the viscosity of the sinking body. Delamination is likely to grow at a similar time-scale to the thermal diffusion at the Moho. Sustained delamination may subsequently require an additional process to maintain a weak decollement and mantle wedge. A transition from planar to drip morphology, during the initial instability growth, is also likely to require an additional process. A switch to increased coupling between the crust and dense body, due to lateral rheological contrast, could trigger this transition.

Due to the variety in initial mechanism dynamics and later mechanism transitions, the dense lower crust and lithosphere has the potential to be recycled in a number of contrasting ways. Rather than adding further ambiguity to the current debate of how material is dominantly recycled beneath the continents, characterisation of these mechanisms provides new constraints and models which intraplate observations can be tested against, without assuming that one end-member mechanism always

dominates over the other.

Chapter 4

Stalling of Gravitational Instabilities

4.1 Summary

Dense material which has begun sinking from beneath continental crust during the last $\sim$ 10 *Ma* can typically be observed in seismic tomography as it traverses the mantle. Theoretically, this state of high displacement should last for only a short period and their observation appears to be highly coincidental. Instead, we propose that these gravitational instabilities only grew rapidly for a short period of time, before they stalled and reverted to less efficient mechanisms which have evolved slowly enough that they are still observable. As delamination and dripping have growth time-scales which contrast significantly, an instability which begins by delamination and later switches to dripping can produce the required stalling period. Numerical modelling shows that if the region of lower crust which enables delamination to initiate is limited to a lateral distance equivalent to the dense body's thickness, this switch occurs and the dense material hangs in the mantle for five times longer than if delamination proceeded. Alternatively, if the asthenosphere which infiltrates into the opening lower crust rapidly cools or becomes depleted of melt or volatiles, this switch can also plausibly occur. These simple models provide explanations for observations of hanging dense material beneath the Sierra Nevada, California and western Colorado Plateau. The models are also consistent with migration and morphological transitions which can be observed in the evolution of these instabilities.

4.2 Introduction

A fundamental aspect of gravitational instabilities, whether it is dripping or delamination, is that the predicted sinking velocity increases significantly through time until the dense material reaches a mantle discontinuity or breaks off (Chandrasekhar 1961; Canright & Morris 1993; Chapter 3). This means that once dense material has doubled in thickness and can consequently be observed in seismic tomography, its velocity is relatively high and rapidly increasing, such that the remaining life span of the instability should be short. Material of anomalously high density has been inferred in tomography to be hanging at high displacement beneath the continental crust, in at least five cases in the USA alone (Zandt et al. 2004; Schmandt & Humphreys 2010; Levander et al. 2011). These instabilities have generally grown within 10 *Ma*, so that the exponential instability model predicts that this state should only last for < 1 *Ma*. Therefore the exponential instability growth model implies that in the last 10 *Ma* alone there were approximately 50 instabilities in the USA. As the primary sources of anomalously dense material are through partial melting of the lower crust (Lee et al. 2006; Lee 2014) and cooling mantle lithosphere (Houseman & Molnar 1997; Poudjom Djomani et al. 2001), it is unlikely that enough dense material can be generated to be recycled this quickly. The availability of evidence of recent recycling, for example in the Andes (Garzione et al. 2008) and western Canada (Bao et al. 2014), indicates that the number of observations is always < 10 in the last 50 *Ma* per continent. An alternative explanation is that instabilities do not always follow the exponential growth prediction for the entire recycling process. In this case, there may be a mechanism for slowing down instabilities, rather than continually quickening them.

Delamination grows at a significantly quicker time-scale than dripping (Chapter 3). Therefore if delamination stalls and the dominant mechanism switches to dripping, it is plausible that the instability velocity could dramatically decrease. Testing this hypothesis is the primary purpose of this chapter. If dense bodies are typically observed once the instability has reached the slow, stalled phase, this could explain the discrepancy between rapid instability growth and the preservation of highly displaced dense bodies. Dripping mechanisms generally share the same order of magnitude growth-rates and consequently it is predicted that a switch from one style of dripping to a slower dripping mechanism is incapable or generating significant stalling. The stalling mechanisms in this analysis are also applied to instabilities which begin by dripping, to test this prediction.

Observational data is checked for indications that instability stalling may have occurred in well-studied regions. The argument for stalling is primarily based upon the observation of anomalously dense material hanging at high displacements. Any additional data which constrains how the rate of instability growth has varied through time is used to test this argument. Then

Individual instabilities could plausibly record stalling events. For example, the initiation of the Sierra Nevada (western USA) instability is dated at approximately $3-4$ *Ma* (Manley et al. 2000; Jones et al. 2004). By $2-2.5$ *Ma*, the dating of morphological features indicates that the instability migrated westward by approximately 100 *km*, a distance which is much greater than the original restite thickness of approximately 50 *km* (Lee 2014). Both triggered dripping and delamination require an equivalent vertical displacement to achieve any horizontal displacement, indicating that by this time the instability should have entered the rapid descent phase at high displacement (Chapter 3). Complete recycling should have occurred approximately 1 *Ma*. Therefore the presence of hanging restite may indicate a stalling event $1-2$ *Ma*. A second indicator of stalling is the superposition of morphologies corresponding to different mechanisms. For example, the instability in the south-western Colorado Plateau shows evidence of lithospheric peeling, indicative of delamination (Levander et al. 2011). The lithosphere would be expected to delaminate with negligible thickening. The lithosphere however appears to have thickened significantly as it has sunk, which is characteristic of triggered dripping (Chapter 3). The peeling features may have formed during an initial phase of delamination, before the instability stalled, switched to dripping and subsequently evolved through lithospheric thickening.

Numerical models are used to test the hypothesis that a switch in instability mechanism can significantly prolong instability growth. Delamination is highly sensitive to presence of a weak middle to lower crust. This required rheology is likely to be produced by tectonic events which are limited temporally and spatially, so that a plausible mechanism for the cessation of delamination is the migration of the instability out of the zone of weak lower crust. Lateral variations in lower crustal strength are invoked in our numerical models, in order to trigger transitions in instability mechanism and to test the hypothesis that a transition from delamination to dripping can produce the stalling events observed in nature.

4.3 Observations

The observation of hanging, dense bodies is itself indicative of a stalling period. To test this inference using existing observations alone, some well studied instability case studies are initially re-examined for evidence of a stalling event. This may be recorded in a deceleration of instability migration or a deviation from the expected exponential growth model. In addition, a transition in instability behaviour, such as morphology or migration direction, may be indicative of a switch in mechanism and subsequently associated with a stalling event.

4.3.1 Sierra Nevada, California

Geological and geophysical data from the Sierra Nevada, California and the adjacent Great Valley (Figs. 4.1 and 4.2) contain arguably the most complete record of lower crustal recycling. The original existence of dense restite below the Sierra Nevada batholith has been inferred from geochemical melting calculations and xenoliths of it have been observed in volcanics dated at 10 *Ma* (Ducea & Saleeby 1998; Saleeby et al. 2003). The removal of the restite from beneath the Sierra Nevada has been inferred to have occurred $\sim$ 3.5 *Ma* ago. An episode of potassic volcanism originating at a shallow depth and dynamic uplift of the southern Sierra Nevada mountain range indicate the lithosphere was thinned at this time (Manley et al. 2000; Ducea & Saleeby 1998). There is no evidence of restitic xenoliths in the volcanics, supporting the hypothesis that the restite had been removed by this time. The restite is certainly not present beneath the southern batholith today, as the lithosphere is still thin (Frassetto et al. 2011). These observations indicate that significant removal was occurring at $\sim$ 3.5 *Ma*, but does not exclude the initiation of instability before this. Dynamic topography variations are recorded in both the Sierra Nevada and the Great Valley before this time, which could potentially be linked to previous instability (Wakabayashi & Sawyer 2001; Saleeby et al. 2013). However, Jones et al. (2004) demonstrated that localised deformation also occurred at the eastern margin of the Sierra Nevada at 4 *Ma* and migrated westward over 1 *Ma*. This may be a record of the tectonic triggering which initiated the rapid instability. Overall, the evidence is currently in favour of instability initiation at $\sim$ 3.5 *Ma*.

The restite appears to have been completely removed from the base of the southern section of the Sierra Nevada batholith and hanging beneath the Great Valley by 2.5 *Ma*, based on the combination of lithospheric thinning beneath the mountain range and accelerated subsidence in the valley (Stock et al. 2005). Extrapolating this rapid migration using the expected exponential growth, it would be expected that the restite would have either reached the transition zone or broken off by at least $\sim$ 1 *Ma* ago. The restite however is clearly still hanging beneath the Great Valley, down to approximately 250 *km* (Saleeby et al. 2012).

There is evidence that the dynamics of restite removal have recently switched. The migration of the restite has switched from westward to northward, as it has recently decoupled from a southern region of the Great Valley, exhuming the Kern Arch (Cecil et al. 2014). Secondly, the significant initial westward migration indicates that the restite was effectively decoupled from the base of the batholith. It is currently coupled to the overlying crust today however, producing subsidence (Saleeby & Foster 2004). Finally, the extent of thinned lithosphere beneath the southern Sierra Nevada indicates the restite had a planar morphology when it was removed. It currently has a drip morphology however, indicating a transition in morphology. In Chapter 3, this occurred as the result of coupling between the dense material and the crust. It therefore appears that restite has migrated from a region of weak to

strong lower crust. To summarise, there is evidence for a stalling event ~ 2 *Ma* ago, which coincides with migration into a region which is rheologically unsuitable for the propagation of delamination.

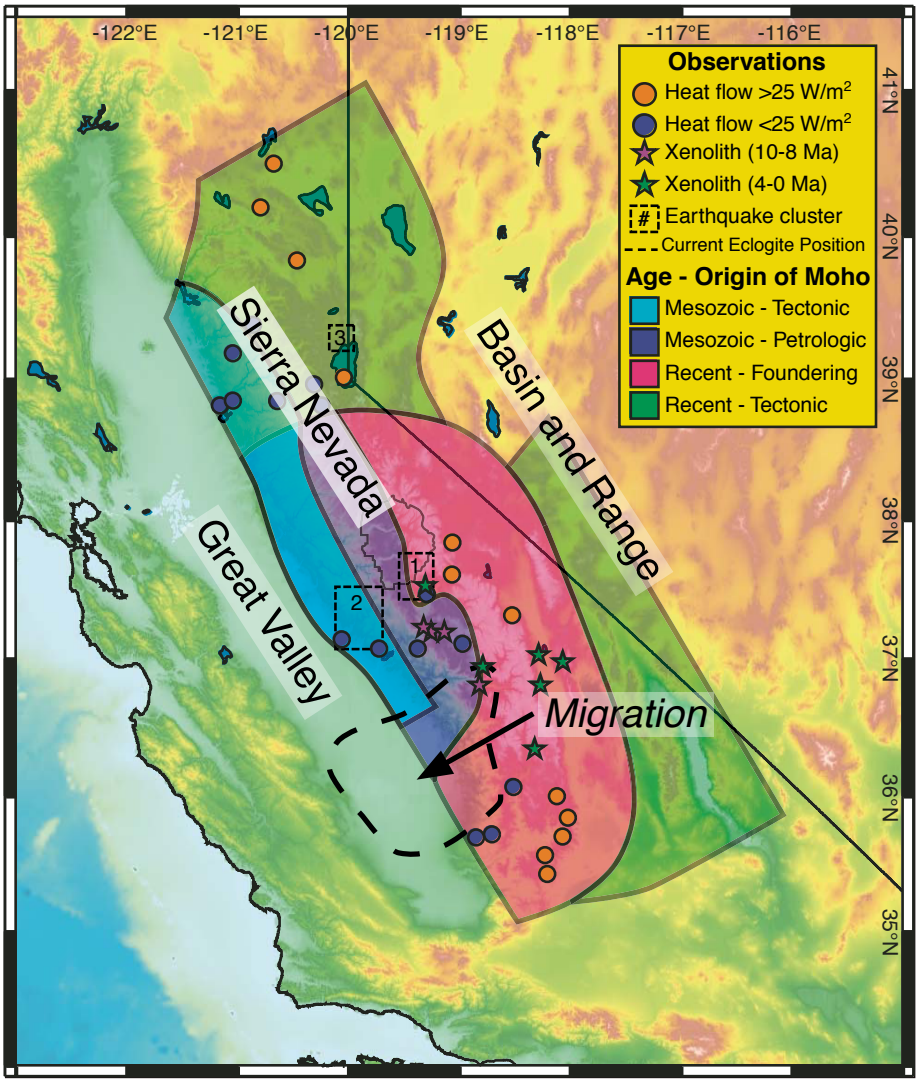

Figure 4.1: Initial position of the restite beneath the Sierra Nevada (pink shading) and its current position beneath the south-eastern Great Valley (dashed). Green and red colours represent the lowest and highest elevations respectively. Modified from Frassetto et al. (2011).

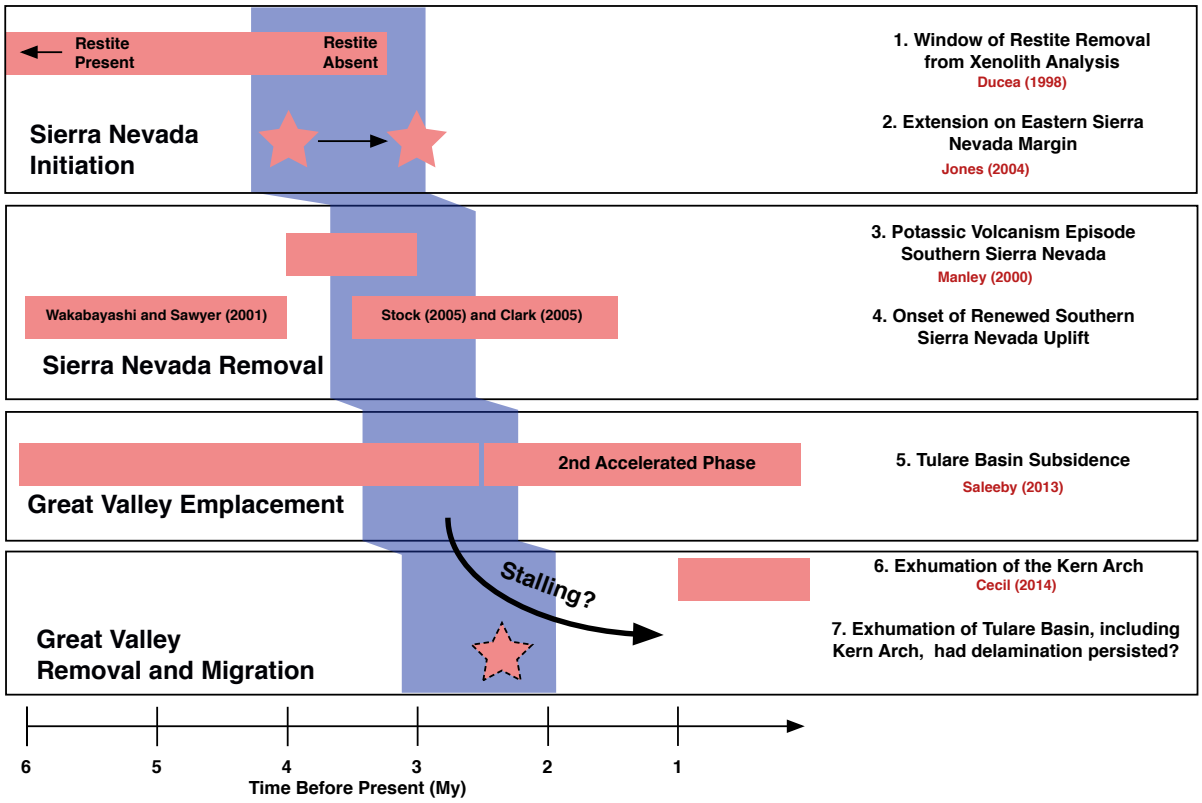

Figure 4.2: Summary of key instability-related events constrained in the Sierra Nevada (top two) and the adjacent Great Valley (bottom two). Instability is likely to have begun ~ 3.5 *Ma and migrated to the Great Valley within* ~ 1 *Ma. As migration and sinking occur concurrently, the exponential growth model predicts approximately predicts complete removal by* $\sim 1.5-2$ *Ma ago. As the restite is still hanging beneath the Great Valley, a stalling event may have occurred. The transition may also be reflected by the change in migration direction, which is inferred from exhumation of the Kern Arch.*

4.3.2 Colorado Plateau

A density anomaly which extends from the Moho to $>$ 250 *km* depth has been observed in seismic tomography beneath the western Colorado Plateau (Levander et al. 2011). Levander et al. linked this deep anomaly to an overlying dipping reflector, which they inferred to be a Moho which was peeled away by delamination (Fig. 4.3). The Colorado Plateau as a whole has a complicated and heterogeneous uplift history. The small region where the deep anomaly and dipping Moho have been observed may correspond to recent uplift (Pederson et al. 2002). There is a broader pattern of volcanism surrounding the entire west to south margin of the Colorado Plateau, which has migrated inwards towards the plateau recently (Crow et al. 2011; Roy et al. 2009). However, the direction of migration is not consistent with the geometry of delamination proposed by Levander et al. and occurs at a larger scale. This pattern of migrating volcanism then may be potentially constrain the timing of the onset

of tectonic triggering generally in the plateau, but arguably does not constrain the growth time-scale of the proposed delamination.

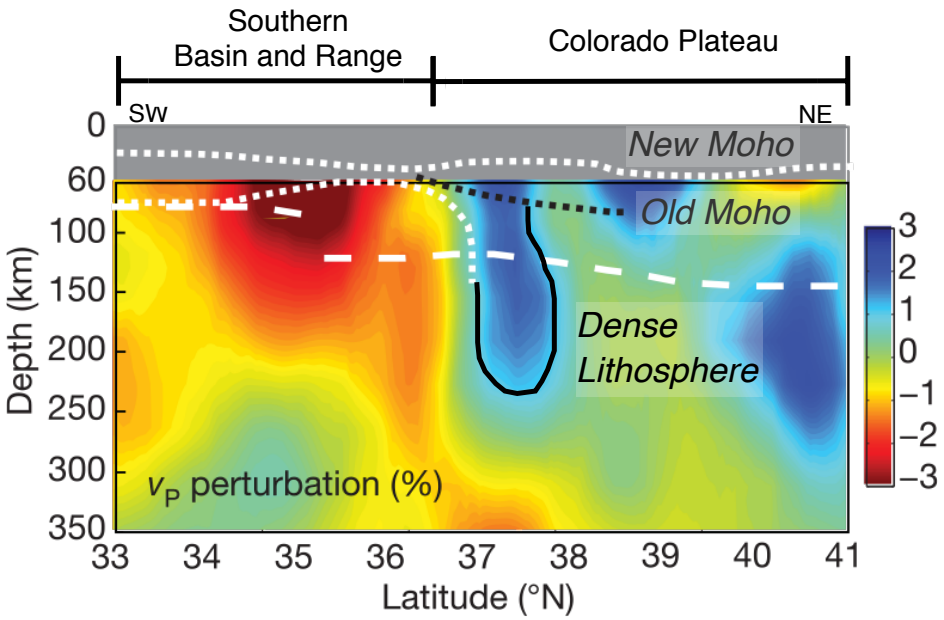

Figure 4.3: Density anomaly beneath the western Colorado Plateau, modified from Levander et al. (2011). The Moho appears to have peeled way by a significantly smaller amount than the dense lithosphere has been displaced. As these displacements should be approximately equivalent for delamination, this may indicate that instability began by delamination, before stalling and reverting to dripping and subsequently producing the high internal shear-strain. The lithosphere beneath the Basin and Range, west of the Colorado Plateau, is thin. The instability therefore migrated towards what is generally a relatively weaker region, before stalling.

The geometry of the delaminating body inferred by Levander et al. (2011) may still on its own indicate that the instability has undergone a stalling period. Based purely on the Moho displacement and original lateral extent of the dense body, it may be the expected that the lithosphere would have been displaced to ~ 150 *km*, based on the constant thickness typically maintained during delamination. Therefore, as the lithosphere's current displacement is at least 100 *km* higher than expected, the displacement cannot be described purely by delamination. The high internal shearing of the dense body, required to thicken it much more than the Moho has been displaced, is typical of dripping. One way to produce both peeling and significant internal shearing may be for the instability to begin by delamination, producing the former feature, before stagnating and reverting to dripping, so that the latter can be produced. The hanging dense body is currently at a terrain edge, with a distinctly younger mantle lithosphere adjacent. This younger zone, at which the instability may have reached and stagnated, is likely to be weaker than the Colorado Plateau. This may exclude the possibility that the instability has stalled by encountering a strength increase which is is inherent in the typical rheological profile. Instead, the strength increase may have occurred dynamically within the Colorado Plateau,

due to cooling or a limited extent of dynamic weakening. The region directly above where the mantle lithosphere appears to have peeled away does not correspond to any surface volcanism, however there is volcanism at its edges which originated from melting of mantle lithosphere at depths of $50 - 100$ *km* (Levander et al. 2011; Reid et al. 2012). If the mantle were actively flowing into the decollement zone, this region should experience shallow decompression melting. As this is not the case, the cooling of the decollement zone may be the dominant process, which may have resulted in stalling.

4.3.3 Carpathians

The Carpathians together form an arcuate region of thrust sheets and subsequently thickened crust (Fig. 4.4), which delineates a collision zone related to the closure of an ocean ~ 20 *Ma* (Horváth et al. 2006; Wortel & Spakman 2000). The sinking slab was south to west dipping and the ocean closure occurred as a result of its rollback. The Pannonian Basin, bounded by the Carpathians, is underlain by two Mesozoic blocks which underwent significant thinning as collision occurred as well as afterwards. During the thinning of the Pannonian Basin, the crust and lithosphere within the collision zone thickened significantly, forming the Carpathians. The complicated interplay of Pannonian Basin deformation and volcanism as well as uplift of the Carpathians has occurred continuously over the past 20 *Ma*. During this time, volcanism and deformation have migrated from the north-west to the south-east. Additionally, some form of gravitational instability is still occurring, as there is a region in the south-east which features seismicity at < 200 *km* depth (Lorinczi & Houseman 2009) and a corresponding density anomaly in the seismic tomography of Wortel and Spakman, which may potentially continue down to the 440 and 660 *km* discontinuities. There are also density anomalies at the mantle transition zone directly below the Pannonian Basin (Hetényi et al. 2009), which may correspond to remnant slab or continental lithosphere, which has recently been recycled from the continental crust.

The mechanism for producing the extreme thinning of the Pannonian Basin, the simultaneous thickening the Carpathians and the north-west to south-east migration of volcanism and deformation is still debated. Generally, models either describe the dynamics as being controlled by the sinking slab (Wortel & Spakman 2000) or unstable sub-continental lithosphere (Houseman & Gemmer 2007; Fillerup et al. 2010; Göğüş et al. 2016). In the sinking slab hypothesis, the rollback of the slab during ocean closure produced significant mantle upwelling and subsequently thermal and mechanical thinning of the Pannonian Basin. During collision, the initial slab break-off is suggested to have begun in the north-west, before the slab tear, as well as subsequent volcanism and deformation, propagated towards the south-east. The currently observed density anomaly in the south-east is interpreted as the remaining piece of attached slab. In the unstable sub-continental lithosphere hypothesis of Houseman & Gemmer (2007), the crust in the Pannonian Basin region was initially overthickened above dense mantle lithosphere.

During collision, the Pannonian Basin crust spread out, while the mantle lithosphere dripped into the asthenosphere at its margins, both by gravitational instability. Some heterogeneity in the instability process may have triggered it to begin in the north-west, before migrating. In this hypothesis, the current density anomaly in the tomography is sinking mantle lithosphere. A variation to this hypothesis is the suggestion, for example by Göğüş et al. (2016), that this sinking mantle lithosphere originated from beneath only the south-eastern Carpathians, during their thickening, rather than beneath the Pannonian Basin. In this scenario, the progression of volcanic and deformation ages must surely indicate a causative relationship with the Pannonian basin-scale instability.

Dating of volcanism provides a record of instability evolution through the entire Pannonian Basin. Instability migration along a transect from the north-west to the south-east varies significantly through time (Fig. 4.4b). In the northern section of the basin, volcanic activity spreads out over a distance of ~ 300 *km* within 5 *Ma*. By contrast, when the instability reaches the southern half of the basin, it takes almost 10 *Ma* to migrate 200 *km*. It therefore appears that the instability slowed down significantly, midway through its evolution. Even if the most recent instability was limited to the south-east Carpathians, the migration is slowing, rather than increasing through time. There is therefore a recorded stalling period in the Carpathian system, which occurred ~ 10 *Ma* ago.

Reconciling the observations with a particular mechanism is still contentious. However, each of the mechanisms involve a gravitational instability, whether it is a remnant slab or dense material from beneath the Pannonian Basin. Houseman noted that the initial migration velocity is extremely fast, > 200 *km* in 2 *Ma*, using this as justification for the onset of gravitational instability. However slab tearing could occur rapidly and it is unclear whether the sudden decoupling from the crust could produce a sinking slab which accelerates through time, therefore with a similar signature to a Rayleigh-Taylor type instability. Regardless of the mechanism, there appears to be an event at ~ 15 *Ma* which triggers the rapid growth of an instability, before another event ~ 10 *Ma* decelerates it. In a general way, the analysis of the stalling of delaminating bodies may provide a simplistic insight into the kind of process which occurred in the south-eastern Carpathians to slow down instability enough that a hanging density anomaly is still visible.

A)

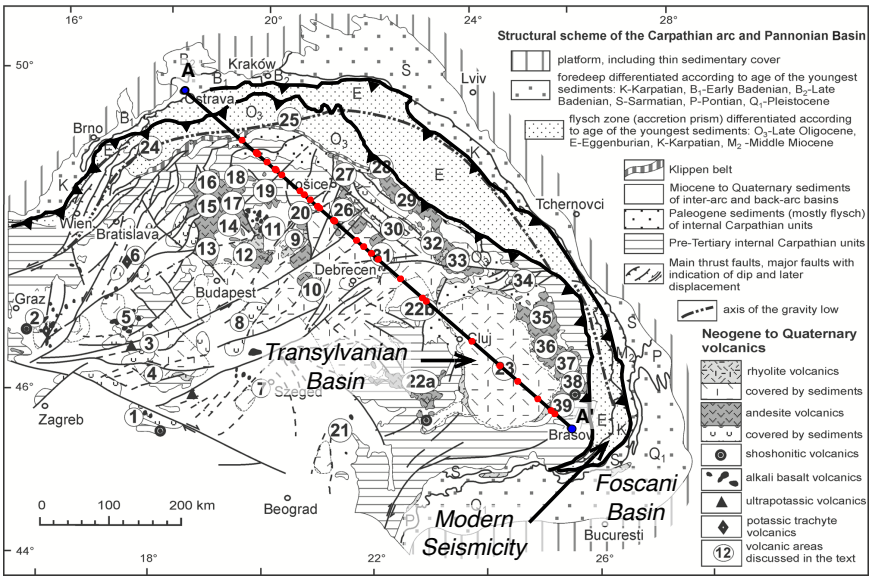

B)

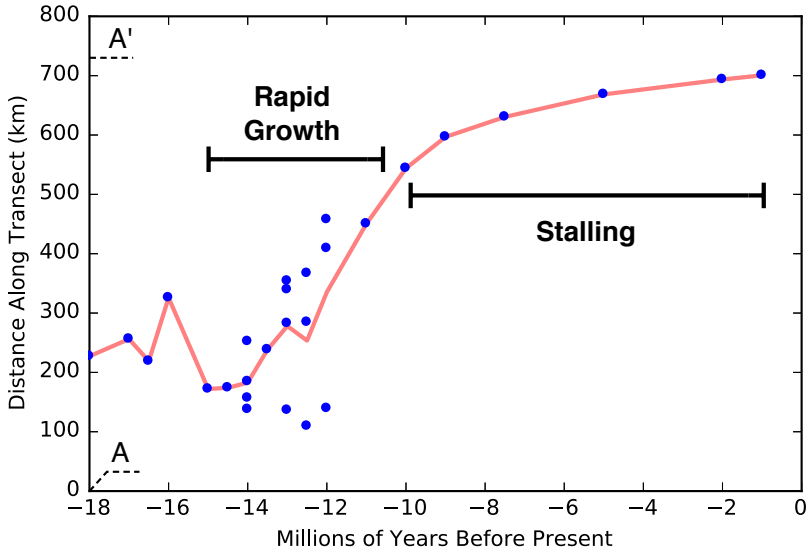

Figure 4.4: **A)** *A map of the Carpathians, delineated by the thrust zones (thick black), with the Pannonian basin inside, modified from Pecskay et al. (2006). The numbers correspond to the sampling sites from which Pecskay et al. collated geochronological data. The average age of each sampling site with andesitic volcanics is taken and projected (red points) onto the transect from Ostrava to Brasov.* **B)** *The distance, from A towards A', of the andesitic eruption sites as a function of their average age. The clearest north-west to south-east migration occurred from* 14*Ma ago and is a period of rapid migration which indicates rapid growth of the instability. There is likely to have been west to east migration prior to this, unclear due to the orientation of the transect, though the focus in this analysis migration in the transect direction. From* 10 *Ma ago, the migration velocity clearly slows down. The moving average shows the general trend (red).*

4.4 Methods

Stalling is invoked in the numerical models by introducing two styles of lower crustal rheology variation (Fig. 4.5). The first scenario is that the region in which the instability initiates has a weak lower crust of limited lateral extent. In this zone, the lower crust is $2-3$ orders of magnitude weaker than the dense body: $\eta_c' = 10^{-2} - 10^{-3}$. The weak zone, required for delamination to occur, extends from the step in the direction of instability migration for a distance W_c. This is the primary parameter and is non-dimensionalised to the thickness of the dense material, $W_c' = W_c/L$. The larger it is, the further delamination is able to propagate unhindered. The lower crust beyond the weak zone is significantly stronger, $\eta_c' = 1$, so that dense body becomes strongly coupled to the crust. The finite weak zone could represent weakening by plastic failure or melt intrusion, which is limited to the step region. Alternatively, the weak zone may be limited to a particular terrane, so that the change to a stronger rheology represents the suture zone with a stronger terrane.

The alternative mechanism for producing rheological heterogeneity is dynamic strengthening of the peeling zone (Fig. 4.5b). This strengthening is modelled as a thermal process: the upwelling asthenosphere may cool down, so that its temperature-dependent viscosity increases, more quickly than delamination propagation can occur. When the asthenosphere cools at the Moho, its viscosity increases from its initial value of $10^{-3}\eta$ by two to three orders of magnitude. If this cooling occurs, the decollement viscosity is too high for delamination to proceed. The cooling model assumes that $Ra_\delta = 10$, which is low enough to stall delamination and revert to dripping (Chap. 3).

Aside from the introduction of the W_c' parameter, the general model setup is identical to that of Chapter 3. The models are run until at least the time at which dense material reaches the base of the upper mantle. This longer model time is required, as the instability transitions occur when a high displacement has been reached. The models use resolutions of 256×768 and 128×384 for the mechanical and thermo-mechanical models respectively. No small initial perturbation Rayleigh-Taylor instabilities are modelled, so the models are no longer sensitive to the small initial perturbations.

A)

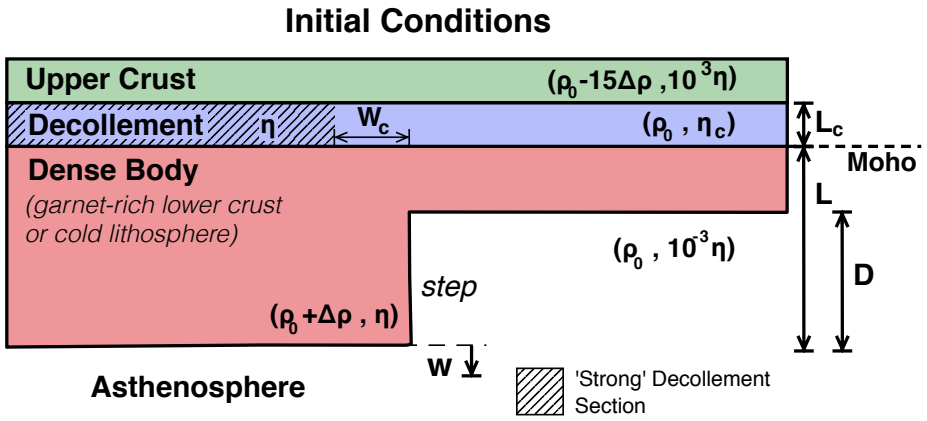

B)

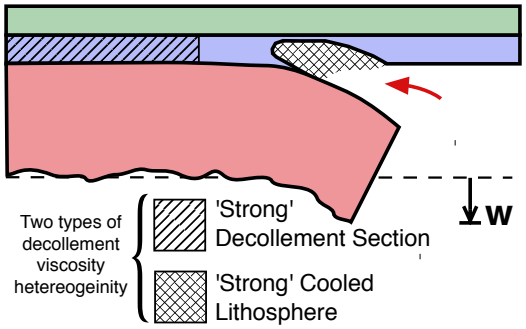

Figure 4.5: Schematic of model setup. **A)** *The lateral extent of the weak decollement between the step and a stronger section, W_c', is the primary parameter which is varied in the models. The weak decollement is set to either $\eta_c' = 10^{-3}$ or $\eta_c' = 10^{-2}$. Delamination is invoked by $D' = 1$ and triggered dripping by a perturbation in the range of $D' = 0.5 - 0.75$. The other parameters are described in Chapter 3.* **B)** *The models introduce a viscosity contrast in the decollement zone by one of two ways. The first is set in the initial conditions an increase in the decollement viscosity by two orders of magnitude (striped). The second occurs dynamically in thermal models with a temperature-dependent viscosity. The asthenosphere cools as it rises (red arrow) into the decollement zone, to a viscosity which is two to three orders of magnitude higher than the decollement material. There are no variable parameters in this second method and thermal diffusion is assumed to be quick relative to rate of viscous flow.*

4.5 Numerical Results

The results are separated into the two stalling processes analysed: stalling due to a time-independent heterogeneous decollement viscosity and stalling due to cooling of the rising asthenosphere.

4.5.1 Time-Independent Lateral Decollement Heterogeneity

The lateral switch in decollement viscosity is sufficient to force delamination to revert to dripping. When the peeling material reaches this viscosity contrast, it slows significantly and transitions from bending to high internal shearing (Figs. 4.6 and 4.7). The shear-strain when it has reverted to dripping resembles the magnitude of triggered dripping (Chap 3) and Moho displacement becomes negligible.

The initial instability growth is similar for all models, up to $w' \leq 1$ when $\eta'_c = 10^{-3}$ and $w' \leq 0.6$ for $\eta'_c = 10^{-2}$. Therefore all of the instabilities begin as delamination and initially reproduce the associated features. At larger displacements, the models with $W'_c \leq 2.0$ experience a substantial deceleration when the strong decollement is reached. Because the instability has to travel a shorter distance to reach the viscosity transition for lower W'_c, the switch to a slower growth-rate occurs slightly earlier and at a smaller w'. The exponential growth when the model has reverted to dripping is generally similar, irrespective of W'_c, though the earlier the switch happens, the longer the instability's transit time through the mantle is extended.

The time window over which a dense body is likely to be observable is measured as the duration for which the body displacement is in the range $1 < w' < 7$, which corresponds to when the dense material has doubled in thickness to when it reaches the 660 *km* transition. This duration varies significantly depending on W'_c. Compared to delamination with a large W'_c, a weak decollement limited to $W'_c = 1.4$ results in an instability which is observable for $\sim 7\times$ longer. When $\eta'_c = 10^{-2}$, it is $\sim 3\times$ longer. Stalling induced by lateral viscosity variation can therefore have a significant slowing effect.

When delamination stalls, the dense body hangs vertically, while it shears away at the hinge zone (Fig. 4.6). Significant subsidence is required for the near-vertical dense body to be isostatically supported. This subsidence however is of a similar magnitude to that produced by uninhibited delamination, though more localised.

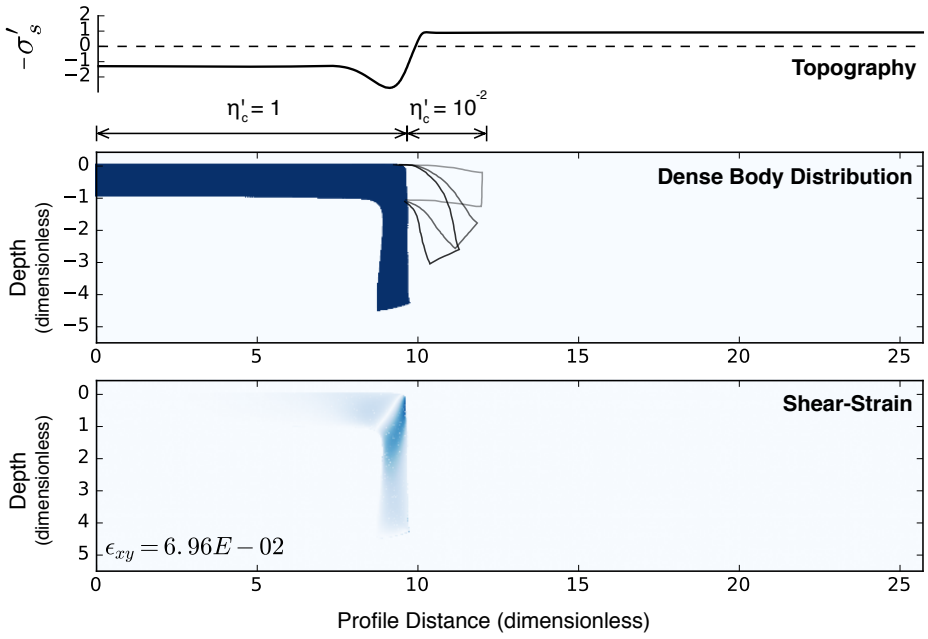

Figure 4.6: The dense body (middle) after delamination has reached the stronger decollement region (at $W'_c = 1.4$) and reverted to dripping. The dense body has sheared significantly near the hinge zone (bottom), resulting in an average shear-strain, ϵ_{xy}, which resembles dripping. The hanging dense body produces a localised zone of subsidence (top), which can be scaled in the same was as in Chapter 3.

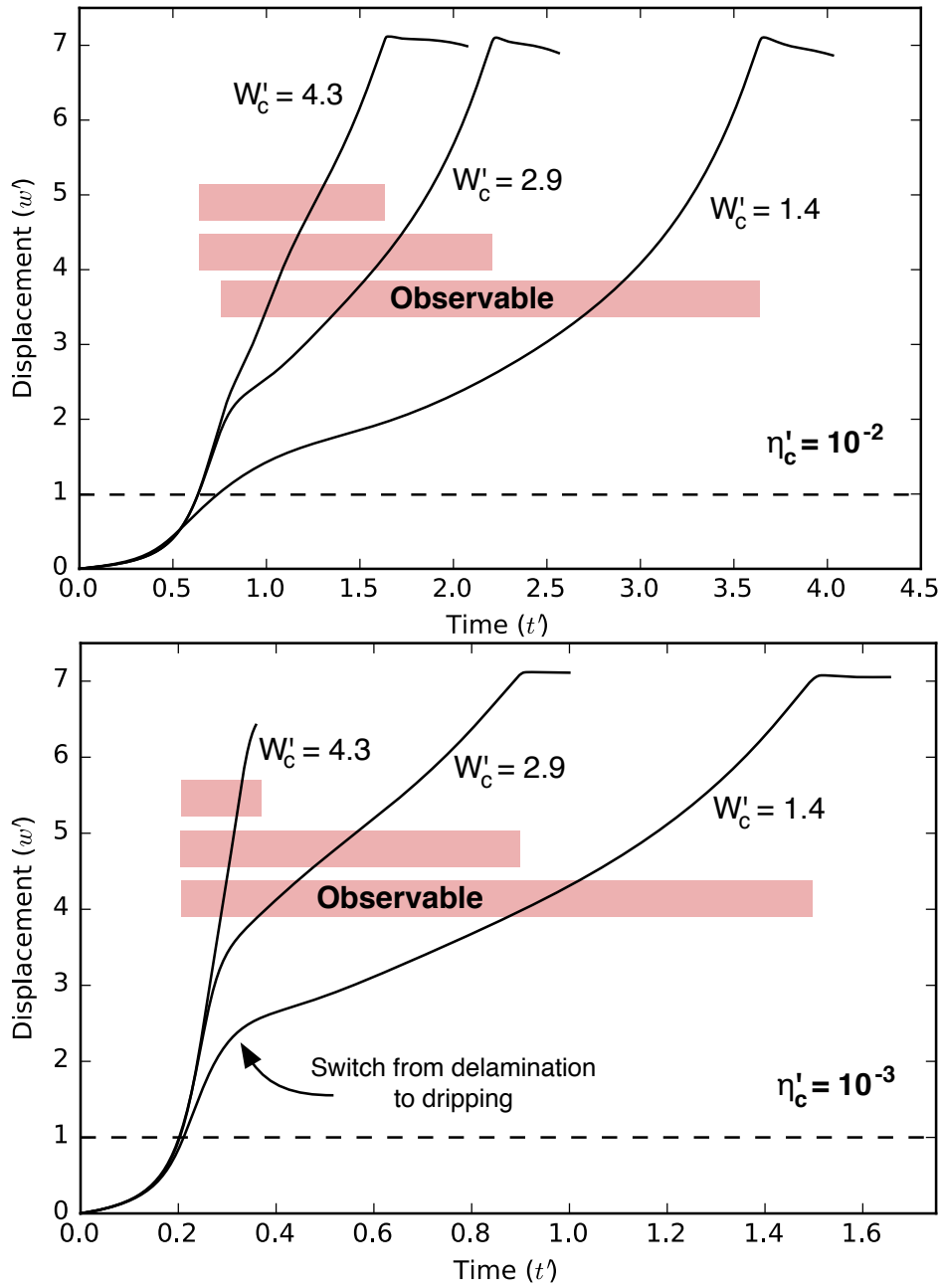

Figure 4.7: Interface displacement through time for varied W_c'. When the weak decollement zone is only as wide as the lithospheric thickness ($W_c' = 1.4$), the switch to dripping is pronounced and results in a significantly longer time for recycling to occur. When $W_c' = 4.3$, the dense body reaches the base of the upper mantle ($w' = 7$) before a switch occurs. The dense body is assumed to be observable using seismology when the displacement is $1 < w' < 7$. The windows of time when the dense body can be observed then differs substantially depending on W_c'. The contrast in these time periods is larger when $\eta_c' = 10^{-3}$ (bottom), compared to $\eta_c' = 10^{-2}$ (above).

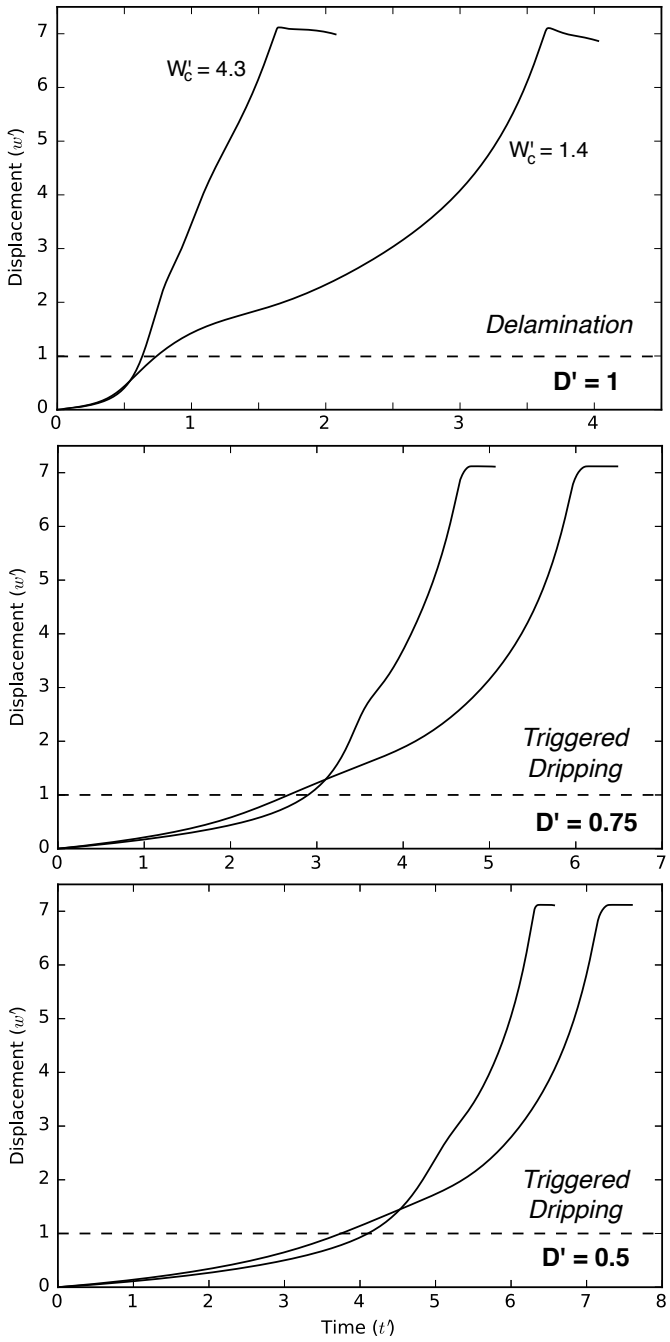

Figure 4.8: End-member cases: a weak decollement of limited width ($W_c' = 1.4$) and a decollement which extends well into the instability path ($W_c' = 4.3$). These sets are compared for $D' = 0.5$, $D' = 0.75$ and $D' = 1$, all with $\eta_c' = 10^{-2}$. The greatest stalling occurs for delamination and becomes negligible as the mechanism becomes dominated by dripping.

The $W_c' = 4.3$ and $W_c' = 1.4$ end-members demonstrate the significant slowing which occurs when delamination stalls. These end-members are also modelled with instabilities which began by triggered dripping with perturbations of $D' = 0.5 - 0.75$ (Fig. 4.8). The weak decollement is still set as $\eta_c' = 10^{-2}$, so that these dripping models are close to the delamination conditions and therefore

represent the upper bound for the stalling of dripping. The stalling time is significantly decreased for $D' = 0.75$ and approximately negligible for $D' = 0.5$. Instabilities which begin by dripping and encounter an region of weak lower crust continue to grow at a similar rate and do not appear to be capable of generating any observable stalling period.

4.5.2 Dynamic Strengthening of the Wedge

Delamination stalls and reverts to dripping when $Ra_\delta = 10$, because the rising asthenosphere cools and raises the viscosity of the decollement zone (Fig. 4.9). When no stalling occurs, delamination has removed most of the dense body by $\Delta t' \sim 2.5$. By contrast, the model in which delamination stalls was stopped at $\Delta t' = 5$, by which only 20% of the dense body had been recycled (Fig. 4.10). At this Ra_δ, convection below occurs much more quickly than dripping, which in the model slowed to a relatively constant velocity. If the velocity does not increase substantially through time, the observable time period could be as much as $10\times$ larger as a result of this type of stalling.

The dense body displacement during the stalling phase is about 1 to $1.5\times$ the dense body thickness. Material beyond this thickness drips away and is entrained by the convection. Additionally, because the Moho region becomes stronger after delamination has already begun, a dipping Moho becomes frozen in place above the dripping body. Heat-flow into the region of thinned lithosphere, which the dense body has migrated from, is high and results in a Moho temperature which is elevated by $1.5\times$ (Fig. 4.11).

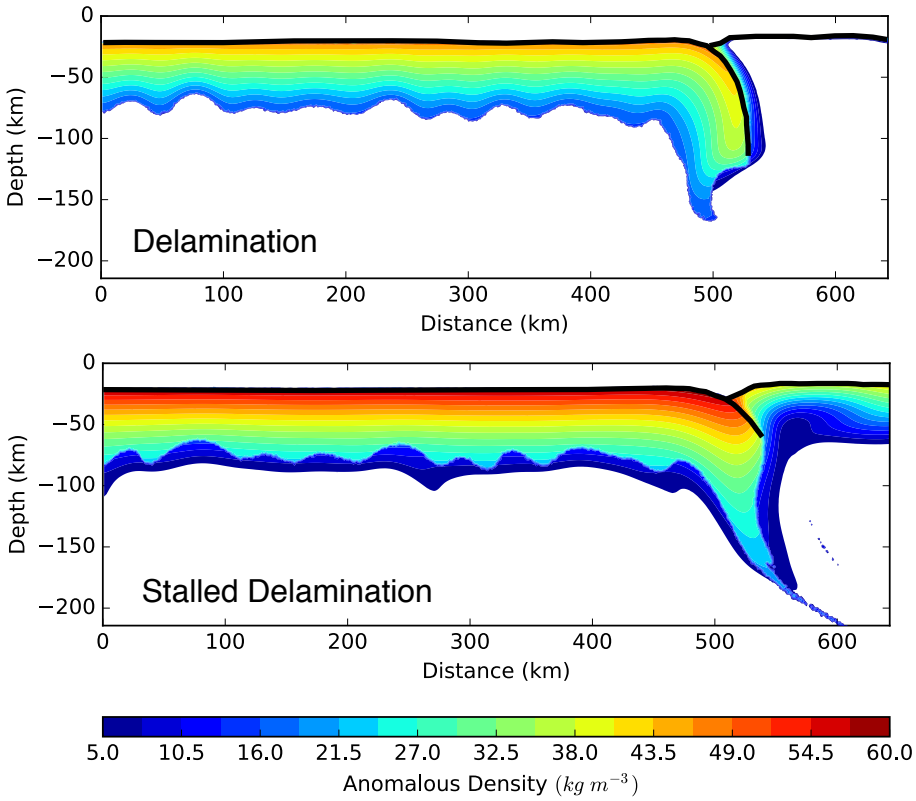

Figure 4.9: Delamination (top) occurs even when there is a large internal density (shown) or viscosity contrast, as long as thermal diffusion is negligible ($Ra_\delta = 10^2$) or another process weakens the cooling asthenosphere. When thermal diffusion is significant ($Ra_\delta = 10$), the rising asthenosphere cools significantly and delamination reverts to dripping (bottom). In this case, the Moho (black line) is still displaced before stalling occurs. The stalled delamination model snapshot is taken long enough after the delamination model that significant cooling of the dense body has occurred, increasing its anomalous density. The viscosity of the upper dense body however has also increased, such that it drips more slowly than the lower part. The length scale is chosen so the dense body is 50 km thick and the density so the average dense body anomaly is 30 kg m^{-3}.

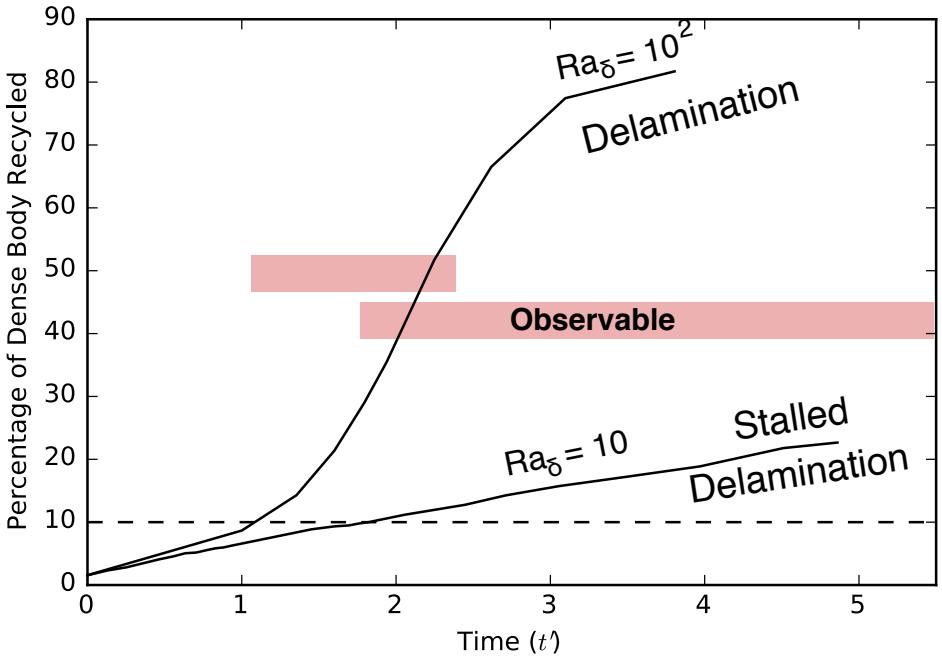

Figure 4.10: Comparison of instability growth through time between persisting ($Ra_\delta = 10^2$) and stalled delamination ($Ra_\delta = 10$). Growth is shown as a percentage of material which has passed the depth of the original dense body base, as a small portion of the lower dense body may drip away quickly, while the majority of the dense body is flowing much more slowly. The dense body is assumed to be observable when the recycling percentage is $> 10\%$, but most of the dense body has not yet reached the 660km discontinuity. The stalled delamination is observable for a significantly longer time than delamination. An upper bound was not calculated, as the relatively shorter time-scale of mantle convection results in a large number of required time-steps.

As a consequence of the temperature dependent rheology, the upper half to three quarters of the dense body can increase in viscosity more quickly than it sinks, so that it is effectively preserved within the thermal boundary layer. In this respect, dripping is able to stall. However, the stalling of material occurs before it has reached a high displacement. If a dripping instability begins with a large finite displacement, such as $D' = 0.75$ in Fig 4.12, a thermal boundary layer forms in the case of rapid thermal diffusion and the step becomes smoother. The lower part of the dense body may drip away while this occurs, but it does not stall at high displacement in the process. The step geometry of the new boundary layer encourages the formation of drips at the step (Fig. 4.12), though these have a small amplitude. The small amplitude of dripping boundary layer and the lack of internal displacement can be used to distinguish dense material which is preserved due to rapid thermal diffusion from the stalling of a delaminated body at high displacement (Fig. 4.11).

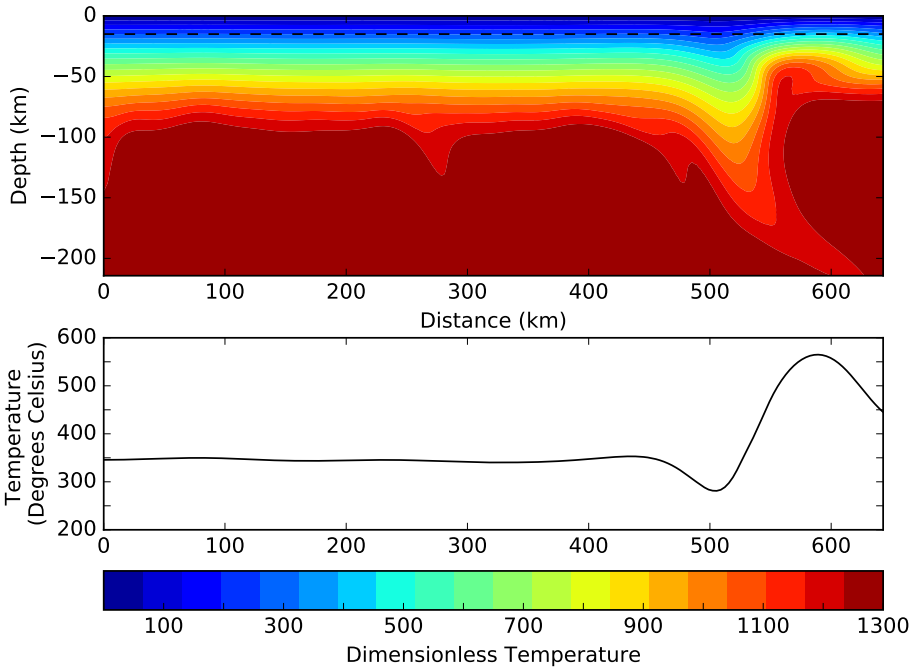

Figure 4.11: The temperature distribution of the stalled delamination model in Fig. 4.9, with a profile plotted for the depth of the original Moho (dashed line). Despite cooling at the decollement zone, a large temperature anomaly still exists in the zone of thin lithosphere (bottom). The temperature is scaled so that the ambient mantle is 1300°.

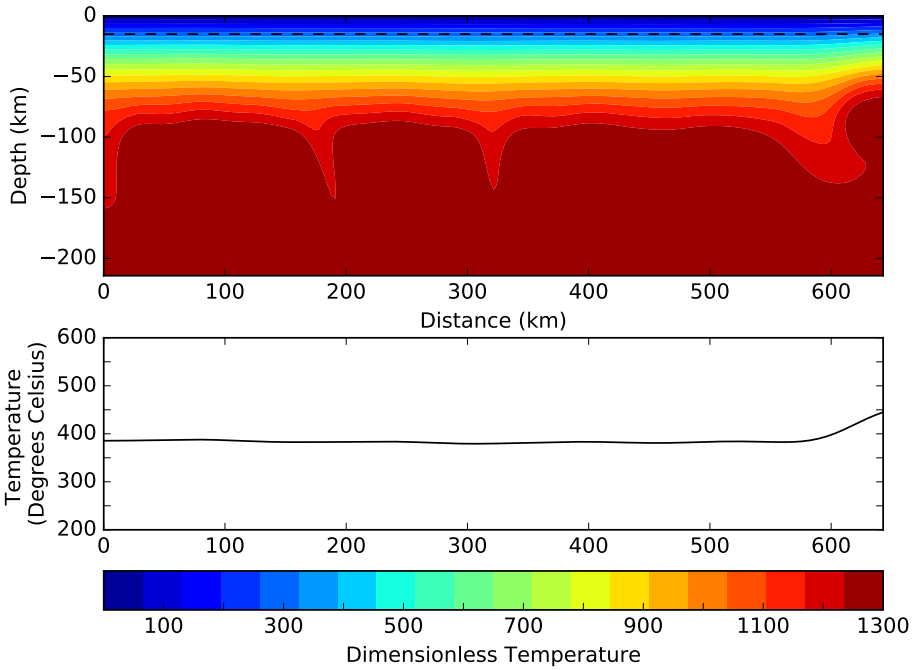

Figure 4.12: A drip which has formed at the step ($\sim$ 650 km), from the initial conditions of $D' = 0.75$ and $\eta'_c = 10^{-2}$. Due to the rapid cooling of the dense body ($Ra_\delta = 10$), the lower part if the dense body is the only section which is weak enough to drip away, doing so as part of the thermal boundary layer. No section of dense body stagnates at high displacement: it either continues to drip off or freezes within the thermal boundary layer at small displacement.

4.6 Discussion

Hanging density anomalies observed in tomography nature generally occur close to the boundary between two contrasting terranes. For example, the boundary of the Great Valley and the Sierra Nevada; the edge of the Colorado Plateau and the south-eastern edge of the Carpathians. Our simple explanation for this is that these instabilities initially had rapid growth and migration which was highly dependent on a weak middle to lower crust, so that a change away these conditions produced a sudden slowing in both migration and sinking. In this interpretation, the observation of hanging density anomalies reflects that delamination generally occurs quickly enough that it is limited primarily by the geological processes which provide the initial large perturbation and region of weak lower crust, rather than by fundamental slowing of the instability. Therefore although sub-continental instabilities are not typically included in the tectonic framework, their dynamics are controlled by tectonics for their entire evolution. Instability initiation is due to the onset of thinning and weakening which occur by localised tectonic deformation. The onset of stalling is a result of a contrast in decollement rheology generated by either a limited

lateral extent of tectonic weakening or the suturing of terranes with contrasting rheologies.

The heterogeneous decollement viscosity could represent a limited extent of melt intrusion or strain localisation. The most significant stalling occurs when the width of the weak decollement region is approximately equivalent to the lithosphere's thickness. This implies for stalling to occur, delamination must be able to outpace the propagation of the initial decollement weakness at the step. Le Pourhiet et al. (2006) suggested that plastic failure was able to propagate from the deformation at the eastern margin of the Sierra Nevada, to a horizontal decollement between the batholith and restite. In this scenario, the stresses generated by delamination must somehow be less than the initial eastern deformation. Alternatively, if the decollement zone was produced by a high concentration of partial melt and volatiles, then it is unlikely that the rising asthenosphere during delamination can produce large volumes of melt intrusion into the lower crust where the dense body is still attached to the crust.

Stalling is only prominent for instabilities which begin by delamination. Triggered dripping close to the conditions for delamination may stall to a lesser extent and all other types of dripping are unable to stall by the mechanisms analysed. Therefore, the common observation of stalling supports the hypothesis that delamination plays a significant role, at the least comparable to dripping, in subcontinental recycling on Earth. The prevalent mechanism for removing highly viscous bodies appears to be the following: a tectonic episode produces the conditions for delamination in a confined region, such that the body which is too viscous to drip suddenly peels away rapidly and attains a significant displacement before switching to dripping. The velocity of this late stage dripping is higher than before the tectonic episode, due to the high displacement, but remains slow enough that the hanging body can be observed. This interplay between tectonic triggering, dripping and delamination is able to explain the episodic nature of observed instabilities.

If stalling has occurred, the most recent instability dynamics are not indicative of the initial dynamics of growth. For example, though the dense body below the Great Valley is currently coupled to the crust and producing subsidence, it must have been effectively decoupled from the Sierra Nevada batholith during its initial growth. Additionally, it is typical for volcanism to change during instability evolution. Significant recent volcanism beneath the Sierra Nevada only occurred during a short window ~ 3 *Ma* and volcanism in the Carpathians has become less contaminated by the crust through time (Manley et al. 2000). Rather than reflecting the evolution of volcanism associated with a typical instability, these switches could be related to the onset of stalling.

Finally, we have also shown that the stalling event can be triggered from the zone above the delaminating body, where asthenosphere is rising. In Chapter 3, the typical velocity of delamination was shown to be still slow enough that thermal diffusion can produce stalling, if no other weakening occurs. If weakening by infiltrating melt and volatiles is insignificant in delamination propagation, the

observed stalling may actually be the typical evolution of delamination. Alternatively, if the persistence of delamination requires the presence of melt and volatiles in the upwelling asthenosphere, the stalling period may mark the onset of their depletion. This is difficult to test, as stalling may produce a decrease in melting, rather than result from it. Also, the focus of geochemical studies has been the interaction between the crust and melt (Manley et al. 2000; Wang & Currie 2015), rather than volatiles in the original asthenospheric melt.

Stalling may occur as a combination of the two proposed mechanisms. After delamination migrates into a zone of stronger lower crust and stalls, a sharp lithospheric step is preserved as thermal processes were considered negligible. The stagnation however is likely to allow thermal diffusion to begin to dominate, as in the thermal models, producing a thermal boundary layer in the wedge zone. This would slow down the instability further, as it effectively strengthens the lower crust and reduces the density perturbation. The strengthening effect of thermal diffusion is greater than the increased density of the dense body in the models, due to the respective exponential and linear dependences. The mechanical models therefore underestimate the length of the stalling period and the two mechanisms are likely to complement each other to produce a longer observation period.

Stalling of delamination by dynamic strengthening of the wedge zone may be responsible for the apparent stalling of the hanging body in the western Colorado Plateau. This instability appears to have migrated towards the Basin and Range, which could generally be considered weaker and likely to accelerate, rather than stagnate, gravitational flow. In this case, delamination is initially triggered by localised tectonic strain, provoking rapid instability of the otherwise stable, thick lithosphere. After the initial peeling occurs, the wedge zone becomes congested with stronger material and delamination switches to dripping. This final stage of slow dripping provides an explanation for the current observable state, as well as the high degree of internal strain which is uncharacteristic of delamination.

4.7 Conclusion

Rapid instabilities can clearly switch from acceleration to a stalling period, if they encounter a region of increased viscosity. This could occur if delamination migrates into a region where the decollement region is strong or if a volume of rising asthenosphere is stronger. Surface observations appear to support the hypothesis that this switch from rapid instability to stalling is a typical feature of sub-continental instability evolution on Earth. The analysed mechanisms provide a new method for inferring heterogeneities in the crust. Further scrutiny of surface data against these types of mechanisms is required to assess which one dominates in nature and whether the required viscosity contrasts are

dynamic or time-independent.

Chapter 5

Interaction Between Dome-and-Keel and Lower Crustal Instabilities

Summary

Archean crust $>$ 3Ga old was typically weak enough to allow large scale crustal reorganisation, in the form of dome and keel formation. However, this weak state seemingly did not record superimposed deformation caused by sinking dense restitic material from below the crust, despite the large volume of recycling inferred to have occurred during crust formation. The relationship between these two instabilities, restite recycling and dome and keel formation, is analysed using the analytic Rayleigh-Taylor Instability model for multiple interacting instabilities and validated at high displacement numerically. The wavelength of the preserved domes requires the greenstone layer to be one to two orders of magnitude weaker than the granitoid, the keel and dome material respectively, which supports experimental rheological models. This weak greenstone layer acts acts as a trigger for dome and keel formation. In turn, the presence of a strong mantle lithosphere can control the recycling of restite. Restite can be recycled at the 10Ma time scale once it reaches a similar thickness to the granitoid, or twice the thickness if it is trapped by the lithosphere. There is no record of a thick restite dripping away below a weak crust, as this would lead to significant large wavelength deformation, but may have occurred prior to weakening and the subsequent dome and keel formation. During the latter, restite may have simultaneously sunk in places where granitoid domes rose. This is the result of a growing instability at a single wavelength, which involves the displacement of multiple interfaces. This coupled growth requires that the final part of restite was a similar thickness to the granitoid and can occur for the most likely crustal rheology. Therefore restite recycling can plausibly occur continuously beneath a strong crust

and then the weak crust corresponding to dome and keel formation, without disrupting the preserved structures. As a result, a crust with a net positive buoyancy and a felsic upper part, characteristics which Archean crust shares with modern stable crust, could form in an environment free of tectonics, by multiple Rayleigh-Taylor Instabilities, each growing at the 10Ma order of magnitude time-scale.

5.1 Introduction

Dome-and-keel structures provide insight into a mode of continental crust formation and stabilisation which has only occurred in the early Earth (Van Kranendonk et al. 2007; Sandiford et al. 2004). What this unique mechanical process, of sinking dense greenstone keels around rising granitoid domes, implies about mass and energy transfer in the early Earth is therefore of interest (Mareschal & West 1980; Robin & Bailey 2009). Inference of the other half of crustal fractionation, sinking of the dense lower crustal restitic bodies produced during granitoid genesis (Bédard 2006; Lee et al. 2006), has not been extracted from the rock record. Sub-continental gravitational instabilities are difficult to observe even on the modern Earth and typically rely on tomography during the sinking event or indirect surface features (Zandt et al. 2004; Levander et al. 2011), which are in this case either not possible or no longer preserved. We hypothesise however that should the two juxtaposed body-force flows have interacted, the dome-and-keel structures alone could infer the nature of sinking restite and therefore provide insight into how the entire fractionated crust was mechanically separated in the Archean.

Dome-and-keel structures are preserved from the Mesoarchean and earlier (> 3.2 Ga) in the Pilbara (Australia, Fig. 5.1) and Barberton (South Africa) provinces. They appear to have been dominated by internal body-forces and in the absence of far-field 'tectonic' stresses, which has been referred to as 'vertical tectonics' (Van Kranendonk et al. 2007; Van Kranendonk 2011; Lin 2005). Younger Neoarchean ($2.5 - 2.8$ Ga) terrains such as the Yilgarn (Australia) and Superior (North America) have preserved dome-and-keel structures which appear to have formed by combination of local buoyancy and far-field stresses (Whitney et al. 2004), as if they formed through a mixture of vertical tectonics and plate tectonics. Local buoyancy stresses may still play a substantial role in the vertical segregation of modern granitoid domes (Weinberg & Podladchikov 1995), though clearly to a lesser extent than in the Archean. If any interference between rising and sinking bodies has occurred on the Earth, the simplest setting, free of any superposition with plate tectonics, was during and before the Mesoarchean. Therefore a study of interference may provide both new insights into an elusive period of Earth's evolution and provide a framework for exploring its effects more recently.

The existence of restitic material in granite-greenstone terranes is theoretical, as none of this ma-

terial is preserved. Restitic by-products of modern granites have been observed as xenoliths (Ducea & Saleeby 1998; Lee et al. 2006) and their generation is a necessary step in the production of felsic melts (Hawkesworth & Kemp 2006) through refining an originally mafic material. A similar process is required for the generation of Archean granitoids (Bédard 2006). The partial melting which generated Palaeo-archean granitoids appears to have occurred predominately within the crust, without the interaction with the mantle lithosphere which is common on the modern Earth (Smithies et al. 2003). In the absence of tectonics, it is therefore likely that dense restitic material accumulated at the base of the crust, as felsic melt was progressively extracted, residing until it could be removed by gravitational instabilities. The felsic bulk composition of Palaeo-Archean crust today (Yuan 2015) indicates that such instabilities must have been efficient, as there is no longer any significant volume of restitic material.

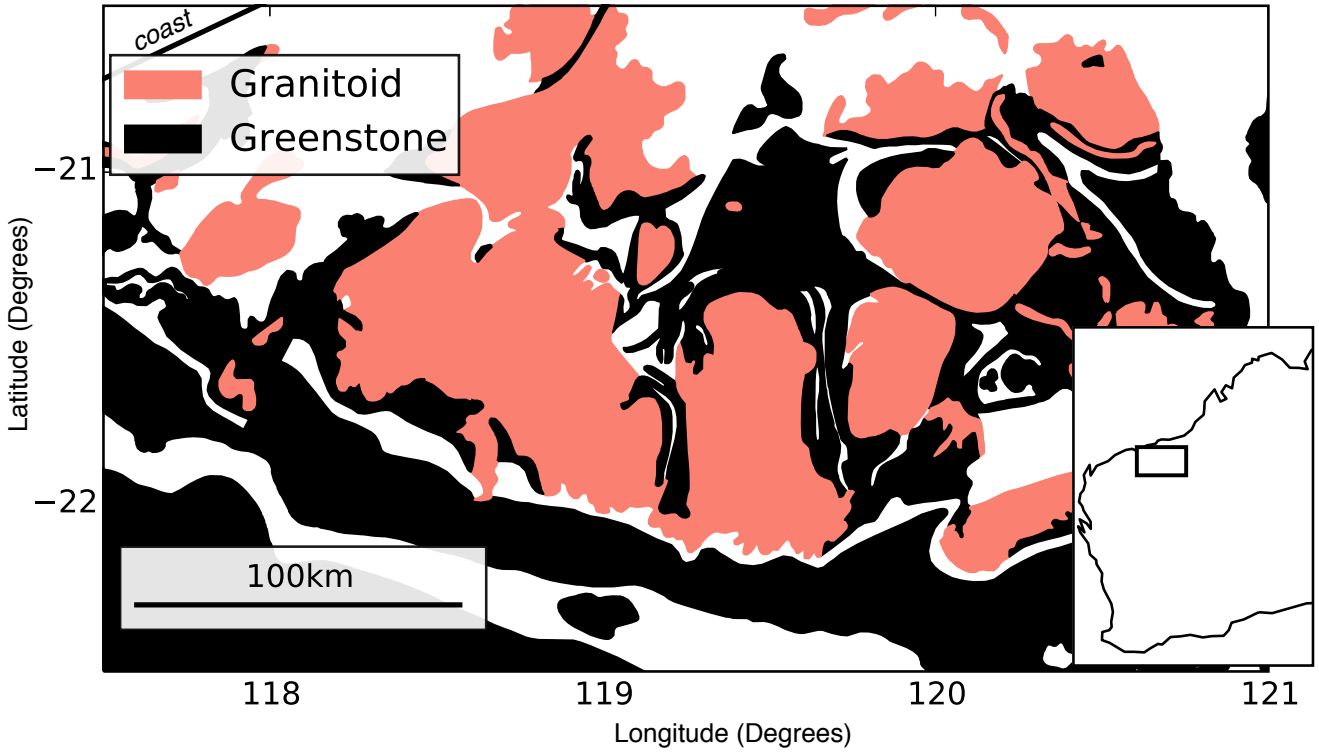

Figure 5.1: A simplified example of dome-and-keel geometry from the Pilbara, location within Australia inset. The distance between the dome centres, the dome-and-keel wavelength, is approximately 50 *km.*

5.2 Methodology

The Rayleigh-Taylor Instability (RTI) is the fluid dynamic model for the growth of a perturbation at the interface between materials of contrasting density (Chandrasekhar 1961). They are typically dominated by flow at one particular wavelength (λ), which can be highly dependent on a number of parameters,

including viscosity and thickness contrasts. The greenstone, granitoid and restite material are modelled as initially flat layers above the mantle (Fig. 5.2), with the interfaces between each perturbed by a small amount ($\sim 0.1\times$ the granitoid thickness). Each of these interfaces represents a change in density and therefore a change in normal stress, which the materials balance by viscous stress and therefore flow. Flow of materials can be represented by displacement of each interface, which is found as a solution to the RTI. The relevant interfaces are between the greenstone and granitoid, granitoid and restite, and restite and mantle, which are referred to as the GG, GR and RM interfaces. The GG and RM are unstable interfaces, as they represent a decrease in density downward. Where the GG interface is perturbed upward, a granitoid dome is rising and the granitoid is thickening and greenstone thinning. The GR interface is stabilising, in that the granitoid will tend to flow to remain above the restite, however it will still be displaced and requires modelling for accuracy in the overall normal stress.

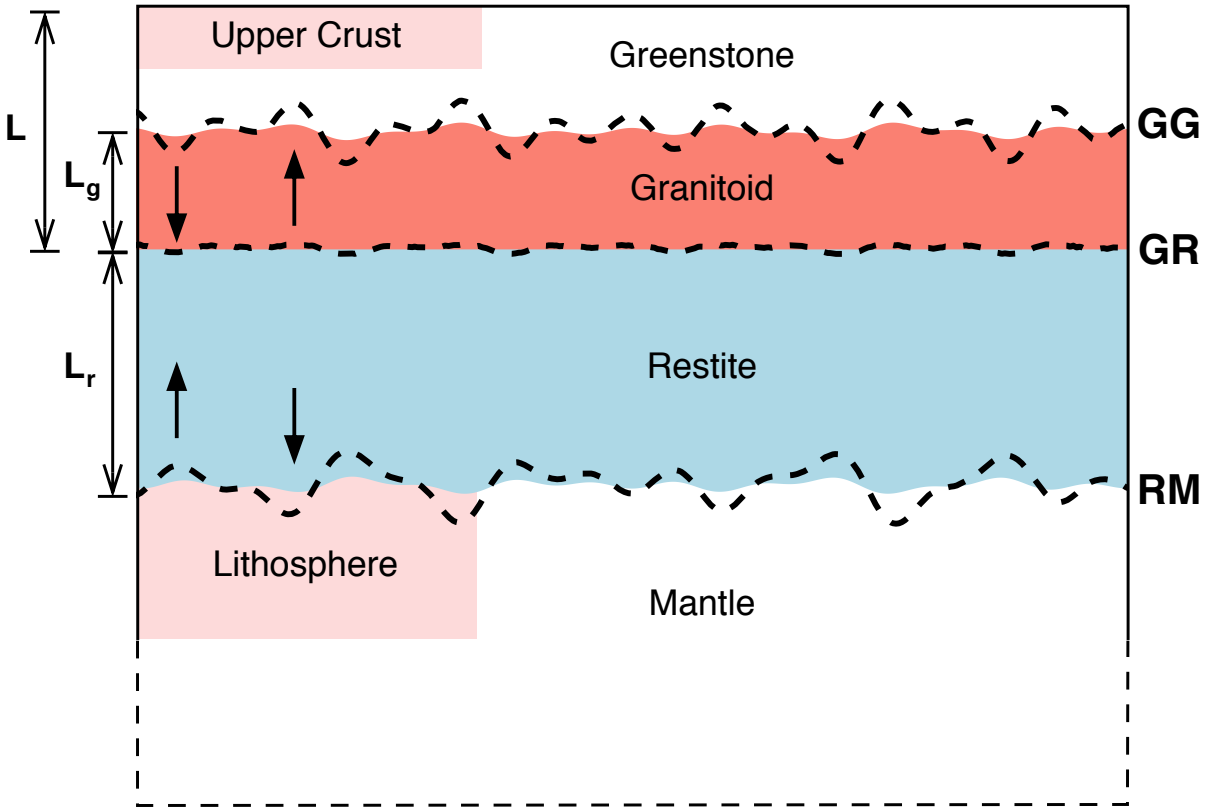

Figure 5.2: Schematic diagram of the conceptual model. Dashed lines demonstrate how the interfaces may evolve. In this example they are strongly coupled, i.e. they have similar amplitudes, and are evolving perfectly out of phase as emphasised by the arrows pointing in flow direction. Free-slip conditions are used at the surface (roller symbol). The mantle is an inviscid half-space in the analytical solutions. In the numerical calculations the sides and base are also free-slip.

The RTI model has previously been expanded for the case of a stratified fluid with multiple interfaces of contrasting density (Bassi & Bonnin 1988; Neil & Houseman 1999; Molnar & Houseman

2013). These solutions have been predominately applied to thickening of a buoyant crust above sinking mantle lithosphere. In such a case there is one growing instability corresponding to the lithosphere-asthenosphere interface and one mode of shrinking, stable flow corresponding to the upward buoyancy of the Moho. We follow the same approach as these studies, described by Bassi & Bonnin (1988), the only difference being the presence of multiple growing instabilities due to the density stratification (Fig. 5.2). The solution involves formulating a matrix relationship between the velocity ($\dot{w}$) and displacement (w), and therefore the exponential growth-rate, at each interface (Eq. 5.1)

$$\sum_i M_{ij} w_i = \dot{w}_j \tag{5.1}$$

The growth-rate at each interface depends on each of the other interfaces. The exponential growth of a particular interface is then the sum of multiple exponential growth equations. The analysis is simpler if the system can be described by one dominating exponential growth equation, so following Bassi & Bonnin (1988), the system is viewed in terms of a group of instabilities, hereon in referred to as growth modes, each with only one exponential growth-rate. For a particular mode, every interface grows by the same exponential growth-rate, but varies by a linear factor. These modes and their corresponding growth-rates and interface factors are found by numerically calculating the eigenvectors and eigenvalues of M_{ij}.

The eigenvectors are combined to form a new matrix P_{ij}, for which each column corresponds to a growth mode and the rows to each interface. The eigenvalues correspond to the growth-rate of each growth mode. The total growth through time of each interface can be reconstructed by summing up the contributions from each mode for each interface (Eq. 5.2). As with the two layer RTI, the growth of the instabilities depend on the initial displacement of each perturbation, which are integrated using the scaling factors, α_j. This displacement is assumed to be small and similar for each interface, so that it is primarily the components of P_{ij} which dictate the relative interface growth. To simplify Eq. 5.2, flow will be dominated by the growth mode with the highest growth-rate. We then only consider the mode with the highest growth-rate (eigenvalue) and the corresponding column of P_{ij} quantifies the relative extent to which each interface is displaced through time by this mode. This is illustrated in Fig. 5.3.

$$\begin{aligned} w_i'(t) &= \sum_j P_{ij} \alpha_j e^{\tau_j' t} \\ i &\in \{\mathrm{GG}, \mathrm{GR}, \mathrm{RM}, n_{layers}\} \\ j &\in \{1, 2, .., n_{solutions}\} \end{aligned} \tag{5.2}$$

For a particular growth mode, one interface may be displaced at a higher velocity than the other interfaces, while each of the velocities are increasing at the same rate. Due to this difference in velocity, one interface may reach a high displacement significantly more quickly than the other interfaces. This relative velocity is quantified by comparing the components of P_{ij}, where j is set to the fastest growth mode. The vector describing the contributions of each interface is normalised to length 1. Then $P_{RM,max}$ and $P_{GG,max}$ are the components corresponding to the RM and GG interfaces. For example, if displacement of GG dominates, $P_{GG,max} \approx \pm 1$ and $P_{RM,max} = 0$. The degree to whether both GG and RM interfaces are involved in the fastest growing mode, or just one of them, is quantified by defining the coupling (Eq. 5.3), which is close to 1 if both interface velocities are always similar, or 0 if one is always much larger than the other.

$$C = 1 - ||P_{RM,max}| - |P_{GG,max}|| \tag{5.3}$$

$P_{RM,max}$ and $P_{GG,max}$ may not have the same signs. If one is negative and the other positive, where the GG interface is perturbed upwards, RM will be perturbed downwards. This is referred to as 'out of phase' flow and is illustrated in Fig. 5.2. The converse, if the signs are identical, is referred to as 'in phase' flow and would result in rising mantle beneath rising granitoid domes.

It is assumed that the dominating flow can be well approximated by selecting the growth mode with the highest growth-rate. This is because one solution tends to dominate due to the exponential nature of its growth. However, as well as decomposing the overall growth into modes, the solution is also decomposed into wavelengths. There can then be two growth modes with an approximately equal growth-rate, but with different wavelengths. This is the definition of 'decoupled' of flow. In this case the flow may need to be approximated by the growth of two modes, which for example may involve the dome and keel forming at a small wavelength, while the restite simultaneously sinks at a larger wavelength. Due to the exponential nature of growth, this is a special case as it requires the growth-rates to be very similar.

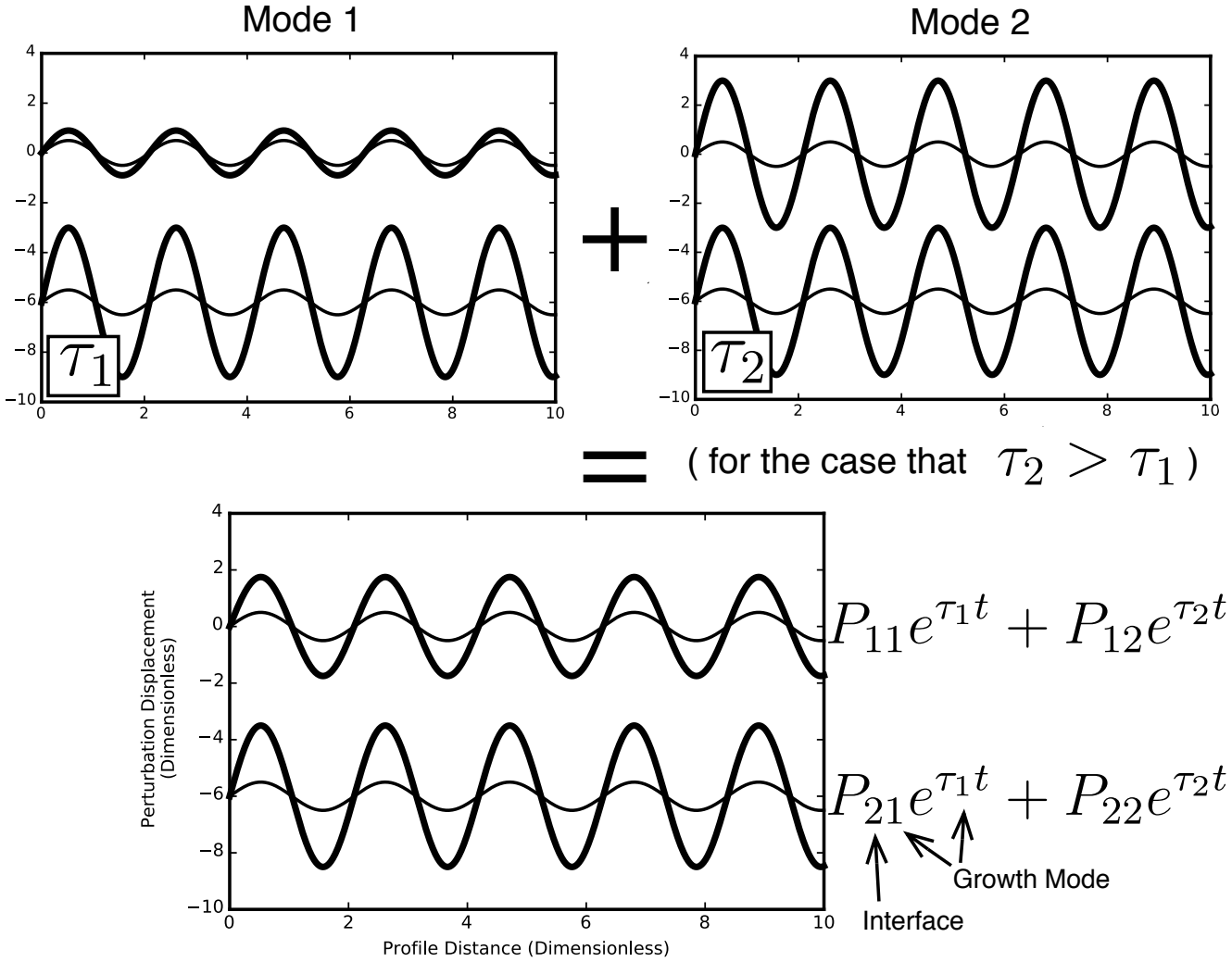

Figure 5.3: Growth mode example for two interfaces. Mode 1 and Mode 2 show the relative contributions of each interface to each growth mode. In the case that the growth-rate of the Mode 2 is much greater than that of Mode 1, the interface evolution is well approximated by the growth-rate of Mode 2 and the corresponding interface contributions. Mode 1 and Mode 2 are examples of low and high coupling growth modes.

Two additional layers are also added in some options in order to model an upper greenstone layer, with a different rheology to the lower greenstone, and a mantle lithosphere layer below the restite (Fig. 5.2). These two optional interfaces do not introduce any new changes in density, only altering the viscosity for a particular depth range.

5.2.1 Non-dimensionalisation

Solutions of the RTI are non-dimensionalised, such that each solution depends only on a small set of ratios between parameters. The exponential growth-rate (τ') is scaled by the ratio of buoyancy stress to viscous time-scale, ($\tau = \tau' \Delta\rho_{rm} g L/\eta$), where ρ_{rm}, g, L and η correspond to the RM density contrast, gravitational acceleration, the entire thickness of the crust and the viscosity of the restite. As the solutions are developed using the Fourier transform, they depend on a perturbation wavenumber, $k = (2\pi)/\lambda$, where λ is the wavelength. The wavenumber is non-dimensionalised using the crustal thickness L, such that $k' = kL$. An approximate wavenumber can be estimated based on the wavelength of dome-and-keel structures and the likely crustal thickness during formation.

The viscosity of the granitoid is set relative to the restite, $\eta'_g = \eta_g/\eta$. The granitoid thickness is constantly set to $0.5L$ and the restite thickness varied, so the restite thickness (L_r) is non-dimensionalised relative to the granitoid thickness: $L'_r = 2L_r/L$. Which interface dominates the flow field depend partly on the relative density contrasts at GG and RM. As the time-scale non-dimensionalisation depends on $\Delta\rho_{rm}$, the relative buoyancy is controlled by the relative GG density contrast: $\Delta\rho'_{gg} = \Delta\rho_{gg}/\Delta\rho_{rm}$.

5.2.2 Boundary Conditions

The surface of the Earth is also an interface with a stabilising buoyancy force which produces a decaying RTI. This resists GG growth, provided the interface is close enough to the surface. There is therefore a natural bias towards growth of the RM interface, which is unimpeded by the weak mantle below. If the density contrast at the surface is much greater than at the GG interface, the Earth's free surface can be approximated as having zero vertical velocity (free slip), which simplifies the numerical calculations. For our given material thicknesses, the GG contrast needs to be at least ten times greater than at the surface (Supp. Data 5.8), which is satisfied. The numerical calculations additionally use the free-slip condition at the walls, such that flow is periodic at the wavelength of the horizontal model domain. All perturbations are chosen to satisfy this condition.

The mantle in the analytic solutions is modelled by an inviscid half-space, but with a density contrast at the RM interface. In the numerical models, this is approximated by setting the mantle viscosity to $10^{-3}\eta$ and with a free-slip lower boundary condition. As the initial instability growth is of primary interest, the mantle layer is three times the thickness of the crust. The low viscosity of the mantle dissipates the instability stresses over a short distance and this small thickness is a good approximation for the actual upper mantle thickness, while significantly reducing the computational running time.

5.2.3 Numerical Calculation

The preceding methodology is referred to as the analytic RTI analysis as the formulation is analytic and only the final eigenvalue solution step is solved numerically, without the need for a weak formulation and discretisation. The analytic equations are linearised and therefore only accurate for small interface displacements. Due to the exponential nature of growth, it is likely however that the mode which is dominating during the initial small-displacement growth period will continue to dominate in the evolving flow. This prediction however must be tested by numerically solving a weak finite-element formulation of the Stokes equations. Additionally, numerical calculation can be used to quantify the interface wavelengths and velocities, as well as the degree of internal deformation of the granite and restite bodies, at high displacement.

Numerical solutions to the Stokes equations are found using the finite element, particle-in-cell solver Underworld (Moresi et al. 2007). The simplistic material properties; homogeneous viscosity and density, are maintained for the calculations, as the primary goal is to compare the numerical and analytic solutions. The interface perturbations in the numerical models are the sum of five cosine waves of random wavelengths and amplitudes. The wavelengths are set as *model domain width* $/n$, where n are integers which are chosen to give wavenumbers in the range $0 < k < 5$. The initial GG and RM perturbations were chosen to be identical, to prevent any bias in relative flow. For each case, a second model was calculated with the RM interface reflected, in order to compare the growth-rate of the 'out of phase' solution.

5.3 Constraints and Rheology

Dome-keel structures are typically $10 - 15$ *km* thick, giving an original granite-greenstone thickness of 25 *km* (neglecting the restite below) assuming there has been 10 *km* of erosion, as in Robin & Bailey (2009). The wavelength of dome-and-keel structures is typically about 50 *km* (e.g. the eastern Pilbara, Fig. 5.1). Allowing for generous uncertainty of these estimates gives an approximate wavenumber of $k' = 3 \pm 1$. This range is referred to as $k_{obs.}$. Calculated dominant wavenumbers are then compared against this approximate range (i.e. Fig. 5.7), in order to assess their likelihood for producing the preserved dome-and-keel structures.

The viscosity, thickness and density contrast of each layer are then additional parameters and represented as ratios to the reference values in the growth-rate scaling. The partial melting process creating the granitoid is inferred to occur in the crust (Martin et al. 2005), as there is no evident mantle

interaction. The initial layering represents the materials after they have separated, but are still adjacent to each other in crust base (Fig. 5.2). The degree of partial melting is likely to be $< 20\%$, which would require the restite to be at least five times thicker than the granitoid, if the melting and local differentiation process occurred before any restite could be removed from the crust. This would result in a $50 - 75$ *km* restite layer at the base of the crust, if it were efficiently differentiated from the granitoid and no recycling occurred. This is an upper bound, as instabilities may have occurred during granitoid generation. As the growth-rate of dripping scales with the layer thickness, the corresponding instability would grow extremely quickly. However in the case of an internal viscosity contrast of two orders of magnitude, the instability is likely to leave behind the stable upper half of the restite (Conrad & Molnar 1999). Most likely, the instability's growth would become significant before the restite becomes this thick and we are instead concerned with the sinking of the final section of restite which is removed. We therefore calculate for $L'_r = 1$ or 2, where the latter is certainly still a plausible value and will reproduce the larger wavelength restite flow associated with thicker layers.

The restite is likely to follow a pyroxene flow law, which yields a relatively high effective viscosity even at high temperatures, for example $\sim 10^{20} - 10^{21}$ Pa s at $800 - 900^{\circ}$C, assuming that it lost its volatiles during partial melting (Bystricky & Mackwell 2001). If the restite begins sinking before it has efficiently devolatised, its viscosity could be reduced by almost two orders of magnitude (Bürgmann & Dresen 2008), illustrated in Fig. 5.4. Newly forming basalt and komatiite is likely to have been exposed to water and subsequently altered to greenschist and serpentinite. Both rock types are extremely weak, likely to have viscosities as low as $10^{17} - 10^{19}$ Pa s (Hilairet et al. 2007; Hilairet & Reynard 2009; Reynard 2013). Depending on the relative time-scales of volcanism and pervasive serpentinisation, the greenstone layer or only the lower part may be weakened (Lee et al. 2008; de Bremond d'Ars et al. 1999). Deformation of the near-surface greenstone would be limited by its brittle strength, but would switch to ductile deformation at depths of $5 - 10$ *km* (Reynard 2013). The dome-and-keel structures often feature ring faults (Van Kranendonk et al. 2007), indicating that the greenstone deformed with at least some plasticity. Configurations of differing strength contrasts between the upper and lower greenstone are considered (Fig. 5.4). These are simplified as either one weak greenstone layer, or the additional inclusion of a strong upper crustal layer (Fig. 5.2). The granitoid may likely follow a 'wet granitoid' flow law (Rutter et al. 2006), which is highly temperature dependent (Fig. 5.4). On average, solid-state granitoid is likely to have a viscosity approximately two orders of magnitude higher than the greenstone.

Partial melt was likely to be present in the granitoid, during dome formation (Collins et al. 1998). The presence of melt can reduce the granitoid by many orders of magnitude and melting at the base of granitoid layers has been argued as an important trigger for dome formation (Thébaud & Rey 2013). In the models of Robin & Bailey (2009) however, the low viscosity of the serpentinised and heated lower

greenstone cover was the dominant viscosity contrast. It is therefore also important to consider how the relative weakening effects of partial melting, compared to serpentinisation, affect the dome-and-keel instability growth.

As well as experimental uncertainties associated with these rheological models, each is highly dependent on other particular local parameters, such as melt and volatile content, as well as temperature and stress dependence. However the following models are designed to capture fundamental dynamics using effective viscosities which encapsulate the dominant viscosity contrasts. The layers can plausibly follow the average relative viscosities shown in Fig 5.4, though the described uncertainty may result, for example, in the granitoid having a similar or larger viscosity to the restite. Therefore, it is also important to explore other viscosity contrasts, to test how sensitive instability morphology and relative growth is to their variation.

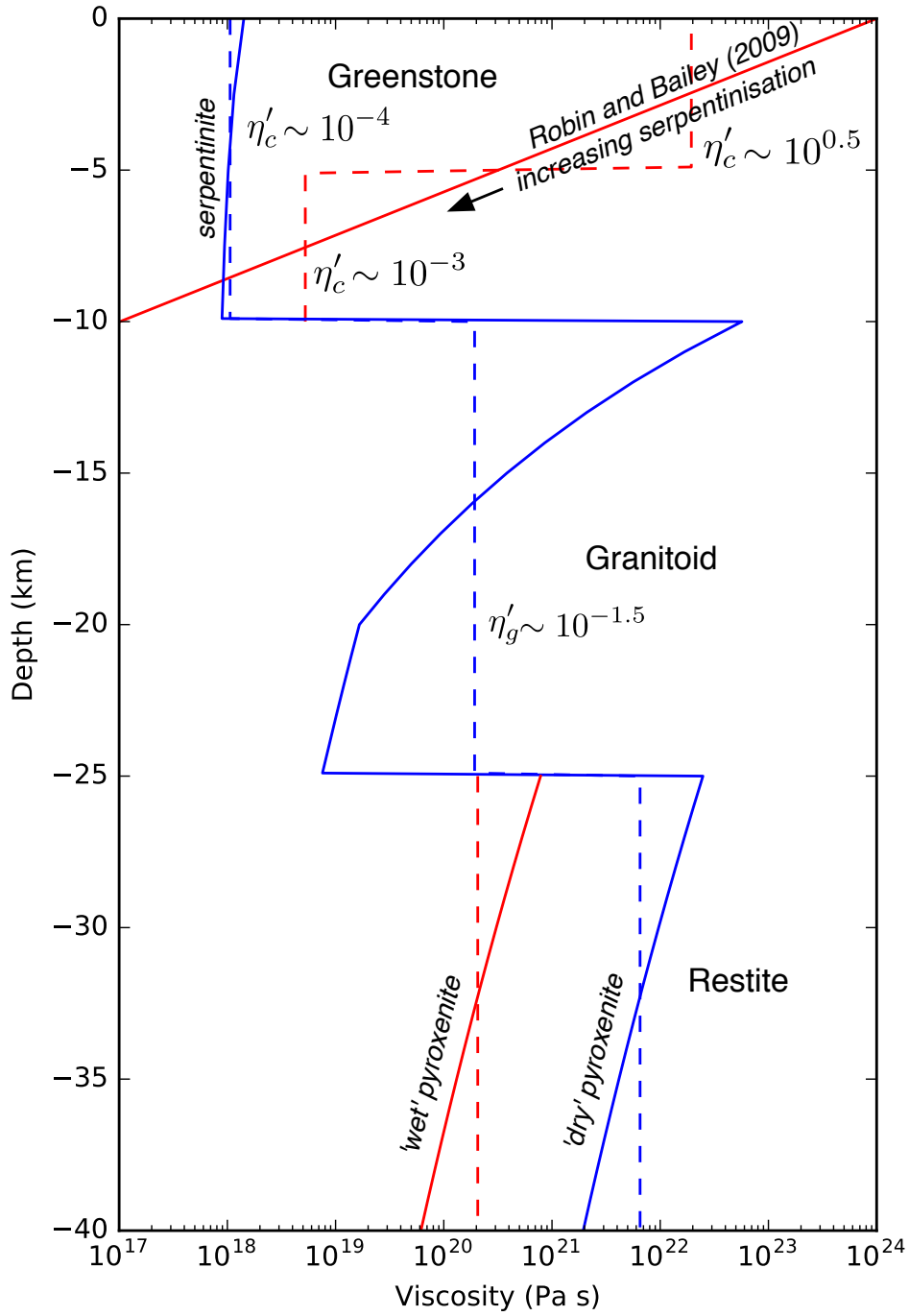

Figure 5.4: An example of a plausible stratified rheology, based upon experimental data, when the GR interface is 800°C. The restite and granitoid layers use the results of Bystricky & Mackwell (2001) and Rutter et al. (2006) respectively. If the entire greenstone layer is serpentinised, the crust could follow the rheology proposed by Hilairet et al. (2007), which is weakly temperature dependent. Robin & Bailey (2009) modelled (red) the greenstone as being highly serpentinised at its base, following the serpentinite rheological data of Raleigh & Paterson (1965), while transitioning to the top which with negligible serpentinisation, instead following the diabase rheology of Caristan (1982). Robin and Bailey's calculations are based upon high temperatures at the GG interface due to radioactive decay and thermal blanketing by the greenstone layer. Average viscosities are also plotted (dashed) and an approximate relative value labelled.

We take the mantle density as being a reference and non-dimensionalise material densities to the density contrast between the restite and the mantle, such that $\Delta\rho'_{rm} = 1$, $\Delta\rho'_{gg} = (\rho_c - \rho_g)/\Delta\rho_{rm}$, $\Delta\rho'_{gr} = (\rho_g - \rho_r)/\Delta\rho_{rm}$ for the GG, GR and RM density contrasts respectively. We set the difference in densities between the greenstone crust and the restite, $\Delta\rho'_{cr} = (\rho_c - \rho_r)/(\rho_r - \rho_0) = -1$, such that we assume that the greenstone crust is as positively buoyant as the restite is negatively buoyant. We then allow $\Delta\rho'_{gg}$ to be free and calculate its given value for particular conditions. The choice of $\Delta\rho'_{cr}$ is primarily suitable for greenschist or the lower range of amphibolite facies and thus may no longer be a reasonable choice at high displacement when the material equilibrates in the lower crust. Our primary concern however is the initial growth period for which this estimation is valid and the relative granite-greenstone density difference is a more critical parameter for the evolving dynamics anyway.

Though the GG density contrast is a free parameter in the calculations, we require a reference value in order to discuss what is reasonable when interpreting the results. Estimates of material densities come from both measurement (Peschler et al. 2004) and geochemical studies (Bédard 2006). A restite which is deep enough in the crust for garnet to be stable, is approximately 200 $kg\ m^{-3}$ denser than the average asthenosphere. Similarly, approximate densities for the granite and greenstone of 2700 and $2900 - 3000\ kg\ m^{-3}$ gives a relative GG density contrast of $\Delta\rho'_{gg} = 1 - 1.5$. The upper limit could plausibly become two when considering granitoid density decrease with increasing temperature and inclusion of melt.

5.4 Benchmarking

The analytic solutions require numerical calculation of the matrix eigen decomposition. The accuracy of these can be easily tested using the eigenvalue equation and are robust. As the analytic formulation is only accurate for small displacements, some analytic solutions were compared to high displacement numerical calculations to check that predictions about instability growth held at high strain. For each model configuration, there is a specific relative density contrast at which both interfaces grow at similar time-scales. This was tested by altering $\Delta\rho'_{gg}$ and recording which interface has the higher initial velocity and then confirming that this interface doubled in thickness first. The analytic prediction of this switch was confirmed numerically (Fig. 5.5). Each of the predictions of relative growth, within this doubling interface displacement, were reproduced numerically. Divergence between qualitative analytic and numerical predictions occurred when the domes reached the surface or when the restite had perturbed the GG interface and altered the subsequent dominant GG wavelength. When GG growth is negligible, granitoid strain due to restite flow is still predicted by the analytic solution, though this was not quantified and is likely to also differ to the numerical calculation at high displacement.

The dominant wavenumber in each numerical model was compared to the analytic prediction, which always agreed. The analytic predictions generally predict that the 'out of phase' solution would grow more quickly than when the interfaces are 'in phase', which was always confirmed by the numerical models. Additionally, numerical models with each interface perturbed by random noise also supported the preference for 'out of phase' flow.

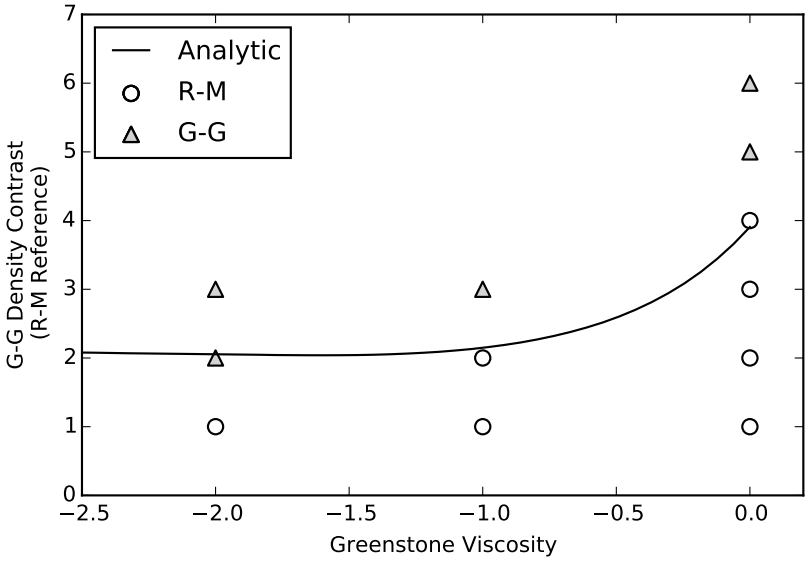

Figure 5.5: Comparison between the analytic prediction of the density at which GG growth becomes dominant and numerical calculation of which interface dominates the initial flow. This particular case is for $L'_r = 2$, homogeneous viscosity for restite and granitoid layers and varying greenstone viscosity.

5.5 Results

There are three scenarios of instability growth which result in dominating dome-and-keel growth occurring with a wavenumber close to $k_{obs.}$ (Fig. 5.6). In the first, both the GG interface and the RM interfaces are displaced through time at a similar wavelength, satisfying $k_{obs.}$, as well as a similar growth-rate. Dome-and-keel formation and restite removal occur simultaneously due to the growth of one instability mode and are therefore 'coupled'. Growth of the two interfaces also occurs with similar growth-rates in the second scenario, but the dominant wavelengths of the two interfaces differs. This is the result of two superimposed growth modes. Each mode involves predominately either the GG or RM interface and the modes are therefore 'decoupled'. In the third scenario, sinking of the restite is negligible due to either its absence or the presence of strong lithosphere below. In this case, dome-and-keel formation occurs in isolation.

Each of these modes requires specific ranges of relative viscosities and density anomalies, otherwise wavelengths dissimilar to $k_{obs.}$ are produced. The three scenarios described can occur within the constraints of Section 5.3. Generally, each of these scenarios can occur if the crust, consisting of the granite and greenstone layers, is of similar viscosity to the immediate layer below. There are more subtle features to be described, which may favour scenarios of others. However, these three scenarios are generally considered to be possible models for the evolution of Archean crust and capture the different fundamental styles of superimposed growing RTIs.

A) Coupled Instabilities

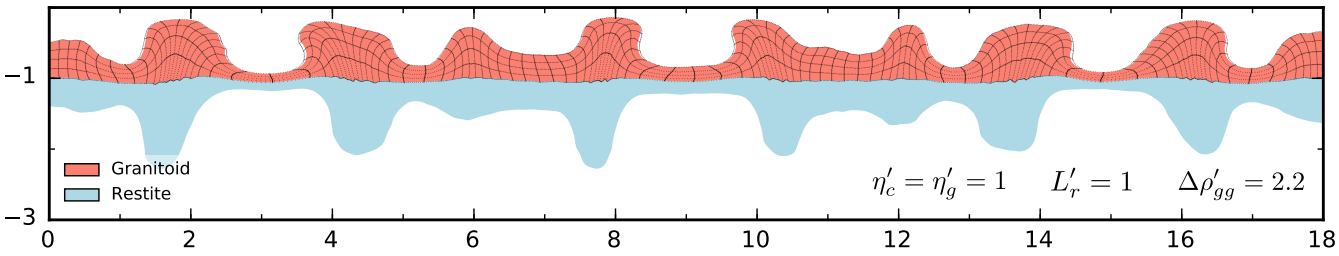

B) Decoupled Instabilities with Similar Growth-Rates

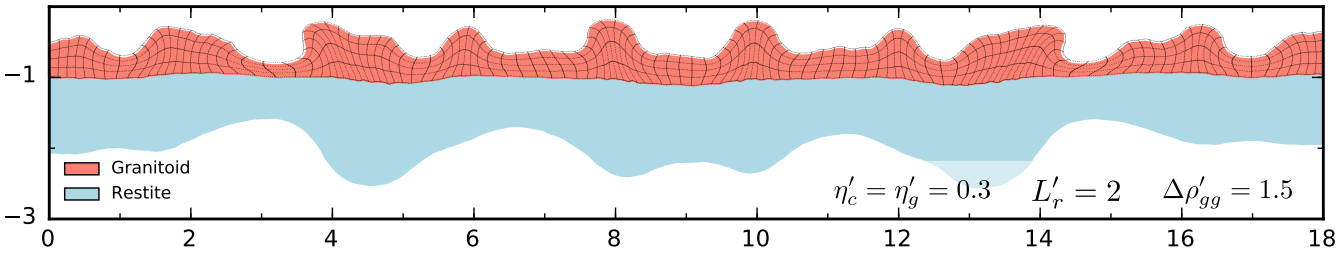

C) Isolated Dome and Keel Instability

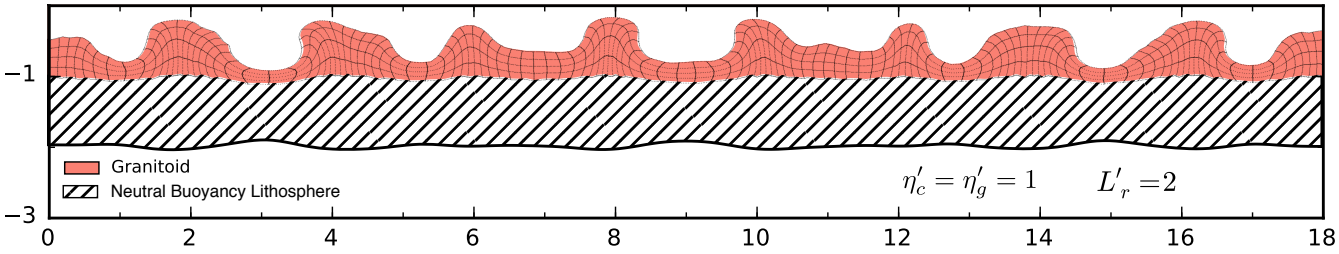

Figure 5.6: **Three model types which reproduce the observed dome-and-keel wavelength: A)** *Coupled growth occurs when the fastest growing mode involves the growth of both the GG and RM interfaces at similar displacements over time, for the same wavelength. This only occurs for the observed wavelength at* $L'_r = 1$, $\Delta\rho'_{gg} \sim 2$ *and* $\eta'_c \geq 10^{-1}$. **B)** *For most configurations, the restite wavelength is much greater than the observed wavelength. However, if* $\Delta\rho'_{gg}$ *is large enough, there can be two dominating growth modes each only involving one of the interfaces and is therefore decoupled. Then the GG interface can evolve at the observed wavelength, even if the RM interface does not. This mechanism requires a highly specific, large value for* $\Delta\rho'_{gg}$ *and is therefore unlikely to be applicable to the Pilbara.* **C)** *If the density anomaly at the RM interface is not present or negligible, the dome-and-keel instability occurs in isolation. The observed wavelength is reproduced only for* $\eta'_c \geq 10^{-1}$.

5.5.1 Coupled Instabilities

If the dominating growth mode involves the exponential growth of both the RM and GG interfaces, the growth of a single instability could simultaneously produce the dome-and-keel structures and remove the restite (Fig. 5.6a). If an instability involves the displacement of both interfaces, it is referred to as 'coupled'. Coupling is quantified by C (Eq. 5.3). The greatest decoupling and coupling are measured as $C = 0$ and $C = 1$ respectively. By definition, coupled flow occurs at a single wavelength. It appears to occur only when there is only one growth-rate maxima, as in Fig. 5.9.

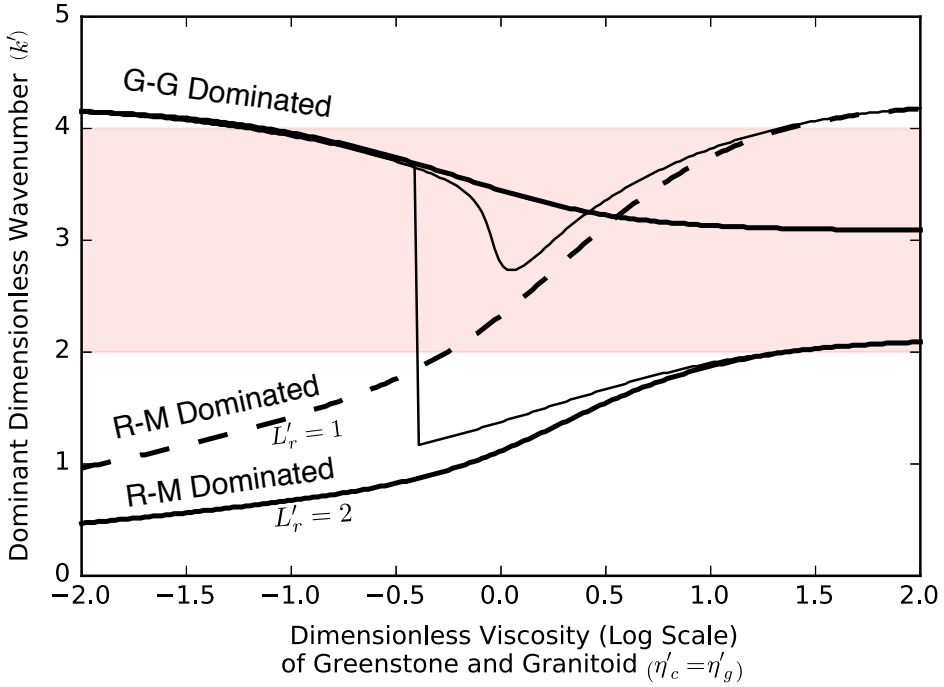

Figure 5.7: Dominant wavenumber depending on the crustal viscosity ($\eta'_c = \eta'_g$), for the end-members in which only one of the GG or RM interfaces has a non-zero density contrast, 'GG dominated' and 'RM dominated respectively'. When plotting the models for $\Delta\rho'_{gg} = 2$ (thin curves), models with extreme crust to restite density contrasts resemble one of the end-members, whereas modest viscosity contrasts produce a mixture. The switch is smooth when $L'_r = 1$, which corresponds to high coupling. This switch becomes piece-wise when $L'_r = 2$, as there is then a switch between two growth-rate maxima with contrasting wavenumbers.

Coupling only occurs when the granite and restite have similar viscosities ($\eta'_g = 1$) and thicknesses ($L'_r = 1$). Otherwise, there is no case for which their dominant wavelengths are equivalent (Fig. 5.7). An example which generates coupled flow within the $k_{obs.}$ range is $\eta'_g = \eta'_c = 1$, $L'_r = 1$ (Figs. 5.6a, 5.8 and 5.9). The coupling is significant for a large range of relative buoyancy, $1 < \rho'_{gg} < 4$, all of which occur well within $k_{obs.}$. The highest coupling occurs for $\Delta\rho'_{gg} = 2.2$, which is beyond the expected range for the GG interface. Provided $\Delta\rho'_{gg}$ is in this range, the high coupling and correct wavelength occur

regardless of whether the GG or RM evolves more quickly. This is an attractive property of the coupled solutions: generation of $k_{obs.}$ is not sensitive to small variations of the relative interface buoyancy.

Coupling can also occur for crustal viscosity gradients, still satisfying $k_{obs.}$ (Fig. 5.10). If the greenstone is an order of magnitude weaker than the granitoid, the dominant wavelength is larger, but still within $k_{obs.}$. The range of high coupling is approximately $0.5 < \Delta\rho'_{gg} < 1.5$. Peak coupling occurs at $\Delta\rho'_{gg} = 1$, which is more easily justified than the previous range considered. If the greenstone is weaker than this, the wavelengths becomes too small for $k_{obs.}$, while if it is much stronger than $\eta'_c = 1$, no coupling occurs.

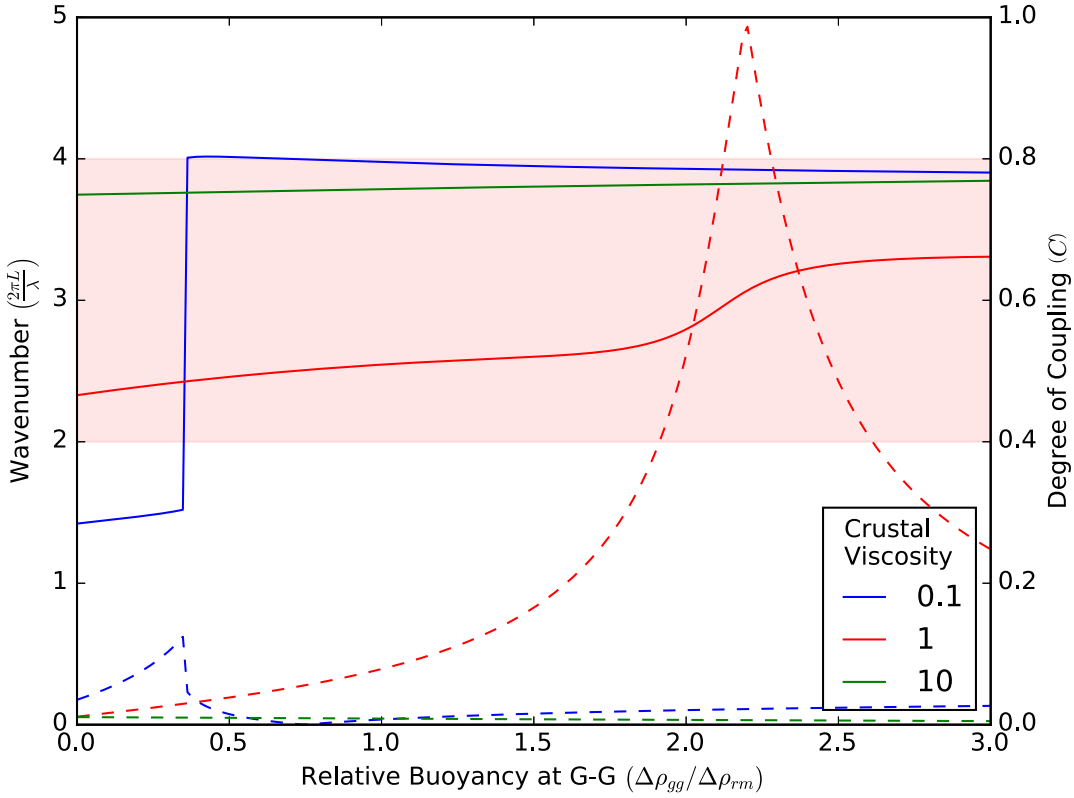

Figure 5.8: The wavenumber (solid) of the mode with the fastest growth-rate, depending on $\Delta\rho'_{gg}$, which controls which interface grows more quickly. The coupling (dashed) also varies significantly with $\Delta\rho'_{gg}$, where there is only one relative buoyancy for which the dominant wave mode involves both interfaces equally ($C = 1$). Different values of $\eta'_c = \eta'_g$ are shown, where only $\eta'_c = \eta'_g = 1$ is coupled. The other two viscosity values result in the RM and GG interfaces having individual growth solutions at different wavelengths, so that the dominant wavelength abruptly switches depending on which interface grows more quickly.

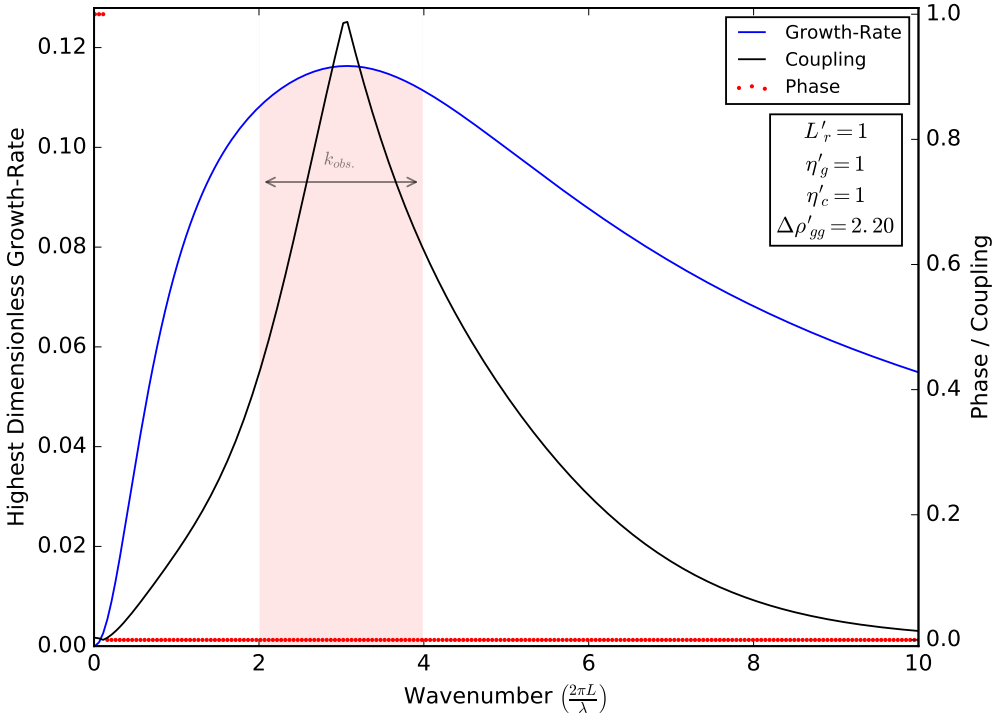

Figure 5.9: Growth-rate of the fastest mode, depending on wavenumber. η'_c, η'_g and L'_r are chosen in order to produce coupled flow and $\Delta\rho'_{gg} = 2.2$ is the relative buoyancy which produces the highest coupling, as shown in Fig. 5.8.

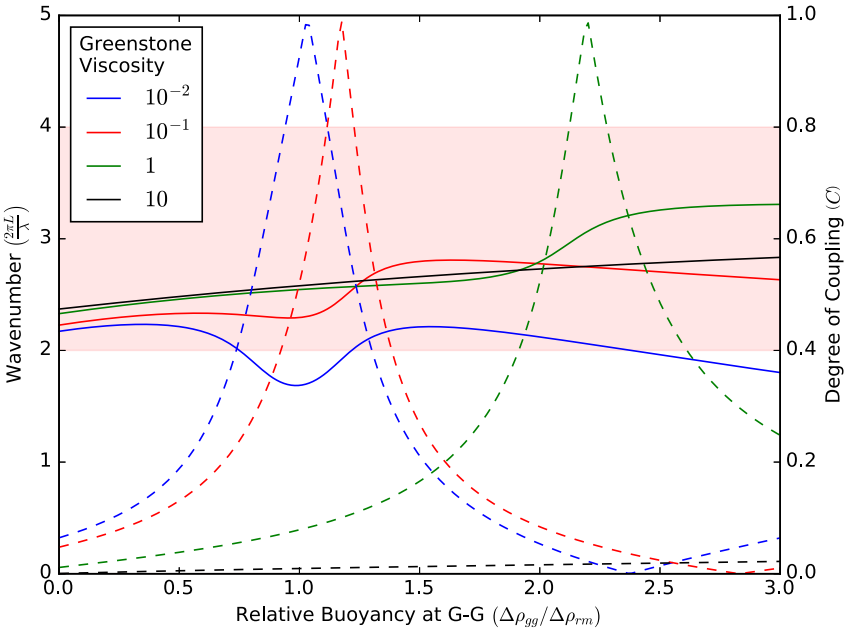

Figure 5.10: **A)** *The wavenumber (solid) and coupling (dashed) of the mode with the fastest growth-rate, depending on* $\Delta\rho'_{gg}$*. Identical to Fig 5.8, except the only the greenstone viscosity is varied, while the granitoid viscosity is constant with* $\eta'_c = 1$*. Provided the granitoid is the same viscosity as the restite, coupling can still occur. However, once the granitoid is stronger or weaker (not shown), coupling does not occur for any* η'_c*.* **B)** *Identical to A), but now the upper half of the greenstone has a viscosity* $10^3\times$ *that of the restite.*

Coupling can still occur when a strong upper crustal layer, representing the unserpentinised and brittle crust, is included (Fig. 5.11). In the case of a strong 'dry' restite, the upper greenstone crust can be set as $\eta'_c = 1$. Then the highest coupling occurs at $\Delta\rho'_{gg} = 2.2$,1.6 or 1.2, for $\eta'_c = 1$, 10^{-1} or 10^{-2}. The wavelength is highly sensitive to $\Delta\rho'_{gg}$ for $\eta'_c = 10^{-1}$, suddenly nearing the upper bound of $k_{obs.}$ with increasing $\Delta\rho'_{gg}$. The most plausible case is $\eta'_c = 10^{-2}$, for which $k_{obs.}$ is easily satisfied and $\Delta\rho'_{gg}$ is reasonable. This is also the case for a weak 'wet' restite, where the upper crust is set as $\eta'_c = 10^2$.

Finally, a coupled solution reproducing $k_{obs.}$ also exists for the presence of a layer of mantle lithosphere beneath the restite. The lithosphere must have a similar or lower viscosity than the restite. The former is less ideal, as the degree of coupling is lower and the wavelength more sensitive to $k_{obs.}$. Therefore the presence of a lithospheric layer which is stronger than the restite is not compatible with models of coupled instability growth.

A)

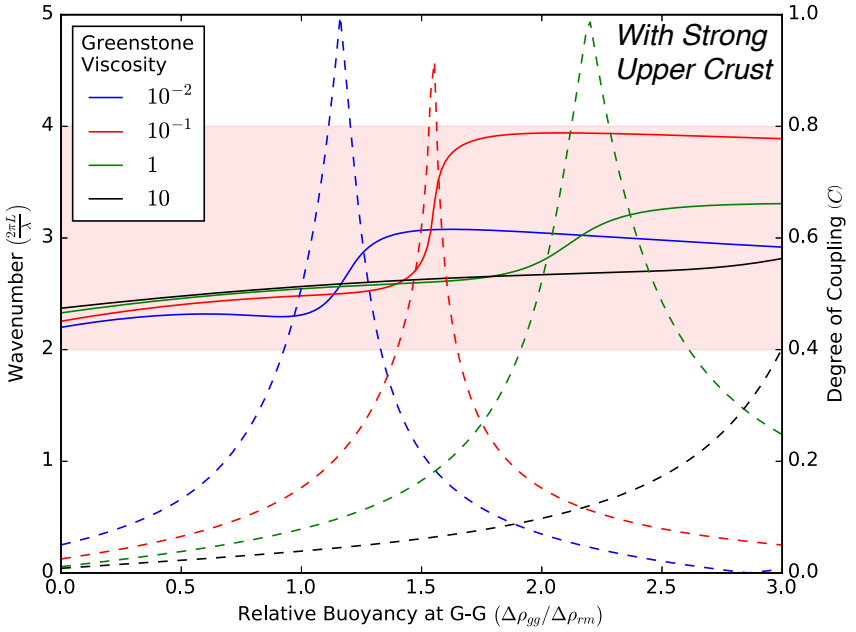

B)

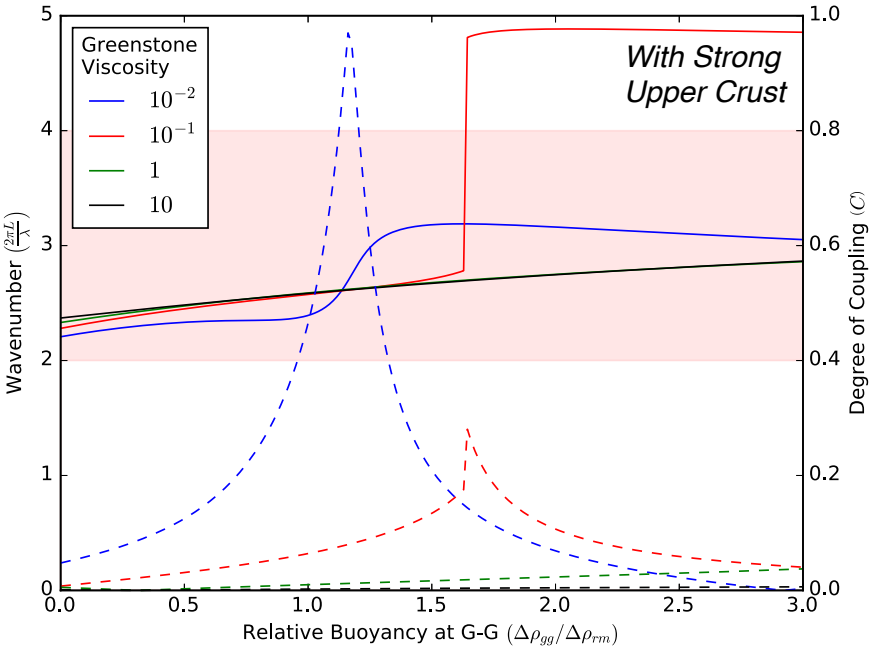

Figure 5.11: **A)** *Varying greenstone viscosity and granitoid set to* $\eta_c' = 1$*, identically to (Fig. 5.10) but now with a strong upper crust with* $\eta_c' = 1$*.* **B)** *Identical to A), but the strong upper crust is set to* $\eta_c' = 10^2$*.*

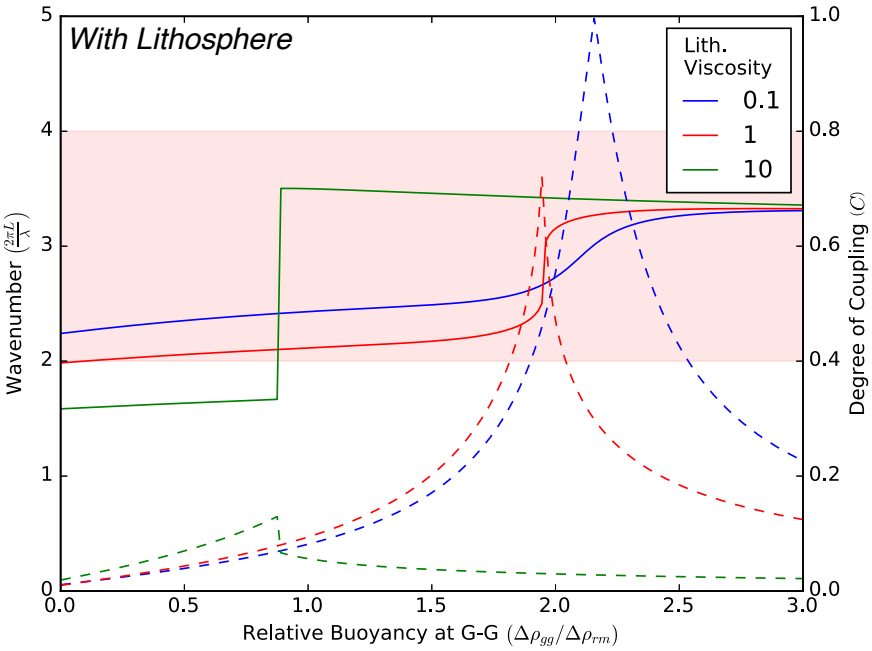

Figure 5.12: The wavenumber (solid) and coupling (dashed) of the mode with the fastest growth-rate, depending on $\Delta\rho'_{gg}$. Models are identical to the high coupling case from Figs. 5.8 and 5.9: $\eta'_c = \eta'_g = 1$, but now with a lithospheric layer of equal thickness to the granitoid and restite and a variable viscosity. A strong lithosphere prevents coupling.

The predictions based on the analytic small displacement solutions hold at high displacement. When solved numerically, both interfaces grow predominately at the same predicted wavelength and with the predicted relative time-scales (Fig. 5.6a). The fastest modes in the analytic solutions are also 'out of phase', which is confirmed numerically. Therefore where domes have risen in the crust, restite is likely to have sunk below in the coupled scenario. The zones of any increased heat-flow and melting resulting from rising mantle, are therefore predicted to occur in the keels.

5.5.2 Decoupled Instabilities

Instabilities are referred to as decoupled when the fastest growing mode results in the displacement of either the GG or RM interface, rather than both. There are decoupled solutions in which both instabilities grow at similar time scales, but at different wavelengths. These solutions are highly sensitive on $\Delta\rho'_{gg}$. Fig 5.13 shows a case where the GG interface grows at a wavelength within $k_{obs.}$, while the RM interface simultaneously grows at a much larger wavelength. Numerical solutions show that the these separate wavelengths are still dominating when the layers have doubled in thickness (Fig. 5.6b).

Regardless of which instability begins first, each interface should still deform at its corresponding

dominating wavelength, as $C \approx 0$. Therefore according to the analytic small displacement solutions, provided the wavelength of the fastest GG growth mode is in $k_{obs.}$, the dome-and-keel structures should form at the correct wavelength and not be affected by the RM growth. However, this is no longer true at high displacements (Fig. 5.14). Provided the granitoid is not significantly stronger than the restite (as discussed later), the initially decoupled restite will produce large wavelength deformation of the granitoid when it reaches high displacement. Subsequently, the domes are separated by a larger wavelength which is not predicted analytically and is outside of $k_{obs.}$. Parts of the granitoid are highly sheared as a result, though not every dome is sheared and so this prediction would be affected by the degree of preservation. This coupling at high displacement also occurs for the models which begin with a high degree of coupling, but both instabilities in that case occur at the same wavelength and so this affect would not be observable in the crust.

In the case that the upper half of the greenstone has a high viscosity as a result of its low temperature, the GG interface requires a much greater density contrast or a lower viscosity, in order to still occur at a similar time-scale to the RM interface instability. The latter is required to produce a wavelength in $k_{obs.}$. For example, if the greenstone is comprised of an upper and lower layer with $\eta'_c = 10^3$ and $\eta'_c = 10^{-2}$ respectively, a wavelength in $k_{obs.}$ can dominate and the $\Delta\rho'_{gg}$ required for simultaneous instabilities becomes achievable (Fig. 5.15).

As the crust has clearly halted its instability mid-overturn, solutions in which the dome-and-keel structures can form at a wavelength within $k_{obs.}$, while the restite is simultaneously sinking at wavelength, are of interest. The crust is still deformed at large wavelengths by the sinking restite when it reaches high displacements in the models, but the dome-and-keel may have halted by this stage.

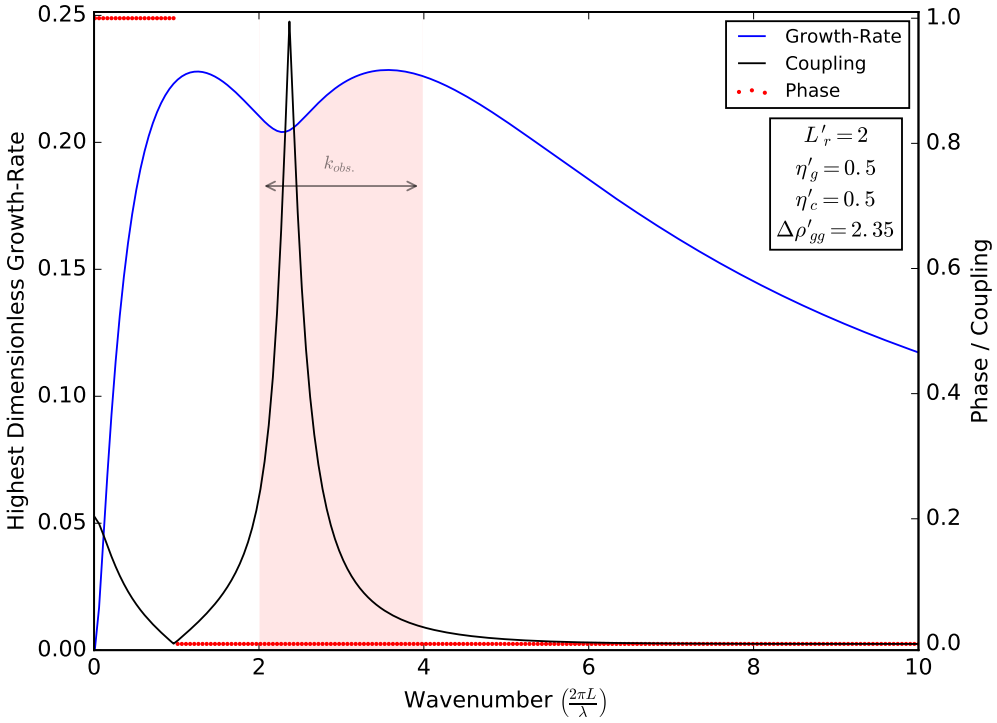

Figure 5.13: Growth-rate of the fastest mode, depending on wavenumber. η'_c, η'_g and L'_r are chosen in order to produce coupled flow and $\Delta\rho'_{gg} = 2.2$ is the relative buoyancy which produces the highest coupling, as shown in Fig. 5.8.

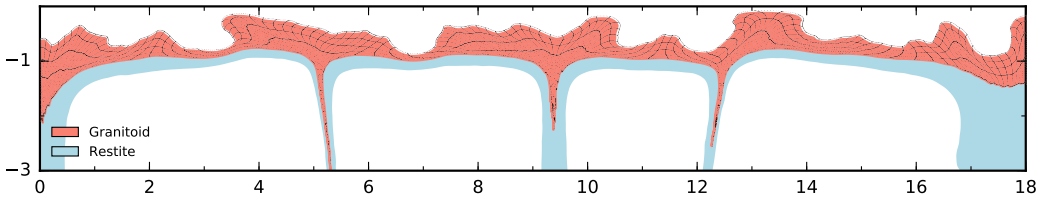

Figure 5.14: An example with the same parameters as Fig. 5.13: $L'_r = 2$ and $\eta'_g = \eta'_c = 0.5$, but with $\Delta\rho'_{gg} = 2$, which is low enough for RM to dominate, but close to the threshold. The sinking restite, as it reaches high displacement, has increased the spacing between the rising domes and overprinted some domes with a sheared fabric.

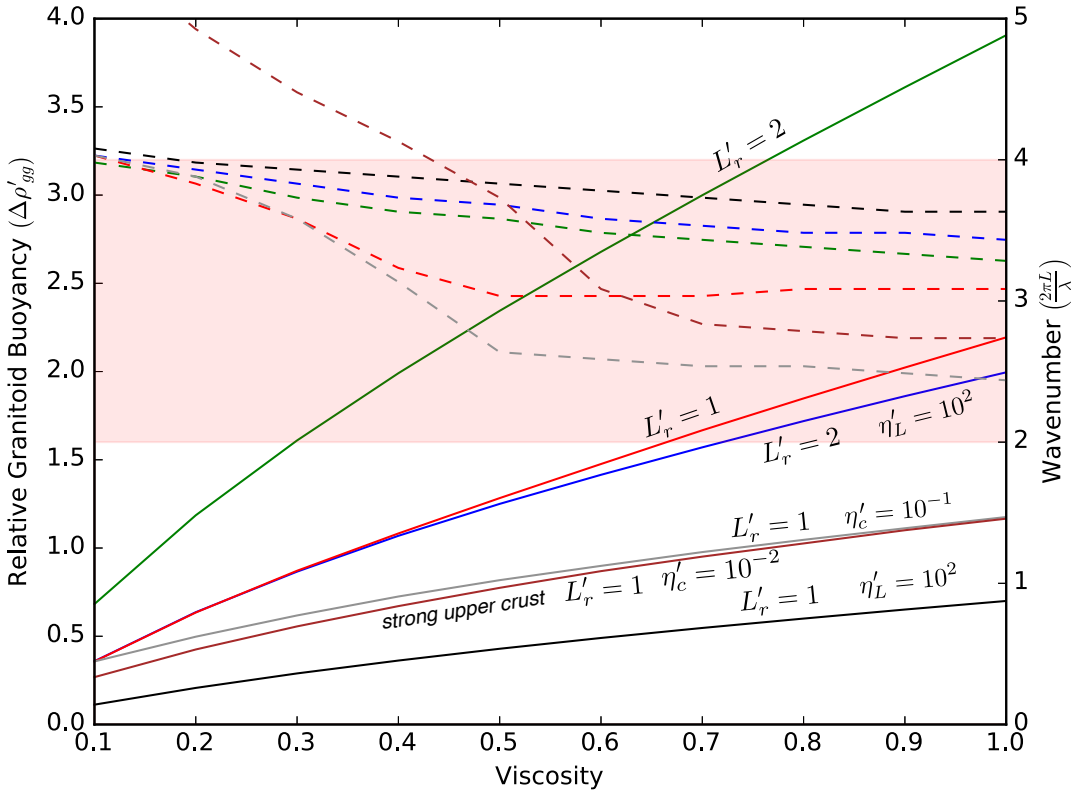

Figure 5.15: The minimum value of $\Delta\rho'_{gg}$ (solid) for the GG interface to grow more quickly than RM, as a function of the crustal viscosity. The varying crustal viscosity is for $\eta'_c = \eta'_g$, except for the two cases for which the greenstone viscosity (η'_c) is prescribed and only η'_g varied. Two curves also include a strong lithospheric mantle layer, $\eta'_L = 10^2$, beneath the restite. The curve labelled 'strong upper crust' includes the upper crustal layer with a viscosity of $1 < \eta'_c < 10^3$. The dominant GG wavelength is also shown (dashed). They plot within $k_{obs.}$ (shaded pink) for only a modest viscosity contrast.

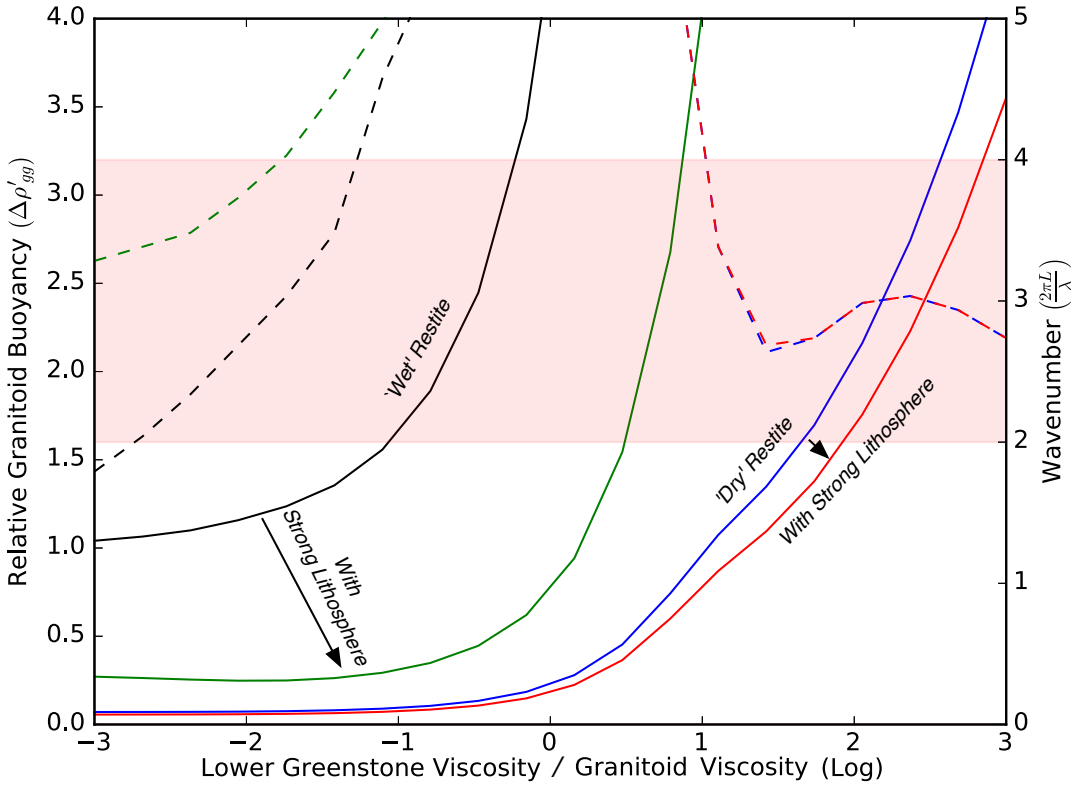

Figure 5.16: Threshold density $\Delta\rho'_{gg}$ (solid), as in Fig. 5.15, for a strong upper crust ($\eta'_c = 10^2$, relative to the granitoid) and a restite which is either the same viscosity as the granitoid (wet) or stronger (dry, $\eta'_g = 10^{-1.5}$). The lower greenstone viscosity is varied relative to the granitoid, to demonstrate the maximum viscosity allowed for the dome and keel instability to dominate (left of the curve) as well as the correspond wavenumber (dashed). A dry, stronger restite allows dome and keel formation to dominate, but requires the lower greenstone to be relatively stronger to reproduce $k_{obs.}$. The presence of a strong lithosphere ($\eta'_L = 10^2$) is also shown and plays a larger role when the granitoid and restite are of similar viscosity.

The viscosity contrast between the granitoid and restite significantly influences which instability grows more quickly. Where the restite is a similar viscosity to the granitoid ('wet' restite), the restite instability dominates unless the lower greenstone viscosity is low, $\eta'_c < 10^{-1}$ (Fig. 5.16). This example assumes that the upper crust is strong, with $\eta'_c = 10^2$ for a 'wet' restite and $\eta'_c = 1$ for 'dry'. A small lower greenstone viscosity, $\eta'_c < 10^{-1.5}$, is also required in the 'wet' restite case for the domes to form with a wavenumber within $k_{obs.}$. For a relatively strong 'dry' restite, the dome and keel instability can easily dominate. However, the $k_{obs.}$ constraint is no longer reproduced, unless the lower greenstone is strong enough, $\eta' > 10$, that the dome and keel is slowed down and the two instabilities occur at a similar time-scale. The simultaneous instabilities in this 'dry' restite case would grow at a time-scale controlled by the higher viscosity, equivalent to the upper crust, therefore evolving more slowly than observed. Additionally, it would require the granitoid to be the weakest layer in the crust.

The presence of a strong lithosphere ($\eta'_L = 10^2$) allows the dome and keel instability to dominate, while still reproducing $k_{obs.}$ (Fig. 5.16). This is because the restite is weak enough to allow the granitoid to flow, but the restite instability is slowed down by the viscous lithosphere. Where the restite and lithosphere have equivalent viscosities, as in the 'dry' restite case, the lithosphere has a negligible impact on instability competition.

5.5.3 Conditions for Overprinting

If the restite sinks much more quickly or slowly than dome-and-keel formation occurs, then the wavelength of the dome-and-keel structures are altered to differ from $k_{obs.}$ and/or an additional strain fabric may be observed in the preserved granitoid (Fig. 5.14). If the granitoid was sufficiently stronger than the restite however, strain could have partitioned into the sinking restite and not the granitoid. This was quantified by calculating the average strain in the granitoid when the restite had reached high displacement, for a variety of relative crustal viscosities and restite thicknesses (Fig. 5.17). The sinking restite strains the granitoid predominately at high displacement. This strain reduces significantly when the crust is only one order of magnitude more viscous than the restite and would be unlikely to be evident in the preserved material. In the models, the strain is negligible once the crust is two orders of magnitude stronger. The thickness of the restite alters the dominant instability wavelength, but produces little difference in granitoid strain. Therefore, in the case that the dome-and-keel structures formed first, their original fabric could be preserved provided the restite is an order of magnitude weaker by the time it sinks to a significant displacement. Likewise, if the restite was recycled first, a strong granitoid would be unaffected.

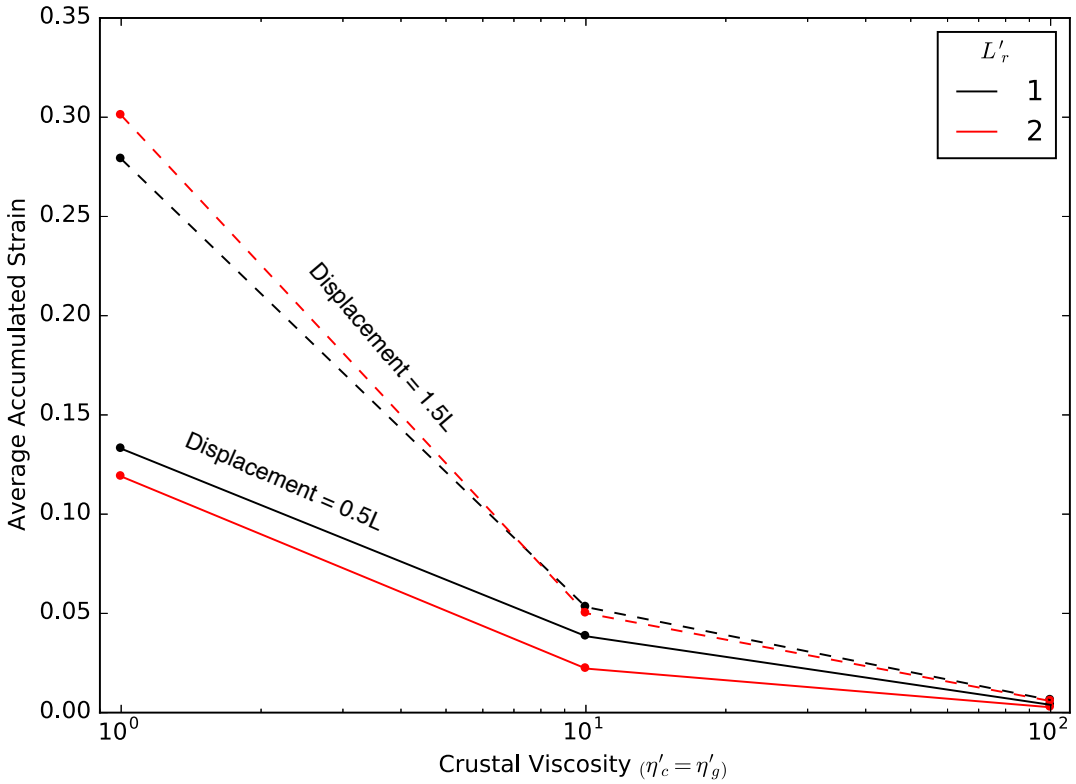

Figure 5.17: Average accumulated strain throughout the granitoid, as a function of crustal viscosity, where $\eta'_c = \eta'_g$. $\Delta\rho'_{gg}$ *is set to zero, so that any strain is a result of flow at the RM interface. Six numerical models are used, as the strain is measured at high displacement. Accumulated strain is measured as the second strain-rate invariant, integrated over each time-step. This is measured when the RM interface has been displaced by an amount equivalent to the initial granitoid thickness (*0.5L*) and then* 3$\times$ *this thickness (*1.5L*). The strain is highly sensitive to the crustal viscosity and less so to the restite thickness which calculated for* $L'_r = 1$ *and* $L'_r = 2$.

5.5.4 Isolated Restite Recycling

Strengthening the crust slows down the dome and keel instability and allows restite recycling to comparatively dominate, but the latter may still be slowed down. Additionally, it was previously shown that a strong lithosphere can slow down the restite instability enough to allow dome and keel to dominate, but it is of interest to know whether the restite can still be recycled on geologically relevant time-scales. The dependence of restite recycling on crustal and lithospheric strength is analysed in isolation, setting $\Delta\rho'_{gg} = 0$ and varying the strength of a reference crustal rheological profile and a lithospheric layer (Fig. 5.18). In this comparison, the restite instability would occur at a similar time-scale to the dome and keel instability, for the reference crustal rheology and $L'_r = 1$, which can be taken as a reference time-scale.

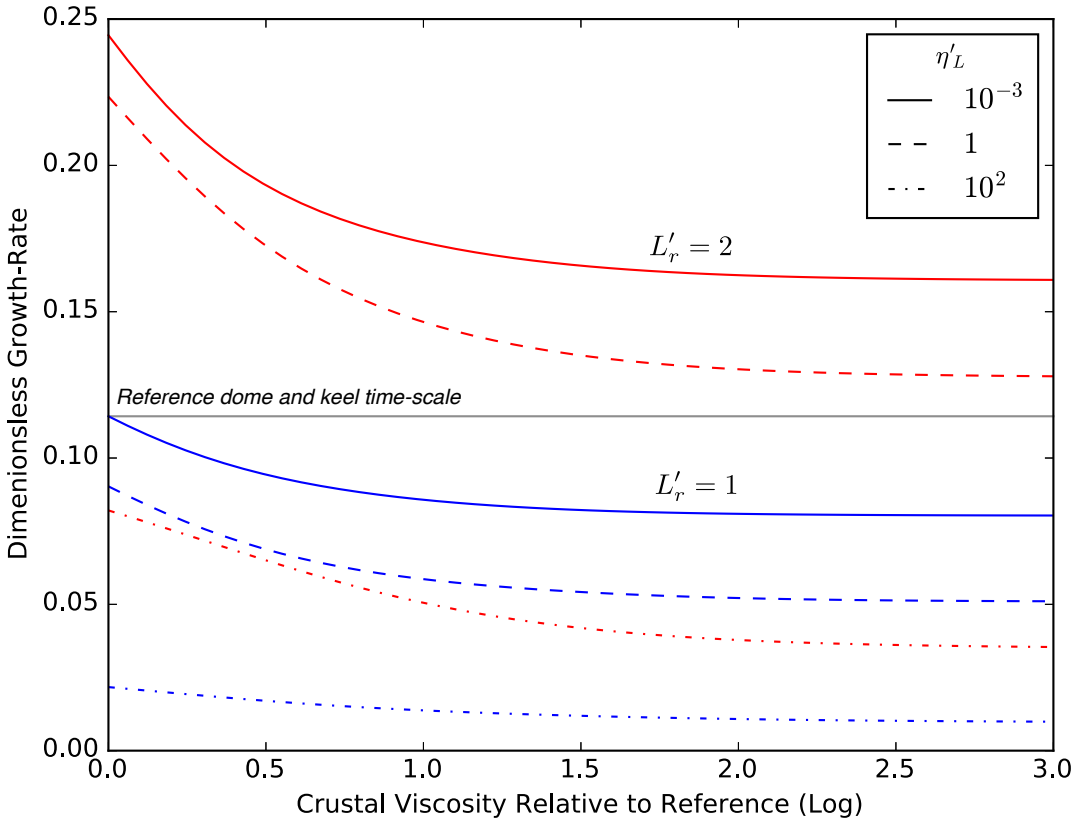

Figure 5.18: Growth-rate of the restite instability, for varying crustal strength. The reference viscosity profile is taken as $\eta'_c = 10^2$ and $\eta'_c = 10^{-2}$ for the upper and lower greenstone layers, while the granitoid is set to $\eta'_c = 1$. This whole profile is strengthened by up to three orders of magnitude. The lithosphere, which is a layer of $1L$ thickness beneath the restite, is varied from $\eta'_L = 10^{-3}$, representing no lithosphere, and $\eta'_L = 10^2$, a lithosphere which is significantly stronger than the restite. It is assumed that $\Delta\rho'_{gg} = 0$, so that the growth-rate is a slight over-estimate, but should vary in the same way. The thick restite case, $L'_r = 2$, is also shown to demonstrated the competition between higher negative buoyancy and a strong lithosphere. The reference time-scale (grey) shows the scale at which the dome and keel instability grows when the reference viscosity profile is generated.

Strengthening the crust slows down restite recycling by $\sim 30\%$. Therefore strengthening the crust can effectively halt the dome and keel instability, but restite recycling still occurs at the same order of magnitude, though taking $\sim 1.5\times$ longer than it would with a weaker crust. The presence of a strong lithosphere has a larger impact, causing the restite to take approximately $2\times$ or $10\times$ longer if the lithosphere is the same strength as or $10^2\times$ stronger than the restite respectively. This significant slowing for $\eta'_L = 10^2$ can be compensated for by a thicker restite, as increasing the restite thickness to L'_r results in a restite which only takes $3\times$ longer than the reference. Therefore for example, the dome and keel instability time-scale can be assumed to be 10Ma. A strong lithosphere would prevent the restite from being recycled at any less than the 100Ma scale. However, progressive melting doubles

the restite thickness, this reduces to $\sim$ 30Ma.

5.5.5 Isolated Dome and Keel

In the event that the restite has been recycled much before or after dome-and-keel formation, the formation of the latter would be an isolated instability. The subsequent dynamics still depend on the crustal boundary conditions and relative viscosity between the greenstone and granitoid. Figure 5.5 shows that in the case that the granitoid and greenstone layers have similar viscosity, this viscosity should be similar to that of the restite, $\eta'_c = \eta'_g \approx 1$, in order to produce a wavelength in $k_{obs.}$. However, if the greenstone and granitoid layers have differing viscosities (Fig. 5.19), the $k_{obs.}$ criteria could be met for any η'_g. The most convenient solution is for $\eta'_c/\eta'_g = 10$, in which case the granitoid could be any viscosity relative to the restite and still produce a wavelength in $k_{obs.}$. The greenstone is unlikely to be more than two orders of magnitude stronger than the granitoid, as the wavelength is then larger than $k_{obs.}$, regardless of η'_g. Overall, either the granitoid is required to be a similar viscosity as the restite or higher, unless the combination of $\eta'_c/\eta'_g \approx 10$ occurs. It is therefore plausible that the dome-and-keel structures formed in isolation from other processes and the observed wavelength is what is expected when there are no extreme viscosity contrasts.

In the case that there is a strong upper crust (Fig. 5.19b), many of the viscosity configurations just described no longer produce a wavelength in $k_{obs.}$. In this case the greenstone is required to be much weaker than the granitoid, the orders of magnitude $\eta'_c = 10^{-2}$ or 10^{-3}. The granitoid is also required to be slightly weaker than the restite, or it can be stronger if close to $\eta'_c/\eta'_g = 10^{-2}$. These solutions are highly sensitive to the viscosity contrasts in the crust, so if the upper crust was significantly stronger than the lower crust, the preserved domes would be required to have formed with very similar rheological profiles.

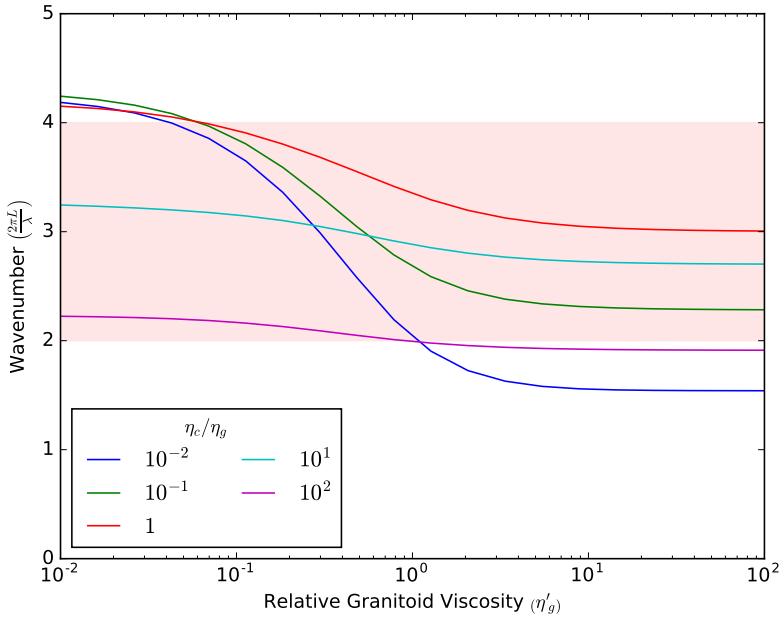

Figure 5.19: Dominant wavenumber for varied granitoid viscosity, η'_g, assuming that the GG instability dominates and that the RM density contrast is negligible. Depending on the ratio of greenstone to granitoid viscosities, η'_c/η'_g, there is a wide range of granitoid viscosities which produce a wavelength in k_{obs}..

A)

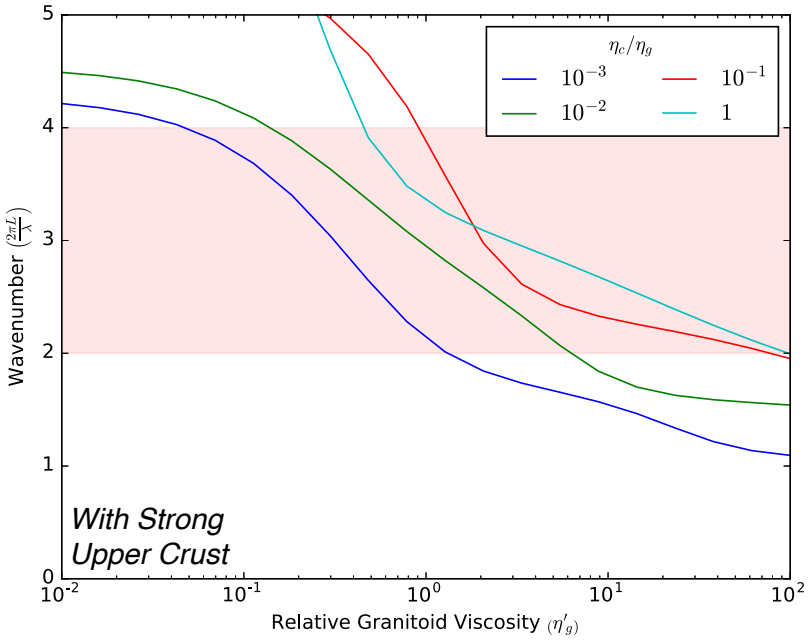

B)

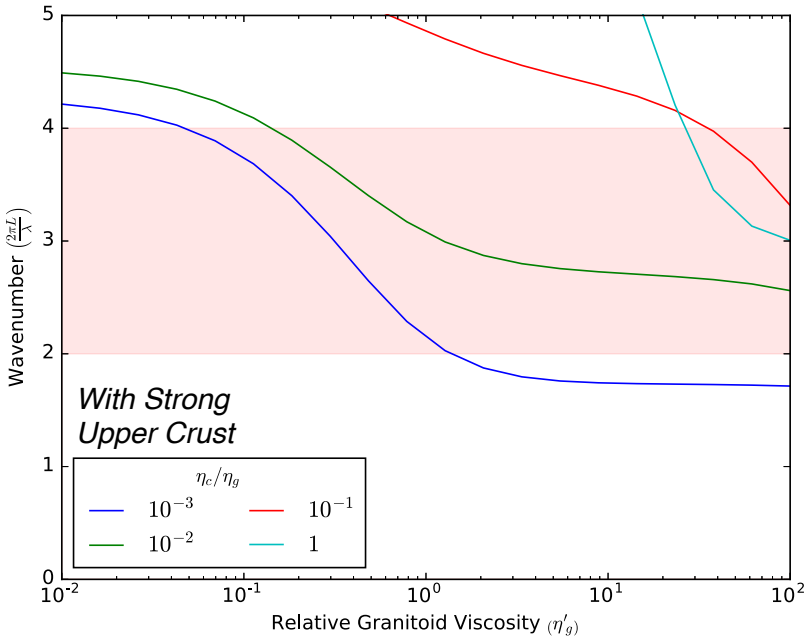

Figure 5.20: **A)** *Identical to (Fig. 5.19), but with an upper crustal layer of viscosity* $\eta'_c = 1$ **B)** *Identical to (Fig. 5.19), but with an upper crustal layer of viscosity* $\eta'_c = 10^2$

5.5.6 Dynamic Influence of Partial Melt at the Base of the Granitoid

Weakening of the lower half of the greenstone layer, plausibly generated by serpentinisation and plasticity, has been shown to be important for generating dome-and-keel instabilities with wavelengths which agree with observation and grow at a similar rate to recycling of the restite below. Previous dome-and-keel modelling has placed much importance on the presence of a weak melt-rich layer at the base of the granitoid (Thébaud & Rey 2013). The implications of such a layer for the growth-rate and dominating wavelength of the dome-and-keel instability is quantified here by adding a melt-rich layer in the analytical models (Fig. 5.21). The melt-rich layer is assumed to encompass the lower half of the granitoid, in order to give a conservative estimate of its influence. A model without any weak layers, but with a strong upper crust ($\eta'_c = 10^2$ as earlier), is included as a reference. Reducing the viscosity of the lower greenstone layer by two orders of magnitude results in generation of the correct wavelength and approximately a 4$\times$ increase of the growth-rate. This represents the triggering effect that weakening of the greenstone layer has, shown earlier in Fig. 5.16.

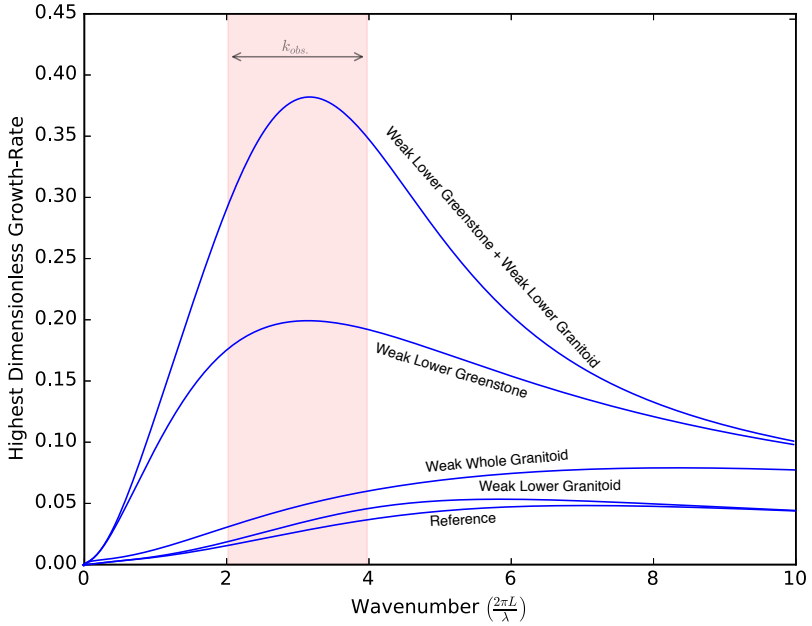

Figure 5.21: Dome-and-keel growth-rate τ' as a function of the wavenumber k', for cases with and without weakening of the lower granitoid and/or the lower granitoid. This shows the dynamic effects of serpentinisation and/or yield in the greenstone, compared to the presence of partial melt in the lower half of the granitoid. The reference model assumes that $\eta'_g = 1$, the upper half of the greenstone layer to $\eta'_c = 10^2$, the lower half of the greenstone layer to $\eta'_c = 1$ and $L'_r = 1$. Including a weak lower greenstone involves setting the lower half of the greenstone layer to $\eta'_c = 10^{-2}$. A weak lower or whole granitoid involves setting the lower half or whole granitoid layer respectively to $\eta'_g = 10^{-2}$.

The presence of a weak ($\eta'_g = 10^{-2}$) melt-rich layer in the lower half of the granitoid has a negligible

effect on the growth-rate and generates domes of a much smaller wavelength than observed (Fig. 5.21). Decreasing the viscosity of the melt-rich layer further or assuming the entire layer has been weakened both have a negligible effect. This is because the dome-and-keel instability is dominantly controlled by the viscosity of the greenstone layer, due to its proximity to the free-slip boundary condition. The focus on the greenstone rheology in this study and in Robin & Bailey (2009) is therefore justified.

If it is assumed that the lower greenstone layer has been weakened, then the combination of partial melt at the base of the granitoid layer does significantly increase the instability growth-rate (Fig. 5.21). Melting therefore does help to speed up the dome-and-keel instability, but does not have the important control on triggering instability onset at the correct wavelength that the greenstone rheology has.

5.6 Discussion

During dome and keel formation, it is plausible that restite was being recycled below at a similar time-scale. This is based on reasonable estimates of rheology and density contrasts. The analysis has shown that the final part of the restite can be removed from below a weak crust, without leaving superimposed strain, due to the simultaneous operation of two coupled instabilities occurring at the same wavelength. In this case the preserved dome and keel structures record the complete fractionation of the crust: generation of a felsic upper crust and removal of anomalously dense lower crust. On the modern Earth, this fractionation occurs and is required for crustal stability (Sandiford 2010), but it is likely to be facilitated by tectonics. For example in the western USA, partial melting has generated the Sierra Nevada batholith and a layer of restite below (Saleeby et al. 2003). The batholith has been transported to the upper crust through micro-plate tectonics and dynamic uplift, while localised extension at its eastern margin has destabilised the restite, allowing it to be rapidly recycled. The model of simultaneous restite recycling and dome and keel formation is an equivalent mechanical fractionation process which can occur in the absence of tectonics, as is expected for the Pilbara and Kaapvaal cratons (Van Kranendonk et al. 2007). Therefore the similarity between Archean and modern stable crust; both generally have a felsic upper crust and a net positive buoyancy, is the result of these equivalent processes operating in different tectonic regimes, but resulting in the same crustal reorganisation at a similar time-scale.

Part of the difficulty in estimating the relative time-scale of restite removal is the uncertainty in restite rheology, compared to more common crustal rocks. As the restite is assumed to be in direct contact with the granitoid base, a result of intra-crustal rather than lithospheric mantle partial melting, it influences dome formation. A crustal rheology of strong upper crust and weak greenstone, relative

to the granitoid, has been inferred based on experimental data and thermal modelling Robin & Bailey (2009). The analytic models here support this rheological profile, as it is the only configuration with a strong upper crust which can generate dome wavelengths within $k_{obs.}$. Using this profile, the restite is required to have a similar viscosity to the granitoid during dome and keel formation. The 'wet' pyroxenite rheology therefore better describes the restite dynamics, as a result of possibly a mixture of the presence of melt and the thermal blanketing effect required to weaken the crust generally (Sandiford et al. 2004; Robin & Bailey 2009).

The restite and dome and keel instabilities are triggered or halted when differing rheological criteria are satisfied. Dome and keel formation is highly sensitive to the strength of the lower greenstone crust. Sandiford et al. (2004) demonstrated that the thermal blanketing of the granitoid with its high heat-production, by a rapidly erupted, thick greenstone layer, would heat up the middle crust and reduce its viscosity by two to five orders of magnitude or even more if partial melting is considered. The weakening of the granitoid layer has been considered as the triggering condition for dome-and-keel initiation (Sandiford et al. 2004; Thébaud & Rey 2013). Our small amplitude instability calculations however show that growth is most sensitive to the viscosity of the lower greenstone and weakening of the granitoid would have a negligible impact without this. If the greenstone begins with a viscosity approximately equivalent to the restite and granitoid, once it weakens by two orders of magnitude, there is a significant increase in its growth-rate, which can effectively initiate dome and keel formation. This weakening could also be triggered by the emplacement of a thick cover. While the viscosity of serpentinite is not particularly temperature-dependent (Hilairet et al. 2007), it switches from brittle to ductile failure at about 0.1 *GPa* (Reynard 2013), which corresponds to the base of the greenstone cover. Ductile flow could then drive stress build-up and plastic failure in the upper brittle part. The heating of the middle-crust may plausibly have occurred simultaneously as the greenstone cover was deposited, which would result in the melting and weakening of the granitoid layer, which would still contribute to accelerating the dome-and-keel growth-rate.

The strength of the middle crust has little effect on restite removal, so continuous recycling could occur while the granitoid becomes further chemically evolved and the greenstone cover thickens. Even though a large volume of restite is required to generate the granitoid layer, melting could be progressive without the restite layer thickening beyond $L'_r > 1$. The restite is however sensitive to a strong lithosphere, becoming trapped, while dome and keel formation occurs unaffected. A strong lithosphere is predicted by the stagnant lid convection model (Moresi & Solomatov 1995; O'Neill et al. 2007). In the case of trapping by strong lithosphere, the restite layer would be likely be required to grow, by continual melting, to twice the thickness of the granitoid layer. It could subsequently still be recycled at a time-scale of the same order of magnitude as dome and keel formation. Alternatively, as melt would be required to migrate through any lithosphere to produce crustal melting, the lithosphere could

be weakened to a similar or lower viscosity than the restite and allow recycling.

The lack of an extremely thick restite, for example $L'_r = 2$, present during dome and keel formation is also supported by the dome wavelengths and lack of significant overprinting. The thick restite layer would impart a large wavelength shear strain on the domes as it sinks. A restite layer of that thickness would not be stable at a time-scale longer than dome and keel formation, unless it was significantly more viscous, which appears unlikely as discussed. Alternatively, a weak restite layer may have been trapped beneath the granitoid, by strong lithosphere. In this situation, it could have been recycled at a later time of lithospheric weakening and by which time the crust had strengthened, preventing overprinting.

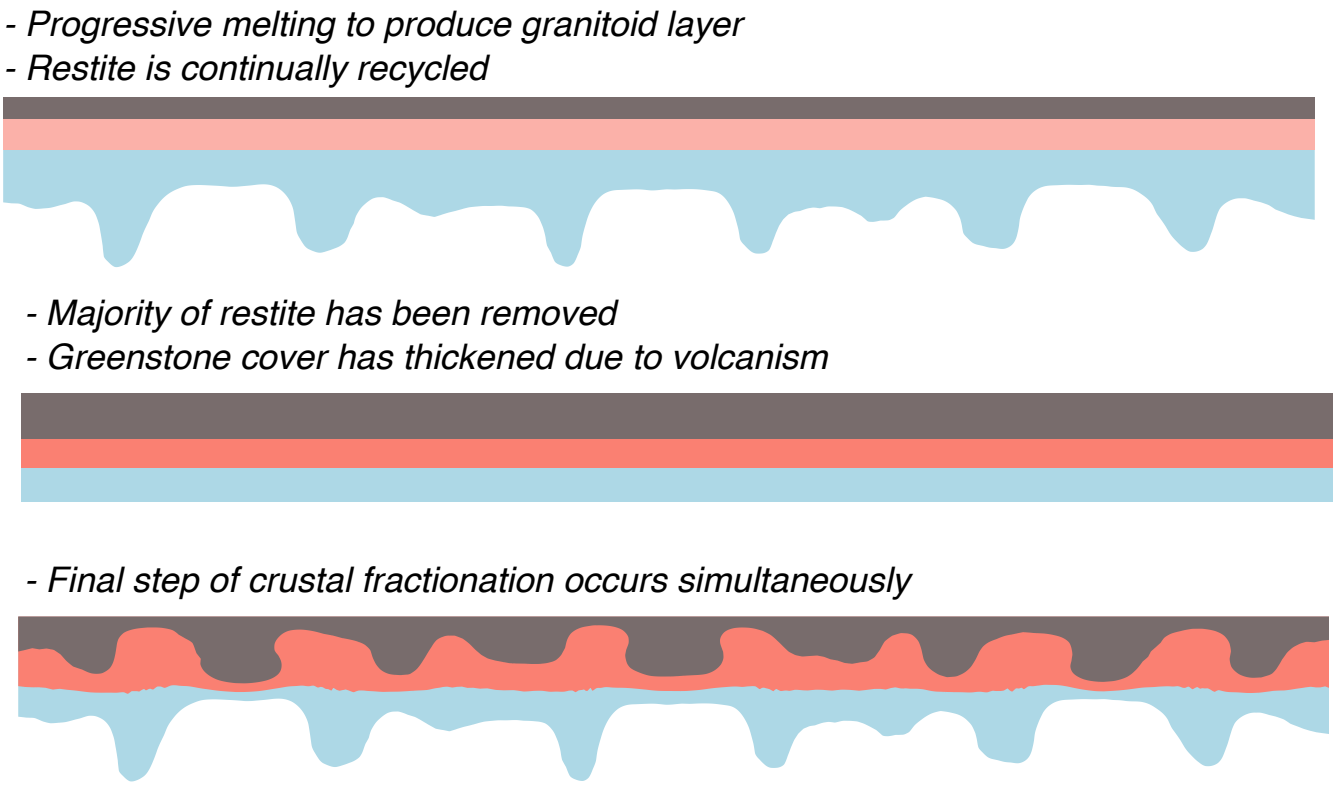

Figure 5.22: A plausible crustal evolution following three stages. Initially the restite (blue) can progressively be recycled from below a strong crust. The crust, particularly the base of the greenstone layer (grey), eventually weakens and triggers dome (red) and keel formation. Any remaining restite can sink simultaneously.

The general conceptual model in Fig. 5.22 can describe the crustal fractionation stages while satisfying the various inferences of relative instability time-scales. As dome and keel formation requires a thick greenstone cover to generate significant negative buoyancy and reduce the mid-crustal viscosity, its initial absence is likely to result in a granitoid lower crust which is stable at the 100Ma scale. This does not prevent restite recycling, which can occur continually in order to process the large volume required to extract enough melt to form the granitoid layer. Restite recycling is likely to occur at the 10Ma scale, sinking when reaching $L'_r = 1$, or $L'_r = 2$ in the case of a strong lithosphere below. As the

crust is stronger than the restite, it does not record strain from these sinking events. By the time at which both a thick cover and a highly fractionated granitoid layer have formed, the layers satisfy the initial conditions for $L'_r = 1$, or the restite may have been completely recycled. Then any last part of the restite can drip while the domes simultaneously rise. Alternatively a small volume of weak restite may have been trapped by the lithosphere and would require some lithosphere weakening event to be recycled. This model is similar to the geochemically motivated conceptual models of Bédard (2006) and Johnson et al. (2014), but is instead motivated by the instability dynamics implied by the preserved dome and keel structures.

5.7 Conclusion

The interaction and relative time-scales of intra-crustal (dome and keel) and lower crustal (restite) instabilities have been analysed using analytic Rayleigh-Taylor Instability models. Generally, dome and keel formation and restite recycling can plausibly occur at similar time-scales and at the same wavelength, as the result of one coupled instability. In order to reproduce the observed dome wavelengths, the lower greenstone viscosity is required to be significantly weaker than the granitoid, which in turn is required to have a similar viscosity to the restite. The former condition acts as a trigger for dome and keel formation, whereas the strength of the lithosphere has the same effect for the restite. Restite removal can plausibly occur continuously, while progressive intracrustal melting occurs, before the last part is potentially removed simultaneously with dome and keel formation. The wavelengths and local buoyancy dominated strain of the preserved dome and keel structures do not preclude high volume recycling below, of which the instability growth time scale can be inferred from time scale constraints on dome and keel formation.

5.8 Supplementary Data: Free-Slip Approximation

The models have approximated that the Earth's surface has a free-slip condition, which assumes that the shear-stress vanishes and the vertical velocity is zero. This assumption allows a non-zero normal stress at the surface, which is typically justified because this would be balanced isostatically by the dynamic topography which is also neglected from the model. In modelling Rayleigh-Taylor Instabilities, there is the additional justification that stabilising density contrast at the surface is much greater than the unstable density contrast at depth. The latter subsequently behaves as if there were a zero vertical velocity condition at the surface. This effect is calculated analytically using a model with a free surface

(Fig. 5.23). Provided the density contrast between air and rock is at least $10\times$ $\Delta\rho'_{gg}$, a free-slip boundary condition is a good approximation.

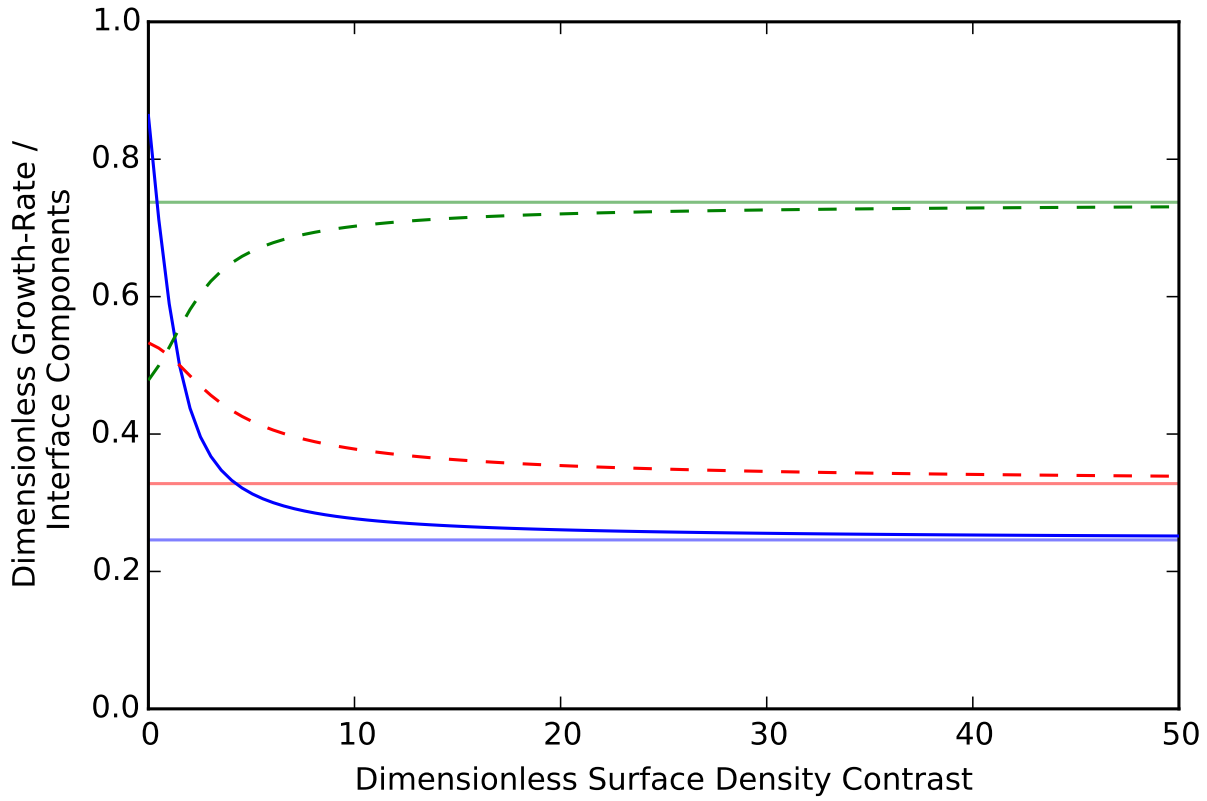

Figure 5.23: Comparison between free-surface fastest growth-rate (solid) and interface vector contributions (dashed) for $k' = 2$. The faint lines are the free-slip solutions and the red and green lines are the GG and RM contributions. Calculations were for $\rho'_g = 1$, $L'_r = 1$, $\eta'_c = 1$ and $\eta'_g = 1$.

Chapter 6

Formation of Cratonic Keels During the Initiation of Plate Tectonics

6.1 Summary

Preserved Archean crust is typically underlain by anomalously thick lithosphere, formed through a process which is arguably not analogous to modern lithosphere thickening processes. A new mechanism is proposed in which strong continental material formed at a shallow depth ($<$ 80 km) in a stagnant lid convective regime and was thickened to $\sim$ 300 km during a pulse of rapid and high stress lithospheric recycling when plate tectonics initiated. The stress magnitude experienced by the keel during the lid breaking event is at least four times higher than during the subsequent mobile lid convection (plate tectonics). As a result of this anomalous stress, the strong depleted lithosphere can have an order of magnitude higher yield strength than allowed for mobile lid thickening models, while being able to thicken. The lid breaking event can therefore allow the lithosphere to be extremely strong before formation, without requiring the complex strengthening mechanisms needed for thickening by subduction. The keel stresses experienced during mobile lid immediately after lid breaking can be scaled for a cooling mantle. For an order of magnitude decrease in Rayleigh number over the last 3Ga, the keels are expected to still be stable. A weakening event is required to destroy keels in this case. Alternatively, a Rayleigh number decrease of two orders of magnitude results in keels which are no longer unconditionally stable and require buffering by mobile belts or strengthening events. A record of the stress at subduction zones, using crustal thickness through time as an analogue, indicates that subduction stress rapidly increased after the initiation of tectonics, but peaked 1Ga ago at 75% of the keel formation stress state. The comparison of calculated lid breaking stress and the recorded peak stress therefore predict that keels are

stable, unless significantly weakened, which is consistent with the link between volatile influx and keel destruction observed beneath North China and North America. Additionally, geological predictions arise from the keel formation models which can be tested. The middle-crust of Archean terranes is typically exposed, requiring an exhumation event, but often without significant crustal deformation in the case of Paleoarchean terranes. This exhumation may record the keel formation event, as once the keel has thickened and the dense mantle lid breaks off, the models predict a rapid uplift of ~ 10 km. The large scale compressional regime during keel formation may be responsible for the thrusting observed for crust which was plausibly weak, therefore partitioning strain, at a similar time to the onset of tectonics.

6.2 Introduction

Preserved Archean and Early Proterozoic crust is often underlain by anomalously thick mantle lithosphere ($<$ 300km), called the cratonic keel (Jordan 1975; Polet & Anderson 1995; Artemieva & Mooney 2001) which generally formed at a similar time to the crust (Griffin et al. 2003). These keels appear to be a fundamental feature of ancient, stable regions, but how they formed is still unclear. It is likely that there is no modern analogue process, as keels generally only formed during the Archean and modern lithosphere is significantly thinner and less depleted. Melting during lithosphere formation occurred at shallow depths (Lee et al. 2006) and therefore a thickening process is required. Subduction is able to thicken lithosphere on the modern Earth (McKenzie & Priestley 2008) and a similar process has been proposed for keel formation (Jordan 1988; Cooper et al. 2006). We will argue however that the process which thickened the cratonic keels is unlikely to have been analogous to modern subduction-related thickening. An alternative source of negative buoyancy is the collapse of the stagnant lid, during the onset of plate tectonics. Early Earth convection is likely to have occurred by some form of stagnant lid (Moresi & Solomatov 1995; Solomatov & Moresi 2000). Stagnant lid convection involves the formation of a thick thermal boundary layer. Models of the transition from stagnant lid to mobile lid (tectonics) convection (Van Thienen et al. 2004; O'Neill et al. 2007; Moore & Webb 2013) typically involve the rapid recycling of this entire boundary layer during the switch to mobile lid (tectonics). We hypothesise that the recycling of the stagnant lid provides a pulse of boundary layer convection which can thicken depleted peridotite into the thick keels. Additionally, we hypothesise that this keel formation event involved a high keel stress-state, due to coupling between the boundary-layer and keel, which has not reoccurred, therefore ensuring keel stability.

6.2.1 Arguments Against Keel Formation by Subduction

The most significant continental thickening on the modern Earth occurs at subduction zones, during continental collision. For example, during the Indian-Eurasian collision, the lithosphere beneath the Tibetan Plateau has been thickened to 260 km (McKenzie & Priestley 2008). However, there are primarily two issues with using modern collision as an analogue for keel formation. Firstly, subduction occurring in the late Archean is likely to be localised and episodic. Subducting slabs tear more quickly in a hotter mantle and subsequently are not attached to the overriding lithosphere for long enough to produce significant thickening (van Hunen et al. 2002; van Hunen & van den Berg 2008). This limits Archean thickening by subduction to smaller thicknesses than analogous to the Tibetan plateau. Keel thickening has occurred over the 1000 km scale, which is indicative of either a widespread or long-lived thickening process, of which episodic subduction is neither.

Secondly, subduction is likely to be capable of applying higher stresses to the continental lithosphere over time. A cooling mantle increases in viscosity and therefore applies greater stresses to the keels over time (O'Neill et al. 2008; Sandu et al. 2011). An increase in stress at subduction zones can also be inferred for the period of $3 - 1$ Ga. The changing Rb / Sr signature of magmatic rocks through this period is indicative of a $2\times$ increase in crustal thickness at subduction zones (Dhuime et al. 2015), which requires a general increase in the negative buoyancy of subducting slabs over time.

When keels first stabilise, the plastic and buoyancy stress they can resist is in equilibrium with the stress transmitted from the negative buoyancy of the sinking slab. This is a similar argument to Cooper et al. (2006) and elaborated upon later. It follows that if their plastic strength and buoyancy do not change, a return to this stress state will produce further deformation (Fig. 6.1). Further deformation should then occur once there is even a slight increase in convective stress and keel stability would depend fortuitously on the stress buffering of mobile belts (Lenardic et al. 2000).

The secular increase in mantle convective stress does not disprove the model of keel formation by subduction, but requires ad-hoc complexity in that an additional strengthening mechanism, which balances the stress increase, is required. Additionally, there must also be reason as two why keels predominately formed in the Archean, when this was a relatively low stress environment and the conditions for thickening have become increasingly favourable over time. The simplest solution to these issues is to investigate the possibility of a non-uniformitarian process which was more efficient at thickening lithosphere and only operated in the Archean.

6.2.2 Recycling During Stagnant Lid Collapse

The transition from stagnant lid to mobile lid convection is likely to involve the rapid recycling of a large volume of thermal boundary layer (Moresi & Solomatov 1998; O'Neill et al. 2007). This is the case whether the lid breaking event is the result of a cooling mantle or large scale eclogitisation (Van Thienen et al. 2004). It is possible that parts of the lid may survive if these transition models were to be reproduced in 3D, though this would only lead to the preservation of small volumes which would be dense enough to sink at a later time. Plate tectonics is likely to have initiated during the late Archean (Van Kranendonk et al. 2007; Dhuime et al. 2012), though crust is clearly preserved from this time and older (Condie et al. 2009a). We hypothesise that fragments of crust and lithosphere were sufficiently buoyant, as a result of chemical evolution, to remain at the Earth's surface during the lid breaking event. This is following a similar argument for why cold continents resist sinking on the modern Earth, though an even lower density may be required for the continents to be in isostatic equilibrium with over thickened boundary layer rather than just the asthenosphere.

Estimates of continental volume over time support the hypothesis that a large volume of the lithosphere was rapidly recycled at $\sim$ 3 Ga. Dhuime et al. (2012) inferred rates of crustal growth through time from geochemical markers of crustal reworking. There was a greater rate of crustal growth prior to $\sim$ 3 Ga, which results in a mode of continental crust volume which was much greater at 3 Ga than 2.5 Ga. Hawkesworth (2016, pers. comm.) has used this to infer that at least half of the continental crust was recycled over this interval. Given that continental crust covers approximately one third of the modern Earth's surface, these geochemical models predict that $\sim$ 10% of the surface preserved continental crust as plate tectonics initiated. These inferences from geochemical data independently support the prediction of large scale recycling which comes from the hypothesis of a stagnant lid to mobile lid transition, while providing predictions of preserved crustal volume.

6.2.3 Mechanics of Lithospheric Thickening

The stability of cratonic lithosphere against sinking has long been hypothesised to result from its unusually low density (Jordan 1975), compared to modern lithosphere, which results from low iron content and is specific to Archean and to a lesser extent Proterozoic lithosphere (Poudjom Djomani et al. 2001). As keels have not deformed in billions of years, they are likely to be in thermal equilibrium and therefore cold. In the isopycnic hypothesis (Jordan 1978), the density-increasing effect of the keel's low temperature is offset by its chemical buoyancy, in a perfect balance so that the density of the keel is equivalent to the asthenospheric density at all depths. However, keels require some positive buoyancy to resist being dragged down by mantle downwellings, as well as mechanical strength to resist entrainment

or spreading (Lenardic et al. 2003).

During the thickening process, the lithosphere must not fulfil the stability criteria. However, by the time it has thickened to the observed 250 – 300 km, it must have somehow become stable, in order to resist further thickening and entrainment into the mantle. Cooper et al. (2006) proposed a model in which the lithosphere stabilises as it thickens. Provided the keel is less dense than the mantle, its overall buoyancy increases during thickening. A lower keel density results in a lower equilibrium thickness - if it is too buoyant, it will barely thicken, whereas if it is too dense it will over-thicken. If the thickening occurs plastically, i.e. by overcoming a yield stress, then a depth-dependent yield stress will result in an equilibrium thickness above which the keel can no longer yield. Cooper et al. (2006) suggested that progressive strengthening could also occur by shear-zone healing or increasing the yield stress by pore-pressure release. Alternatively, the breakdown of serpentinite at depth could significantly strengthen shear-zones (Lee et al. 2008).

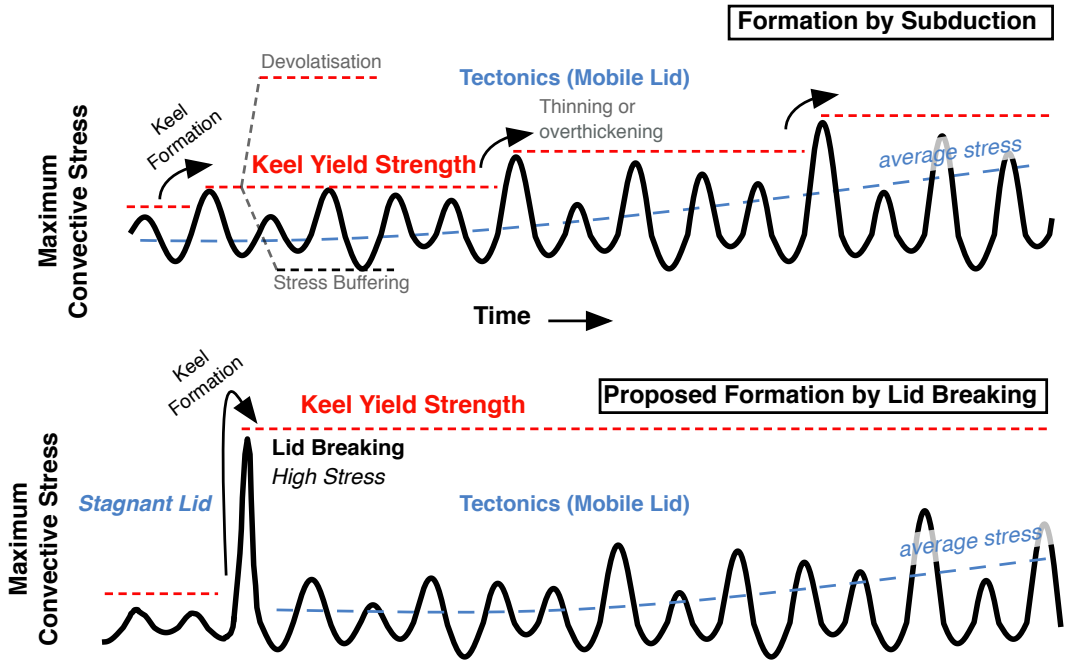

Figure 6.1: Schematic of keel stability through time, in a cooling Earth with increasing convective stress, for keel formation by subduction and by lid breaking. When the convective stress exceeds the keel yield stress, the keel becomes unstable and either thickens and stabilises or is entrained into the mantle. The difference with the new models is that the lid breaking event produces extremely high stresses which are not repeated, even in a cooling Earth.

Regardless of the strengthening mechanism, the final yield stress of the keel must be greater than the stresses produced during the last three billion years of mantle convection. This is a major issue with models of keel thickening by subduction. As illustrated in Fig. 6.1, though a keel may reach a stable

thickness in the Archean, cooling of the Earth results in increasing subduction stresses and the keel's thickness will no longer meet the stability criteria (Cooper et al. 2006). A keel which becomes unstable may possibly thicken to a newly stable thickness, but there is no evidence for repeated deformation and the keel would most likely over-thicken and become entrained into the mantle. Cooper et al. suggested that at the end of, or after, the initial keel formation event, some process acted to increase the keel's yield strength, such as shear-zone healing or the devolatisation mechanism discussed in Lee et al. (2008). The proposed alternative is that the cratonic crust and lithosphere began with a high yield strength and thickening occurred at stresses which were so high that they have not been repeated. The relative changes in stress state before, during and after the initiation of tectonics, marked by the breaking of the lid, are unclear and so computational modelling is required to test this hypothesis.

6.3 Methods

Convection of an infinite Prandtl number fluid with a temperature and stress dependent rheology is modelled using Underworld (Moresi et al. 2001). A simple melting system is implemented following previous heat-pipe modelling (Moore & Webb 2013; Kankanamge & Moore 2016), where mantle temperatures are buffered when they meet a linear solidus. It is assumed that the when melt is generated, it is efficiently transported to the surface and its latent and thermal energy is lost to the atmosphere instantaneously. Moore & Webb (2013) modelled the mass transfer of large volume volcanism using the parameterisation of a thermal advection term, which is proportional to the amount of melt generated in a column. This proportionality constant depends on how efficiently melt is transported to the surface and results in a thicker lid if it is higher. A lower bound of lid thickness is calculated here, by setting the advection term to zero, so that the volume of negative buoyancy prior to lid collapse is conservative. The switch to plate tectonics occurs when the mantle temperature drop below the solidus, as a result of the decaying heat generation term. Melt generation halts at this point and as discussed by Kankanamge & Moore (2016), the base of the lithosphere begins to slope, generating the high stresses required for yielding.

The viscosity of the mantle is temperature-dependent, following the Frank-Kamenetskii approximation (Frank-Kamenetskii 1969) for the Arrhenius rheology: $\eta = \eta_0 e^{E(T-\Delta T)}$, where ΔT is the initial internal asthenosphere temperature, η_0 is the corresponding reference viscosity and E controls the degree of temperature-dependence. E is set to $E = 5$, such that the largest viscosity contrast in the system is initially five orders of magnitude. The mantle rheology is approximated as Newtonian, as well as having a finite plastic strength, as implemented in Moresi & Solomatov (1998). It is assumed that plasticity is the most important stress-dependence and therefore any stress-dependence in the form of

a stress exponent n larger than one is neglected. The mantle most likely deforms by dislocation creep with $n = 3$, however the boundary layer thicknesses and velocities are similar to that of a Newtonian rheology (Solomatov & Moresi 1997) and so the Newtonian approximation still captures the first-order dynamics.

The stress dependence of the mantle viscosity is calculated as a function of the second invariant of the stress tensor. If the yield stress, which is linearly depth-dependent, is reached then an effective viscosity is used to mimic the stress state of yielding material (Moresi & Solomatov 1998). The yield stress is depth-dependent, $\sigma_y = \mu y$ and defined by the depth gradient μ. The whole mantle is modelled and assumed to be thermally insulated at its base, so that the entire heat input is from internal heat production. The Rayleigh number (Ra) is defined as $\alpha g \rho H L^5 / (\kappa k \eta_0)$, where α is thermal expansivity, g gravity, ρ the reference mantle density, H the volumetric heat-production, L the thickness of the mantle, κ thermal diffusivity, k thermal conductivity and η_0 the reference mantle viscosity. At 3.5 *Ga* before present, H is 2.75$\times$ the present value, which increases the Ra by the same amount, as well as the larger dependency on the temperature-dependent mantle viscosity. Also, the stagnant lid decreases the heat-flow out of the Earth's surface. These two effects result in a significantly hotter mantle. For an Arrhenius rheological law, the viscosity of the convecting mantle should lower by many orders of magnitude. To avoid the numerical difficulties of calculating for convection at high Ra, the Ra at 3.5 *Ga* is set to 10^9, with a maximum viscosity contrast of five orders of magnitude. The rigorous convection of this Ra requires the high resolution of 256×256 and mesh refinement of $2\times$ in the upper mantle. $Ra = 10^9$ is likely to be an underestimate of Archean convective rigour, though the Ra dependence is not explicitly modelled here.

All measurements in the models are non-dimensionalised, so that they can be easily applied to other systems of contrasting dimensions, etc. Although the Rayleigh number defines the driving temperature gradient as $HL^2/(\kappa c_p)$, for comparative scaling purposes the temperature difference between the surface and the interior of the starting model, T_0, is taken as the representative ΔT. This choice means that any temperature dimensionalisation depends on an estimate of the Earth's temperature, immediately prior to the failure of the stagnant lid. This choice may not necessarily agree with the actual temperature decline if the model is run for 3.5 *Ga*, however stresses during the Earth's evolution after craton formation are explored using analytic scalings, so that a variety of temperature evolution pathways can be calculated. Additionally, the lag time between H decay and ambient mantle temperature decline is consistent with previous studies (Korenaga 2016) and therefore the H decline is not unrealistically high. Then the stress scale is taken as $\sigma' = \sigma / \alpha \rho_0 g \Delta T L$. Time is non-dimensionalised using the thermal diffusion time-scale: $t' = t\ \kappa / L^2$. The dimensionalised time scale will then be an overestimate, if our chosen Ra is underestimated. Our reported velocities should therefore be considered as conservative. The calculated velocities are generally extremely high compared to typical tectonic velocities, so this is unlikely to be an

issue. All distances are non-dimensionalised to the depth of the whole mantle, for example $d' = d/L$. Quantities are generally non-dimensional, unless otherwise stated, so the corresponding notation is dropped from hereon in.

Thermal expansivity is assumed to be homogeneous throughout the mantle. It varies by almost an order of magnitude in the Earth (Chopelas & Boehler 1992), which should result in a reduction of mantle upwellings (Leitch et al. 1991). As our models are internally heated, no plumes are generated and the dominant density contrast is between the cold near surface material and the hot shallow asthenoshphere. Therefore the assumption of a homogeneous expansivity is justified. The near surface thermal expansivity of $3 \times 10^{-5} K^{-1}$ is used for calculating dimensional stresses, which assumes that instabilities of and near the lid dominate the stress field. Additionally, there is a phase change at about 660 *km* depth in the Earth's mantle, which results in an increase in viscosity of one to two orders of magnitude (Schubert et al. 2001). This is ignored in the models, for simplicity. A lower mantle viscosity of two orders of magnitude was included to check this assumption and the keel formation process was not significantly different. This assumption however is likely to result in the velocity calculations being over-estimated, particularly when lid instabilities reach high displacements.

Chemically distinct continental material is represented by a homogeneous layer at the surface of the model, with a thickness of $d_0 = 0.025L$ (72.5 km). This material is identical to the mantle material, except its reference density (ρ_c) and yield stress are different. The density of the continental material is characterised by the ratio B of its buoyancy relative to the ambient mantle, to the buoyancy of mantle material at the surface temperature, T_0 (Eq. 6.1). ρ_c is the average density of the continental material for the steady-state geotherm within the stagnant lid. $B = 0$ for a continent which is on average isopycnic and $B = 1$ if it is of equal positive buoyancy to an equivalent volume of negative buoyancy cooling at the Earth's surface. The continent still shares the same value of α as the mantle, so that the average density can vary dynamically. This definition of B follows Cooper et al. (2006), with the exception that the temperature gradient between the surface and interior are used, rather than the temperature gradient across the entire mantle in their models.

$$B = \frac{\rho_0 - \rho_c}{\rho_0 \alpha T_0} \tag{6.1}$$

Both the mantle and continental materials have plastic rheologies, with a yield stress of $\sigma'_y = -\mu y$, where y is the model depth and the coefficient of depth-dependence is non-dimensionalised using the stress scale. The mantle depth-dependence is set as $\mu = 0.044$, which is sufficient for both lid breaking and persistent mobile lid convection to occur. The continental depth-dependence is varied in the range $0.044 \leq \mu \leq 0.7$.

For each set of B and μ, there is a minimum thickness, d_s, at which the continent is too buoyant to thicken further and the depth-dependent yield stress is high enough that no yielding occurs (Cooper et al. 2006). The continental material may begin at this thickness, $d_0 \geq d_s$, in which case no thickening will occur. Otherwise, if $d_0 < d_s$, the material will thicken until it either reaches d_s or is entrained into the mantle. Cooper et al. (2006) developed scaling models for d_s as a function of Ra, by assuming that in the case of stability, the maximum buoyancy and viscous stress of the keel will equal or exceed the negative buoyancy of the thermal boundary layer. The focus here is not on investigating the dependency of keel stability on lid thickness and so the Ra dependence of keel stability during lid breaking is not of concern. However, the same approach is taken in quantifying the dependency of d_s on B and μ using a conceptual model of stress balance, though only applicable to the specific lid breaking event investigated here.

A keel which has no strength can still resist sinking into the asthenosphere, albeit for the short term before entrainment occurs, provided it has sufficient buoyancy. In this case, the excess buoyancy provided by its thickening must be in equilibrium with the maximum negative buoyancy of the sinking mantle lid below. Therefore if the negative buoyancy of the sinking lid is constant throughout the models with varying B, $d_s B$ should also be constant. Therefore $d_s \propto 1/B$ and this dependence can be captured for this particular lid breaking event by the buoyancy criterion in Eq 6.2. Here β_1 and β_2 are proportionality constants, which will be determined from the numerical models.

$$\begin{aligned} d_s &= \frac{\beta_1}{B} \quad \text{(Buoyancy Criterion)} \\ d_s &= \frac{\beta_2(B)}{\mu} \quad \text{(Yielding Criterion)} \end{aligned} \tag{6.2}$$

Likewise, provided the continental material is insufficiently buoyant to attain stability according to the buoyancy criterion Eq. 6.2, the net continental stress is directed downward and drives thickening. The keel however can still attain stability if this net stress is balanced by the plastic strength of the keel. By definition in the models, the maximum keel stress is μd_s. Therefore if the negative buoyancy of the sinking lid is not varied, $d_s \mu$ is constant with respect to μ. The net stress at the base of the keel depends on B, so there is a particular proportionality constant for each B, resulting in the yielding criterion (Eq. 6.2). The dependence of β_2 on B could be determined by stress balance, leaving a proportionality constant which is independent of B. However, for simplicity a value of β_2 is fitted for $B = 0.38$ and 0.25, to give a sense of its variability.

6.4 Cooling Mantle Dynamics

Long model runs without yielding (Fig. 6.2) can qualitatively reproduce the increase of stress, which results with the absence of melting, proposed by Moore & Webb (2013). Despite the early switch to mantle cooling and the choice of a solidus which is close to the initial geotherm, it takes $\sim$ 35 dimensionless time units for melting to switch off. This period encompasses many convective overturns below the lid and demonstrates that the stagnant lid system, with melting, has a very weak coupling between changes in heat-production and average mantle temperature. This behaviour follows the recent predictions of Korenaga (2016) and so is not completely unexpected. The energy balance between heat-production and surface heat-flow continually moves further away from equilibrium through time, even when melting becomes negligible.

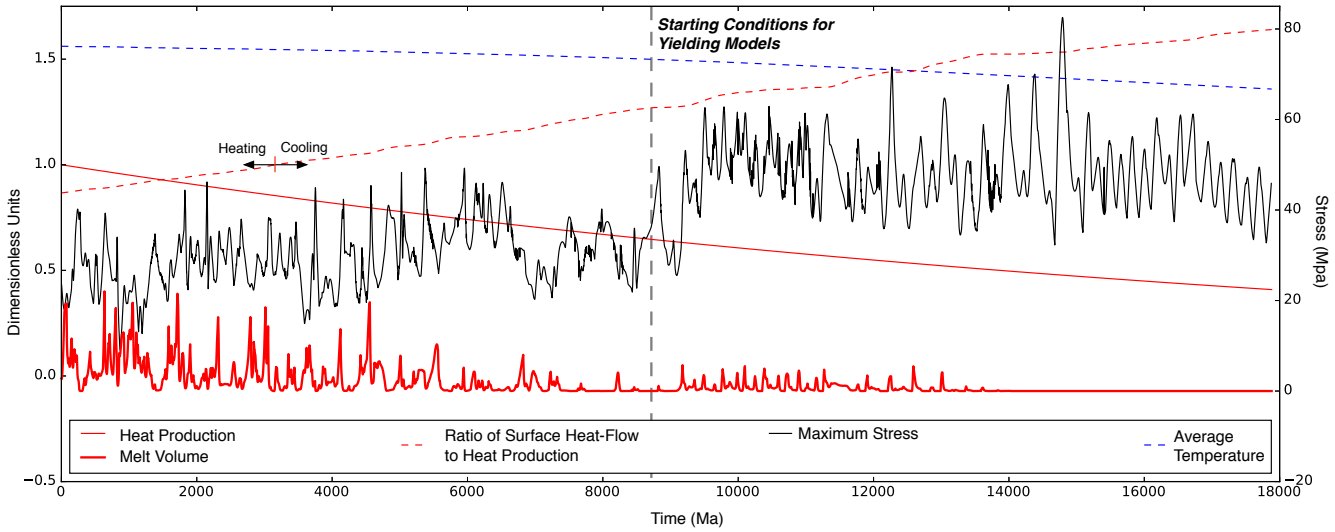

Figure 6.2: Decaying production through time and the subsequent decrease in average temperature and melting, while the maximum stress increases. The increase in stress occurs when melting first switches off, as described by (Moore & Webb 2013). The ratio of surface heat-flow to the total internal heat-production shows when the mantle switches from net heating to cooling. There is a significant time delay between the reduction in internal heat-production and subsequent decrease in the ambient mantle temperature, which results in melt switching off much later than the switch to mantle cooling. Time is dimensionalised from the thermal diffusion rate and corresponds to a non-dimensional period of $\Delta t' = 68$. This does encompass a relatively long period, as 2.8×10^5 time steps were taken for this plot.

The lid breaking event is of primary interest in this study. Modelling the dependence of lithospheric stresses on cooling mantle temperature and melting is only necessary in order to be consistent in the initial conditions of lid breaking models and subsequent mantle evolution. Following this motivation, the lid breaking models are started with initial conditions which represent the mantle just prior to the

decrease and increase of melt and lithospheric stresses respectively. Though it takes $\Delta t = 35$ (9Ga) for melt to switch off in Fig. 6.2, these models are started from steady-state and therefore the cooling period can be significantly shorter if the mantle was already cooling. Alternatively there may be another mechanism for switching off the melt. Regardless, the lid breaking models begin with initial conditions which initiated lid breaking and there are no issues with the subsequent time-scale. Assuming the initial lid thickness is insensitive to the mechanism of lid breaking, the stagnant lid to mobile lid transition is not sensitive to the cooling time-scaling during stagnant lid.

Models with yielding rheology and beginning prior to the stress increase (Fig. 6.2) start with stagnant lid convection, before the yield stress is met and lid breaking occurs (Fig. 6.3). As the lid is negatively buoyant, the entire boundary layer is recycled. Some parts sink more quickly than others, providing momentary relative stability for some lid fragments, but no part of the lid is stable for more than one convective overturn in these models. This lid breaking model is taken as a reference and is repeated with a 'continental' layer with varied values of density and yield stress.

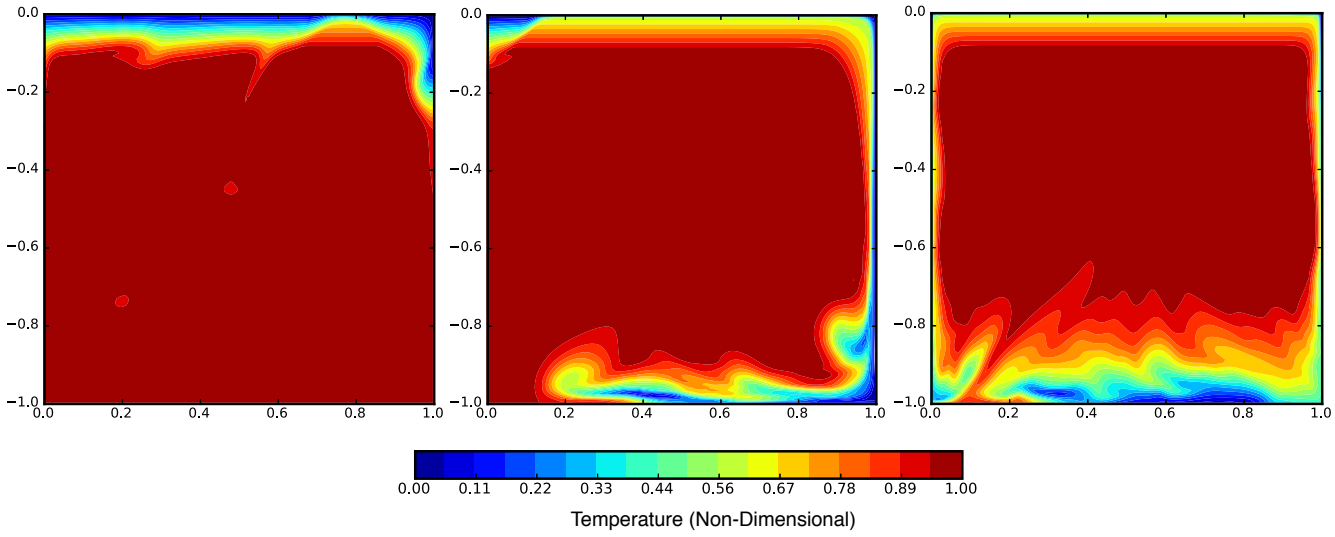

Figure 6.3: Lid breaking event, without any 'continental' material. Temperature is plotted from time at which the lid has yielded and gravitational instability has begun (left), to complete recycling of the stagnant lid thermal boundary layer and establishment of mobile lid convection. The sequence happens extremely rapidly, $\Delta t' = 0.08$. The mobile lid regime at high Rayleigh number produces an extremely thermal boundary layer and rapidly cools down the mantle as the foundered lid absorbs energy.

6.5 Results

The continental material is able to thicken to a point at which it resists further thickening and yielding switches off. There are critical values of continental density and yield strength which must be met in order for this stability to occur. If the continental density is higher than this criterion, it becomes entrained into the mantle, even if it is still less dense than the average mantle (Fig. 6.4). Likewise, if the yield strength is too low, the keel can be buoyant and still be entrained into the mantle in small fragments.

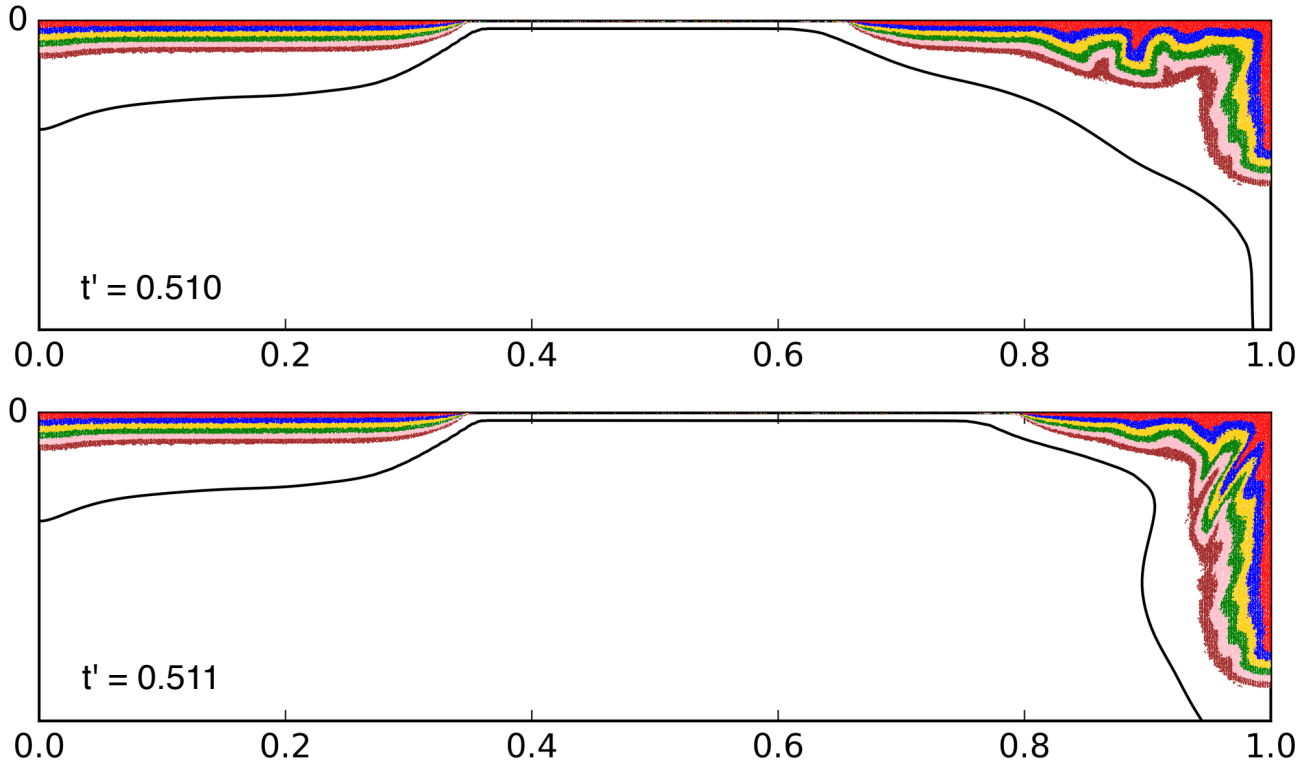

Figure 6.4: Thickening when the keel density is higher than the stability density: $B = 0.09$, which is 64% lower than the required stable buoyancy. The keel initially appears to have stabilised, but then rapidly over-thickens and is entrained into the mantle. The buoyancy of the keel is set as $B = 0.09$.

B and μ are varied, while Ra is held constant at 10^9. The dependence of d_s on B is calculated by setting μ low enough that only the continental buoyancy is providing stability (Fig. 6.5, left). The best fit of these models gives $d_s = 0.082/B$. For a 300km keel without any strength to survive the lid breaking event, the buoyancy is required to be $B = 0.8$. However, when the keel has a yield stress larger than that of the mantle, $\mu > 0.044$, keels with lower buoyancy can stabilise. This dependency is analysed for $B = 0.38$ and $B = 0.25$ (Fig. 6.5, right), where the latter requires double the yield strength compared to the former, for stability. In order for a 300km keel to reach stability during lid

breaking, the yield strength is required to be $\mu = 0.29$ and 0.56 for $B = 0.38$ and 0.25 respectively.

A higher initial yield strength for a given d_s increases the stress magnitude required to return the keel to yielding and so provides greater stability. The stability of less buoyant continental material with a higher yield stress may also allow the keel material to be a realistic harzburgite density and still attain stability. Archean lithosphere is typically 40 $kg\ m^{-3}$ less dense than the asthenosphere at equivalent lithospheric depths (Poudjom Djomani et al. 2001). If the density contrast driving convection is approximately 100 $kg\ m^{-3}$ (Turcotte & Schubert 2014), this results in $B = 0.4$ on the modern Earth. The calculation of B in the models uses the stagnant lid mantle temperature as a reference. If the mantle was hotter in the Archean, but then density of the keels was approximately the same, B is effectively reduced. For example, assuming the mantle was 200°C hotter and taking the thermal expansivity as $3 \times 10^{-5}\ K^{-1}$, the density contrast reduces to approximately 20 $kg\ m^{-3}$. If the density contrast driving convection was approximately the same in the Archean, this results in $B \approx 0.2$. If convective density contrast or keel density were lower in the Archean, the decrease in B would be less significant. The keel buoyancy can therefore be approximately constrained to $0.2 < B < 0.4$. The compensation between yield strength and buoyancy therefore not only allows the keel to start with a higher strength, but also a more realistic buoyancy. There is no need to invoke the presence of material with a lower density than harzburgite in the keel (Cooper et al. 2006).

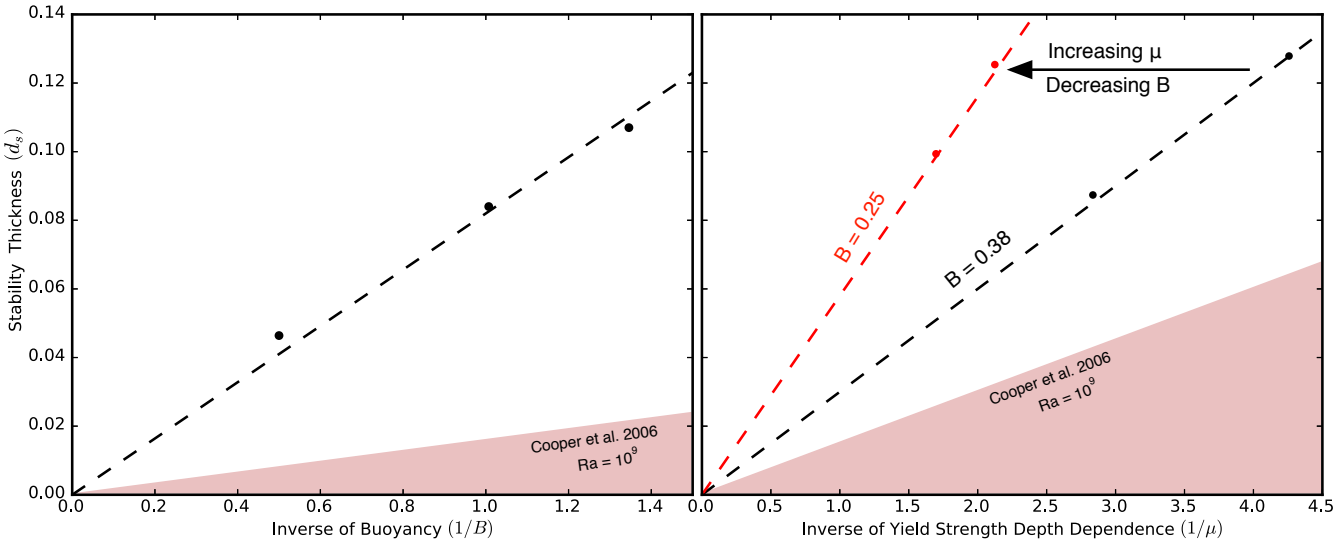

Figure 6.5: Stable thickness d_s as a function of B and μ. **Left)** *The continental material has the same yield strength as the mantle, $\mu = 0.044$. Only its buoyancy subsequently provides stability and fitting $d_s(B)$ (Eq. 6.2) results in $\beta_1 = 0.082$.* **Right)** *The dependence of d_s on μ is found for specific values of B. Fitting $d_s(\mu)$ (Eq. 6.2) results in $\beta_2 = 0.03$ and $\beta_2 = 0.058$ for $B = 0.38$ and $B = 0.25$ respectively. The increase in β_2 with decreasing buoyancy demonstrates that yield strength can compensate for a lower buoyancy of continental material. The range of unstable d in a convecting, isoviscous mantle cell as a function of B and η (shaded pink), according to the scaling of Cooper et al. (2006), is shown for $Ra = 10^9$.*

A relatively higher B and μ are expected to be required for stability during the lid breaking event, compared to the recycling of the thinner boundary layers which are stable in a convective system without the stagnant lid (Cooper et al. 2004). This prediction partly agrees with the comparisons of d_s in the lid breaking models compared to the values of Cooper et al. (2006) for $Ra = 10^9$. Stabilisation in the lid breaking models occurred at a d_s which is thicker than the minimum d required for stability in the models of Cooper et al. (2006). This is due to the higher stresses generated in these models, which result from our temperature-dependent viscosity (opposed to isoviscous) and the high stress lid breaking event. Their stability scaling predicts that the keels formed in these lid breaking models have a yield strength which results in high degree of stability, but buoyancy which are close to instability. For example, a keel with $B = 0.25$ and $\mu = 0.56$ will stabilise at 300km in the lid breaking model. The scaling of Cooper et al. (2006) predicts that within one order of magnitude decrease in Ra, the keel will have insufficient buoyancy for stability. However, if buoyancy were not an issue, the keel yield strength would ensure stability for six orders of magnitude Ra decrease. It is difficult to tell whether these lid breaking models can be consistently compared to the models of Cooper et al. (2006), as there are many differences in model design. Instead, our stability analysis is based on the assumption that a keel will fail if it returns to the stress state of its previous failure, i.e. the lid breaking stress. By continuing the models into the mobile lid regime and measuring the evolving stress state, this definition of stability provides rigorous self-consistency and is the primary focus.

6.5.1 Thickening Process

The lid breaking event occurs when the convective stresses are high enough that localised failure occurs in both the mantle and continental material (Fig. 6.6). As a result of plastic failure, the mantle part of the lid becomes unstable, thickening in a localised drip over a convective downwelling and thinning elsewhere in a thinner part of the lid. Subsequently, parts of the previously stable continental material enter regimes of shortening and extension (Fig. 6.7), depending on the style of mantle lid deformation below. Where the lid rapidly thins, the continental material also thins in an analogous way to newly formed passive margins during the opening of oceans on the modern Earth. Where the mantle lid is dripping downward, the continent is rapidly thickened and strain is accommodated by localised shear zones. As thickening occurs, fragments of intact lid are drawn towards the downwelling zone, where the mantle part becomes unstable and provides further negative buoyancy to drive thickening. Thickening of the continental material is therefore the result of the entire mantle part of the lid becoming unstable and sinking, rather than just the fragment initially positioned in the thickening zone. This is a point of distinction from continental collision, where thickening primarily occurs due to the sinking of the vestige of oceanic crust and lithosphere, rather than the continental mantle lithosphere.

The keel formation event is triggered by thinning of the mantle lid, analogous to modern rifting, while simultaneously in another location convergence occurs where the mantle lid is sinking into the asthenosphere. This relationship between mantle upwellings and downwellings, as well as the related thinning and thickening of the lithosphere, is somewhat similar to the mantle flow that drives modern tectonics. The major contrast is the episodic nature of the lid breaking event and the thickening of the wide zone of buoyant lithosphere, rather than the movement of rigid oceanic plates. In Fig. 6.7, one keel forms while a lid fragment resides on the other side of the model, relatively undeformed. The keel which forms first also accumulates a significantly larger volume of material than the second keel. This sequence is the result of the exponential nature of Rayleigh-Taylor Instabilities; the first instability to form accelerates quickly and dominates the flow field until break-off occurs. In these models, the initial keel formation takes place simply where the lid happened to be thicker. Mantle flow is dominated by the first instability and is reversed, from clockwise to anticlockwise, once the second instability begins. The location and relative size of keels is dependent on the initial conditions, due to the homogeneity of the continental layer, through it is plausible that a heterogeneous lid could influence these factors.

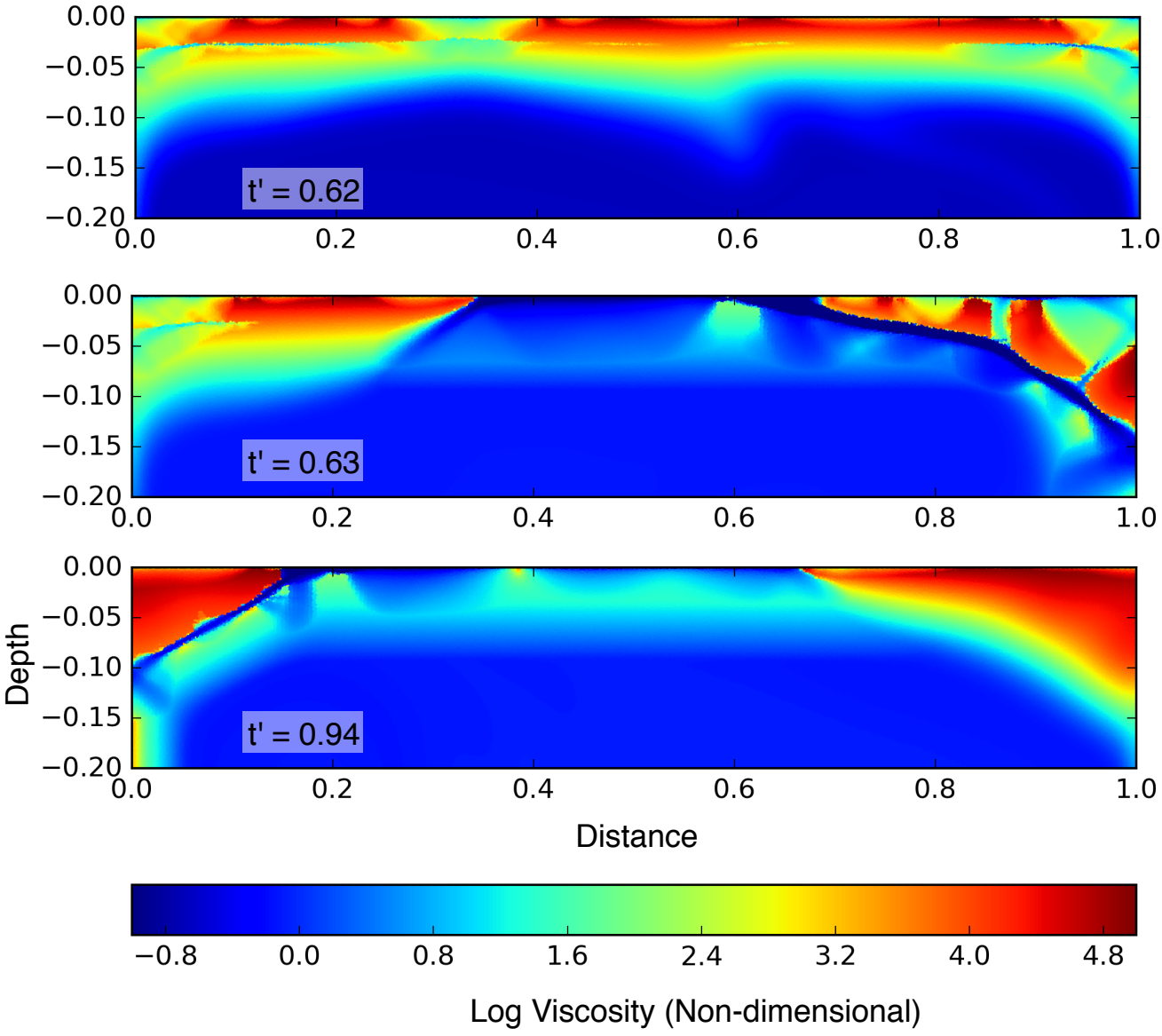

Figure 6.6: Effective viscosity in the upper mantle, from lid breaking to keel stabilisation.

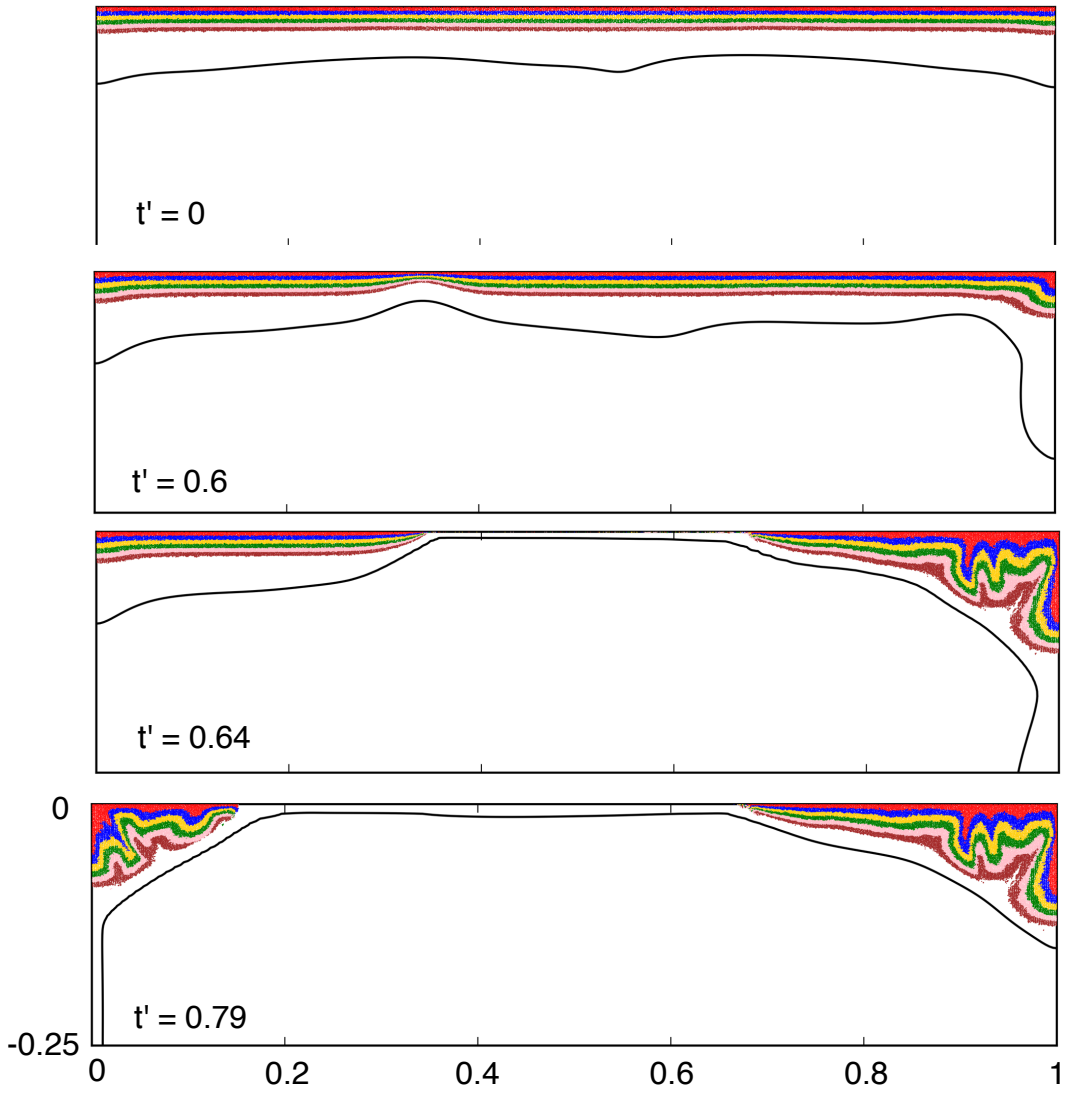

Figure 6.7: Continental layer marks, advected through time. The coloured markers show the extent of the buoyant and strong material, where the layers are used to plot internal strain and do not correspond to material properties. The $T = 0.94$ geotherm is shown (black curve), in order to track the initially stable portion of the stagnant lid.

Shallow continental material is transported to great depths, as a result of the localised thickening. For example, upper crustal rocks are transported down on average down to ~ 50 km and in the deepest part of the keel > 250 km. Thickening occurs more quickly than thermal diffusion, so the juxtaposition of continental material from different depths results in a strongly perturbed continental geotherm (Fig. 6.8). This initial temperature perturbation has a negligible influence on the keel's buoyancy (Fig. 6.9). However, as the keel moves towards a new equilibrium geotherm, the top and bottom cool and heat up respectively. The heating is a result of a separation of the linear stagnant lid geotherm as the base of the lid is completely removed. The next effect is that the average buoyancy of the continent increases,

by $< 10\%$, which is relatively minor.

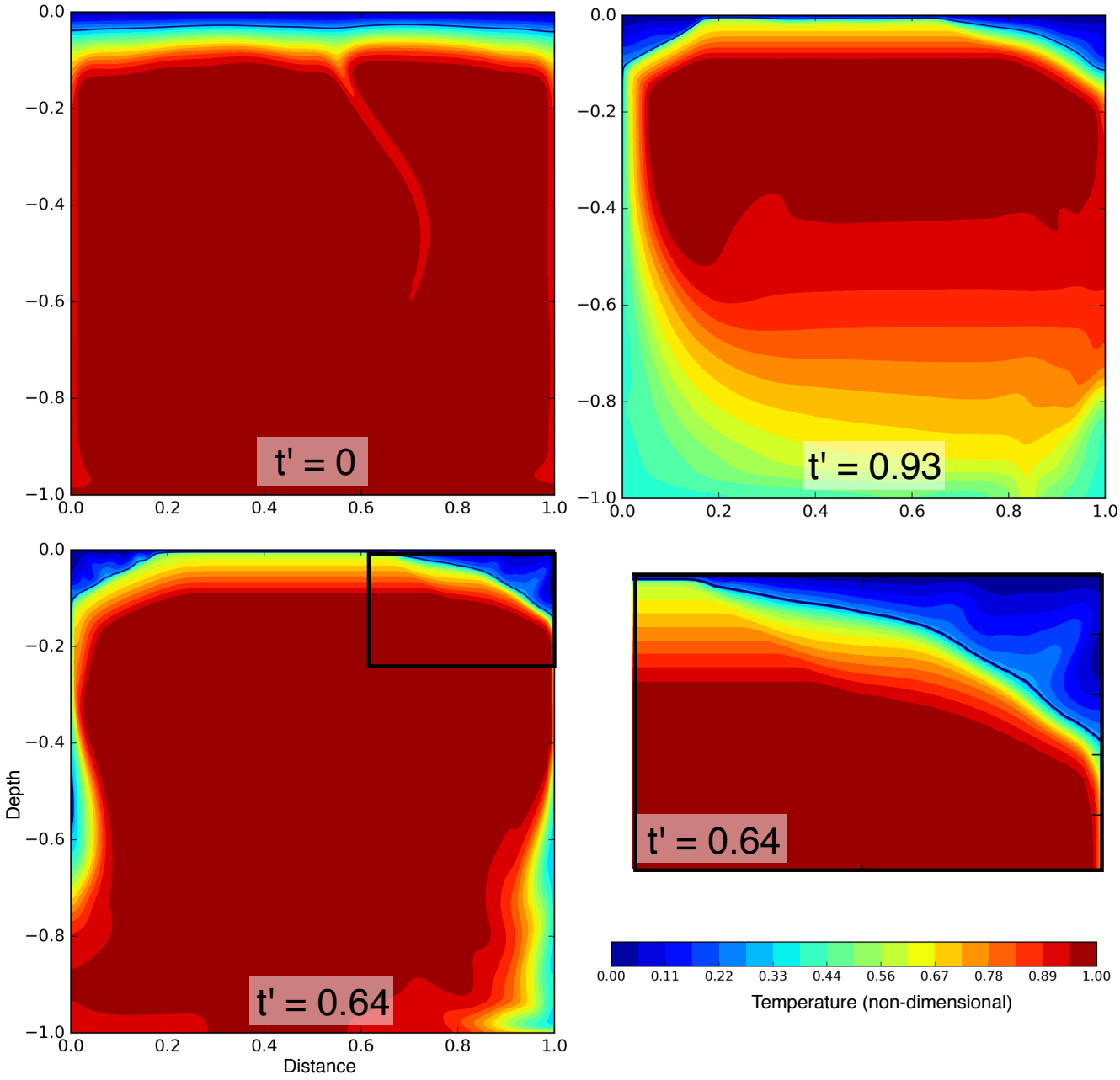

Figure 6.8: Whole mantle temperature distribution, from stagnant lid ($t' = 0$) to keel formation ($t' = 0.64$), to mobile lid convection ($t' = 0.93$). Dimensionalised, these plots span $\sim 250 Ma$. The enlarged box shows the perturbed geotherm in the keel, soon after formation.

Models which survive the lid breaking event remain stable as steady mobile lid convection is established. Because one anticlockwise convection cell forms, one keel is resisting downward mantle flow and the other upward. The mantle is clearly far from thermal equilibrium as mobile lid convection begins. When the models are stopped, the mantle has cooled significantly (Fig. 6.8), demonstrating

self-consistently the significant contrast in mantle temperatures under the stagnant lid and mobile lid regimes. The average mantle temperature drops rapidly initially, though the rate of cooling decays through time. After 200Ma ($\Delta t' = 0.75$), the average mantle temperature has lowered to 80% of the stagnant lid temperature.

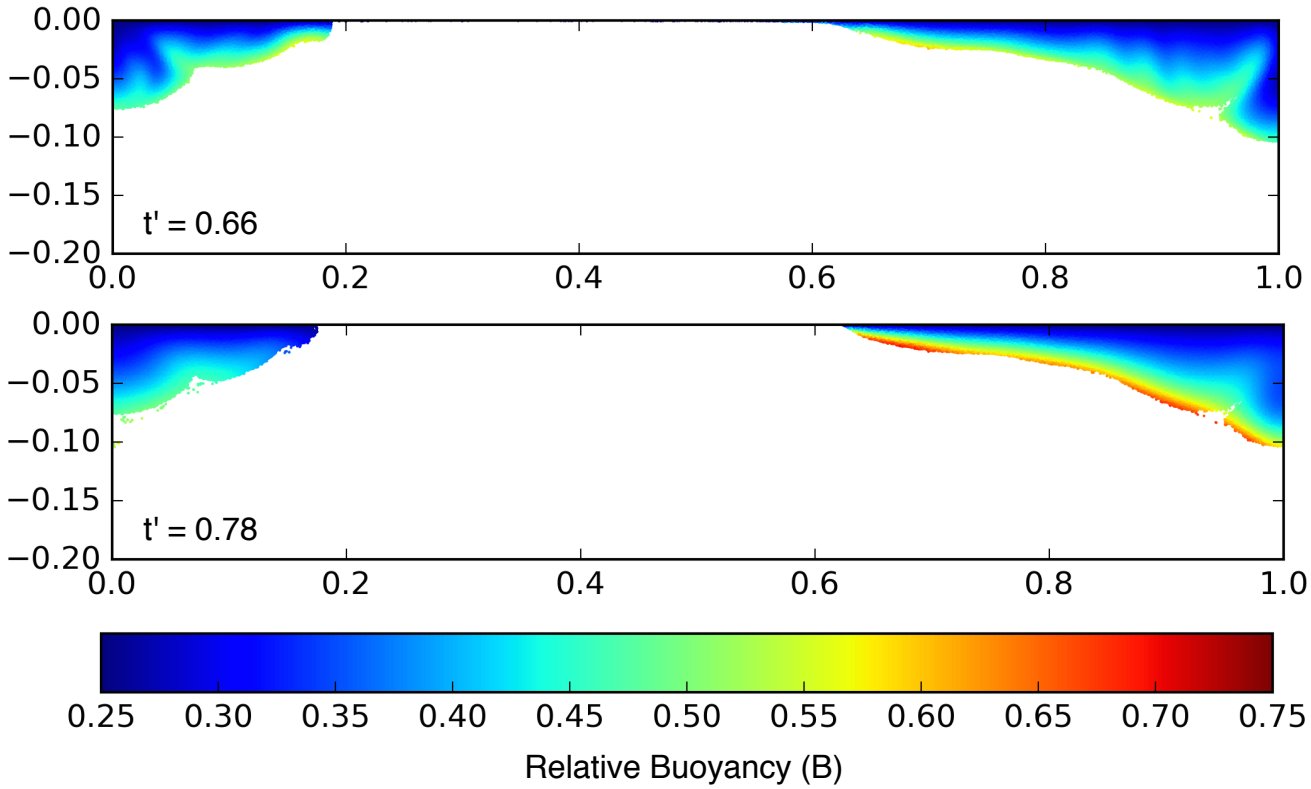

Figure 6.9: The evolution of continent buoyancy during keel formation: the average buoyancy of the continent on the right is $B = 0.38$ during stagnant lid convection and when it initially thickens (top), this increases only marginally by $\sim 1\%$. When thermal diffusion has begun erasing the temperature perturbations (bottom), its buoyancy has increased by $\sim 8\%$ to $B = 0.40$.

6.5.2 Dynamic Topography

The keel formation event generates an initial period of minor subsidence of the crust directly above the keel, followed by significant uplift. Topography is quantified by measuring the total vertical normal stress at the top of the model (Fig. 6.10). Within the stagnant lid regime, subsidence and uplift occur above thickened and thinned sections of the lid respectively. As the lid breaks, there is subsidence above where the mantle part of the lid is sinking and the keel is thickening. This subsidence occurs because the column during thickening has a net negative buoyancy and is approximately twice the magnitude which occurs during stagnant lid. When the mantle part of the lid breaks off, the crust switches to uplift

and exhumes approximately 4$\times$ the topographic variation which occurs during stagnant lid. Though the buoyancy of the continent increases slightly, as it moves towards thermal equilibrium, this is not reflected in increased uplift (Fig. 6.10b). The uplift reaches an maximum shortly after the mantle lid break-off, though remains relatively constant, indicating that the increasing buoyancy is balanced by cooling thermal boundary layer.

Topography can be dimensionalised using the stress scale and assuming that excess stress at the surface is balanced by the extra weight of the thickened crust. The magnitude of exhumation is then $4 \times 10^{-2} \alpha \rho_0 \Delta T L / \rho_C$, where ρ_C is the crustal density and may be less than ρ_c. If the mantle were 1500°C in the Archean and assuming $\kappa = 10^{-6}\ m^2 s^{-1}$, $\alpha = 3 \times 10^{-5}\ K^{-1}$ and $\rho_C = 2700\ kg\ m^{-3}$, the predicted exhumation is about 7km. Depending on the density and temperature parameters, this could plausibly be at least $\pm$2km. This agrees with the typical approximate estimate of $5 - 10$km (Sandiford et al. 2004; Robin & Bailey 2009; Flowers et al. 2004). The assumption that the Archean α is the same value as today potentially ignores differences in eclogitisation dynamics. This approach assumes that the large volumes of eclogite predicted by Van Thienen et al. (2004) can be modelled by the lower temperature of the thick stagnant lid boundary layer. As Cooper et al. (2006) predict that for stability, B must be $4 - 5\times$ higher than in these models, the magnitude of uplift in their models would be significantly higher. The agreement between the degree of uplift predicted by these models and observed exhumation further supports the choice of B, which is based upon the typical density of harzburgite and allows the thickening of lithosphere with a higher yield strength.

A)

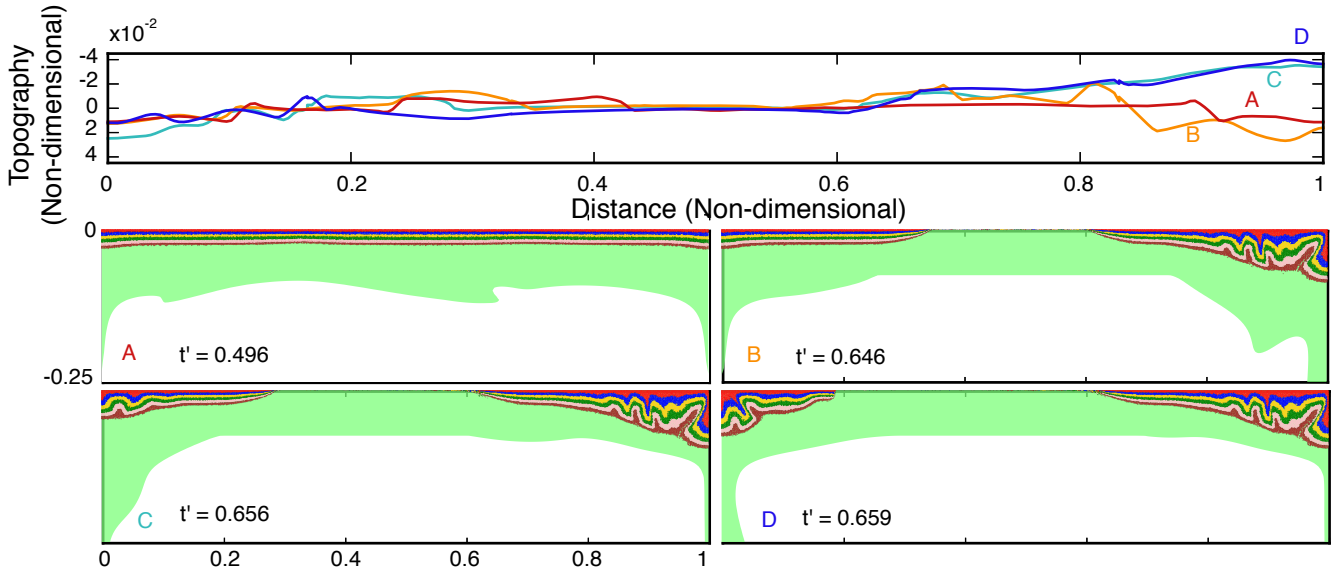

B)

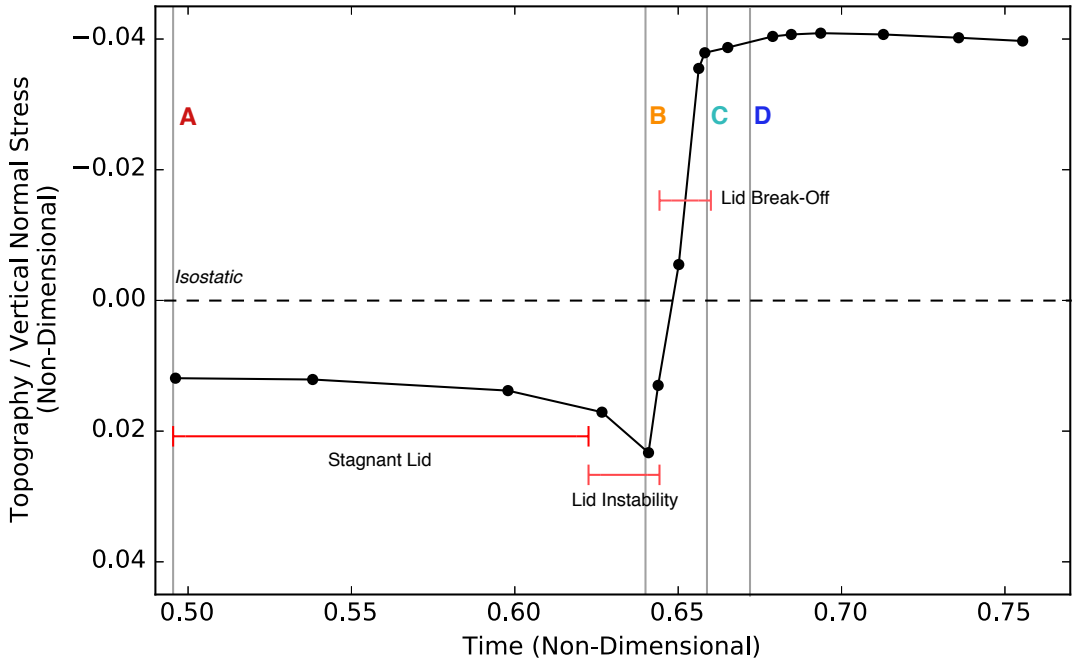

Figure 6.10: **A)** *Topography over time for a keel stabilising model. Topography is measured as the normal stress at the top of the model, though the sign is reversed so as to have the same sign as the resulting elevation.* **B)** *Plot of the topography in the centre of the first formed keel (distance* 1*), through time.*

6.5.3 Keel Stress Regime

The hypothesis that the lid breaking event involves anomalously high stresses is supported by the evolving continental stress state in the models (Fig. 6.11). The peak stress during the thickening process is approximately $4\times$ the ambient stress during stagnant lid convection. Stress in each keel reaches a maximum when they reach d_s and their effective viscosity increases again. As the sinking mantle lid breaks off, this stress reduces significantly, moving towards the stress state typical of the mobile lid regime. The average continental stress in the mobile lid regime is about twice that of stagnant lid. This is still less than half the stress magnitude experienced during keel formation, even as the mantle equilibrates with the new thermal regime and cools. The pulse of high stress is limited to local lid breaking and can therefore occur in different locations at different times. This isolation of keel forming events is likely to become more prominent in larger model domains and in 3D.

During the mobile lid regime, one keel, Keel A (Fig. 6.11), is directly above a mantle downwelling and the other, Keel B, above an upwelling. This results in a higher stress in Keel B than A. The stress in Keel B is slightly overestimated, as the measurement includes some particles which are being entrained, though taking an average reduces this effect. The stress in the mobile lid regime is likely to be an upper bound, as keels on the modern Earth are typically buffered by mobile belts (Lenardic et al. 2003).

The increasing stress of the past $3Ga$ as the Earth cooled may have returned the keels to a similar stress state as during formation, which would eventually lead to destabilisation. This is explored by scaling the mobile lid stress state to a Ra increase which corresponds to a decaying mantle temperature (Fig. 6.12). Mobile lid stress scales as $\sigma \propto Ra^{-\frac{1}{3}}$ (Schubert et al. 2001). An exponentially temperature-dependent viscosity with a maximum variation of five orders of magnitude and a temperature decrease of $200^{\circ}C$, both reasonable assumptions, result in a Ra decrease of one order of magnitude over the past 3Ga. Altering this to ten orders of magnitude viscosity contrast or $400^{\circ}C$, gives two orders of magnitude Ra decrease. A decrease in Ra of one order of magnitude is not sufficient to return the mantle to the keel formation stress. However, if the decrease is closer to two orders of magnitude, the convective stress would have surpassed the keel formation stress approximately $1Ga$ ago. This results in the destruction of keels if they move too close to subduction zones or plumes.

The typical stress state of continents at subduction zones, through time, is estimated from the variation in continental crust thickness through time (Fig. 6.12). Collated Rb/Sr data shows that crustal thickness at the time of crustal melting at subduction zones systematically increase from 3Ga to 1Ga (Dhuime et al. 2015). Any crustal thickening will be in isostatic equilibrium with the negative buoyancy of the subducting slab. Crustal thickness should vary proportionally to the negative buoyancy and therefore the peak stress experienced by continents at subduction zones. Using this variation to

scale the modelled stress at 3Ga results in a stress variation which is initially similar to the $Ra^{-\frac{1}{3}}$ scaling of a Ra decrease of two orders of magnitude. However, the maximum crustal thickness at $\sim$ 1Ga scales to a peak stress which is only 75% of the keel formation stress.

A)

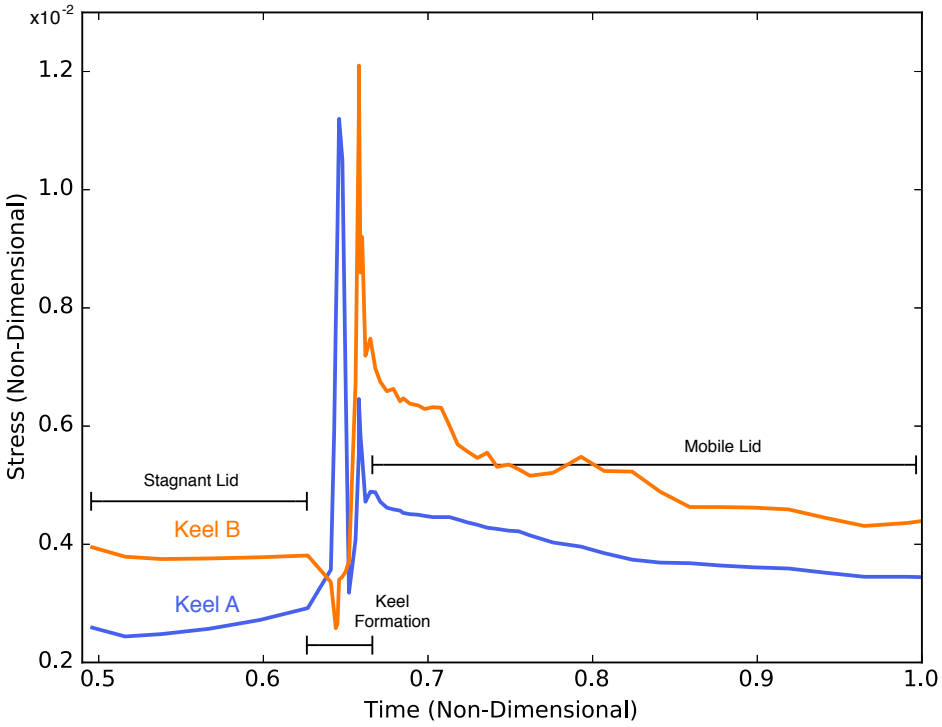

B)

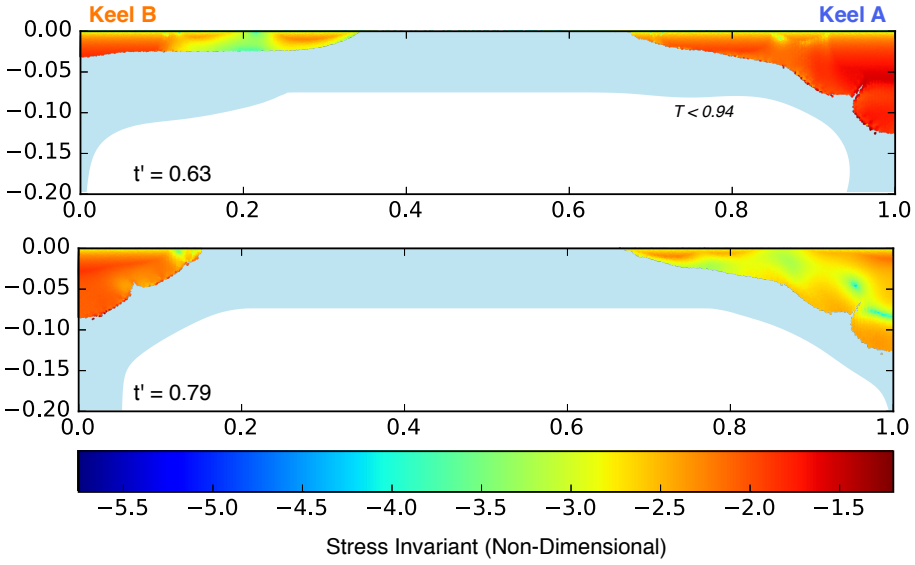

Figure 6.11: **A)** *Average continental stress through time for a typical, stabilising keel formation model.* **B)** *Continental layer marks, advected through time. The coloured markers show the extent of the buoyant and strong material, where the layers are used to plot internal strain and do not correspond to material properties.*

6.6 Discussion

The keel formation by lid breaking hypothesis is simple, but consistent with the expected mantle evolution at the billion year scale. The combination of the cratonic lithosphere's anomalous properties, limited formation time and the mantle's increasing ability to thicken lithosphere through time, is inconsistent with a secular subduction thickening mechanism and therefore a non-uniformitarian mechanism is required. The switch from stagnant lid to mobile lid convection is an intuitive and simple source for the episodic, anomalously large pulse of negative buoyancy required to deform the strong Archean lithosphere. If the keels formed during the lid breaking event, the keel formation process becomes much simpler compared to subduction and plume analogues. There is no longer a requirement for strengthening of the keel at a particular time, as the lithosphere can begin with the high strength before lid formation. There is no requirement for a plume to produce high degrees of melting in one particular place, as the lithosphere can form over a large, uniform region by large scale mantle melting, before being drawn in to form keels. High degrees of melting occur during the stagnant lid regime, as an alternative heat-loss mechanism to tectonics (Moore & Webb 2013). This can result in lithosphere which has melted to a high degree and as a result ends up with low density and high strength, after iron and volatiles have been respectively extracted. A strong crust can also form through continuous intra-crustal melting, as a result of the generation of felsic crustal rocks and redistribution of heat-producing elements by vertical tectonics (Sandiford et al. 2004). Despite the simplicity, the mechanics of the model are valid, as demonstrated by the numerical models. Thick keels can form in a high stress environment which is difficult to repeat, for reasonable material properties. As well as validating the conceptual keel formation model, the numerical models provide scalings for material properties and make predictions about the crust which is still preserved on the modern Earth.

The destruction of the North China Craton and removal of part of the keel beneath the Colorado Plateau have both been attributed to weakening of the lithosphere by metasomatism (Griffin et al. 1998; Lee et al. 2001, 2011). Therefore keel destruction appears to require a special weakening event, rather than simply the presence of nearby convective flow alone. This indicates that the typical keel strength is currently still higher than convective stresses. If the continental stress state varies with the convective stress scaling, a Ra decrease of just one order of magnitude can explain the current keel stability. The geochemical estimate of crustal thickness through time (Dhuime et al. 2015) appears to instead agree with a stress increase immediately after tectonics initiates which scales to a project Ra decrease of two orders of magnitude. However, as crustal thickness reached a maximum 1Ga, it appears that this rate of stress increase was not sustainable. An explanation is that mantle cooling has reduced the Ra by two orders of magnitude, but there is a limit to the stress transmitted into the keels. Based on the scaling to crustal thickness, this maximum stress would then be 75% of the keel formation stress and would

explain why keels are still generally stable, unless they can be significantly weakened.

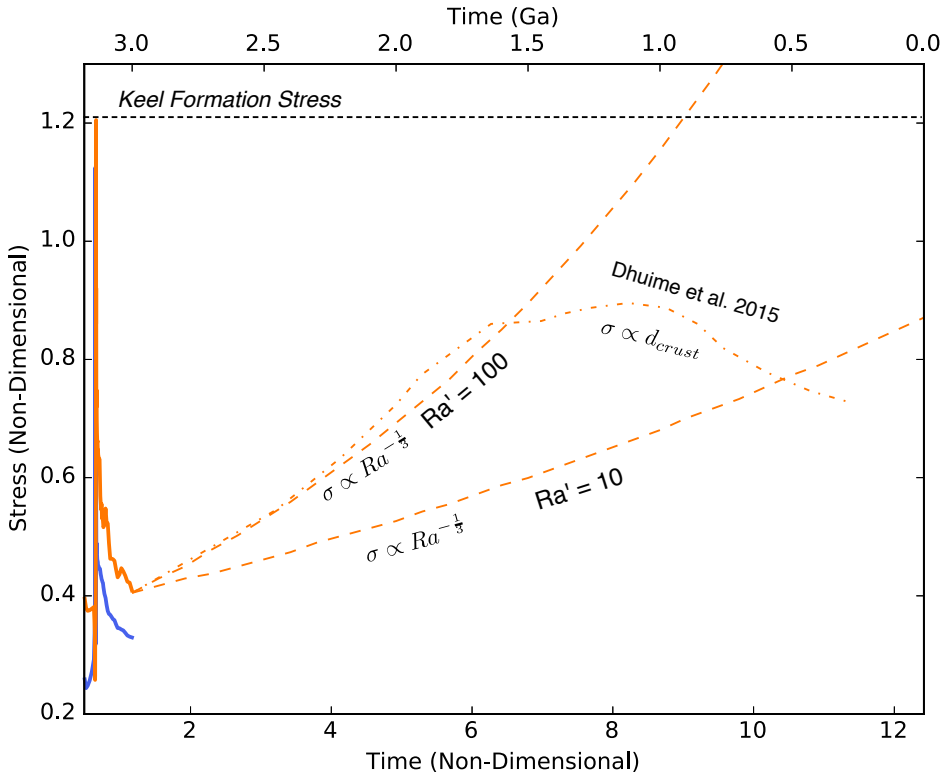

Figure 6.12: Increase in mobile lid stress, using the $\sigma \propto Ra^{-\frac{1}{3}}$ scaling. The plot spans approximately three billion years, demonstrating that a Ra increase of one order of magnitude since the initiation of plate tectonics is not sufficient for keel destruction. If Ra has decreased by two orders of magnitude, the keels may have started being destroyed in the last billion years. The crustal thickness variation over time, calculated by Dhuime et al. (2015), should vary proportionally to the negative buoyancy at subduction zones and is plotted for comparison.

Stagnant lid collapse is modelled as occurring due to declining melting. However, the keel formation process is unlikely to be dependent on the mechanism which triggers lid breaking, only the initial lid thickness. Most plate tectonics initiation mechanisms involve the build up of gravitational potential energy as the lid cools and eclogite forms (Moresi & Solomatov 1995; Van Thienen et al. 2004; Moore & Webb 2013; O'Neill et al. 2007). This build up can occur because the lid is too strong to be recycled, until the yield stress is reached. The mechanism for reaching this yield stress may differ between models, but the lid breaking event would be identical if the models do not differ in lid thickness and yield stress. For an equivalent Rayleigh number, these should not differ significantly. Recent models have modelled the initiation of tectonics without the formation of a thick, strong lid (Rey et al. 2014; Gerya et al. 2015). How the thermal regime of the mantle interacts with the lid dynamics in these models is unclear, so it is difficult to assess the applicability of our keel formation model. Rapid keel strengthening is again required in the case of a weak lid and it is difficult to see which mechanism would thicken the keels and prevent them from rapidly spreading apart.

The transition from stagnant lid to mobile lid has previously been modelled by complete recycling of the lid (Van Thienen et al. 2004; O'Neill et al. 2007). However Archean terranes, such as the Pilbara and Kaapvaal cratons, are preserved from before the beginning of plate tectonics ($>$ 3Ga) (Van Kranendonk et al. 2007). The numerical models demonstrate that for these lid fragments can be systematically preserved as the upper part of the thickened buoyant and strong lithosphere. Geochemical models of continental crustal volume through time (Dhuime et al. 2012, 2015; Hawkseworth pers. comm. 2016), predict that about 38% of the current crust volume was present immediately after the lid recycling event, which is equivalent to 15% of the Earth's surface. This is four times the area which forms in the models. One reason for this is that the square model domain forces the newly formed oceans to be smaller than is energetically optimal. The Earth's oceans can be more than three times wider than the whole mantle's depth and this is typically reproduced numerically when wider domains are used. Additionally, the edges of the keels are thin and can plausibly be replaced or combined with new material, forming mobile belts. If the geochemical signature of these belts are dominated by new crust, then this could lower the preserved Archean crustal volume.

The depleted and buoyant mantle lithosphere has been assumed here to have formed during the stagnant lid regime. This would correspond to the regime described by Van Kranendonk et al. (2015), where mantle upwellings generate plateaus of thick mafic crust and a depleted harzburgite mantle lithosphere below. Progressive remelting then leads to remelting of the mafic crust, forming granitoids and pervasive depletion of the lithosphere. This can occur at the 100 *Ma* time scale, such that the evolved crust and depleted mantle lithosphere have cooled and have low degrees of partial melt, by the time of the lid breaking event. Newly depleted lithosphere however may also be generated during the lid breaking event in regions of mantle upwelling. This newer harzburgite would then be swept into the zones of convergence and could provide more material to form the keels. It is unclear however whether new harzburgite would be cool and strong enough to survive this process, given the rapid overturn time-scales calculated. If this process is effective, it may even lead to subduction congestion and a subsequent return to stagnant lid convection. In this case, continuous tectonics would begin when the mantle has cooled down after a few overturns.

The lid breaking event can reproduce geological features of preserved Archean crust. The middle crust has been exposed in most Archean terranes, implying whole-craton exhumation of about 10 *km* (Collins et al. 1998; Sandiford et al. 2004; Flowers et al. 2004), by a predominately vertical mechanism, rather than crustal thickening (Van Kranendonk et al. 2007). This uplift has previously been modelled by Flowers et al. (2004) as a lowering of the lithospheric density at the scale and subsequent isostatic compensation, as a result of heating by heat-producing elements. Alternatively, the exhumation may the result of a dramatic lowering of river base levels, due to deepening of the oceans (Condie et al. 2009b). Our topographic calculation is relative and would still generate the required topographic contrast,

regardless of whether the ocean is deepening or cratons uplifting. The keel formation by lid breaking model predicts exhumation, without the need for heating, as a consequence of the high initial buoyancy the lithosphere requires in order to avoid recycling. The modest buoyancy of $B = 0.25$ generates the same magnitude of uplift as currently observed, occurring rapidly on a large scale when the mantle lid breaks off. Exhumation still results from isostatic compensation for thickened, buoyant lithosphere, but in this case marks the completion of the keel formation process. The keel heats in these models as a stable geotherm forms, but this has little impact on topography. Further significant uplift resulting from radioactive heating is difficult to incorporate into the model, as the keel would need to begin with a lower buoyancy to result in the same magnitude of uplift and $B = 0.25$ is close to the minimum B required for stability.

There would certainly be crustal deformation in some regions, particularly in order for the opening of oceans to occur. To accommodate the crustal strain, large scale thrusting must occur somewhere. This thrusting could be preserved in younger, weaker terranes such as the Yilgarn, which has a mixture of Pilbara-style internal buoyancy-driven deformation and significant subduction-style thrusting (Zibra et al. 2014; Drummond et al. 2000). The formation of the oldest preserved thrust sheets are thought to have formed as plate tectonics was beginning (Van Kranendonk et al. 2007) and it is feasible that these are remnants of crust which were still weak during the lid breaking event and record the regional compressional stress regime. Thickening of weak crust would result in the transport of some upper crustal fragments to great depths and in the case of devolatising serpentinised oceanic crust, could produce melting which was more similar to modern subduction zone melting than to the Early Archean intra-crustal melting (Smithies et al. 2003; Champion & Sheraton 1997). If the crust in and around the Yilgarn were weak at the lid scale and contained large volumes of serpentinite, this may explain the large scale melting and geochemical subduction signature of the granitic Yilgarn crust, without a modern subduction setting.

6.7 Conclusion

A new model for keel formation has been proposed, where strong crust and lithosphere is thickened by the anomalously high stresses generated during stagnant lid collapse. Mobile lid convection cannot generate the same stress magnitude, at least for a couple of billion years after formation, so subsequent keel deformation is prevented. The model explains the stability of keels over the past approximately three billion years since their formation. It is consistent with the likely evolution in mantle convection regimes as well as preserved geological features, such as uplift and mixed horizontal and vertical tectonics. The required buoyancy of continental material is similar to previous studies and is plausible, while a much

higher pre-thickening yield stress is required for stability than previously thought. Geochemical evolution during the stagnant lid mode can produce this strong lithosphere, which is a strength of the model as there is then little need for post thickening strengthening events to stabilise the keel. The lid breaking keel formation model is simple, but addresses difficulties in explaining keel stability and can make a variety of predictions about crustal and lithospheric evolution, which could further constrain the keel formation mechanism in future work.

Chapter 7

Conclusions

The dynamics of sub-continental gravitational instabilities and their interaction with the crust above have been explored using numerical and analytical modelling. The most fundamental result is the characterisation of the dripping and delamination mechanisms. While it has been shown that delamination evolves as a non-linear instability in the same way as the Rayleigh-Taylor Instability (dripping), for the same rheology it grows significantly more quickly. How much quicker, depends on a new scaling involving the relative strength of the lower crust decollement, though it is typically an order of magnitude. The rate at which dense material can be recycled from below a continent is therefore highly dependent on the mechanism which occurs, which in turn is highly dependent on the particular conditions which arise as a result of tectonics. There is also a third type of instability, triggered dripping, which is a mixture of dripping and delamination. It is difficult to distinguish triggered dripping from delamination, which is problematic as the former can evolve much more slowly than the latter. The range of mechanisms also means that the predicted instability growth-rate no longer depends simply on rheology, as the type of mechanism must be also determined. The theoretical characterisation of instabilities however leads to a general model of sub-continental recycling, where relatively strong bodies can only be delaminated, while weak material will tend to drip.

The characterisation of instability mechanisms with strongly contrasting growth-rates can lead to complicated recycling evolutions. Delamination can only occur if a weak decollement layer and large edge perturbation are present, and will switch back to dripping if these conditions cease. Such an instability would initially grow rapidly, before significantly slowing down once the mechanism transition occurs. This model explains why multiple instabilities have grown rapidly, but can still be observed in tomography. The prevalence of this mechanism switch supports the occurrence of delamination, albeit short lived, on the Earth, as dripping cannot be slowed down enough to produce this effect.

There are Rayleigh-Taylor Instability solutions for the growth of two unstable interfaces which are consistent with both dome and keel formation, at the specific wavelength observed and without superimposed strain, as well as restite recycling. The lower part of the greenstone cover is required to be weak, consistent with previous experimental data and modelling, and its weakening acts as a trigger for dome and keel formation. At the time as dome and keel formation, the restite and granitoid are likely to have had similar viscosities. Using this state as a reference, restite could plausibly drip away at a rapid time-scale, without for example requiring delamination. The limiting factor for restite recycling is the strength of the lithosphere below, which can effectively trap the restite if it is a similar thickness to the granitoid layer. However, once the restite layer thickens through progressive fractionation, it reaches a thickness at which instability becomes rapid again. Simultaneous instability of a thick restite layer is not consistent with the observed dome and keel formation, so either efficient restite recycling could occur through the lithosphere, or it was removed at a later time. Modern crust bears similarity to Archean crust in that it is generally restite-free and the upper crust is highly felsic. This end-member is reached on the modern Earth as a result of tectonic processes. Both dome and keel formation and restite dripping could have plausibly been driven by local buoyancy forces. Therefore a similar differentiation process could have occurred without tectonics, purely through Rayleigh-Taylor Instabilities.

When the stagnant lid breaks, the continental stresses generated by the subsequent instability are significantly higher than during the subsequent mobile lid regime. A new keel formation model has been subsequently proposed in which the preserved cratonic keels were thickened during the lid breaking event. Provided the keel stress states do not return to similar magnitudes as the lid breaking event, their stability through time can be a result of an initially high strength established through depleted lithosphere formation during the stagnant lid regime. The stress state could have returned to this high magnitude if Earth's convective stresses have increased by a value corresponding to two orders of magnitude decrease in Rayleigh number. Geochemical data indicates that stress at subduction zones peaked well below the lid breaking stress $\sim$ 1Ga. The lid breaking model then predicts that keels on the modern Earth should be stable, unless they are weakened, which is consistent with geochemical models of craton destruction. Significant exhumation of the upper crust at a regional scale is predicted to have occurred immediately after keel formation, at a magnitude which is consistent with preserved crust.

Bibliography

Abbott, D. H., Mooney, W. D., & VanTongeren, J. A., 2013. The character of the Moho and lower crust within Archean cratons and the tectonic implications, *Tectonophysics*, **609**, 690–705.

Artemieva, I. M. & Mooney, W. D., 2001. Thermal thickness and evolution of Precambrian lithosphere: a global study, *Journal of Geophysical Research: Solid Earth*, **106**(B8), 16387–16414.

Bajolet, F., Galeano, J., Funiciello, F., Moroni, M., Negredo, A.-M., & Faccenna, C., 2012. Continental delamination: Insights from laboratory models, *Geochemistry, Geophysics, Geosystems*, **13**(2).

Bao, X., Eaton, D. W., & Guest, B., 2014. Plateau uplift in western Canada caused by lithospheric delamination along a craton edge, *Nature Geoscience*, **7**(11), 830–833.

Bassi, G. & Bonnin, J., 1988. Rheological modelling and deformation instability of lithosphere under extension, *Geophysical Journal International*, **93**(3), 485–504.

Bédard, J. H., 2006. A catalytic delamination-driven model for coupled genesis of archaean crust and sub-continental lithospheric mantle, *Geochimica et Cosmochimica Acta*, **70**(5), 1188–1214.

Bercovici, D., 2003. The generation of plate tectonics from mantle convection, *Earth and Planetary Science Letters*, **205**(3), 107–121.

Bird, P., 1979. Continental delamination and the Colorado Plateau, *J. geophys. Res*, **84**(B13), 7561–7571.

Bird, P. & Baumgardner, J., 1981. Steady propagation of delamination events, *Journal of Geophysical Research: Solid Earth (1978–2012)*, **86**(B6), 4891–4903.

Bürgmann, R. & Dresen, G., 2008. Rheology of the lower crust and upper mantle: Evidence from rock mechanics, geodesy, and field observations, *Annual Review of Earth and Planetary Sciences*, **36**(1), 531.

Burov, E., Watts, A., et al., 2006. The long-term strength of continental lithosphere: "jelly sandwich" or "crème brûlée"?, *GSA Today*, **16**(1), 4.

Bystricky, M. & Mackwell, S., 2001. Creep of dry clinopyroxene aggregates, *Journal of Geophysical Research: Solid Earth (1978–2012)*, **106**(B7), 13443–13454.

Canright, D. & Morris, S., 1993. Buoyant instability of a viscous film over a passive fluid, *Journal of Fluid Mechanics*, **255**, 349–372.

Capitanio, F., Morra, G., & Goes, S., 2007. Dynamic models of downgoing plate-buoyancy driven subduction: Subduction motions and energy dissipation, *Earth and Planetary Science Letters*, **262**(1), 284–297.

Caristan, Y., 1982. The transition from high temperature creep to fracture in Maryland diabase, *Journal of Geophysical Research: Solid Earth*, **87**(B8), 6781–6790.

Cecil, M. R., Saleeby, Z., Saleeby, J., & Farley, K., 2014. Pliocene–quaternary subsidence and exhumation of the southeastern San Joaquin Basin, California, in response to mantle lithosphere removal, *Geosphere*, **10**(1), 129–147.

Champion, D. & Sheraton, J., 1997. Geochemistry and nd isotope systematics of Archaean granites of the Eastern Goldfields, Yilgarn Craton, Australia: implications for crustal growth processes, *Precambrian Research*, **83**(1), 109–132.

Chandrasekhar, S., 1961. Hydrodynamic and hydrostatic stability, *Clarendon, Oxford, England*.

Chopelas, A. & Boehler, R., 1992. Thermal expansivity in the lower mantle, *Geophysical Research Letters*, **19**(19), 1983–1986.

Collins, W., Kranendonk, V., MJ, & Teyssier, C., 1998. Partial convective overturn of Archaean crust in the east Pilbara craton, Western Australia: driving mechanisms and tectonic implications, *Journal of Structural Geology*, **20**(9), 1405–1424.

Condie, K. C., Belousova, E., Griffin, W., & Sircombe, K. N., 2009a. Granitoid events in space and time: constraints from igneous and detrital zircon age spectra, *Gondwana Research*, **15**(3), 228–242.

Condie, K. C., O'Neill, C., & Aster, R. C., 2009b. Evidence and implications for a widespread magmatic shutdown for 250 My on Earth, *Earth and Planetary Science Letters*, **282**(1), 294–298.

Conrad, C. & Molnar, P., 1999. Convective instability of a boundary layer with temperature-and strain-rate-dependent viscosity in terms of available buoyancy, *Geophysical Journal International*, **139**(1), 51–68.

Conrad, C. P. & Molnar, P., 1997. The growth of RayleighTaylor-type instabilities in the lithosphere for various rheological and density structures, *Geophysical Journal International*, **129**(1), 95–112.

Cooper, C., Lenardic, A., & Moresi, L., 2004. The thermal structure of stable continental lithosphere within a dynamic mantle, *Earth and Planetary Science Letters*, **222**(3), 807–817.

Cooper, C., Lenardic, A., Levander, A., & Moresi, L., 2006. Creation and preservation of cratonic lithosphere: seismic constraints and geodynamic models, *Archean Geodynamics and Environments*, pp. 75–88.

Crow, R., Karlstrom, K., Asmerom, Y., Schmandt, B., Polyak, V., & DuFrane, S. A., 2011. Shrinking of the Colorado Plateau via lithospheric mantle erosion: Evidence from Nd and Sr isotopes and geochronology of Neogene basalts, *Geology*, **39**(1), 27–30.

Davies, G. F., 1999. *Dynamic Earth: Plates, plumes and mantle convection*, Cambridge University Press.

de Bremond d'Ars, J., Lécuyer, C., & Reynard, B., 1999. Hydrothermalism and diapirism in the Archean: gravitational instability constraints, *Tectonophysics*, **304**(1), 29–39.

Dhuime, B., Hawkesworth, C. J., Cawood, P. A., & Storey, C. D., 2012. A change in the geodynamics of continental growth 3 billion years ago, *Science*, **335**(6074), 1334–1336.

Dhuime, B., Wuestefeld, A., & Hawkesworth, C. J., 2015. Emergence of modern continental crust about 3 billion years ago, *Nature Geoscience*, **8**(7), 552–555.

Drummond, B., Goleby, B., & Swager, C., 2000. Crustal signature of Late Archaean tectonic episodes in the Yilgarn craton, Western Australia: evidence from deep seismic sounding, *Tectonophysics*, **329**(1), 193–221.

Ducea, M. N. & Saleeby, J. B., 1998. The age and origin of a thick mafic–ultramafic keel from beneath the Sierra Nevada batholith, *Contributions to Mineralogy and Petrology*, **133**(1-2), 169–185.

Elkins-Tanton, L. T., 2007. Continental magmatism, volatile recycling, and a heterogeneous mantle caused by lithospheric gravitational instabilities, *Journal of Geophysical Research: Solid Earth*, **112**(B3).

Fillerup, M. A., Knapp, J. H., Knapp, C. C., & Raileanu, V., 2010. Mantle earthquakes in the absence of subduction? continental delamination in the Romanian Carpathians, *Lithosphere*, **2**(5), 333–340.

Flowers, R., Royden, L., & Bowring, S., 2004. Isostatic constraints on the assembly, stabilization, and preservation of cratonic lithosphere, *Geology*, **32**(4), 321–324.

Frank-Kamenetskii, D. A., 1969. *Diffusion and heat transfer in chemical kinetics*, Plenum Press.

Frassetto, A. M., Zandt, G., Gilbert, H., Owens, T. J., & Jones, C. H., 2011. Structure of the Sierra Nevada from receiver functions and implications for lithospheric foundering, *Geosphere*, **7**(4), 898–921.

Garzione, C. N., Hoke, G. D., Libarkin, J. C., Withers, S., MacFadden, B., Eiler, J., Ghosh, P., & Mulch, A., 2008. Rise of the Andes, *science*, **320**(5881), 1304–1307.

Gerya, T., 2009. *Introduction to numerical geodynamic modelling*, Cambridge University Press.

Gerya, T. V., Connolly, J. A., & Yuen, D. A., 2008. Why is terrestrial subduction one-sided?, *Geology*, **36**(1), 43–46.

Gerya, T. V., Stern, R., Baes, M., Sobolev, S., & Whattam, S., 2015. Plate tectonics on the Earth triggered by plume-induced subduction initiation, *Nature*, **527**(7577), 221–225.

Gilbert, H., Yang, Y., Forsyth, D., Jones, C., Owens, T., Zandt, G., & Stachnik, J., 2012. Imaging lithospheric foundering in the structure of the Sierra Nevada, *Geosphere*, **8**(6), 1310–1330.

Göğüş, O. H., 2015. Rifting and subsidence following lithospheric removal in continental back arcs, *Geology*, **43**(1), 3–6.

Göğüş, O. H. & Pysklywec, R. N., 2008a. Near-surface diagnostics of dripping or delaminating lithosphere, *Journal of Geophysical Research: Solid Earth (1978–2012)*, **113**(B11).

Göğüş, O. H. & Pysklywec, R. N., 2008b. Mantle lithosphere delamination driving plateau uplift and synconvergent extension in eastern anatolia, *Geology*, **36**(9), 723–726.

Göğüş, O. H., Pysklywec, R. N., & Faccenna, C., 2016. Postcollisional lithospheric evolution of the Southeast Carpathians: Comparison of geodynamical models and observations, *Tectonics*.

Gorczyk, W., Hobbs, B., & Gerya, T., 2012. Initiation of Rayleigh–Taylor instabilities in intra-cratonic settings, *Tectonophysics*, **514**, 146–155.

Griffin, W., Andi, Z., O'reilly, S., & Ryan, C., 1998. Phanerozoic evolution of the lithosphere beneath the sino-korean craton, *Mantle dynamics and plate interactions in East Asia*, pp. 107–126.

Griffin, W., OReilly, S., Abe, N., Aulbach, S., Davies, R., Pearson, N., Doyle, B., & Kivi, K., 2003. The origin and evolution of Archean lithospheric mantle, *Precambrian Research*, **127**(1), 19–41.

Hawkesworth, C. & Kemp, A., 2006. Evolution of the continental crust, *Nature*, **443**(7113), 811–817.

Hetényi, G., Stuart, G. W., Houseman, G. A., Horváth, F., Hegedűs, E., & Brückl, E., 2009. Anomalously deep mantle transition zone below Central Europe: evidence of lithospheric instability, *Geophysical Research Letters*, **36**(21).

Hilairet, N. & Reynard, B., 2009. Stability and dynamics of serpentinite layer in subduction zone, *Tectonophysics*, **465**(1), 24–29.

Hilairet, N., Reynard, B., Wang, Y., Daniel, I., Merkel, S., Nishiyama, N., & Petitgirard, S., 2007. High-pressure creep of serpentine, interseismic deformation, and initiation of subduction, *Science*, **318**(5858), 1910–1913.

Horváth, F., Bada, G., Szafián, P., Tari, G., Ádám, A., & Cloetingh, S., 2006. Formation and deformation of the Pannonian Basin: constraints from observational data, *Geological Society, London, Memoirs*, **32**(1), 191–206.

Houseman, G. & Molnar, P., 2001. Mechanisms of lithospheric rejuvenation associated with continental orogeny, *Geological Society, London, Special Publications*, **184**(1), 13–38.

Houseman, G. A. & Gemmer, L., 2007. Intra-orogenic extension driven by gravitational instability: Carpathian-Pannonian orogeny, *Geology*, **35**(12), 1135–1138.

Houseman, G. A. & Molnar, P., 1997. Gravitational (Rayleigh–Taylor) instability of a layer with non-linear viscosity and convective thinning of continental lithosphere, *Geophysical Journal International*, **128**(1), 125–150.

Hughes, T. J., 2012. *The finite element method: linear static and dynamic finite element analysis*, Courier Corporation.

Johnson, T. E., Brown, M., Kaus, B. J., & VanTongeren, J. A., 2014. Delamination and recycling of Archaean crust caused by gravitational instabilities, *Nature Geoscience*, **7**(1), 47–52.

Jones, C. H., Farmer, G. L., & Unruh, J., 2004. Tectonics of pliocene removal of lithosphere of the Sierra Nevada, California, *Geological Society of America Bulletin*, **116**(11-12), 1408–1422.

Jones, C. H., Reeg, H., Zandt, G., Gilbert, H., Owens, T. J., & Stachnik, J., 2014. P-wave tomography of potential convective downwellings and their source regions, Sierra Nevada, California, *Geosphere*, **10**(3), 505–533.

Jordan, T. H., 1975. The continental tectosphere, *Reviews of Geophysics*, **13**(3), 1–12.

Jordan, T. H., 1978. Composition and development of the continental tectosphere, *Nature*, **274**(5671), 544–548.

Jordan, T. H., 1988. Structure and formation of the continental tectosphere, *Journal of Petrology*, (1), 11–37.

Jull, M. & Kelemen, P., 2001. On the conditions for lower crustal convective instability, *Journal of Geophysical Research: Solid Earth*, **106**(B4), 6423–6446.

Kankanamge, D. G. & Moore, W. B., 2016. Heat transport in the Hadean mantle: From heat pipes to plates, *Geophysical Research Letters*, **43**(7), 3208–3214.

Kaus, B. J. & Podladchikov, Y. Y., 2001. Forward and reverse modeling of the three-dimensional viscous Rayleigh-Taylor instability, *Geophysical Research Letters*, **28**(6), 1095–1098.

Korenaga, J., 2016. Can mantle convection be self-regulated?, *Science Advances*, **2**(8), e1601168.

Kreemer, C., Haines, J., Holt, W. E., Blewitt, G., & Lavallee, D., 2000. On the determination of a global strain rate model, *Earth, Planets and Space*, **52**(10), 765–770.

Lamb, S., 2011. Cenozoic tectonic evolution of the New Zealand plate-boundary zone: A paleomagnetic perspective, *Tectonophysics*, **509**(3), 135–164.

Le Pourhiet, L., Gurnis, M., & Saleeby, J., 2006. Mantle instability beneath the Sierra Nevada mountains in California and death valley extension, *Earth and Planetary Science Letters*, **251**(1), 104–119.

Lee, C.-T., 2014. 4.12 - physics and chemistry of deep continental crust recycling, in *Treatise on Geochemistry (Second Edition)*, pp. 423 – 456, eds Holland, H. D. & Turekian, K. K., Elsevier, Oxford, second edition edn.

Lee, C.-T., Yin, Q., Rudnick, R. L., & Jacobsen, S. B., 2001. Preservation of ancient and fertile lithospheric mantle beneath the southwestern United States, *Nature*, **411**(6833), 69–73.

Lee, C.-T. A., 2006. Geochemical/petrologic constraints on the origin of cratonic mantle, *Archean geodynamics and environments*, pp. 89–114.

Lee, C.-T. A., Cheng, X., & Horodyskyj, U., 2006. The development and refinement of continental arcs by primary basaltic magmatism, garnet pyroxenite accumulation, basaltic recharge and delamination: insights from the Sierra Nevada, California, *Contributions to Mineralogy and Petrology*, **151**(2), 222–242.

Lee, C.-T. A., Luffi, P., Höink, T., Li, Z.-X. A., & Lenardic, A., 2008. The role of serpentine in preferential craton formation in the late Archean by lithosphere underthrusting, *Earth and Planetary Science Letters*, **269**(1), 96–104.

Lee, C.-T. A., Luffi, P., & Chin, E. J., 2011. Building and destroying continental mantle, *Annual Review of Earth and Planetary Sciences*, **39**, 59–90.

Leitch, A., Yuen, D., & Sewell, G., 1991. Mantle convection with internal heating and pressure-dependent thermal expansivity, *Earth and Planetary Science Letters*, **102**(2), 213–232.

Lenardic, A. & Kaula, W., 1996. Near-surface thermal/chemical boundary layer convection at infinite Prandtl number: two-dimensional numerical experiments, *Geophysical Journal International*, **126**(3), 689–711.

Lenardic, A., Moresi, L., & Mühlhaus, H., 2000. The role of mobile belts for the longevity of deep cratonic lithosphere: the crumple zone model, *Geophysical Research Letters*, **27**(8), 1235–1238.

Lenardic, A., Moresi, L.-N., & Mühlhaus, H., 2003. Longevity and stability of cratonic lithosphere: insights from numerical simulations of coupled mantle convection and continental tectonics, *Journal of Geophysical Research: Solid Earth*, **108**(B6).

Levander, A., Schmandt, B., Miller, M., Liu, K., Karlstrom, K., Crow, R., Lee, C.-T., & Humphreys, E., 2011. Continuing colorado plateau uplift by delamination-style convective lithospheric downwelling, *Nature*, **472**(7344), 461–465.

Lin, S., 2005. Synchronous vertical and horizontal tectonism in the neoarchean: Kinematic evidence from a synclinal keel in the northwestern Superior craton, Canada, *Precambrian Research*, **139**(3), 181–194.

Lorinczi, P. & Houseman, G., 2009. Lithospheric gravitational instability beneath the Southeast Carpathians, *Tectonophysics*, **474**(1), 322–336.

Manley, C. R., Glazner, A. F., & Farmer, G. L., 2000. Timing of volcanism in the Sierra Nevada of California: Evidence for pliocene delamination of the batholithic root?, *Geology*, **28**(9), 811–814.

Mareschal, J.-C. & West, G. F., 1980. A model for Archean tectonism. part 2. numerical models of vertical tectonism in greenstone belts, *Canadian Journal of Earth Sciences*, **17**(1), 60–71.

Martin, H., Smithies, R., Rapp, R., Moyen, J.-F., & Champion, D., 2005. An overview of adakite, tonalite–trondhjemite–granodiorite (TTG), and sanukitoid: relationships and some implications for crustal evolution, *Lithos*, **79**(1), 1–24.

McEwan, A. & Taylor, G., 1966. The peeling of a flexible strip attached by a viscous adhesive, *Journal of Fluid Mechanics*, **26**(01), 1–15.

McKenzie, D. & Priestley, K., 2008. The influence of lithospheric thickness variations on continental evolution, *Lithos*, **102**(1), 1–11.

Molnar, P. & Houseman, G. A., 2013. Rayleigh-Taylor instability, lithospheric dynamics, surface topography at convergent mountain belts, and gravity anomalies, *Journal of Geophysical Research: Solid Earth*, **118**(5), 2544–2557.

Molnar, P. & Jones, C. H., 2004. A test of laboratory based rheological parameters of olivine from an analysis of late cenozoic convective removal of mantle lithosphere beneath the Sierra Nevada, California, usa, *Geophysical Journal International*, **156**(3), 555–564.

Molnar, P., England, P. C., & Jones, C. H., 2015. Mantle dynamics, isostasy, and the support of high terrain, *Journal of Geophysical Research: Solid Earth*, **120**(3), 1932–1957.

Moore, W. B. & Webb, A. A. G., 2013. Heat-pipe earth, *Nature*, **501**(7468), 501–505.

Morency, C. & Doin, M.-P., 2004. Numerical simulations of the mantle lithosphere delamination, *Journal of Geophysical Research: Solid Earth (1978–2012)*, **109**(B3).

Moresi, L. & Solomatov, V., 1998. Mantle convection with a brittle lithosphere: thoughts on the global tectonic styles of the Earth and Venus, *Geophysical Journal International*, **133**(3), 669–682.

Moresi, L., Muhlhaus, H., & Dufour, F., 2001. Particle-in-cell solutions for creeping viscous flows with internal interfaces, *In Bifurcation and Localization in Soils and Rocks*, pp. 345–353.

Moresi, L., Quenette, S., Lemiale, V., Meriaux, C., Appelbe, B., & Mühlhaus, H.-B., 2007. Computational approaches to studying non-linear dynamics of the crust and mantle, *Physics of the Earth and Planetary Interiors*, **163**(1), 69–82.

Moresi, L.-N. & Solomatov, V., 1995. Numerical investigation of 2D convection with extremely large viscosity variations, *Physics of Fluids (1994-present)*, **7**(9), 2154–2162.

Neil, E. A. & Houseman, G. A., 1999. Rayleigh–Taylor instability of the upper mantle and its role in intraplate orogeny, *Geophysical Journal International*, **138**(1), 89–107.

O'Neill, C., Lenardic, A., Moresi, L., Torsvik, T., & Lee, C.-T., 2007. Episodic Precambrian subduction, *Earth and Planetary Science Letters*, **262**(3), 552–562.

O'Neill, C., Lenardic, A., Griffin, W., & O'Reilly, S. Y., 2008. Dynamics of cratons in an evolving mantle, *Lithos*, **102**(1), 12–24.

ONeill, C., Lenardic, A., Weller, M., Moresi, L., Quenette, S., & Zhang, S., 2016. A window for plate tectonics in terrestrial planet evolution?, *Physics of the Earth and Planetary Interiors*, **255**, 80–92.

Paczkowski, K., Bercovici, D., Landuyt, W., & Brandon, M. T., 2012. Drip instabilities of continental lithosphere: acceleration and entrainment by damage, *Geophysical Journal International*, **189**(2), 717–729.

Parsons, B. & McKenzie, D., 1978. Mantle convection and the thermal structure of the plates, *J. geophys. Res*, **83**(B9), 4485–4496.

Pecskay, Z., Lexa, J., Szakacs, A., Seghedi, I., Balogh, K., Konecny, V., Zelenka, T., Kovacs, M., Poka, T., Fulop, A., et al., 2006. Geochronology of neogene magmatism in the Carpathian arc and intra-Carpathian area, *GEOLOGICA CARPATHICA-BRATISLAVA-*, **57**(6), 511.

Pederson, J. L., Mackley, R. D., & Eddleman, J. L., 2002. Colorado Plateau uplift and erosion evaluated using GIS, *GSA Today*, **12**(8), 4–10.

Peschler, A., Benn, K., & Roest, W., 2004. Insights on Archean continental geodynamics from gravity modelling of granite–greenstone terranes, *Journal of Geodynamics*, **38**(2), 185–207.

Polet, J. & Anderson, D. L., 1995. Depth extent of cratons as inferred from tomographic studies, *Geology*, **23**(3), 205–208.

Pollack, H. N., Hurter, S. J., & Johnson, J. R., 1993. Heat flow from the Earth's interior: analysis of the global data set, *Reviews of Geophysics*, **31**(3), 267–280.

Poudjom Djomani, Y., OReilly, S., & Griffin, W., 2001. The density structure of subcontinental lithosphere through time, *Earth and Planetary Science Letters*.

Pysklywec, R. N. & Beaumont, C., 2004. Intraplate tectonics: feedback between radioactive thermal weakening and crustal deformation driven by mantle lithosphere instabilities, *Earth and Planetary Science Letters*, **221**(1), 275–292.

Raleigh, C. & Paterson, M., 1965. Experimental deformation of serpentinite and its tectonic implications, *Journal of Geophysical Research*, **70**(16), 3965–3985.

Reid, M. R., Bouchet, R. A., Blichert-Toft, J., Levander, A., Liu, K., Miller, M. S., & Ramos, F. C., 2012. Melting under the Colorado Plateau, USA, *Geology*, **40**(5), 387–390.

Rey, P. F., Coltice, N., & Flament, N., 2014. Spreading continents kick-started plate tectonics, *Nature*, **513**(7518), 405–408.

Reynard, B., 2013. Serpentine in active subduction zones, *Lithos*, **178**, 171–185.

Ribe, N., 1998. Spouting and planform selection in the Rayleigh–Taylor instability of miscible viscous fluids, *Journal of Fluid Mechanics*, **377**, 27–45.

Robin, C. & Bailey, R., 2009. Simultaneous generation of Archean crust and subcratonic roots by vertical tectonics, *Geology*, **37**(6), 523–526.

Roy, M., Jordan, T. H., & Pederson, J., 2009. Colorado Plateau magmatism and uplift by warming of heterogeneous lithosphere, *Nature*, **459**(7249), 978–982.

Rudnick, R. L. et al., 1995. Making continental crust, *Nature*, **378**(6557), 571–577.

Rudnick, R. L. & Fountain, D. M., 1995. Nature and composition of the continental crust: a lower crustal perspective, *Reviews of geophysics*, **33**(3), 267–309.

Rutter, E., Brodie, K., & Irving, D., 2006. Flow of synthetic, wet, partially molten granite under undrained conditions: an experimental study, *Journal of Geophysical Research: Solid Earth (1978–2012)*, **111**(B6).

Saleeby, J. & Foster, Z., 2004. Topographic response to mantle lithosphere removal in the southern Sierra Nevada region, California, *Geology*, **32**(3), 245–248.

Saleeby, J., Ducea, M., & Clemens-Knott, D., 2003. Production and loss of high-density batholithic root, southern Sierra Nevada, California, *Tectonics*, **22**(6).

Saleeby, J., Le Pourhiet, L., Saleeby, Z., & Gurnis, M., 2012. Epeirogenic transients related to mantle lithosphere removal in the southern Sierra Nevada region, California, part I: Implications of thermo-mechanical modeling, *Geosphere*, **8**(6), 1286–1309.

Saleeby, J., Saleeby, Z., & Le Pourhiet, L., 2013. Epeirogenic transients related to mantle lithosphere removal in the southern Sierra Nevada region, California: Part II. implications of rock uplift and basin subsidence relations, *Geosphere*, **9**(3), 394–425.

Sandiford, M., 2010. Why are the continents just so?, *Journal of Metamorphic Geology*, **28**(6), 569–577.

Sandiford, M., Van Kranendonk, M. J., & Bodorkos, S., 2004. Conductive incubation and the origin of dome-and-keel structure in Archean granite-greenstone terrains: A model based on the eastern Pilbara craton, western australia, *Tectonics*, **23**(1).

Sandu, C., Lenardic, A., O'Neill, C., & Cooper, C., 2011. Earth's evolving stress state and the past, present, and future stability of cratonic lithosphere, *International Geology Review*, **53**(11-12), 1392–1402.

Schmandt, B. & Humphreys, E., 2010. Complex subduction and small-scale convection revealed by body-wave tomography of the western United States upper mantle, *Earth and Planetary Science Letters*, **297**(3), 435–445.

Schubert, G., Turcotte, D. L., & Olson, P., 2001. *Mantle convection in the Earth and planets*, Cambridge University Press.

Smithies, R. & Champion, D., 2000. The Archaean high-mg diorite suite: links to tonalite–trondhjemite–granodiorite magmatism and implications for early Archaean crustal growth, *Journal of Petrology*, **41**(12), 1653–1671.

Smithies, R., Champion, D., & Cassidy, K., 2003. Formation of Earths early Archaean continental crust, *Precambrian Research*, **127**(1), 89–101.

Solomatov, V. & Moresi, L.-N., 1997. Three regimes of mantle convection with non-Newtonian viscosity and stagnant lid convection on the terrestrial planets, *Geophysical Research Letters*, **24**(15), 1907–1910.

Solomatov, V. & Moresi, L.-N., 2000. Scaling of time-dependent stagnant lid convection: Application to small-scale convection on Earth and other terrestrial planets, *Journal of Geophysical Research: Solid Earth*, **105**(B9), 21795–21817.

Stern, T., Houseman, G., Salmon, M., & Evans, L., 2013. Instability of a lithospheric step beneath western North Island, New Zealand, *Geology*, **41**(4), 423–426.

Stock, G. M., Anderson, R. S., & Finkel, R. C., 2005. Rates of erosion and topographic evolution of the Sierra Nevada, California, inferred from cosmogenic 26Al and 10Be concentrations, *Earth Surface Processes and Landforms*, **30**(8), 985–1006.

Taylor, S. R. & McLennan, S. M., 1995. The geochemical evolution of the continental crust, *Reviews of Geophysics*, **33**(2), 241–265.

Tesauro, M., Kaban, M. K., & Cloetingh, S. A., 2012. Global strength and elastic thickness of the lithosphere, *Global and Planetary Change*, **90**, 51–57.

Thébaud, N. & Rey, P., 2013. Archean gravity-driven tectonics on hot and flooded continents: Controls on long-lived mineralised hydrothermal systems away from continental margins, *Precambrian Research*, **229**, 93–104.

Turcotte, D. L. & Schubert, G., 2014. *Geodynamics*, Cambridge University Press.

van Hunen, J. & van den Berg, A. P., 2008. Plate tectonics on the early Earth: limitations imposed by strength and buoyancy of subducted lithosphere, *Lithos*, **103**(1), 217–235.

van Hunen, J., Van Den BERG, A. P., & Vlaar, N. J., 2002. On the role of subducting oceanic plateaus in the development of shallow flat subduction, *Tectonophysics*, **352**(3), 317–333.

Van Kranendonk, M. J., 2011. Cool greenstone drips and the role of partial convective overturn in Barberton greenstone belt evolution, *Journal of African Earth Sciences*, **60**(5), 346–352.

Van Kranendonk, M. J., Collins, W., Hickman, A., & Pawley, M. J., 2004. Critical tests of vertical vs. horizontal tectonic models for the Archaean East Pilbara granite–greenstone terrane, Pilbara craton, western Australia, *Precambrian Research*, **131**(3), 173–211.

Van Kranendonk, M. J., Hugh Smithies, R., Hickman, A. H., & Champion, D., 2007. Review: secular tectonic evolution of Archean continental crust: interplay between horizontal and vertical processes in the formation of the Pilbara craton, Australia, *Terra Nova*, **19**(1), 1–38.

Van Kranendonk, M. J., Smithies, R. H., Griffin, W. L., Huston, D. L., Hickman, A. H., Champion, D. C., Anhaeusser, C. R., & Pirajno, F., 2015. Making it thick: a volcanic plateau origin of Palaeoarchean

continental lithosphere of the Pilbara and Kaapvaal cratons, *Geological Society, London, Special Publications*, **389**(1), 83–111.

Van Thienen, P., Van den Berg, A., & Vlaar, N., 2004. Production and recycling of oceanic crust in the early Earth, *Tectonophysics*, **386**(1), 41–65.

Van Wijk, J., Baldridge, W., Van Hunen, J., Goes, S., Aster, R., Coblentz, D., Grand, S., & Ni, J., 2010. Small-scale convection at the edge of the Colorado Plateau: Implications for topography, magmatism, and evolution of Proterozoic lithosphere, *Geology*, **38**(7), 611–614.

Wakabayashi, J. & Sawyer, T. L., 2001. Stream incision, tectonics, uplift, and evolution of topography of the Sierra Nevada, California, *The Journal of Geology*, **109**(5), 539–562.

Wang, H. & Currie, C. A., 2015. Magmatic expressions of continental lithosphere removal, *Journal of Geophysical Research: Solid Earth*.

Weinberg, R. F. & Podladchikov, Y. Y., 1995. The rise of solid-state diapirs, *Journal of Structural Geology*, **17**(8), 1183–1195.

Whitney, D. L., Teyssier, C., & Vanderhaeghe, O., 2004. Gneiss domes and crustal flow, *Geological Society of America Special Papers*, **380**, 15–33.

Wortel, M. & Spakman, W., 2000. Subduction and slab detachment in the Mediterranean-Carpathian region, *Science*, **290**(5498), 1910–1917.

Yuan, H., 2015. Secular change in Archaean crust formation recorded in Western Australia, *Nature Geoscience*, **8**(10), 808–813.

Zandt, G., Gilbert, H., Owens, T. J., Ducea, M., Saleeby, J., & Jones, C. H., 2004. Active foundering of a continental arc root beneath the southern Sierra Nevada in California, *Nature*, **431**(7004), 41–46.

Zibra, I., Gessner, K., Smithies, H., & Peternell, M., 2014. On shearing, magmatism and regional deformation in Neoarchean granite-greenstone systems: Insights from the Yilgarn Craton, *Journal of Structural Geology*, **67**, 253–267.